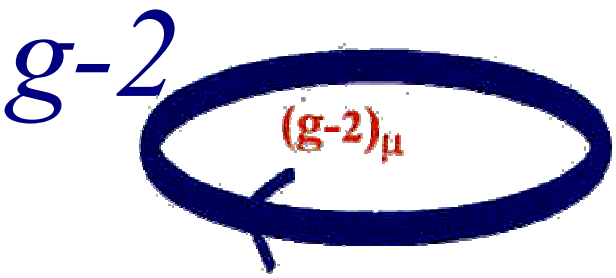

Brookhaven National Laboratory

Brookhaven Science Associates

Upton, New York 11973

Muon g-2 Note No. 421

Title: **Multiparameter ω_a Analysis for the g-2 Data from 2000**

Author: **M. Deile**

Affiliation: **Yale University**

Date: **August 26, 2002**

Multiparameter ω_a Analysis of the g-2 Data from 2000

M. Deile
Yale University

August 26, 2002

Version 1.0

Abstract

The present report describes an ω_a analysis for the g-2 data of the run period in the year 2000. The muon spin precession frequency ω_a was determined by fitting a multiparameter function to the combined positron time spectrum from all 22 usable calorimeters in the g-2 ring.

Three fit functions differring in their degree of accounting for the three aspects of coherent betatron oscillations were applied to the data and compared.

An additional feature of this analysis is the distinction of several run sub-periods with different beam focussing field indices n.

In this document the fit results for R are given with my own secret offset. To convert these numbers into the ones with the official offset, you need to add $+37.811\,\mathrm{ppm}$ to mine.

Our best result comes from a fit incorporating the CBO modulations of acceptance and asymmetry but not the phase modulations. For the latter a systematic error was assigned instead. With the official offset our final number is

$$R = (128.57 \pm 0.64 \pm 0.35)\,\mathrm{ppm}.$$

Contents

1 Data Production

This analysis is based on the g2off data production [1].

2 Run Selection and Division into Run Periods

The run selection by E. Sichtermann [2] was used.

For systematic studies this run list was divided into several periods reflecting changes in the operating parameters of the experimental hardware. The periods are defined in Table 1.

Period	Runs	Comments
1a	6369 - 6621	$f_{\mathrm{CBO}}(50\,\mu\mathrm{s}) \approx 474.1\,\mathrm{kHz}$
1b	6712 - 7151	$f_{\mathrm{CBO}}(50\,\mu\mathrm{s}) \approx 468.3\,\mathrm{kHz}$
2	7226 - 7445	$f_{\mathrm{CBO}}(50\,\mu\mathrm{s}) \approx 465.0\,\mathrm{kHz}$, hardware thresholds changed
3	7446 - 8350	$f_{\mathrm{CBO}}(50\,\mu\mathrm{s}) \approx 465.8\,\mathrm{kHz}$, hardware thresholds changed
4	8351 - 8821	$f_{\mathrm{CBO}}(50\,\mu\mathrm{s}) \approx 466.8\,\mathrm{kHz}$, radial magnetic field changed
0	all runs	just a name convention

Table 1: *Run periods and the reasons for their distinction.*

The main reason for splitting the data in run periods is the variation of the CBO frequency shown in Figure 1. The band structure reflects the frequency resolution $\frac{1}{\text{time range}} = \frac{1}{567\,\mu\mathrm{s}} = 1.76\,\mathrm{kHz}$ of the FFT.

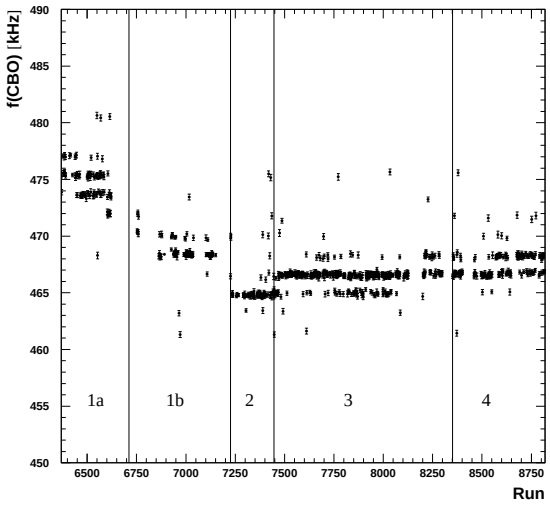

Figure 1: *CBO frequency versus run. Each run was fitted with a 5 parameter function (not accounting for the CBO). Then the residuals (data - fit) were Fourier transformed. The frequencies shown in the plot were obtained by taking the weighted mean of the 7 frequency bins around the CBO peak.*

The changes of the hardware threshold has an impact on the pileup subtraction technique, see Section 4.4. Finally, the radial magnetic field change which moved the beam up by 2 mm into the centre of the storage volume, reduced the muon losses by improving the scraping efficiency.

Apart from the hardware threshold changes, periods 2 and 3 are very similar. In particular, they have almost the same CBO frequency. Therefore, they are only distinguished for pileup subtraction, but joined for the fits.

3 Fill Selection

3.1 Quadrupole Cuts

A fill passes the quadrupole selection if the following criteria are met:

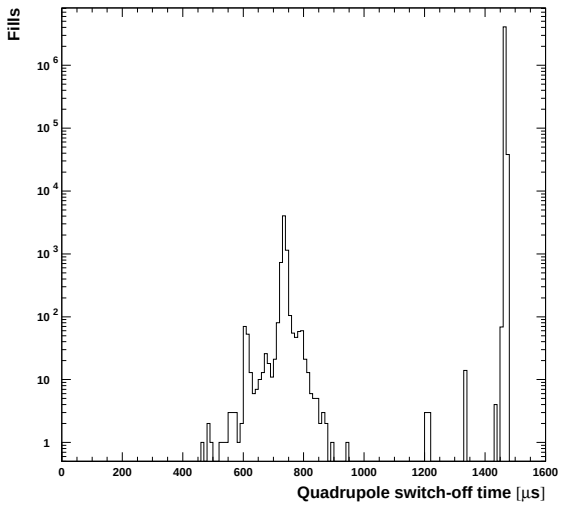

Figure 2: *Distribution of the time when the quadrupole voltage was switched off, with respect to injection time. Note the log scale.*

- The quadrupoles are on for at least $700\,\mu$s after injection. The distribution of quadrupole switch-off times is shown in Figure 2.
- The scraping amplitudes (second minus first quadrupole voltage reading) must be within the limits shown in Figure 3.
- The second and third quadrupole reading must be equal within the limits shown in Figure 4. This requirement discards fills with quadrupole sparks.
- The individual quadrupole readings must lie within $5 \times$ RMS of their distributions.

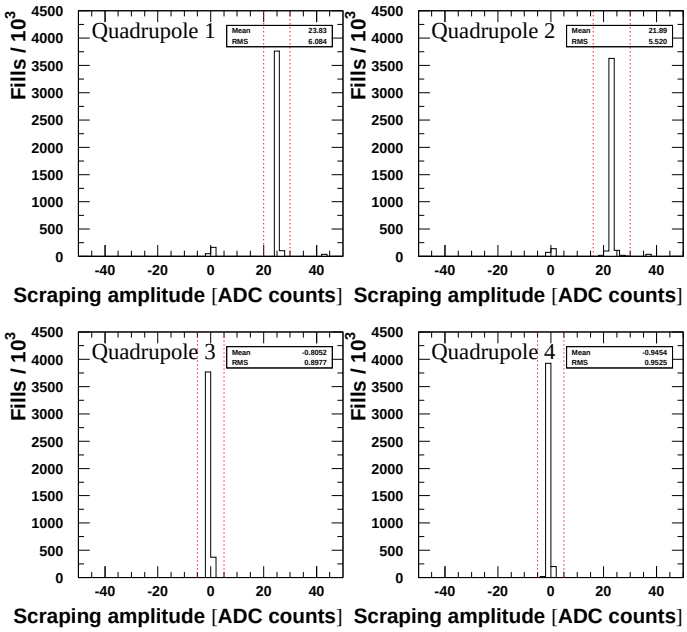

Figure 3: *Distribution of the scraping amplitudes in the four quadrupoles. The dotted lines represent the cuts applied. Quadrupoles 3 and 4 didn't have any scraping.*

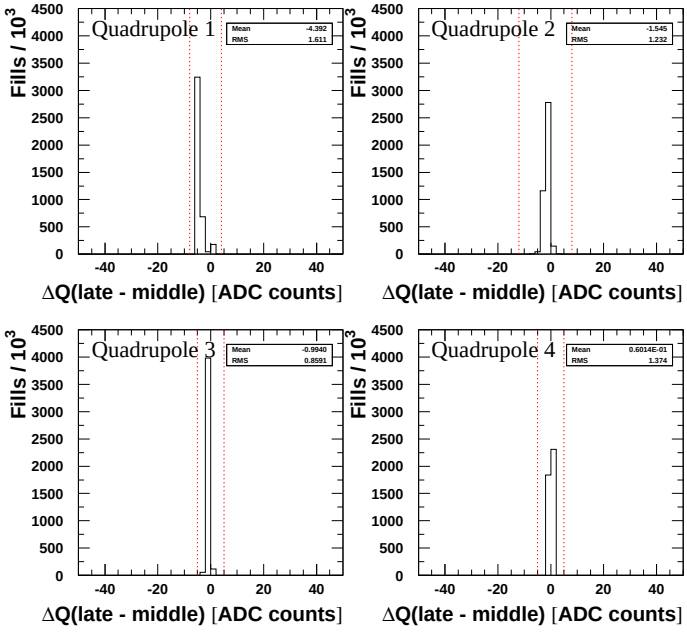

Figure 4: *Distribution of the difference between the third and the second voltage measurement in the four quadrupoles. The dotted lines represent the cuts applied.*

3.2 T0 Cuts

T0 cuts were derived from the distributions of T0 pulse amplitudes and mean times. Outlier fills are discarded.

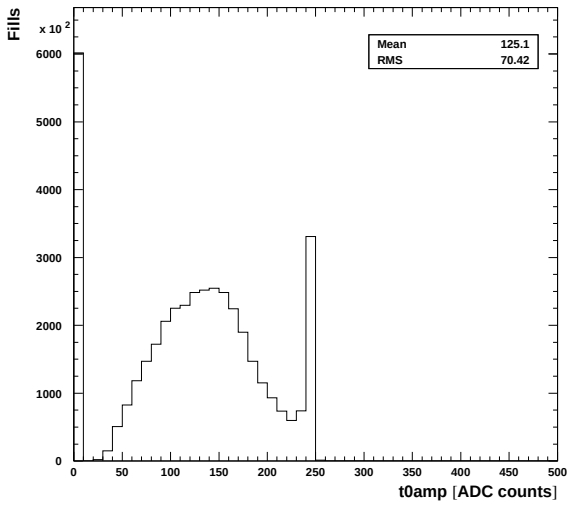

Figure 5: *Distribution of the T0 pulse amplitude. Each entry corresponds to one fill. The spike at 240 comes from the second T0 period (see Table 2) and may be caused by ADC saturation.*

- The pulse amplitude is required to be greater than 30 (see Figure 5).
- The pulse mean time must lie between 50000 ns and 60000 ns (Figure 6). This cut is not very tight and mainly designed for discarding fills without T0 pulse (**t0mean** = 0).

3.3 Laser Cut

Fills with laser pulses in the analysed time window (20 μs to 700 μs) were discarded.

4 Construction of the Positron Decay Time Spectra

4.1 Energy calibration

The energy-spectrum end-points (corresponding to 3.2 GeV) determined by E. Sichtermann were used.

4.2 T0 subtraction

Since the T0 time changed twice, the following run periods were distinguished (see also Figure 6):

Runs	average T0 mean [ns]
6369 - 6439	56620
6440 - 6972	56390
6973 - 8821	56500

Table 2: *T0 run periods.*

These T0 run periods don't coincide with the periods defined in Section 2.

To obtain the positron pulse times with respect to the T0 pulse, the mean time of the T0 pulse (ntuple variable **t0mean**) was averaged over all fills in the respective T0 run period, and this average subtracted from the raw pulse times.

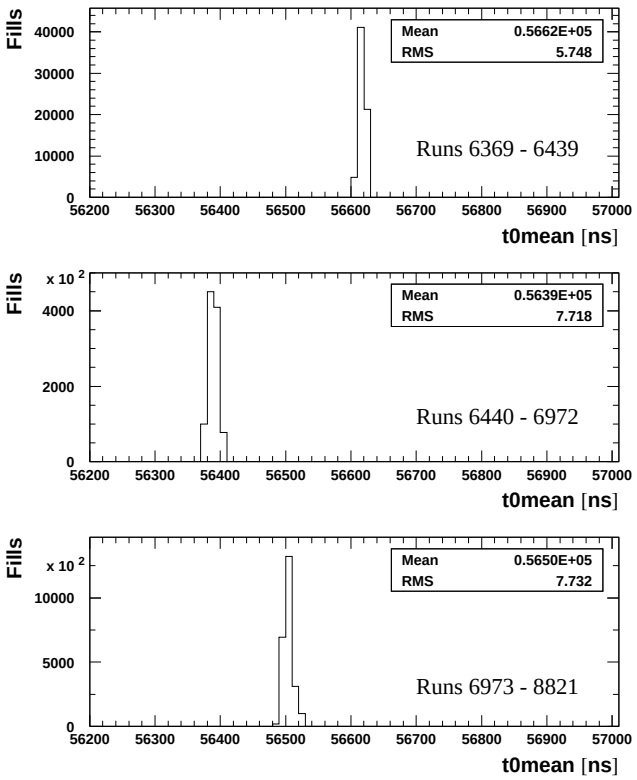

Figure 6: *Distributions of the mean time of the T0 pulse for the three T0 run periods defined in Table 2. Each entry corresponds to one fill.*

The fast rotation peaks were used to correct for differences in the signal propagation times: All detectors were aligned in time such that the fast rotation peaks of two neighbouring detectors were separated by $T_{\mathrm{cyclotron}}/24. = 149.2105\,\mathrm{ns}\ /\ 24.$.

4.3 Binning and Randomisation

For each detector and each run a time spectrum was created. The bin width of the time spectra was 149.2105 ns, i.e. the fast rotation period determined by Cenap with a Fourier analysis [3]. Before filling the individual positron times into their histograms, they were randomised by adding a fill-specific random number taken from a flat distribution in the range $[-\frac{149.2105\,\mathrm{ns}}{2}, +\frac{149.2105\,\mathrm{ns}}{2}]$. This was done to remove the fast rotation structure from the data.

4.4 Pileup Subtraction

Pileup was subtracted with the "Mediterranean Method" [4]. The lower energy cut was 2 GeV.

The time window where shadow pulses ("S2") for the construction of the artificial pileup were looked for, had its centre 13 ns after the trigger pulse ("S1"). The window width was twice the g2off pulse fitter dead time. This dead-time is detector-specific and depends on the energy E_{S2} of the shadow pulse. It is typically about 2.9 ns. The detector and energy dependence of the dead-time (Figure 7) was provided by Vanya [5] who had obtained them from a simulation.

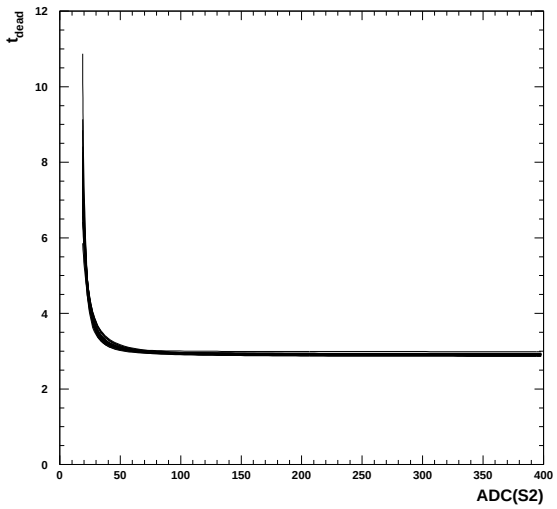

Figure 7: *Deadtime of the pulse finding algorithm as a function of the pulse height of S2 in terms of ADC counts. The conversion from ADC to energy is detector dependent (Section 4.1). Typically ADC = 60 corresponds to 1 GeV. The curves for all detectors are superimposed.*

Also, the energy E_D of a constructed double pulse was calculated from the energies E_{S1} and E_{S2} of the two individual overlapping pulses, using Vanya's simulation results:

$$E_{\mathrm{D}} = f_L(E_{S1}, E_{S2}) \cdot (E_{S1} + E_{S2}) \quad , \tag{1}$$

where the function $f_L(E_{S1}, E_{S2})$ replaces the constant "Logashenko coefficient" of 0.96 which had been used in the past. This function is shown in Figure 8.

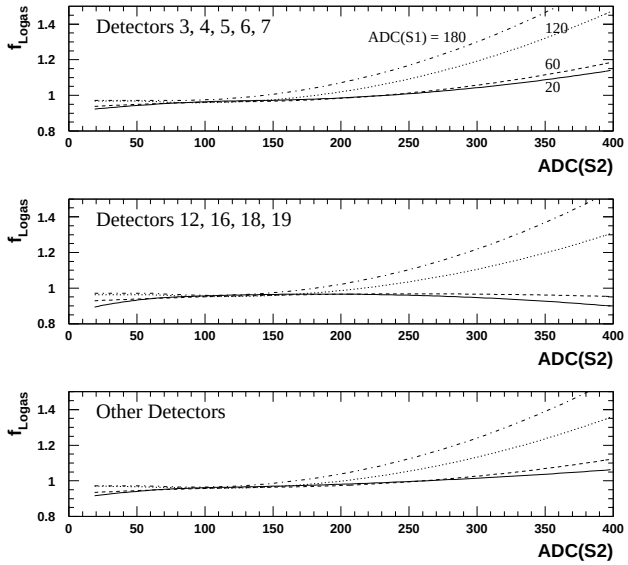

Figure 8: *Logashenko function for three groups of detectors. Typically ADC = 60 corresponds to 1 GeV.*

A complication arose from the level of the hardware energy threshold which – for some detectors in certain run periods – was higher than 1 GeV (see Figures 10 and 11). The highest level is 1.35 GeV for detector 4 in periods 3 and 4. Since at early times the high pedestal effectively reduces this threshold, its level was determined at late times. For the construction of the S1 spectrum this late-time level was then artificially applied as a lower energy cut at all times in order to avoid an early-to-late effect. In the following discussion "hardware threshold" always refers to the late-time level.

Since artificial double pulses can only have energies greater than $2\,f_L\,E_{\text{hardware threshold}} \approx 1.92\,E_{\text{hardware threshold}}$, we cannot directly create pileup spectra with the desired lower energy cut of 2 GeV (see Figure 9 and the detailed discussion in [6]). Raising this cut to $2 \times 1.35\,\text{GeV} = 2.7\,\text{GeV}$ would strongly increase the statistical error of ω_a which scales with $1/(\sqrt{N}A)$. However, the information about the missing part of the double pulse energy spectrum is available in the data: While for triggering the digitisation of a WFD sequence a pulse needs to exceed the hardware threshold, the energy requirement for subsequent pulses within the same digitisation "island" is only limited by the pulse finding algorithm. Such "shadow pulses" following a trigger pulse can be reconstructed down to 250 MeV. Thus, the shadow pulses give us the full single pulse energy spectrum n_S (Figure 12) which allows us to calculate the double pulse spectrum by convolution:

$$n_D(E) = \int_{250\,\text{MeV}}^{E/f_L} dE' n_S(E') n_S(E/f_L - E') \tag{2}$$

Similarly we obtain the number of pileup pulses lost due to the high threshold:

$$n_{D\,\text{lost}} = \int_{2\,\text{GeV/f}_\text{L} - \text{E}_\text{thr}}^{E_\text{thr}} dE_1 \int_{2\,\text{GeV/f}_\text{L} - \text{E}_1}^{E_\text{thr}} dE_2 n_S(E_1) n_S(E_2) \tag{3}$$

In both equations (2) and (3) the energy dependence of f_L was neglected. It plays a role mainly at very high constituent pulse energies whereas the domain of lost pileup is at low

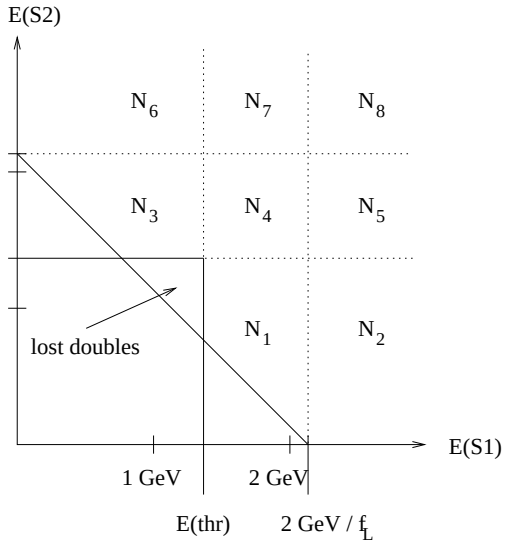

Figure 9: *Illustration of the construction of pileup pulses from single pulses with energies E(S1) and E(S2). For all points above the diagonal line the energy of the constructed double pulse is greater than 2 GeV. If the hardware threshold is greater than 1 GeV, the standard "Mediterranean Method" fails to fill a triangular region of double pulses above 2 GeV. See [6] for more details.*

energies. The fraction of lost double pulses above 2 GeV is then

$$p_{D\,\mathrm{lost}} = \frac{n_{D\,\mathrm{lost}}}{\int_{2\,\mathrm{GeV}}^{\infty} dE\, n_D(E)} \tag{4}$$

Figure 13 shows this fraction as a function of threshold calculated from the shadow spectrum of detector 1 in periods 3 and 4 using Equation (4). Figure 14 shows the fractions for all detectors and run periods based on their actual thresholds. In the worst case (detector 4, periods 3+4) 5% of the doubles are lost. In [6] it was shown that for hardware thresholds between 1 GeV and 1.4 GeV the missing double pulses have an asymmetry of only 0.01 to 0.05 as compared to 0.33 for all doubles together. Thus they carry very little phase information, and it is adequate to apply a non-oscillating correction to the observed time spectrum of the doubles.

$$\begin{aligned} n_{\mathrm{D\,corrected}}(t) &= n_{D0}\mathrm{e}^{-\frac{2t}{\tau}}[1 + p_{D\,\mathrm{lost}} + A_D\cos(\omega t + \phi_D)] \\ &= n_{\mathrm{D\,observed}}(t) + n_{D0}\,\mathrm{e}^{-\frac{2t}{\tau}} p_{D\,\mathrm{lost}} \end{aligned} \tag{5}$$

Technically, the non-oscillating term $n_{D0}\,\mathrm{e}^{-\frac{2t}{\tau}}$ is obtained by binning the observed D time spectrum in g-2 periods and fitting this rebinned spectrum with an exponential. Fit results for Period 3 are shown in Figure 15. The fit range was the same as for the regular ω_a fits (49 μs - 600 μs).

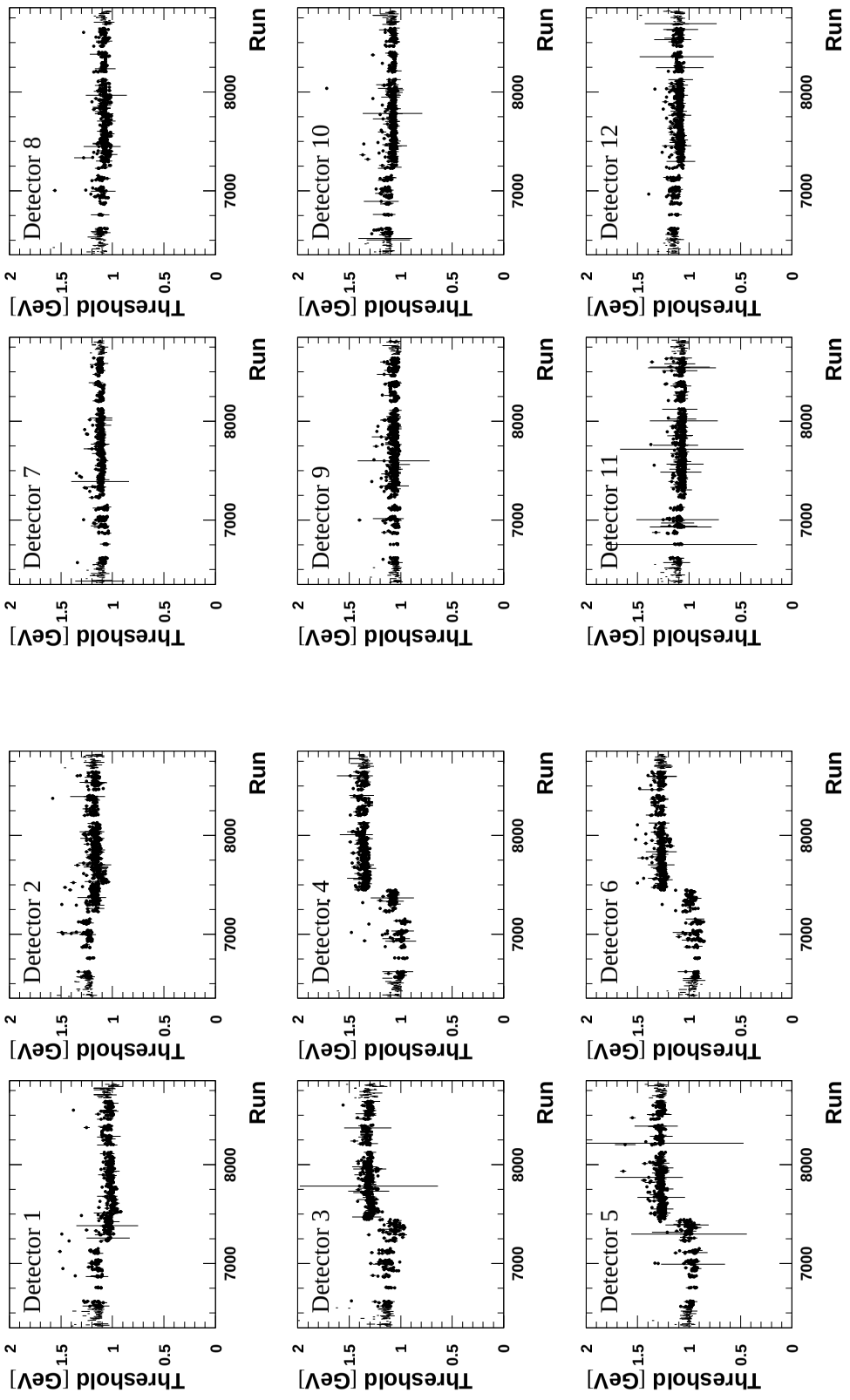

Figure 10: *Hardware threshold as a function of run number for detectors 1-12.*

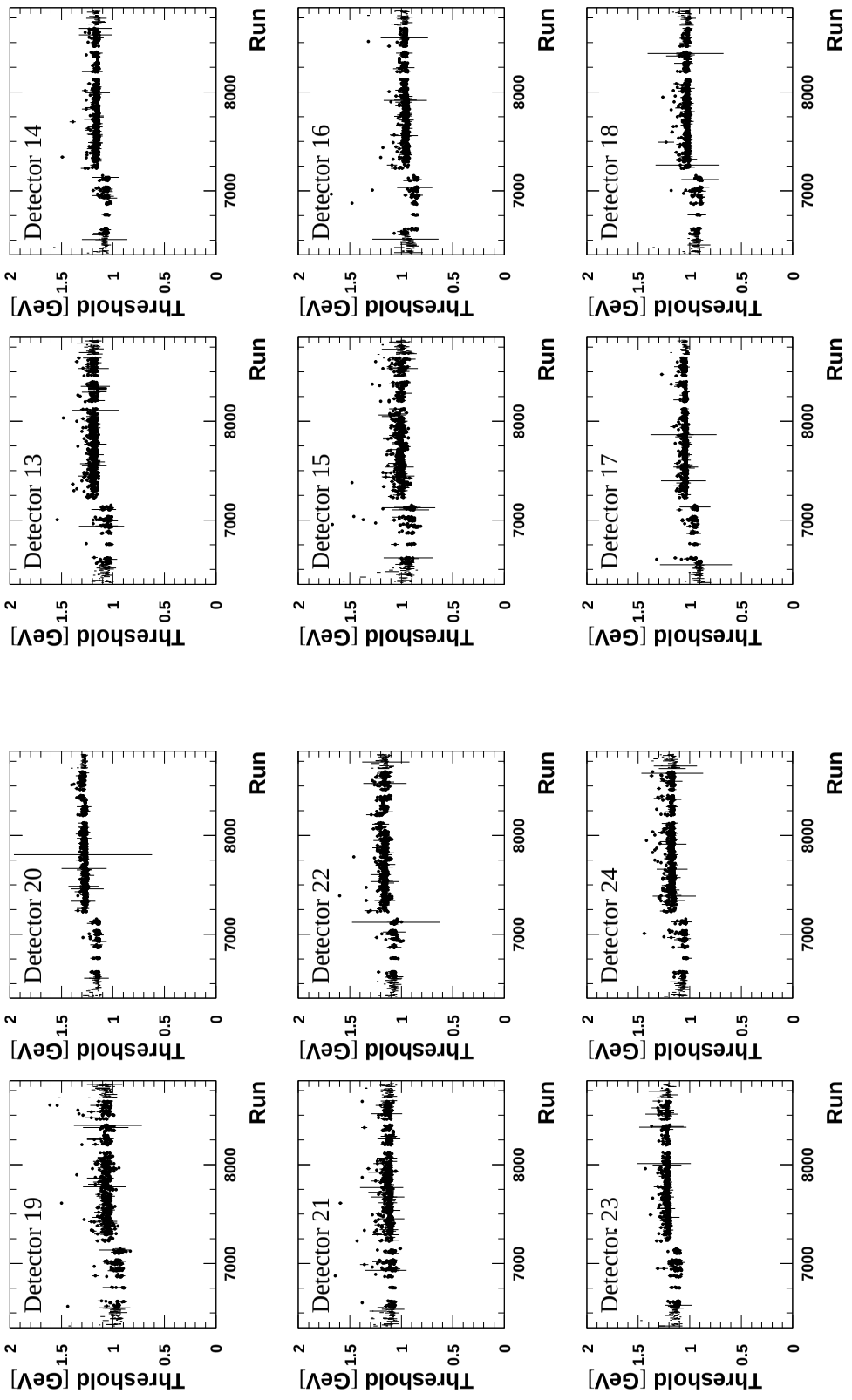

Figure 11: *Hardware threshold as a function of run number for detectors 13-24.*

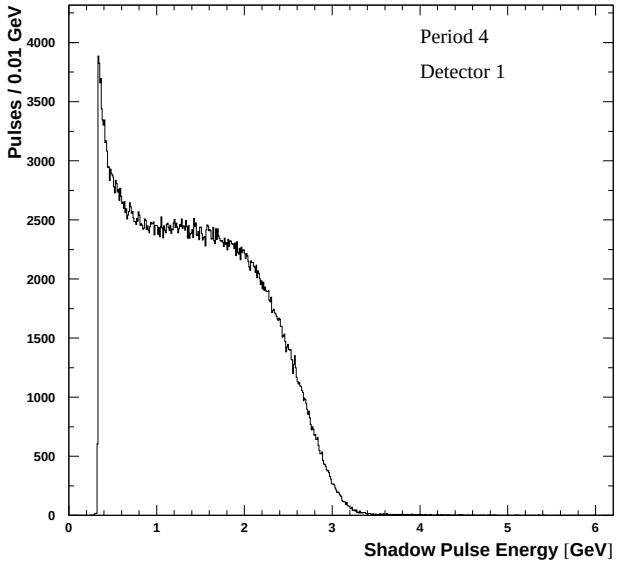

Figure 12: *Shadow pulse energy spectrum for detector 1 in period 4.*

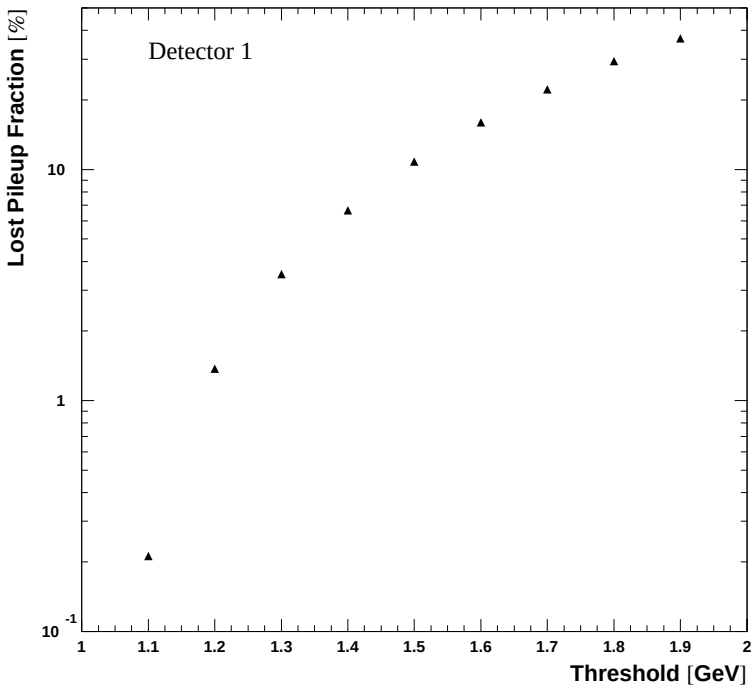

Figure 13: *Fraction of lost double pulses as a function of hardware threshold calculated from the shadow pulse spectrum of detector 1 in periods 3 and 4.*

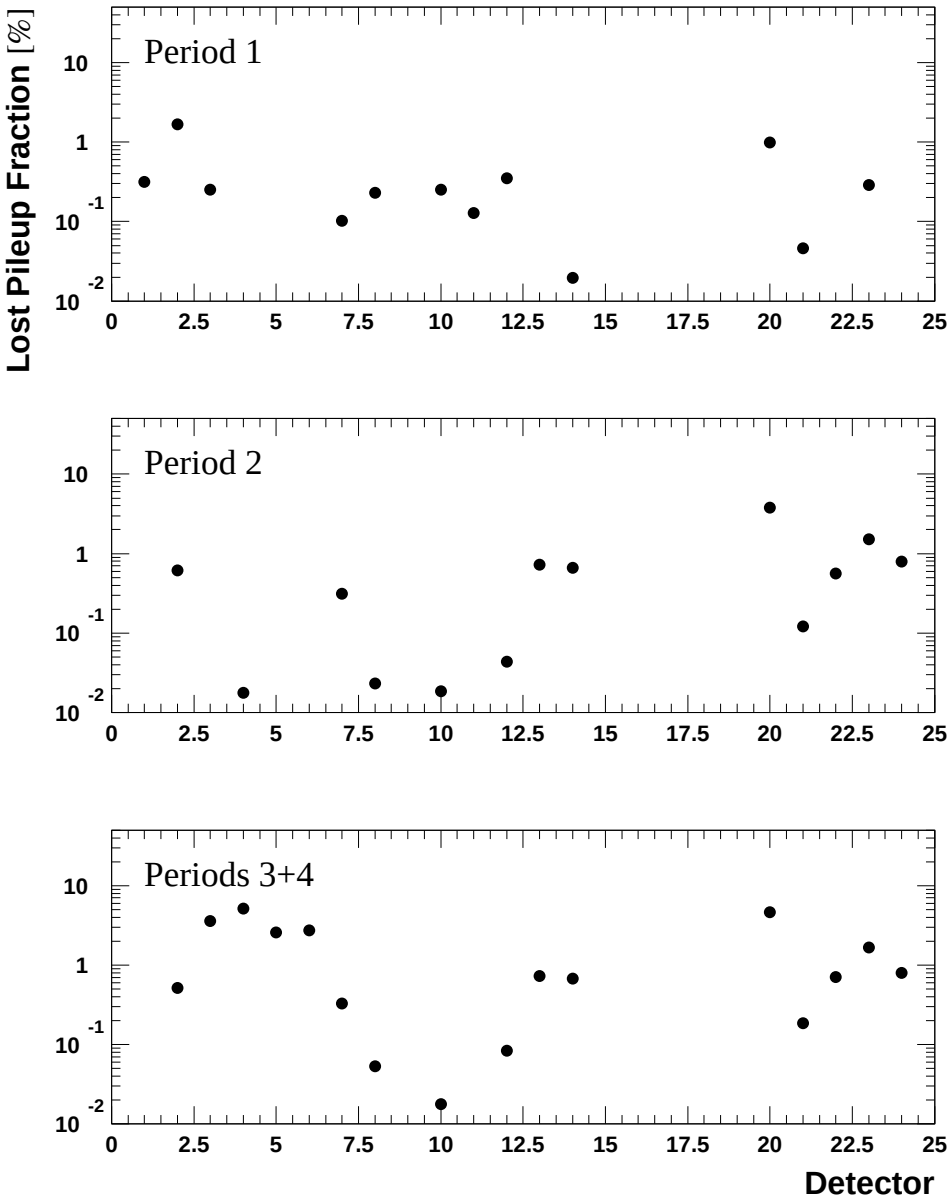

Figure 14: *Fraction of lost double pulses for all detectors and run periods. The missing points are below the lower bound (10^{-2} %) of this logarithmic plot. The statistical error bars are plotted but too small to be seen. The relative size of these errors is below 1 %.*

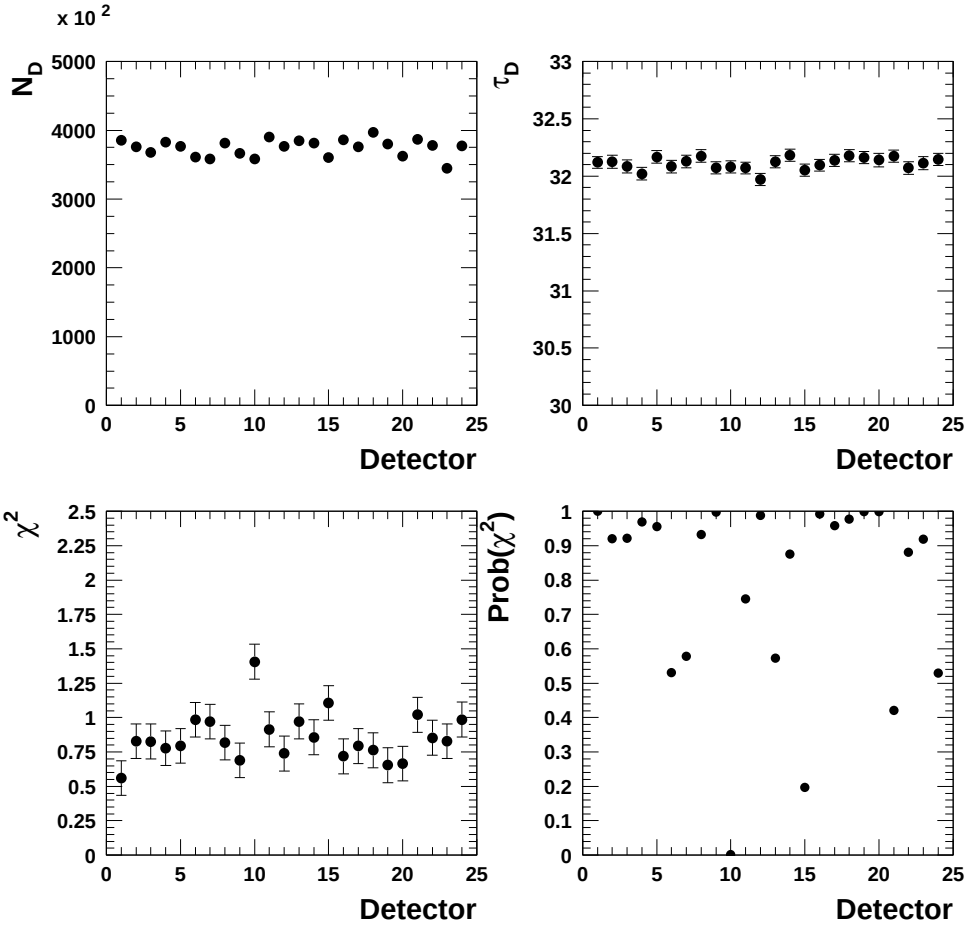

Figure 15: *Fit results for the D spectra of Period 3 after binning in g-2 cycles. The range of these fits was [49 μs; 600 μs]. The error of a bin with n_D entries is given by* $\sigma^2(n_D) = n_D \frac{4(N_1+N_2)+N_4+N_5+N_7+N_8}{2(N_1+N_2)+N_4+N_5+N_7+N_8}$ *in the notation of Figure 9. The enhancement factor accounts for the double counting of N_1 and N_2 due to the non-observability of N_3 and N_6. See [7] and Section 5.2 for a similar discussion in the context of the pileup subtracted spectrum.*

4.5 Energy Scale Correction

For the main analysis no energy scale corrections are applied. Instead, gain effects are addressed in a systematic study.

4.6 Positrons after Pileup Subtraction

The final number of analysable positrons per detector between 49.2 μs and 600 μs after all cuts and pileup subtraction is given in Table 3.

Detector	Period 1a	Period 1b	Periods 2+3	Period 4	Period 0
1	13 669 275	24 009 087	105 031 295	43 765 536	186 868 935
2	(13 560 451)	(23 590 108)	(103 655 426)	(43 238 570)	(184 430 527)
3	12 898 868	22 522 041	99 804 819	41 455 764	177 051 867
4	13 285 524	23 239 356	102 854 495	42 829 458	182 590 013
5	12 929 228	22 474 860	100 045 394	41 734 222	177 555 172
6	11 987 170	20 932 901	93 369 796	38 871 629	165 506 233
7	10 709 435	18 845 146	83 261 079	34 801 926	147 927 815
8	10 340 977	18 091 040	80 018 203	33 350 888	142 097 882
9	11 055 221	19 331 994	86 091 236	35 552 105	152 350 794
10	12 075 745	21 152 994	94 604 705	39 278 599	167 461 134
11	12 883 338	22 541 331	100 952 054	41 994 795	178 742 492
12	11 975 747	20 995 920	93 851 280	38 961 303	166 128 838
13	13 292 337	23 149 999	104 231 802	43 425 833	184 478 789
14	12 415 812	21 627 523	97 410 573	40 596 060	172 406 066
15	12 862 654	22 396 921	100 744 397	41 855 678	178 227 826
16	11 290 162	20 097 125	90 571 259	37 735 948	160 026 626
17	12 673 621	22 432 284	100 250 486	41 728 433	177 452 445
18	12 240 642	21 453 612	95 608 698	39 763 506	169 422 715
19	12 807 972	22 435 696	100 880 750	41 956 222	178 446 592
20	(10 042 923)	(17 407 328)	(76 302 109)	(31 411 694)	(135 450 433)
21	12 860 568	22 474 488	100 688 757	41 968 023	178 360 063
22	12 020 879	21 030 873	93 972 168	38 780 474	166 149 161
23	11 905 936	20 763 931	92 805 280	38 530 910	164 345 208
24	12 016 341	21 270 822	94 008 719	39 076 732	166 718 277
0	270 197 453	473 269 945	2 111 057 246	878 014 045	**3 740 314 945**

Table 3: *Number of positrons between 49.2 μs and 600 μs after all cuts and pileup subtraction.*

5 Fit of the Time Spectra

5.1 Fit Function

5.1.1 Overview

The analysis is based on the following function. Some of its features were only switched on for certain studies.

$$\begin{aligned}\dot{N}(t) = \tfrac{N_0}{\tau} A_N(t) \cdot \mathrm{e}^{-t/\tau} \quad & [1 + A \cdot A_R(t) \cdot \cos(\omega_a t + \phi_a \cdot A_J(t))] \\ \cdot \quad & V(t) \cdot g_{\mathrm{slow}}(t)\end{aligned} \tag{6}$$

with

$$\omega_a = 2\pi \cdot 0.2291\,\mathrm{MHz} \cdot [1 - (R - \Delta R) \cdot 10^{-6}] \tag{7}$$

where R is the actual fit parameter and ΔR a secret offset.

This function accounts for horizontal (radial) CBO oscillations modulating the acceptance $A_N(t)$, the asymmetry A and the g-2 phase ϕ_a. There are contributions from oscillations of the beam centre and from width variations. The latter are not harmonic oscillations with the CBO frequency f_{CBO} but also contain components with the frequency $2f_{\mathrm{CBO}}$. However, this double CBO decays with about half the CBO life time (i.e. roughly $50\,\mu$s) and plays a role only at early times. The following functional forms were used for the CBO terms:

- Acceptance modulation by CBO:

$$\begin{aligned}A_N(t) = \quad 1 \quad & + A_{\mathrm{CBO}} \cdot g_{\mathrm{CBO}}(t) \cdot \cos(\phi_{\mathrm{CBO}}(t)) \\ & + A_{\mathrm{DCBO}} \cdot g^2_{\mathrm{CBO}}(t) \cdot \cos(\phi_{\mathrm{DCBO}}(t))\end{aligned} \tag{8}$$

  The oscillation is described by the terms $\phi_{\mathrm{CBO}}(t)$ (single CBO frequency) and $\phi_{\mathrm{DCBO}}(t)$ (double CBO frequency) which will be further specified below. The time envelope $g_{\mathrm{CBO}}(t)$ was determined empirically as described in Section 5.1.3. For the double CBO envelope the square of $g_{\mathrm{CBO}}(t)$ was used; it has about half the CBO life time.

- Asymmetry modulation by CBO ("Rob effect"):

$$A_R(t) = 1 + A_{\mathrm{R}} \cdot g_{\mathrm{CBO}}(t) \cdot \cos(\phi_{\mathrm{R}}(t)) \tag{9}$$

  For a single detector, this effect is roughly five times smaller than the acceptance CBO. The same time envelope $g_{\mathrm{CBO}}(t)$ was used as for the acceptance CBO. In principle, there is also a double CBO component like for the acceptance CBO. However, it is very small and can be neglected.

- Phase modulation by CBO ("Jim effect"):

$$A_J(t) = 1 + A_{\mathrm{J}} \cdot g_{\mathrm{Jim}}(t) \cdot \cos(\phi_{\mathrm{J}}(t)) \tag{10}$$

  The size of this effect is still being studied in simulation [8]. If it is fitted for, the resulting A_{J} is roughly half A_{R}. The envelope $g_{\mathrm{Jim}}(t)$ of the phase modulation is unknown and may be different from $g_{\mathrm{CBO}}(t)$. Studies were done with $g_{\mathrm{Jim}}(t) = g_{\mathrm{CBO}}(t)$ and with a simple exponential envelope.

Vertical waist and vertical oscillation are small, short-lived effects and only observable with fit start times before about 50 μs. Only the acceptance part was implemented:

$$\begin{aligned} V(t) = \quad 1 \quad & + A_{\mathrm{VW}} \cdot \mathrm{e}^{-t^2/2\tau_{\mathrm{VW}}^2} \cdot \cos(\phi_{\mathrm{VW}}(t)) \\ & + A_{\mathrm{VO}} \cdot \mathrm{e}^{-t^2/2\tau_{\mathrm{VO}}^2} \cdot \cos(\phi_{\mathrm{VO}}(t)) \end{aligned} \tag{11}$$

Not having enough statistics for determining the time envelopes, we empirically used gaussian envelopes which yield reasonable fit results.

The quadrupole voltage V_Q and thus the field index n was not constant during the fill:

- After scraping V_Q and n increase with a saturation time constant τ_{rise} of about 5 μs:

$$n(t) = n_{\mathrm{sat}} \left[1 - A_{\mathrm{rise}} \mathrm{e}^{-(t-15\mu\mathrm{s})/\tau_{\mathrm{rise}}}\right] \tag{12}$$

  The rise time τ_{rise} corresponds to the RC time constant of the quadrupole circuit. It was confirmed by an FSD measurement of the beam centroid during scraping [9]. A_{rise} was determined from the ratio of CBO frequencies with and without scraping, as measured by the fiber harps [10]. This measurement gave $A_{\mathrm{rise}} = 0.13$. These parameters can also be obtained from fits starting at very early times: At 23 μs we found $A_{\mathrm{rise}} = 0.13$, $\tau_{\mathrm{rise}} = 4.3\,\mu$s. In the final fits these parameters were fixed. For their uncertainty a systematic error can be assigned, but fits starting later than 45 μs are insensitive to this very early and short-lived effect (see later in the section about systematic errors).

- After 50 μs the quadrupole plates discharge with a time constant of the order 200 ms:

$$n(t) = n(50\mu\mathrm{s})\, \mathrm{e}^{-(t-50\mu\mathrm{s})/\tau_{\mathrm{decay}}} \tag{13}$$

  By χ^2 minimisation an empirical optimum of τ_{decay} was found at 140 ms. This parameter is always fixed in the final fits. A systematic error will be assigned.

The time dependence of n translates into a time dependence of the frequencies

$$f_{\mathrm{CBO}}(t) = (1 - \sqrt{1 - n(t)})\, f_{cyc} \tag{14}$$

$$f_{\mathrm{VO}}(t) = \sqrt{n(t)}\, f_{cyc} \tag{15}$$

$$f_{\mathrm{VW}}(t) = (1 - 2\sqrt{n(t)})\, f_{cyc} \quad . \tag{16}$$

Therefore the arguments $\phi_{\mathrm{CBO}}(t)$, $\phi_{\mathrm{DCBO}}(t)$, $\phi_{\mathrm{VO}}(t)$ and $\phi_{\mathrm{VW}}(t)$ of the horizontal and vertical oscillation cosines are not simply $\omega_{\mathrm{CBO}} t + \phi_{\mathrm{CBO}}(0)$ etc., but have to be obtained from time integration of the respective frequencies, e.g.

$$\phi_{\mathrm{CBO}}(t) = \int_{50\,\mu\mathrm{s}}^{t} dt'\, 2\pi f_{\mathrm{CBO}}(t') + \phi_{\mathrm{CBO}}(50\mu\mathrm{s}) \tag{17}$$

As fit parameters the frequencies and phases at the reference time 50 μs are chosen. Acceptance, asymmetry and phase modulation share the same CBO frequency parameter. By definition, the double CBO frequency was implemented as $2\, f_{\mathrm{CBO}}$ and is not an additional free parameter.

The positron time spectrum is further modulated by slow effects, mainly muon losses and detector gain variations. These effects correlate strongly with each other and are difficult to separate. Their individual functional forms are not very well known. Therefore, we describe them with the common term $g_{\mathrm{slow}}(t)$. It is dominated by the muon loss function $g_{\mathrm{loss}}(t)$ derived from FSD triple coincidence measurements [11]. This function is known to

about 10 %. The details of the implementation of $g_{\rm loss}(t)$ will be discussed in Section 5.1.4. To achieve an acceptable χ^2 and to avoid phase pulling in R, an empirical correction term is needed:

$$g_{\rm slow}(t) = (1 + g_{\rm loss}(t) - A_{\rm rse} \cdot {\rm e}^{-t^2/\tau_{\rm rse}^2}) \tag{18}$$

If the fits start before about 49 μs another empirical term with an exponential life time around 5 μs is needed. The correction term(s) account for lacking knowledge about $g_{\rm loss}(t)$, for gain variations and unsubtracted pileup. Therefore it is called "residual slow effects" ("r.s.e.", see also Figure 16).

Figure 16: *Graphic illustration of the r.s.e. term.*

The only danger of introducing empirical correction terms lies in their potential correlations with R. This concern will be addressed in Section 6.8.

5.1.2 Free and Fixed Fit Parameters

- N_0: always free.
- τ: the muon life time is always fixed to the theoretical value 64.407 μs corresponding to the mean momentum obtained from a fast rotation analysis [3].
- A: always free.
- R: always free.
- ϕ_a: always free.
- $f_{\rm CBO}(50\mu{\rm s})$: free in fits to the sum of all detector spectra; in fits to individual detector spectra it was fixed to the result from the fit to the sum.
- $A_{\rm CBO}$: always free.
- $\phi_{\rm CBO}(50\mu{\rm s})$: always free.
- $A_{\rm DCBO}$: free in the so-called "physics function", fixed to 0 in the 1999-style function.
- $\phi_{\rm DCBO}(50\mu{\rm s})$: free in the "physics function", fixed to 0 in the "1999-style function".
- $A_{\rm R}$: free in the "physics function", fixed to 0 in the 1999-style function.
- $\phi_{\rm R}(50\mu{\rm s})$: free in the so-called "physics function", fixed to 0 in the 1999-style function.

- A_{J}: free in the "physics function with phase modulation", otherwise fixed to 0.
- $\phi_{\mathrm{J}}(50\mu\mathrm{s})$: free in the "physics function with phase modulation", otherwise fixed to 0 and irrelevant since $A_{\mathrm{J}} = 0$.
- A_{VO}: free for fit start times prior to 44.7 μs, otherwise fixed to 0.
- $f_{\mathrm{VO}}(50\mu\mathrm{s})$: fixed; determined from a Fourier spectrum of the time range 23 - 600 μs and fine tuning by manual χ^2 minimisation; irrelevant for start times after 44.7 μs.
- τ_{VO}: determined by manual χ^2 minimisation at 23 μs; fixed in the final fits; irrelevant after 44.7 μs.
- $\phi_{\mathrm{VO}}(50\mu\mathrm{s})$: free for fit start times earlier than 44.7 μs, otherwise fixed and irrelevant since $A_{\mathrm{VO}} = 0$.
- A_{VW}: free for fit start times prior to 44.7 μs, otherwise fixed to 0.
- $f_{\mathrm{VW}}(50\mu\mathrm{s})$: determined from a Fourier spectrum of the time range 23 - 600 μs.
- τ_{VW}: determined by manual χ^2 minimisation at 23 μs, then fixed; irrelevant after 44.7 μs.
- $\phi_{\mathrm{VW}}(50\mu\mathrm{s})$: free for fit start times earlier than 44.7 μs, otherwise fixed and irrelevant since $A_{\mathrm{VW}} = 0$.
- $A_{\mathrm{rise}} = 0.13$: always fixed.
- $\tau_{\mathrm{rise}} = 4.3\,\mu$s: always fixed.
- $\tau_{\mathrm{decay}} = 140$ ms: always fixed.
- A_{loss}: free in fits to the sum of all detector spectra; in fits to individual detector spectra and in half ring fits it was fixed to the result from the fit to the sum of all detectors.
- A_{rse}: fits to the sum of all detector spectra: optimised at the earliest fit start time, then fixed; free in fits to individual detector spectra and in half ring fits.
- τ_{rse}: fits to the sum of all detector spectra and half ring fits: optimised at the earliest fit start time, then fixed; free in fits to individual detector spectra.

For fit start times later than 44.7 μs, there are 8 free parameters if the "1999-style function" is used; the "physics function without phase modulation" has 12 free parameters, and the the "full physics function" including the phase modulation has 14 free parameters. At earlier start times the inclusion of the vertical oscillation and waist increases the number of parameters to 18.

5.1.3 Determination of the CBO Envelope

Using exponential or gaussian functions as CBO envelopes leads to a bad parameter stability of the CBO amplitude versus fit start time. Therefore the envelope function is determined from the data with a method based on Fourier transformations. This method is also used for measuring the fast rotation envelope and was introduced in [12].

The time spectra of all detectors are time-aligned such that they all have the same CBO phase. Then the spectra are added. In the resulting sum spectrum CBO effects are maximised because no cancellation due to different CBO phases takes place. This CBO-aligned sum spectrum is now fitted with the function

$$\begin{aligned} f_{\text{additive}}(t) = \tfrac{N_0}{\tau} \cdot \mathrm{e}^{-t/\tau} \, [1 \quad & + A \cdot \cos(\omega_a t + \phi_a) \\ & + A_{\text{CBO}} \cdot g_{\text{CBO}}(t) \cdot \cos(\phi_{\text{CBO}}(t)) \\ & + A_{\text{left}} \cdot g_{\text{CBO}}(t) \cdot \cos(\phi_{\text{left}}(t)) \\ & + A_{\text{right}} \cdot g_{\text{CBO}}(t) \cdot \cos(\phi_{\text{right}}(t)) \\ & + \text{vertical terms and DCBO}] \end{aligned} \tag{19}$$

where the left and right CBO side-bands $\omega_{CBO} \pm \omega_a$ are added explicitely. This is different from the regular fit function (6) where the side-bands are produced multiplicatively by including the physical CBO modulations of acceptance, asymmetry and g-2 phase.

Then modified residuals are calculated as

$$R(t) = D(t) - \tilde{f}_{\text{additive}}(t) \tag{20}$$

where $D(t)$ is the measured spectrum and $\tilde{f}_{\text{additive}}(t)$ is constructed from $f_{\text{additive}}(t)$ by setting the CBO amplitude A_{CBO} to zero. Assuming that $f_{\text{additive}}(t)$ describes the data, $R(t)$ is given by

$$R(t) = \frac{N_0}{\tau} \cdot \mathrm{e}^{-t/\tau} \cdot A_{\text{CBO}} \cdot g_{\text{CBO}}(t) \cdot \cos(\phi_{\text{CBO}}(t)) \tag{21}$$

Multiplying $R(t)$ by $\mathrm{e}^{t/\tau}$ we obtain a residual spectrum $\tilde{R}$ which only contains CBO frequency information. Now the fit range is divided in CBO oscillation periods and within each period the CBO envelope is extracted by performing a Fourier transformation. In CBO period k the Fourier sine and cosine amplitudes of the frequency bin l are:

$$a_l(t_k) = \sum_{j=1}^{n} \tilde{R}(t_k + j\delta t) \cos \frac{2\pi j l}{n} \tag{22}$$

$$b_l(t_k) = \sum_{j=1}^{n} \tilde{R}(t_k + j\delta t) \sin \frac{2\pi j l}{n} \tag{23}$$

where n is the number of time bins (width $\delta t = 149.2105$ ns) per CBO period. The CBO amplitude is obtained by selecting $j = 1$ and taking the quadratic sum of sine and cosine amplitude:

$$A_{\text{CBO}}(t) = \sqrt{a_1^2(t) + b_1^2(t)} \tag{24}$$

For each run period an individual envelope is determined (Figure 17) and parametrised with empirical splines of exponentials and gaussians. For times later than 200 μs the CBO signal is below the noise level. The empirical envelopes are only used up to 200 μs and then extrapolated until they reach zero.

Combining all run periods yields an envelope with more kinks and bumps (Figure 18 left). This comes from mixing periods with different CBO frequencies. An extreme example is shown in Figure 18 (right) where periods 1a and 1b whose CBO frequencies differ by 6 kHz are combined.

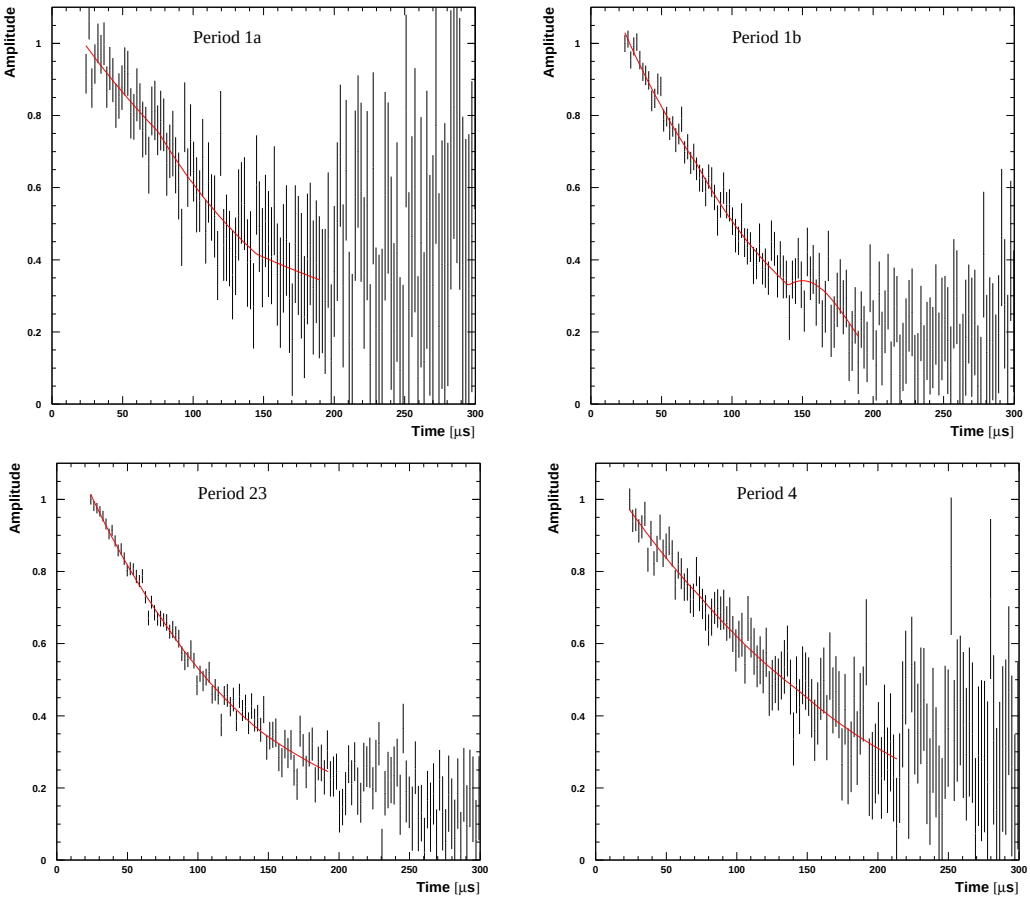

Figure 17: *CBO envelopes for the four run periods, normalised to the value at 23 μs. The lines superimposed correspond to empirical spline parametrisations.*

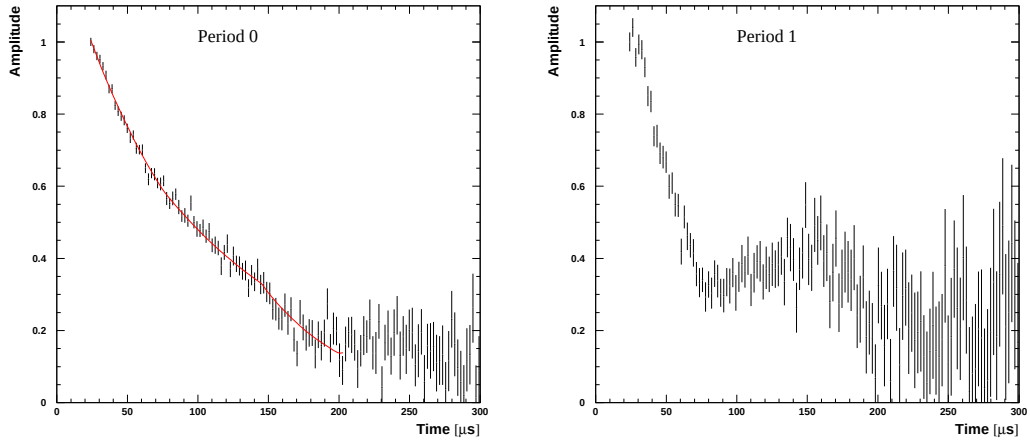

Figure 18: *left: CBO envelope for the sum of all run periods, determined like the individual envelopes; right: CBO envelope for periods 1a and 1b together.*

5.1.4 Implementation of the Muon Loss Function

Neglecting the muon spin precession, the time spectrum of the detected positrons $\dot{N}_\mu(t)$ is given by the differential equation

$$\dot{N}_\mu(t) = -\varepsilon_d \lambda_\mu N(t) \tag{25}$$

where $\lambda = 1/\tau$, $N(t)$ is the total number of muons in the ring at the time t, and ε_d is an efficiency and acceptance factor for the positron detection. The muon losses measured via FSD triple coincidences [11] obey the equation

$$\dot{N}_l(t) = -\varepsilon_l \lambda_l(t) N(t) \equiv C(t) \tag{26}$$

where $\lambda_l(t)$ is the (in general time-dependent) loss time constant, and ε_l an efficiency and acceptance factor for the detection of muons. The number of muons in the ring follows from combining (25) and (26):

$$\dot{N}(t) = -(\lambda_\mu + \lambda_l(t)) N(t) \tag{27}$$

The solution is

$$N(t) = N_0 \, \mathrm{e}^{-\lambda_\mu t} \, \mathrm{e}^{-\int_0^t \lambda_l(t')\,dt'} = N_0 \, \mathrm{e}^{-\lambda_\mu t} \, \mathrm{e}^{-\int_0^t \frac{C(t')}{\varepsilon_l N(t')}\,dt'} \tag{28}$$

Hence, the detected positron spectrum is

$$\dot{N}_\mu(t) = -\varepsilon_d \lambda_\mu N_0 \mathrm{e}^{-\lambda_\mu t} \, \mathrm{e}^{-\int_0^t \frac{C(t')}{\varepsilon_l N(t')}\,dt'} \tag{29}$$

With a different choice of constants, this equation can be rewritten as

$$\dot{N}_\mu(t) = \tilde{N}_{\mu,0} \lambda_\mu \mathrm{e}^{-\lambda_\mu t} \, \mathrm{e}^{-A_l \int_{t_0}^t \frac{C(t')}{\mathrm{e}^{-\lambda_\mu t'}}\,dt'} \tag{30}$$

where t_0 is an arbitrary reference time which for this analysis was chosen to be $23\,\mu$s. Under the integral the spin precession was neglected like in (25), approximating $N(t')$ as $N(0)\mathrm{e}^{-\lambda_\mu t'}$. In (30) we identify

$$g_{\mathrm{loss}}(t) = \mathrm{e}^{-A_l \int_{t_0}^t \frac{C(t')}{\mathrm{e}^{-\lambda_\mu t'}}\,dt'} \tag{31}$$

5.2 Fit Procedure

Here are some details about the fit method:

- The fit start times were varied in 150 ns steps before 60 μs to look for phase pulling. After 60 μs the step size was 5 μs. The earliest start time studied was 23 μs. However, at that time the detectors 3, 4, 5, 6 and 8 were not yet gated on and could not be used. The latest detectors to be gated on were 4 and 5. They are available after 44 μs.

  The spectra of individual detectors were fitted at a start times of 49.2 μs. At this time the g-2 phase passes through $0 \pm n \cdot 2\pi$.

  Start time scans were made for the summed spectra of two different sets of detectors:

  - Scan beginning at 49.2 μs using all detectors except the two bad detectors 2 and 20. At an earlier stage of the analysis scans started already at 44.7 μs, right after the last detector (4) was gated on. However, at this time the systematic uncertainties due to gain variations are still big. Furthermore, by moving to the zero-crossing at 49.2 μs an undesirable additional r.s.e. term with 5 μs life time could be dropped.
  - Scan beginning at 23.0 μs using all detectors except 2, 20 and 3, 4, 5, 6, 8 which are gated on later. These scans are not used for the final analysis. They served for understanding the vertical beam movements.

- The fit stop time was 600 μs or the time when the number of entries per bin went below 42, whichever was earlier. The latter criterion ensures gaussian statistics in each time bin. However, thanks to the big statistics of the 2000 data set, this cut was never needed.

- The fits were performed with the NAGLIB routine e04ycf.

- The fit routine was called several times.

  - First fit level:
    The abscissa of each time bin was approximated to be the centre of the bin. The error on the N_i entries of a time bin i was set to

    $$\sigma_i = \sqrt{N_i \cdot (1 + \gamma \cdot X \cdot \mathrm{e}^{-\frac{t-47\mu\mathrm{s}}{\tau}})} \tag{32}$$

    The correction factor in this equation accounts for correlations from our pileup subtraction method. Some data entries are used to construct the artificial pileup. Their time information is present in the pileup spectrum and in the original non-pileup-subtracted spectrum. Thus, the pileup subtracted spectrum contains their information twice, and its error is no longer given by the simple expression $\sqrt{N_i}$. For a detailed discussion see [7]. The values of the parameters γ and X are given in Tables 4 and 5.
  - Second fit level: The time bin abscissae are still the bin centres, but in the error formula (32) N_i is replaced by the function value from the previous fit. Two iterations of level 2 fits are done.
  - Third fit level: The error definition is like in level 2. The abscissa t_i of time bin i is adjusted to satisfy the condition [13]:

    $$f(t_i) = \langle f(t) \rangle_{\mathrm{bin}} = \frac{1}{\Delta t} \int_{t_{min}}^{t_{min}+\Delta t} f(t)\, dt \tag{33}$$

Obtaining t_i by inversion of $f(t_i)$ requires an approximate knowledge of f. Therefore it is done at an advanced fitting stage where the fit result from the previous iteration is reliable enough to be used. Level 3 fits are iterated until χ^2 changes by less than 0.01 from one step to the next. Usually two iterations are enough. The effect of a corrected abscissa position is best seen in a bin-width independent g-2 asymmetry (Figure 20).

Detector	Period 1a	Period 1b	Period 2	Period 3	Period 4
1	1.28	1.28	1.24	1.24	1.23
2	1.35	1.34	1.31	1.30	1.31
3	1.32	1.31	1.30	1.35	1.35
4	1.26	1.26	1.30	1.34	1.33
5	1.27	1.26	1.26	1.34	1.34
6	1.26	1.26	1.29	1.38	1.38
7	1.42	1.42	1.43	1.43	1.43
8	1.44	1.44	1.41	1.42	1.42
9	1.35	1.35	1.36	1.36	1.36
10	1.33	1.33	1.30	1.31	1.30
11	1.30	1.31	1.29	1.29	1.28
12	1.34	1.35	1.32	1.32	1.33
13	1.26	1.27	1.31	1.31	1.30
14	1.31	1.32	1.35	1.35	1.35
15	1.20	1.20	1.23	1.23	1.23
16	1.28	1.26	1.27	1.27	1.27
17	1.22	1.22	1.27	1.27	1.27
18	1.24	1.24	1.28	1.29	1.29
19	1.22	1.23	1.26	1.26	1.26
20	1.48	1.49	1.50	1.51	1.51
21	1.30	1.31	1.32	1.32	1.31
22	1.33	1.34	1.36	1.37	1.38
23	1.34	1.34	1.36	1.37	1.36
24	1.32	1.31	1.35	1.36	1.36
0	1.30	1.30	1.31	1.32	1.32

Table 4: *Values of* $\gamma \equiv \frac{6N_1+2N_4+2N_8}{2(N_1+N_2)+N_4+N_5+N_7+N_8}$ *for all detectors and runs periods. Detector 0 stands for the sum of all detectors. For the notation used in the definition of gamma and its derivation see [7] and Figure 9.*

Detector	Period 1a	Period 1b	Period 2	Period 3	Period 4
1	0.0079	0.0110	0.0121	0.0148	0.0135
2	0.0080	0.0111	0.0121	0.0148	0.0134
3	0.0080	0.0111	0.0127	0.0154	0.0138
4	0.0083	0.0116	0.0131	0.0157	0.0142
5	0.0084	0.0116	0.0128	0.0159	0.0143
6	0.0087	0.0118	0.0134	0.0160	0.0146
7	0.0093	0.0130	0.0142	0.0175	0.0157
8	0.0103	0.0141	0.0158	0.0193	0.0173
9	0.0090	0.0126	0.0147	0.0172	0.0155
10	0.0081	0.0113	0.0127	0.0153	0.0138
11	0.0082	0.0116	0.0127	0.0156	0.0144
12	0.0087	0.0120	0.0135	0.0161	0.0144
13	0.0081	0.0111	0.0121	0.0150	0.0135
14	0.0086	0.0119	0.0133	0.0161	0.0146
15	0.0076	0.0108	0.0119	0.0144	0.0129
16	0.0090	0.0127	0.0144	0.0171	0.0156
17	0.0081	0.0113	0.0125	0.0152	0.0137
18	0.0090	0.0127	0.0137	0.0169	0.0153
19	0.0083	0.0115	0.0128	0.0154	0.0140
20	0.0106	0.0148	0.0167	0.0201	0.0184
21	0.0084	0.0117	0.0130	0.0156	0.0142
22	0.0087	0.0120	0.0134	0.0165	0.0148
23	0.0082	0.0113	0.0124	0.0152	0.0137
24	0.0088	0.0118	0.0135	0.0163	0.0147
0	0.0085	0.0118	0.0132	0.0160	0.0144

Table 5: *Values of* $X = \frac{doubles\ at\ 47\mu s}{singles\ at\ 47\mu s}$ *for all detectors and runs periods. Single pulses* $N - D + S1 + S2$ *and double pulses* D *are counted over one g-2 period centred at* $47\mu s$*. See also Figure 19.*

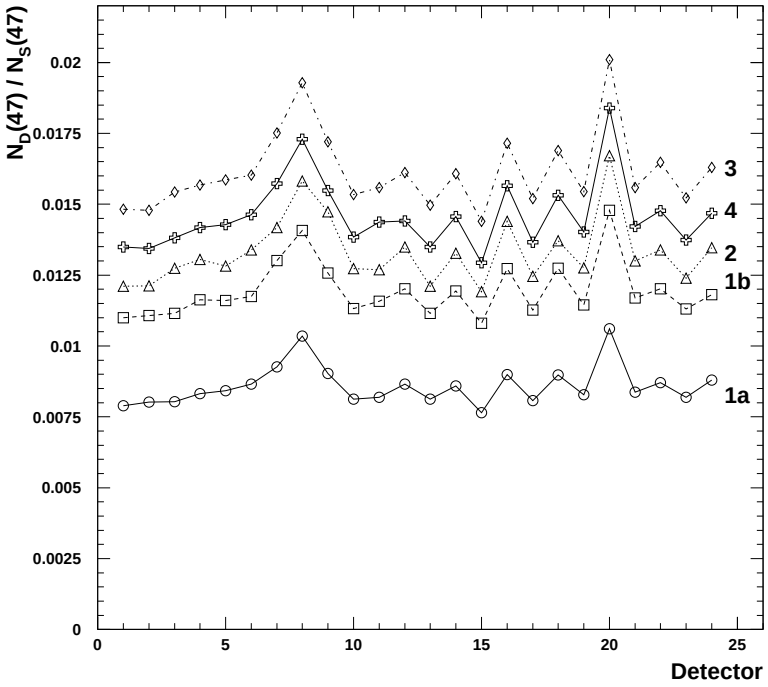

Figure 19: *Values of* $X = \frac{doubles\ at\ 47\mu s}{singles\ at\ 47\mu s}$ *as in Table 5. The energy spectra of the kicker detectors 7, 8, 9 have a different shape which impacts the pileup fraction.*

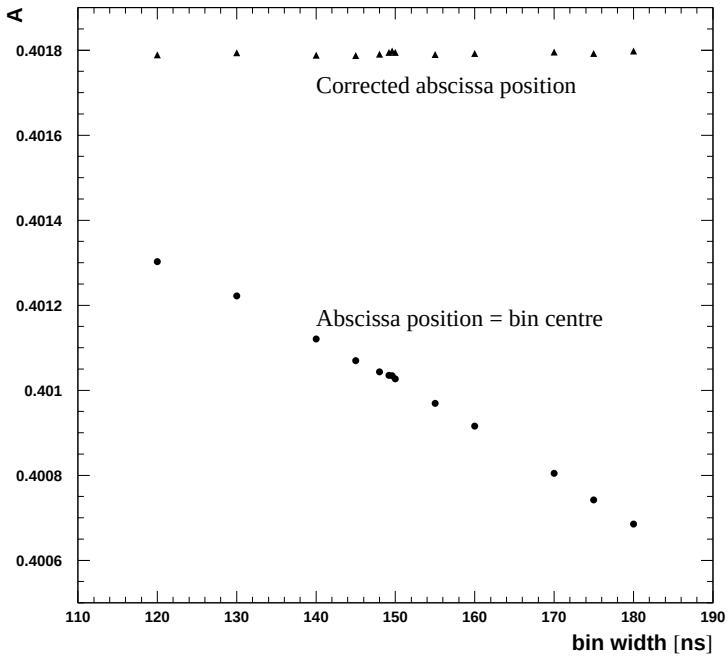

Figure 20: *Fitted asymmetry as a function of the bin width for two different abscissa positions within a bin. These results are based on the data from period 4 randomised over the constant period 149.2105 ns. The seed was the same for all cases.*

5.3 Fit Studies starting at 23 μs

My studies of fits starting at times earlier than 44.7 μs turned out not to be essential to the final analysis. These fits suffer from the problem that 5 detectors were not yet gated on, and hence the g-2 phase modulation by CBO does not cancel sufficiently when the remaining detector spectra are summed up. Thus the g-2 phase modulation is too big for being neglected, but due to lacking knowledge about its envelope it cannot be fitted for with a reasonable systematic error.

Therefore this section is very brief. It is kept for reasons of completeness, but it is not important for the 2000 result.

To give an idea about the effects to be accounted for at early times, Figure 21 shows a Fourier amplitude spectrum of residuals after a 5 parameter fit (which describes only the exponential decay modulated by ω_a).

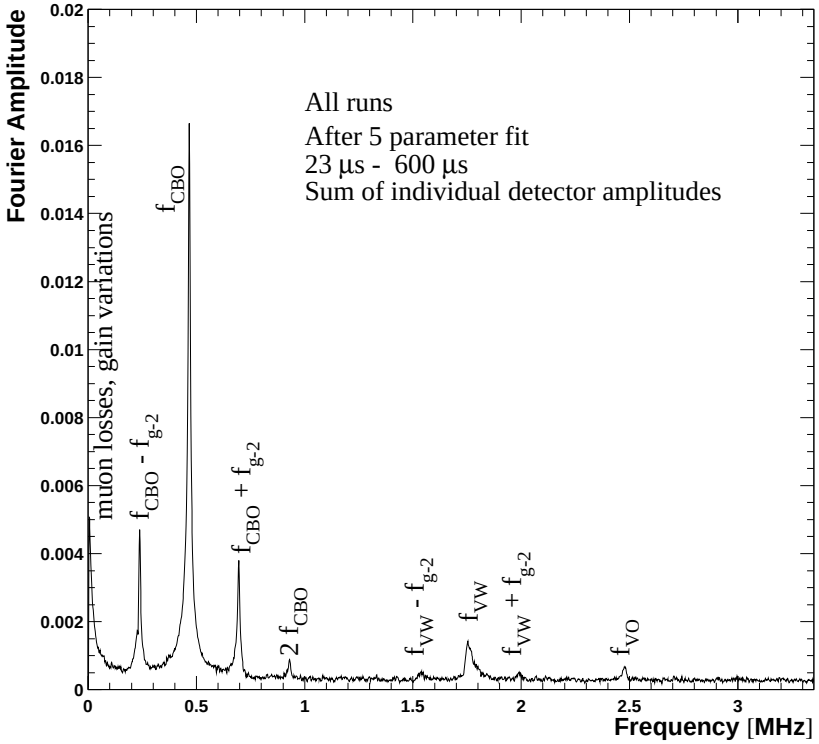

Figure 21: *All detectors available at 23 μs were fitted separately to a 5-parameter function in the fit interval 23.0 μs - 600 μs. The residuals after the fit were Fourier-analysed; then the Fourier amplitudes were added.*

We also show start time scans for R from the sum of detector spectra using three functions differring in their extent of accounting for CBO effects (Figure 22): the first function implements only the acceptance CBO, the second adds the asymmetry modulation, and the third function also includes the phase modulation. All three of them contain both VO and VW. As the figure and Table6 show, the half ring effect from asymmetry and phase modulation is big. The uncertainty from the asymmetry and phase CBO modulation is aggravated by their strong correlations with the g-2 asymmetry and hence with gain variations which are still considerable at 23 μs.

	Func. without Asymm. and Phase Mod.	Physics Func. without Phase Modulation	Physics Func. with Phase Modulation
R	88.86 ± 0.57	90.13 ± 0.60	90.95 ± 0.63
χ^2	1.039 ± 0.023	1.022 ± 0.023	1.018 ± 0.023

Table 6: *R and χ^2 from fits to the sum of all detectors starting at 23.0 μs. The three functions implement CBO effects to different extents.*

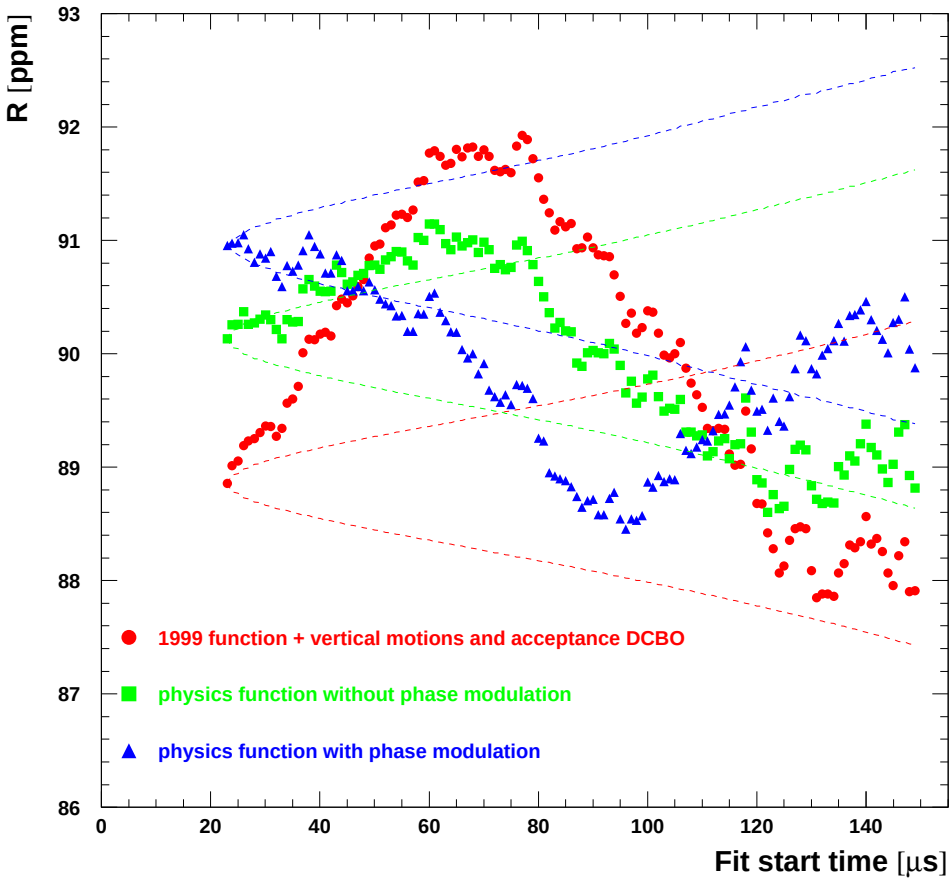

Figure 22: *Start-time scans for the three fit functions studied. Detectors 3, 4, 5, 6 and 8 are not gated on at the earliest times and therefore excluded from this study.*

	N_0	A	ϕ_a	R	f_{CBO}	A_{CBO}	ϕ_{CBO}	A_{Rob}	ϕ_{Rob}	A_{Jim}	ϕ_{Jim}	A_{DCBO}	ϕ_{DCBO}	A_{loss}	A_{VW}	ϕ_{VW}	A_{VO}	ϕ_{VO}
N_0	1.000	0.015	-0.014	**-0.010**	-0.010	0.017	0.009	0.010	0.013	0.018	0.027	-0.005	0.003	-0.885	-0.001	-0.004	-0.000	-0.003
A	0.015	1.000	-0.050	**-0.055**	0.047	-0.004	-0.013	0.207	-0.229	0.209	-0.224	0.006	-0.002	-0.022	-0.006	0.002	0.003	-0.002
ϕ_a	-0.014	-0.050	1.000	**0.844**	-0.000	-0.024	-0.004	-0.381	-0.231	-0.377	-0.233	0.004	-0.008	0.020	-0.002	0.007	-0.003	0.004
R	-0.010	-0.055	0.844	**1.000**	-0.005	-0.018	-0.003	-0.307	-0.150	-0.304	-0.153	0.003	-0.006	0.015	-0.001	0.005	-0.003	0.002
f_{CBO}	-0.010	0.047	-0.000	**-0.005**	1.000	-0.003	-0.070	0.030	-0.001	0.009	-0.022	0.018	0.001	0.016	-0.013	0.017	0.009	0.007
A_{CBO}	0.017	-0.004	-0.024	**-0.018**	-0.003	1.000	0.002	-0.014	0.030	-0.001	0.005	0.019	-0.002	-0.025	-0.007	0.010	0.016	0.006
ϕ_{CBO}	0.009	-0.013	-0.004	**-0.003**	-0.070	0.002	1.000	-0.024	-0.014	-0.001	0.012	-0.021	0.018	-0.015	0.014	-0.020	-0.014	-0.007
A_{Rob}	0.010	0.207	-0.381	**-0.307**	0.030	-0.014	-0.024	1.000	0.038	0.185	0.037	-0.008	0.005	-0.015	-0.004	0.001	0.008	0.001
ϕ_{Rob}	0.013	-0.229	-0.231	**-0.150**	-0.001	0.030	-0.014	0.038	1.000	0.060	0.112	-0.002	-0.013	-0.020	-0.012	-0.007	0.007	-0.008
A_{Jim}	0.018	0.209	-0.377	**-0.304**	0.009	-0.001	-0.001	0.185	0.060	1.000	0.041	0.026	-0.015	-0.027	-0.008	0.012	0.010	0.006
ϕ_{Jim}	0.027	-0.224	-0.233	**-0.153**	-0.022	0.005	0.012	0.037	0.112	0.041	1.000	0.001	0.025	-0.040	0.008	-0.007	-0.002	-0.005
A_{DCBO}	-0.005	0.006	0.004	**0.003**	0.018	0.019	-0.021	-0.008	-0.002	0.026	0.001	1.000	-0.007	0.005	-0.013	0.004	0.008	0.010
ϕ_{DCBO}	0.003	-0.002	-0.008	**-0.006**	0.001	-0.002	0.018	0.005	-0.013	-0.015	0.025	-0.007	1.000	-0.005	0.012	0.007	-0.008	0.002
A_{loss}	-0.885	-0.022	0.020	**0.015**	0.016	-0.025	-0.015	-0.015	-0.020	-0.027	-0.040	0.005	-0.005	1.000	0.002	0.004	-0.003	0.004
A_{VW}	-0.001	-0.006	-0.002	**-0.001**	-0.013	-0.007	0.014	-0.004	-0.012	-0.008	0.008	-0.013	0.012	0.002	1.000	-0.003	0.015	0.008
ϕ_{VW}	-0.004	0.002	0.007	**0.005**	0.017	0.010	-0.020	0.001	-0.007	0.012	-0.007	0.004	0.007	0.004	-0.003	1.000	0.001	0.027
A_{VO}	-0.000	0.003	-0.003	**-0.003**	0.009	0.016	-0.014	0.008	0.007	0.010	-0.002	0.008	-0.008	-0.003	0.015	0.001	1.000	0.016
ϕ_{VO}	-0.003	-0.002	0.004	**0.002**	0.007	0.006	-0.007	0.001	-0.008	0.006	-0.005	0.010	0.002	0.004	0.008	0.027	0.016	1.000

Table 7: *Correlation matrix* $\frac{\mathrm{cov}(\mathrm{p_i},\mathrm{p_j})}{\sigma_i\,\sigma j}$ *from a fit to the sum of detector spectra starting at 23.0* μs.

5.4 Fit Results starting at 49.2 μs

All results in this section are based on a single random seed. More seeds will only be used for a systematic study (Section 6.10).

5.4.1 Fourier Spectrum after a 5-Parameter Fit

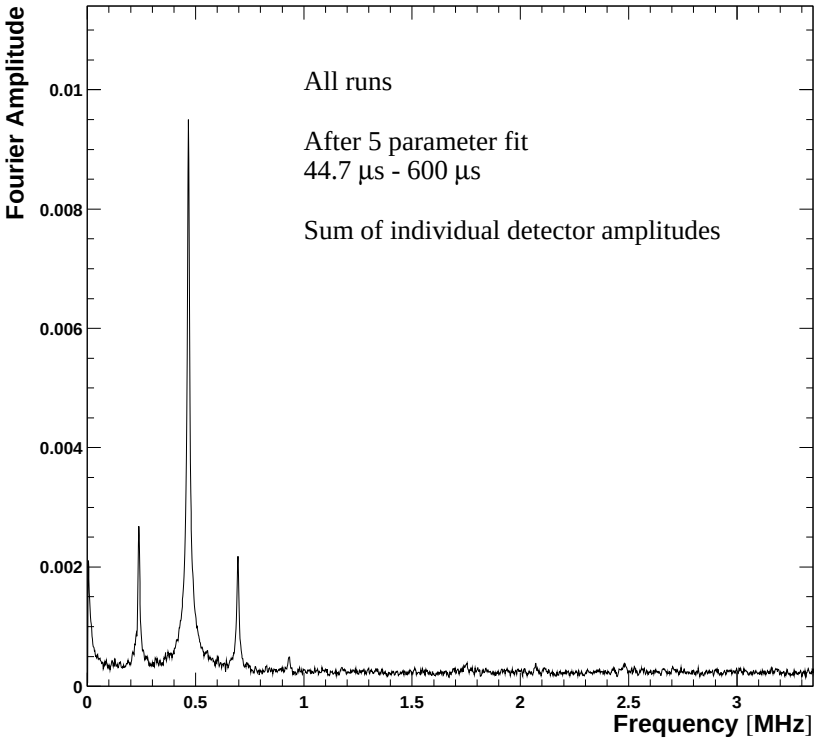

Figure 23: *All detectors were fitted separately to a 5-parameter function in the fit interval 44.7 μs - 600 μs. The residuals after the fit were Fourier-analysed; then the Fourier amplitudes were added.*

The Fourier spectrum of residuals after a 5-parameter fit with a start time of 44.7 μs (Figure 23) shows which effects need to be accounted for by the fit function. At this late time the vertical waist and the vertical oscillation have decayed sufficiently to be neglected in the fit. The double CBO peak is still well visible and can be fitted for. We decided to include it in the "physics function" but not in the "1999-style function". As we will see in the section about systematic errors, this somewhat arbitrary choice has no significant impact on the result.

The Fourier spectrum is dominated by the CBO peak and its satellites from beating with ω_a. Furthermore, there is a peak at zero frequency which is mainly caused by muon losses but also residual slow effects from gain variations and unsubtracted pileup.

5.4.2 Fits without Asymmetry/Phase Modulation (1999 Style)

We define the "1999-style function" as Function (6) with the following parameters fixed:

- No asymmetry modulation by CBO: $A_{\mathrm{Rob}} = \phi_{\mathrm{Rob}} = 0$.
- No phase modulation by CBO: $A_{\mathrm{Jim}} = \phi_{\mathrm{Jim}} = 0$.
- No double CBO: $A_{\mathrm{DCBO}} = \phi_{\mathrm{DCBO}} = 0$.
- No vertical motion: $A_{\mathrm{VO}} = \phi_{\mathrm{VO}} = A_{\mathrm{VW}} = \phi_{\mathrm{VO}} = 0$.

Thus, the remaining function is

$$\dot{N}(t) = \frac{N_0}{\tau} \mathrm{e}^{-t/\tau} \left[1 + A_{\mathrm{CBO}} \cdot g_{\mathrm{CBO}}(t) \cdot \cos(\phi_{\mathrm{CBO}}(t))\right] \left[1 + A \cdot \cos(\omega_a t + \phi_a)\right] \cdot g_{\mathrm{slow}}(t) \quad (34)$$

The individual terms are explained in Section 5.1.1.

With the 1999-style function the fit results for R decouple well from the other fit parameters, as the correlation matrix in Table 8 demonstrates. We shall see that this makes the results relatively insensitive to gain variations and other effects influencing the asymmetry. The disadvantage of this function is that by neglecting the CBO modulations of g-2 asymmetry and phase it does fully describe the physics. The missing effects need to be addressed in systematic error studies.

	N_0	A	ϕ_a	R	f_{CBO}	A_{CBO}	ϕ_{CBO}	A_{loss}
N_0	1.000	0.017	0.010	**0.007**	-0.012	0.003	0.018	-0.912
A	0.017	1.000	-0.006	**-0.003**	-0.002	0.010	0.005	-0.025
ϕ_a	0.010	-0.006	1.000	**0.862**	0.025	-0.006	-0.036	-0.014
R	0.007	-0.003	0.862	**1.000**	0.019	-0.005	-0.026	-0.010
f_{CBO}	-0.012	-0.002	0.025	**0.019**	1.000	0.001	-0.635	0.018
A_{CBO}	0.003	0.010	-0.006	**-0.005**	0.001	1.000	-0.002	-0.004
ϕ_{CBO}	0.018	0.005	-0.036	**-0.026**	-0.635	-0.002	1.000	-0.026
A_{loss}	-0.912	-0.025	-0.014	**-0.010**	0.018	-0.004	-0.026	1.000

Table 8: *Correlation matrix* $\frac{\mathrm{cov}(\mathrm{p_i},\mathrm{p_j})}{\sigma_i \sigma j}$ *from a fit to the sum of detectors starting at 44.7 μs.*

Fits to the Sum of Detectors

A start time scan for R is shown in Figure 24 for the entire 2000 data set. The lower plot shows a zoom for start times up to 60 μs with a step of 150 ns. The absence of obvious phase pulling demonstrates that the slow variations like muon losses are well accomodated by the fit function.

A comparison between the weighted average of the R values for the individual run periods and the result for the full data set is shown in Figure 25 and Table 9. The error on the difference in the last row of the table was calculated with the simple approximation

$$\sigma^2(R_{P0} - \langle R_p \rangle) \approx |\sigma^2(R_{P0}) - \sigma^2(\langle R_p \rangle)| \quad (35)$$

Figure 26 shows start time scans for A. The big deviation of A from the allowed 1 σ error band is not fully understood. It may come partly from gain variations, partly from unseen pileup. A systematic error will be assigned in Section 6.7.

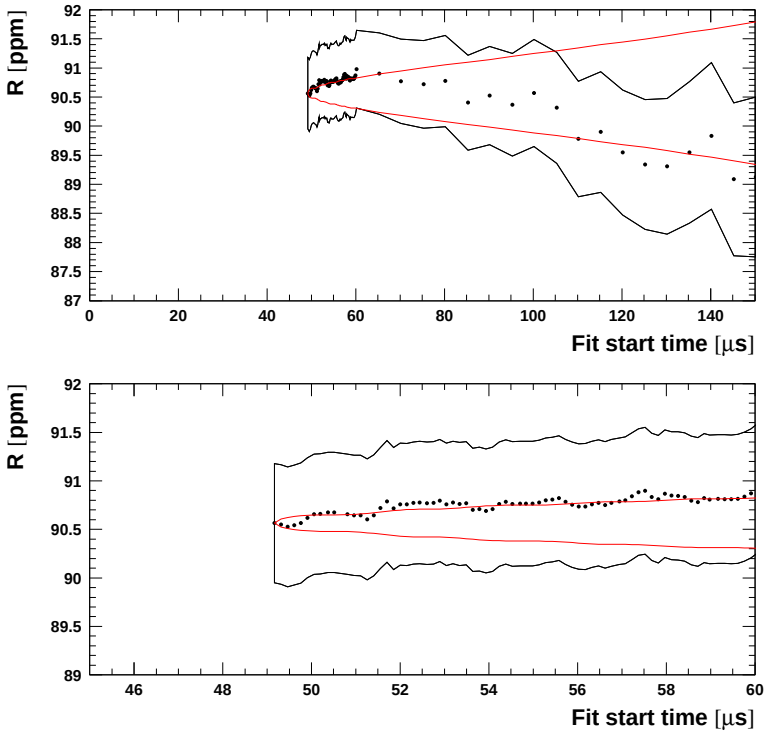

Figure 24: *Start time scan for the sum of all detector spectra of all runs fitted with the 1999-style function.*

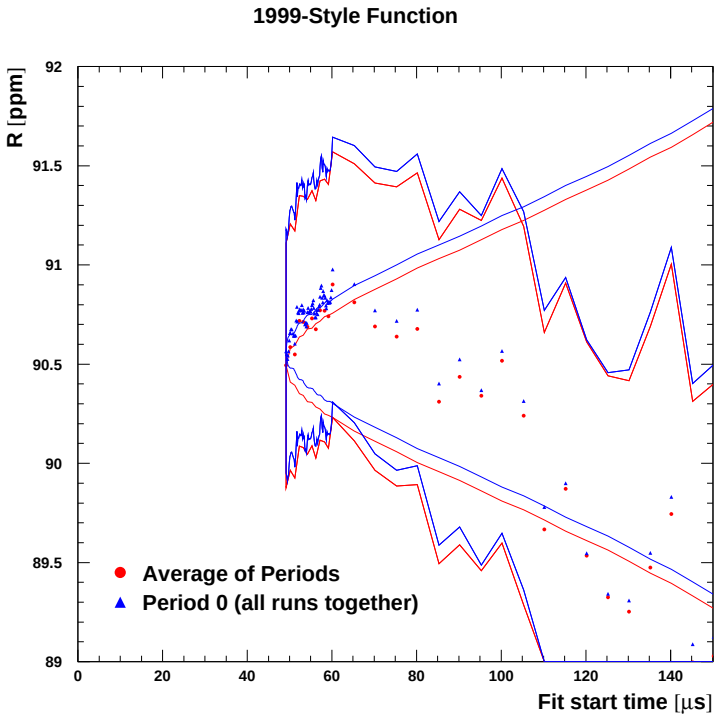

Figure 25: *Comparison between R for the sum and for the average of the run periods.*

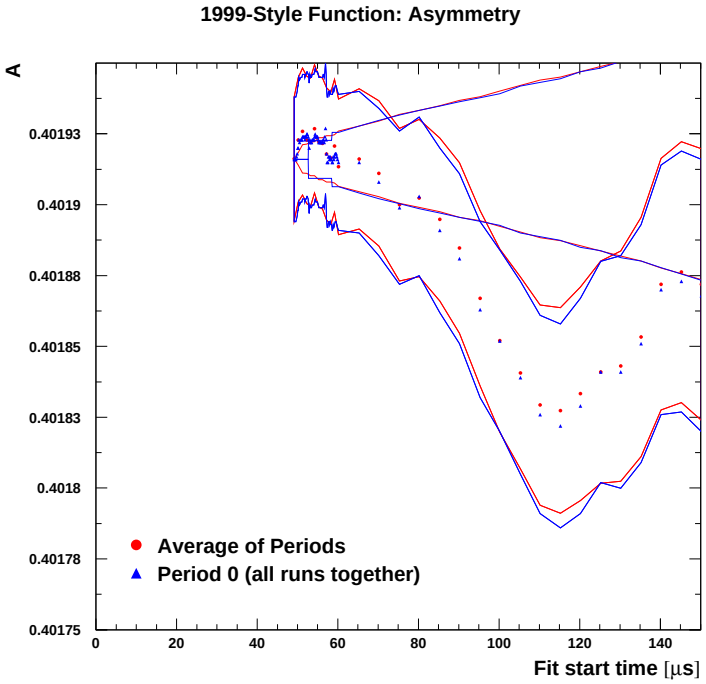

Figure 26: *Comparison between A for the sum and for the average of the run periods.*

The omission of the asymmetry and phase modulation manifests itself in the halfring effect on both R and A, see Figure 27.

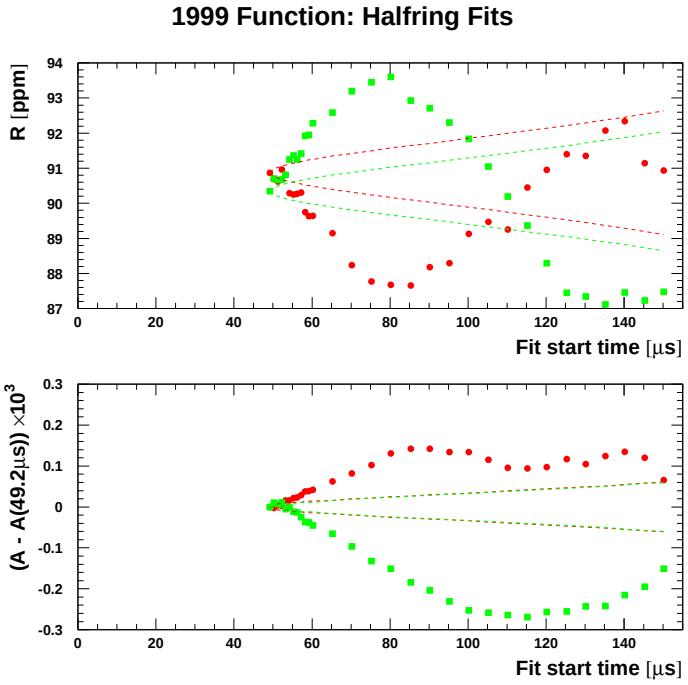

Figure 27: *Fit results for R and A in the two halves of the ring. This figure is for Period 0 (all runs).*

Start time scans for all other parameters and for the different run periods are shown in Appendix A.1. Appendix A.2 shows the same for the first and second half of the ring.

Period	Sum of all detectors	First half	Second half	Average of the halves
1a	92.2437 ± 2.2939	94.7394 ± 3.3004	89.9213 ± 3.1899	92.2483 ± 2.2937
1b	81.5497 ± 1.7222	81.6635 ± 2.4761	81.3826 ± 2.3965	81.5185 ± 1.7220
2+3	92.0583 ± 0.8177	91.9551 ± 1.1786	92.2762 ± 1.1347	92.1217 ± 0.8174
4	91.0478 ± 1.2680	91.7495 ± 1.8279	90.4118 ± 1.7600	91.0553 ± 1.2678
avr.	90.4943 ± 0.6149	90.7899 ± 0.8859	90.2862 ± 0.8538	90.5288 ± 0.6148
0	90.5646 ± 0.6142	90.8715 ± 0.8850	90.3469 ± 0.8529	90.5995 ± 0.6141
|0 - avr.|	0.0703 ± 0.0293	0.0816 ± 0.0399	0.0607 ± 0.0392	0.0707 ± 0.0293

Table 9: *Fit results for R in ppm in the individual run periods with a start time of 49.2 μs. The fits were done with the 1999-style function. "Period 0" stands for all runs fitted together whereas "avr." is the weighted mean of the individual results from periods 1a to 4.*

The R-value of Period 1b is (10.25 ± 1.59) ppm lower than the average of the other periods. However, in Period 1b the magnetic field feed-back system was off most of the time, so for some runs B is up to 39 ppm higher than desired. Using ω_p (with an offset) versus run (Figure 28a, [14]) we can calculate a pseudo-a_μ as $\frac{\frac{\omega_a}{\omega_p}}{\lambda - \frac{\omega_a}{\omega_p}}$. Fitting the pseudo-$a_\mu$ values of the four considered periods to a constant results in χ^2 /dof = 2.62 / 3 (Figure 28b).

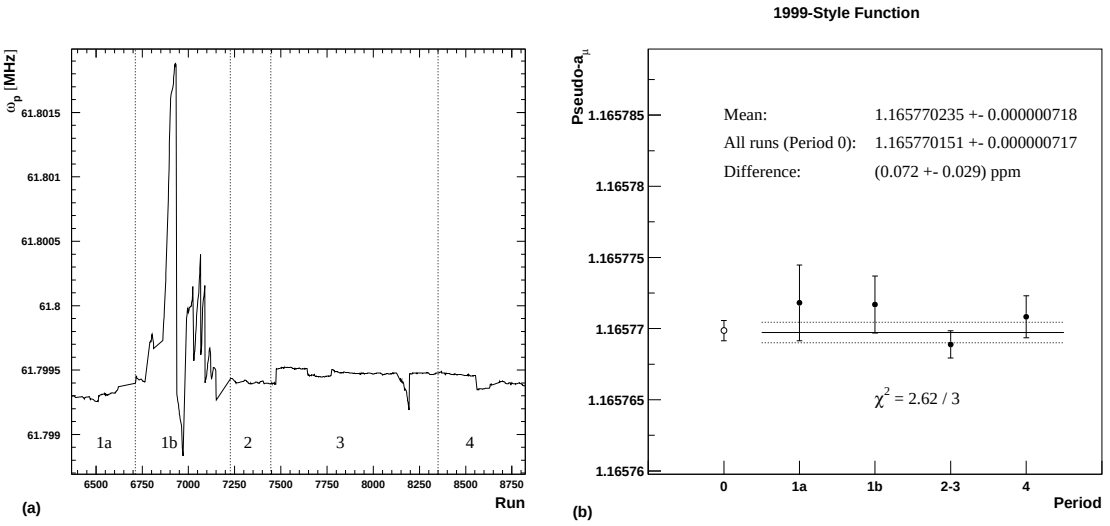

Figure 28: *(a) Magnetic field in terms of ω_p with an offset versus run number. (b) Pseudo-a_μ versus run period. These numbers contain an offset in ω_p and a global scale factor.*

The CBO amplitudes and phases are listed in Table 10. As an additional run-period consistency check, the CBO vectors $(A_{\mathrm{CBO}}, \phi_{\mathrm{CBO}})$ are added coherently (row "vector sum") and compared with the result for Period 0. This vector sum follows from the addition of the time spectra whose relevant part can be written as

$$N_0 A_{\mathrm{CBO},0} \cos(\omega_{\mathrm{CBO}} t + \phi_{\mathrm{CBO},0}) = \sum_{p=1\mathrm{a}}^{4} N_p A_{\mathrm{CBO},p} \cos(\omega_{\mathrm{CBO}} t + \phi_{\mathrm{CBO},p}) \qquad (36)$$

In complex notation the amplitude $A_{\mathrm{CBO},0}$ and phase $\phi_{\mathrm{CBO},0}$ of the sum are given by

$$N_0 A_{\mathrm{CBO},0}(\cos\phi_{\mathrm{CBO},0} + i\sin\phi_{\mathrm{CBO},0}) = \sum_{p=1\mathrm{a}}^{4} N_p A_{\mathrm{CBO},p}(\cos\phi_{\mathrm{CBO},p} + i\sin\phi_{\mathrm{CBO},p}) \qquad (37)$$

Period	$A_{\mathrm{CBO}} \times 10^3$	ϕ_{CBO}
1a	2.86 ± 0.16	2.33 ± 0.08
1b	4.67 ± 0.15	0.33 ± 0.04
2+3	3.89 ± 0.07	5.84 ± 0.03
4	3.71 ± 0.10	5.72 ± 0.04
vector sum	3.32 ± 0.06	5.96 ± 0.02
0	3.20 ± 0.05	5.95 ± 0.02

Table 10: *CBO amplitude and phase from fits to the sum of all detectors with a start time of 49.2 μs. The fits were done with the 1999-style function. The amplitude and phase in the row "vector sum" were calculated as indicated in Eq. (37).*

Fits to the Individual Detectors

The fit results for individual detectors at a start time of 49.2 μs are shown in the figures of Appendix A.3.

As a consequence of omitting the asymmetry and phase modulation in the fit function, R versus detector is not constant (see the bad χ^2 in Table 11), but follows a sine wave

$$R(d) = R_0 + A_{Rc}\cos(2\pi\frac{d}{24}) + A_{Rs}\sin(2\pi\frac{d}{24}) \tag{38}$$

with an amplitude of about (4.2 $\pm$ 0.9) ppm. The centroid value R_0 of this wave differs by (0.16 $\pm$ 0.03) ppm from the weighted average $\langle R\rangle$ (see Table 13).

Period	$\langle R\rangle$	χ^2/ndof (fit to a constant)
1a	92.2429 $\pm$ 2.2920	20.8 / 21
1b	81.5305 $\pm$ 1.7209	30.3 / 21
2+3	92.2338 $\pm$ 0.8168	41.1 / 21
4	91.2730 $\pm$ 1.2945	20.1 / 21
avr.	90.6384 $\pm$ 0.6174	
0	90.6345 $\pm$ 0.6164	40.7 / 21
|0 - avr.|	0.0039 $\pm$ 0.0351	

Table 11: *Average R from the individual detector fits, for the different run periods with a start time of 49.2 μs. Detectors 2 and 20 were excluded. The fits were done with the 1999-style function.*

Period	R_0	A_{Rc}	A_{Rs}	$\sqrt{A_{Rc}^2 + A_{Rs}^2}$	χ^2/ndof
1a	92.3003 $\pm$ 2.2954	1.4701 $\pm$ 3.2359	0.2272 $\pm$ 3.2552	1.4876 $\pm$ 3.2364	20.6 / 19
1b	81.2789 $\pm$ 1.7237	-6.1685 $\pm$ 2.4315	-0.8274 $\pm$ 2.4424	6.2237 $\pm$ 2.4317	23.7 / 19
2+3	92.0513 $\pm$ 0.8181	-4.4731 $\pm$ 1.1528	-0.9929 $\pm$ 1.1606	4.5820 $\pm$ 1.1532	25.1 / 19
4	90.9557 $\pm$ 1.3019	-3.9212 $\pm$ 1.8380	1.9429 $\pm$ 1.8448	4.3762 $\pm$ 1.8393	14.7 / 19
avr.	90.4329 $\pm$ 0.6189	-4.1348 $\pm$ 0.8727	-0.2184 $\pm$ 0.8777	4.1406 $\pm$ 0.8727	
0	90.4720 $\pm$ 0.6173	-4.1948 $\pm$ 0.8660	-0.0633 $\pm$ 0.8798	4.1953 $\pm$ 0.8660	17.2 / 19
|0 - avr.|	0.0391 $\pm$ 0.0445	0.0600 $\pm$ 0.1079	0.1551 $\pm$ 0.0608	0.0547 $\pm$ 0.1079	

Table 12: *R versus detector was fitted with Function (38). The table gives the fit parameters for the different run periods with a start time of 49.2 μs. Detectors 2 and 20 were excluded. The underlying individual detector fits were done with the 1999-style function.*

Period	$\langle R \rangle - R_0$
1a	-0.0574 ± 0.1249
1b	+0.2516 ± 0.0982
2+3	+0.1825 ± 0.0461
4	+0.3173 ± 0.1386
0	+0.1624 ± 0.0333

Table 13: *Difference between fitting R versus detector to a constant and to a wave (Tables 11 and 12).*

Table 14 lists the CBO amplitude averaged over all detectors for the different run periods. We also calculated the CBO vector sum according to Eq. (37) with the only difference that the sum index p runs over the detectors 1 to 24 (without 2 and 20) instead of the run period. These vector sums are in rather good agreement with the results from the fits to the sum of detectors given in Table 10.

Period		vector sum over all detectors	
	$\langle A_{\mathrm{CBO}} \rangle \times 10^3$	$A_{\mathrm{CBO}} \times 10^3$	ϕ_{CBO}
1a	10.27 ± 0.16	2.87 ± 0.16	2.31 ± 0.05
1b	18.90 ± 0.15	4.68 ± 0.15	0.33 ± 0.03
2+3	15.50 ± 0.07	3.88 ± 0.07	5.84 ± 0.02
4	14.28 ± 0.10	3.71 ± 0.14	5.72 ± 0.04
vector sum		3.32 ± 0.06	5.95 ± 0.02
0	12.66 ± 0.05	3.21 ± 0.06	5.95 ± 0.02

Table 14: *First column: CBO parameters from fits to the individual detectors, averaged over all detectors. Second and third columns: vector sum of the CBO parameters over all detectors. Amplitude and phase of the vector sum should be consistent with the corresponding parameters obtained from the summed spectra (cf. Table 10).*

Comparison between Fits to the Sum and the Average of Individual Fits

The R-value from a fit to the sum of detector spectra should agree with the average $\langle R \rangle$ over the results from individual detector fits. The differences shown in Table 15 will serve as systematic errors due to the analysis method. Discrepancies between R_{sum} and the sine wave centroid R_0 are less surprising because the 1999-style function does not include any information about the presence of this sine wave.

Period	$\lvert\langle R \rangle - R_{\mathrm{sum}}\rvert$	$\lvert R_0 - R_{\mathrm{sum}}\rvert$
1a	0.0008 ± 0.0933	0.0566 ± 0.0830
1b	0.0192 ± 0.0669	0.2708 ± 0.0719
2+3	0.1755 ± 0.0384	0.0070 ± 0.0256
4	0.2252 ± 0.2606	0.0921 ± 0.2952
0	0.0719 ± 0.0520	0.0926 ± 0.0618

Table 15: *Difference between R from fits to the sum of all detector spectra and the averages $\langle R \rangle$ or R_0 from fits to individual detector spectra. The 1999 function was used.*

5.4.3 Fits with Asymmetry Modulation

This section describes fits using Function (6) including the asymmetry modulation term (9), but not the phase modulation term (10) (we fix the parameters $A_{\mathrm{Jim}} = \phi_{\mathrm{Jim}} = 0$). The second harmonic of f_{CBO} is switched on in the acceptance CBO term (8) (DCBO). Since the earliest start time regarded here is 49.2 μs, the terms pertaining to the vertical motion are switched off ($A_{\mathrm{VO}} = \phi_{\mathrm{VO}} = A_{\mathrm{VW}} = \phi_{\mathrm{VO}} = 0$).

	N_0	A	ϕ_a	R	f_{CBO}	A_{CBO}	ϕ_{CBO}	A_{Rob}	ϕ_{Rob}	A_{DCBO}	ϕ_{DCBO}	A_{loss}
N_0	1.000	0.016	0.005	**0.004**	-0.012	0.004	0.018	0.006	0.009	-0.005	0.003	-0.912
A	0.016	1.000	-0.029	**-0.030**	0.020	0.011	-0.017	0.238	-0.162	-0.007	0.001	-0.023
ϕ_a	0.005	-0.029	1.000	**0.872**	0.025	-0.016	-0.034	-0.280	-0.265	0.011	0.001	-0.007
R	0.004	-0.030	0.872	**1.000**	0.017	-0.012	-0.024	-0.229	-0.173	0.008	0.001	-0.006
f_{CBO}	-0.012	0.020	0.025	**0.017**	1.000	0.000	-0.636	0.024	-0.063	0.004	-0.034	0.019
A_{CBO}	0.004	0.011	-0.016	**-0.012**	0.000	1.000	-0.001	0.020	0.021	0.017	0.005	-0.004
ϕ_{CBO}	0.018	-0.017	-0.034	**-0.024**	-0.636	-0.001	1.000	-0.032	0.057	-0.006	0.029	-0.027
A_{Rob}	0.006	0.238	-0.280	**-0.229**	0.024	0.020	-0.032	1.000	0.037	-0.005	-0.015	-0.008
ϕ_{Rob}	0.009	-0.162	-0.265	**-0.173**	-0.063	0.021	0.057	0.037	1.000	0.009	-0.003	-0.013
A_{DCBO}	-0.005	-0.007	0.011	**0.008**	0.004	0.017	-0.006	-0.005	0.009	1.000	0.004	0.007
ϕ_{DCBO}	0.003	0.001	0.001	**0.001**	-0.034	0.005	0.029	-0.015	-0.003	0.004	1.000	-0.005
A_{loss}	-0.912	-0.023	-0.007	**-0.006**	0.019	-0.004	-0.027	-0.008	-0.013	0.007	-0.005	1.000

Table 16: *Correlation matrix* $\frac{\mathrm{cov}(\mathrm{p_i},\mathrm{p_j})}{\sigma_i\,\sigma j}$ *from a fit to the sum of detectors starting at 44.7 μs.*

The correlation matrix (Table 16) shows a strong relationship between R and the asymmetry modulation. Also, the correlation between R and A is ten times stronger than for the 1999-style function. The other effect introduced into the fit function, the double CBO, correlates very weakly with R.

Fits to the Sum of Detectors

A start time scan for R is shown in Figure 29 for the entire 2000 data set. The lower plot shows a zoom for start times up to 60 μs with a step of 150 ns.

Comparisons between the weighted average of the fit results for the individual run periods and the result for the full data set are shown in Figure 30 and Table 17 for R, and in Figure 31 for A. The improvement of the start-time stability of A with respect to the 1999 function may stem from the fairly strong correlations between A and A_{Rob} or ϕ_{Rob}.

Inclusion of the asymmetry modulation into the fit function reduces the halfring effect by about one half as compared to the 1999-style function, see Figure 32.

Start time scans for the other parameters and for the different run periods are shown in Appendix B.1. Appendix B.2 shows them for the first and second half of the ring.

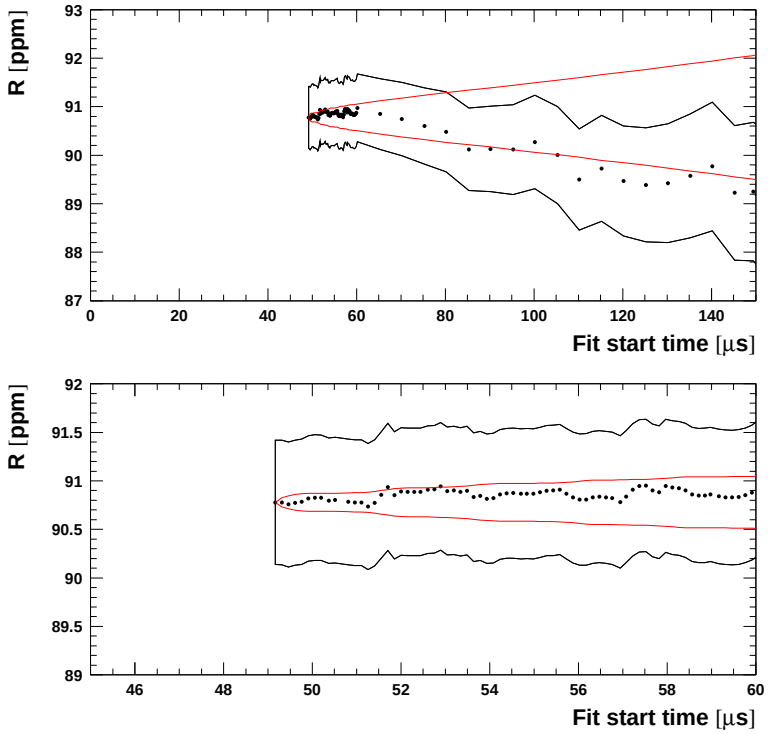

Figure 29: *Start time scan for the sum of all detector spectra of all runs fitted with the physics function without phase modulation.*

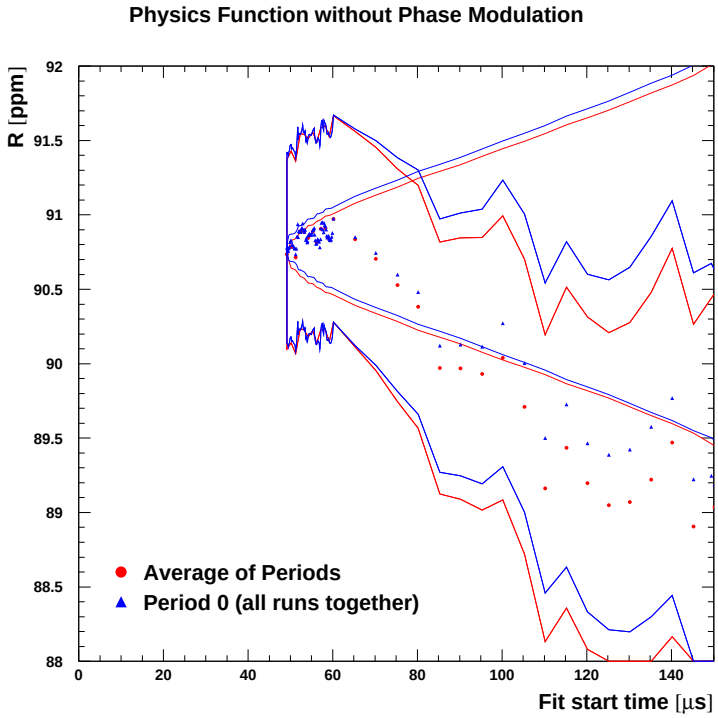

Figure 30: *Comparison between R for the sum and for the average of the run periods.*

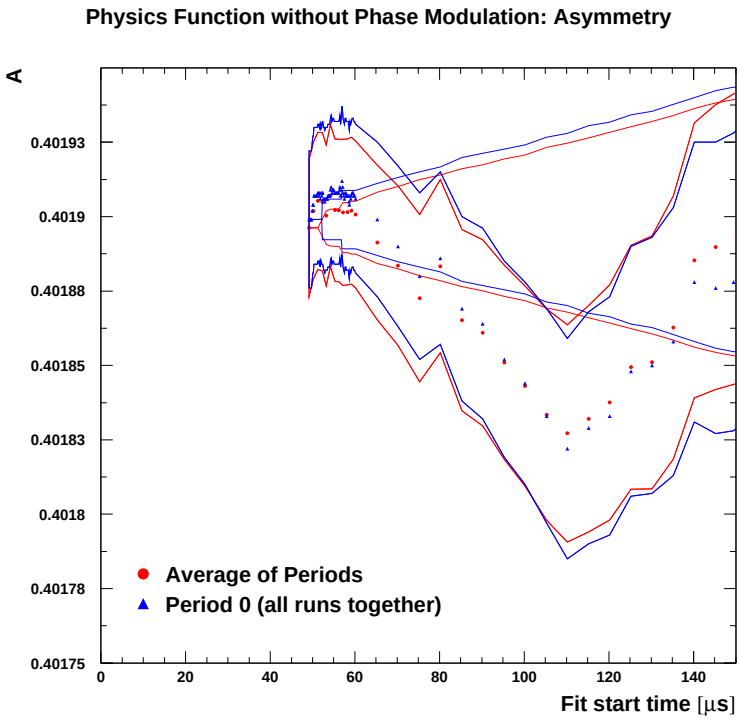

Figure 31: *Comparison between A for the sum and for the average of the run periods.*

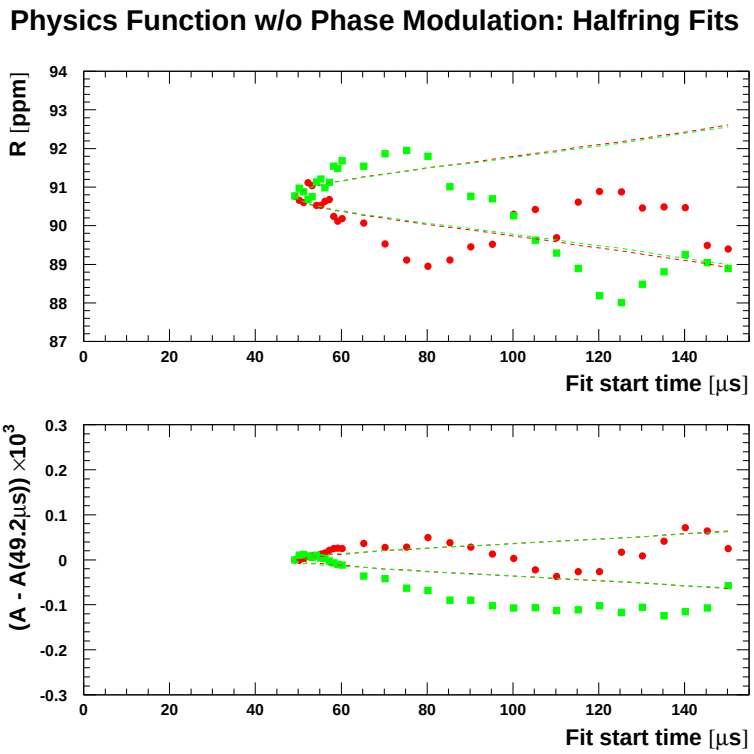

Figure 32: *Fit results for R and A in the two halves of the ring. This figure is for Period 0 (all runs).*

Period	Sum of all detectors	First half	Second half	Average of the halves
1a	92.3638 ± 2.3189	95.2027 ± 3.3377	89.7388 ± 3.2244	92.3764 ± 2.31902
1b	81.8476 ± 1.7693	83.2522 ± 2.5450	80.4163 ± 2.4670	81.7901 ± 1.7714
2+3	92.2853 ± 0.8537	91.5349 ± 1.2300	92.9808 ± 1.1854	92.2845 ± 0.8535
4	91.4369 ± 1.3087	91.4627 ± 1.8877	91.3585 ± 1.8240	91.4088 ± 1.3117
avr.	90.7354 ± 0.6374	90.7170 ± 0.9183	90.7306 ± 0.8864	90.7240 ± 0.6378
0	90.7789 ± 0.6406	90.7651 ± 0.9231	90.7748 ± 0.8900	90.7701 ± 0.6407
|0 - avr.|	0.0435 ± 0.0640	0.0481 ± 0.0940	0.0442 ± 0.0800	0.04610 ± 0.0609

Table 17: *Fit results for R in the individual run periods with a start time of 49.2 μs. The physics function without phase modulation was used.*

Like with the 1999-style function, the R-value of Period 1b is lower than the average of the other periods. From the R-values in Table 18 we compute a discrepancy of (10.21 ± 1.63) ppm. Again, we calculate a pseudo-a_μ, falsified by an offset in ω_p and a global scale factor. Fitting the pseudo-a_μ values of the four considered periods to a constant results in χ^2 /dof = 2.32 / 3 (Figure 33). Thus, this test does not reveal any inconsistency.

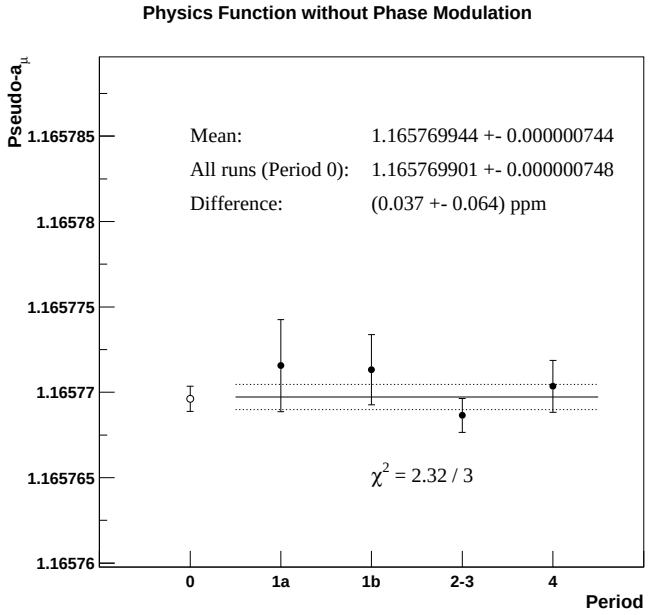

Figure 33: *Pseudo-a_μ versus run period. These numbers contain an offset in ω_p and a global scale factor.*

The run-period consistency check for the CBO parameters was done like with the 1999-style function. The vector sum for the asymmetry modulation was calculated like in Eq. (37), but with the weights N_p replaced by $N_p\,A_p\,\cos\phi_{a,p}$.

Period	$A_{\mathrm{CBO}} \times 10^3$	ϕ_{CBO}	$A_{\mathrm{Rob}} \times 10^3$	ϕ_{Rob}
1a	2.86 ± 0.16	2.33 ± 0.08	0.54 ± 0.53	3.86 ± 0.99
1b	4.68 ± 0.15	0.33 ± 0.04	0.39 ± 0.52	3.37 ± 1.33
2+3	3.89 ± 0.07	5.85 ± 0.03	0.44 ± 0.25	3.98 ± 0.58
4	3.72 ± 0.10	5.73 ± 0.04	0.59 ± 0.34	3.64 ± 0.58
vector sum	3.32 ± 0.06	5.96 ± 0.02	0.47 ± 0.18	3.81 ± 0.39
0	3.21 ± 0.05	5.95 ± 0.02	0.47 ± 0.18	4.05 ± 0.40

Table 18: *CBO parameters from fits to the sum of all detectors.*

Fits to the Individual Detectors

The fit results for individual detectors at a start time of 49.2 μs are shown in the figures of Appendix B.3.

Like for the 1999 function, R versus detector follows a sine wave rather than a constant line (compare χ^2 in Tables 19 and 20), but due to the inclusion of the asymmetry modulation the halfring amplitude declined by 50 % from (4.2 ± 0.9) ppm to (2.1 ± 0.9) ppm. Also, the disagreement between the centroid value R_0 and the average $\langle R \rangle$ is reduced from (0.16 ± 0.03) ppm to (0.08 ± 0.04) ppm for Period 0 (Table 20).

Period	$\langle R \rangle$	χ^2/ndof (fit to a constant)
1a	92.4633 ± 2.3163	24.1 / 21
1b	81.7693 ± 1.7689	25.0 / 21
2+3	92.2984 ± 0.8524	31.5 / 21
4	91.4337 ± 1.3070	16.8 / 21
avr.	90.7421 ± 0.6366	
0	90.7784 ± 0.6396	25.9 / 21
|0 - avr.|	0.0363 ± 0.0619	

Table 19: *Average R from the individual detector fits, for the different run periods with a start time of 49.2 μs. Detectors 2 and 20 were excluded. The physics function without g-2 phase modulation was used.*

Period	R_0	A_{Rc}	A_{Rs}	$\sqrt{A_{Rc}^2 + A_{Rs}^2}$	χ^2/ndof
1a	92.4679 ± 2.3198	-0.0817 ± 3.2703	0.1632 ± 3.2892	0.1825 ± 3.2854	24.1 / 19
1b	81.6549 ± 1.7718	-3.0089 ± 2.4979	0.8163 ± 2.5119	3.1177 ± 2.4989	23.5 / 19
2+3	92.1977 ± 0.8537	-2.1813 ± 1.2031	-1.7096 ± 1.2112	2.7714 ± 1.2062	26.0 / 19
4	91.3775 ± 1.3090	-1.7380 ± 1.8447	1.0801 ± 1.8568	2.0463 ± 1.8481	15.6 /19
avr.	90.6584 ± 0.6376	-2.0247 ± 0.8986	-0.5788 ± 0.9044	2.1058 ± 0.8990	
0	90.6962 ± 0.6406	-2.0124 ± 0.9026	-0.5158 ± 0.9089	2.0775 ± 0.9030	20.6 / 19
|0 - avr.|	0.0378 ± 0.0619	0.0123 ± 0.0849	0.0630 ± 0.0903	0.0283 ± 0.0849	

Table 20: *R versus detector fitted with a sine + cosine function like in Table 12, but for ω_a fits including the asymmetry CBO modulation. The start time was 49.2 μs. As always, detectors 2 and 20 were excluded.*

Period	$\langle R \rangle - R_0$
1a	-0.0046 ± 0.1274
1b	+0.1144 ± 0.1013
2+3	+0.1007 ± 0.0471
4	+0.0562 ± 0.0723
0	+0.0821 ± 0.0358

Table 21: *Difference between fitting R versus detector to a constant and to a wave (Tables 19 and 20).*

In Table 22 we give the average CBO amplitudes and the CBO vector sums like in Table 14.

Period	$\langle A_{\mathrm{CBO}} \rangle \times 10^3$	$\langle A_{\mathrm{Rob}} \rangle \times 10^3$	$\langle \phi_{\mathrm{Rob}} - \phi_{\mathrm{CBO}} \rangle$
1a	10.25 ± 0.16	4.06 ± 0.54	0.04 ± 0.12
1b	18.89 ± 0.15	5.31 ± 0.52	6.09 ± 0.09
2+3	15.48 ± 0.07	3.83 ± 0.25	6.06 ± 0.06
4	13.88 ± 0.10	3.34 ± 0.34	6.08 ± 0.09
0	12.60 ± 0.05	3.16 ± 0.18	6.08 ± 0.06

Period	vector sum over all detectors			
	$A_{\mathrm{CBO}} \times 10^3$	ϕ_{CBO}	$A_{\mathrm{Rob}} \times 10^3$	ϕ_{Rob}
1a	2.87 ± 0.16	2.31 ± 0.05	0.55 ± 0.59	3.68 ± 1.06
1b	4.68 ± 0.15	0.33 ± 0.03	0.27 ± 0.52	3.12 ± 1.97
2+3	3.88 ± 0.07	5.84 ± 0.02	0.34 ± 0.25	4.36 ± 0.76
4	3.71 ± 0.10	5.72 ± 0.03	0.49 ± 0.34	3.84 ± 0.68
vector sum	3.32 ± 0.05	5.96 ± 0.02	0.35 ± 0.18	4.03 ± 0.52
0	3.21 ± 0.05	5.95 ± 0.02	0.39 ± 0.18	4.29 ± 0.48

Table 22: *Upper table: CBO parameters from fits to the individual detectors, averaged over all detectors. Lower Table: coherent sum of the CBO parameters over all detectors. The results should be consistent with the fit parameters obtained from the summed spectra (cf. Table 18).*

We want to point out the following observations:

- Inclusion of the asymmetry modulation into the fit has very little influence on $\langle A_{\mathrm{CBO}} \rangle$: We find $(12.60 \pm 0.05) \times 10^{-3}$ instead of $(12.66 \pm 0.05) \times 10^{-3}$ (Table 14).
- The same holds for the vector sum of $(A_{\mathrm{CBO}}, \phi_{\mathrm{CBO}})$.
- The agreement between the vector sum $(A_{\mathrm{CBO}}, \phi_{\mathrm{CBO}})$ and the parameter values obtained by fitting the sum of detector spectra is good (compare with Table 18).
- The same comparison for $(A_{\mathrm{Rob}}, \phi_{\mathrm{Rob}})$ yields a less good agreement. E.g. for A_{Rob} in Period 0 we find now $(0.39 \pm 0.18) \times 10^{-3}$ instead of $(0.47 \pm 0.18) \times 10^{-3}$. This demonstrates that the asymmetry modulation parameters suffer from other systematic effects, mostly via the asymmetry.

Comparison between Fits to the Sum and the Average of Individual Fits

Period	$\lvert\langle R\rangle - R_{\mathrm{sum}}\rvert$	$\lvert R_0 - R_{\mathrm{sum}}\rvert$
1a	0.0995 ± 0.1098	0.1041 ± 0.0646
1b	0.0783 ± 0.0376	0.1927 ± 0.0941
2+3	0.0131 ± 0.0471	0.0876 ± 0.0000
4	0.0032 ± 0.0667	0.0594 ± 0.0280
0	0.0005 ± 0.0358	0.0827 ± 0.0000

Table 23: *Difference between R from fits to the sum of all detector spectra and the averages $\langle R\rangle$ and R_0 from fits to individual detector spectra.*

5.4.4 Fits with Asymmetry and Phase Modulation

In this section we fit for all three CBO effects: acceptance, asymmetry and phase modulation. The double CBO component is included in the acceptance term (8). Again, the vertical motions are not included in the fit.

A look at the correlation matrix (Table 24) reveals that the inclusion of the phase modulation into the fit leads to a few additional troublesome correlations: both A_{Jim} and ϕ_{Jim} correlate rather strongly with R. Furthermore, A_{Jim} correlates with A. Therefore we have an indirect influence of asymmetry-changing effects (like gain) on R via A_{Jim} and via A_{Rob} like in the fit function without phase modulation. Also, the direct correlation between A and R that had already increased by a factor 10 from the 1999 to the physics function without phase modulation, grows by another factor of 2 when the phase modulation is switched on.

Fits to the Sum of Detectors

A start time scan for R is shown in Figure 34 for the entire 2000 data set. Note the kink around 90 μs. The lower plot shows a zoom for start times up to 60 μs with a step of 150 ns.

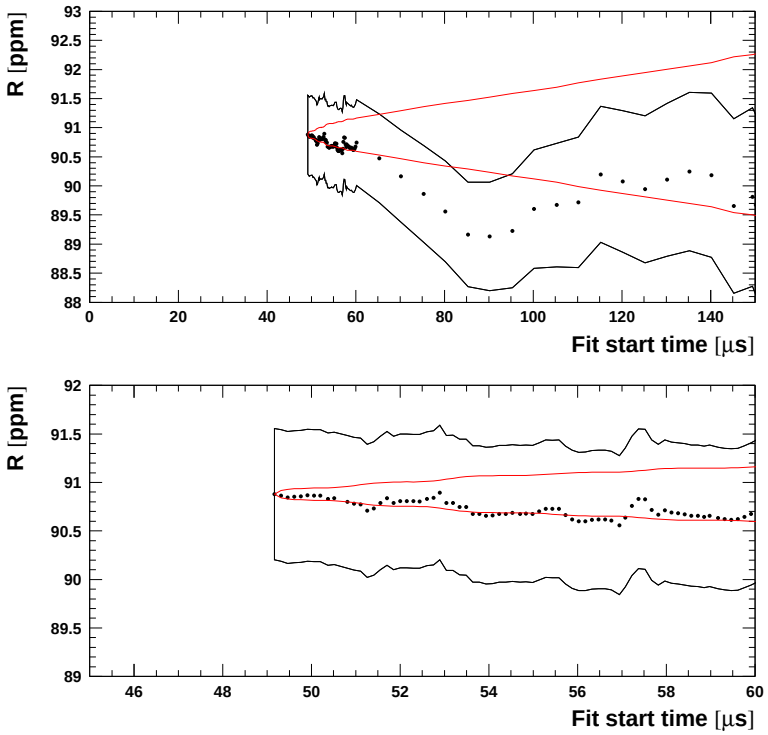

Figure 34: *Start time scan for the sum of all detector spectra of all runs fitted with the physics function including phase modulation by CBO.*

Comparisons between the weighted average of the fit results for the individual run periods and the result for the full data set are shown in Figure 35 and Table 25 for R, and in Figure 36 for A. Unlike with the fit functions previously discussed, the start-time stability of A with the full physics function is good. This may be an artifact of the strong correlation between A and A_{Jim}.

	N_0	A	ϕ_a	R	f_{CBO}	A_{CBO}	ϕ_{CBO}	A_{Rob}	ϕ_{Rob}	A_{Jim}	ϕ_{Jim}	A_{DCBO}	ϕ_{DCBO}	A_{loss}
N_0	1.000	0.018	-0.006	**-0.005**	-0.013	0.003	0.019	0.010	0.012	0.011	0.025	-0.005	0.004	-0.912
A	0.018	1.000	-0.062	**-0.065**	0.030	0.007	-0.024	0.262	-0.152	0.306	0.003	0.001	0.001	-0.026
ϕ_a	-0.006	-0.062	1.000	**0.884**	0.034	-0.014	-0.039	-0.307	-0.300	-0.134	-0.401	0.012	-0.007	0.009
R	-0.005	-0.065	0.884	**1.000**	0.022	-0.010	-0.027	-0.260	-0.208	-0.135	-0.302	0.009	-0.005	0.007
f_{CBO}	-0.013	0.030	0.034	**0.022**	1.000	0.000	-0.641	0.024	-0.071	0.010	-0.039	0.005	-0.036	0.020
A_{CBO}	0.003	0.007	-0.014	**-0.010**	0.000	1.000	-0.001	0.018	0.022	-0.012	0.001	0.017	0.005	-0.004
ϕ_{CBO}	0.019	-0.024	-0.039	**-0.027**	-0.641	-0.001	1.000	-0.032	0.063	-0.010	0.029	-0.007	0.031	-0.028
A_{Rob}	0.010	0.262	-0.307	**-0.260**	0.024	0.018	-0.032	1.000	0.052	0.116	0.115	-0.004	-0.012	-0.013
ϕ_{Rob}	0.012	-0.152	-0.300	**-0.208**	-0.071	0.022	0.063	0.052	1.000	-0.004	0.145	0.006	-0.000	-0.018
A_{Jim}	0.011	0.306	-0.134	**-0.135**	0.010	-0.012	-0.010	0.116	-0.004	1.000	0.041	0.026	0.004	-0.016
ϕ_{Jim}	0.025	0.003	-0.401	**-0.302**	-0.039	0.001	0.029	0.115	0.145	0.041	1.000	-0.015	0.021	-0.036
A_{DCBO}	-0.005	0.001	0.012	**0.009**	0.005	0.017	-0.007	-0.004	0.006	0.026	-0.015	1.000	0.004	0.007
ϕ_{DCBO}	0.004	0.001	-0.007	**-0.005**	-0.036	0.005	0.031	-0.012	-0.000	0.004	0.021	0.004	1.000	-0.006
A_{loss}	-0.912	-0.026	0.009	**0.007**	0.020	-0.004	-0.028	-0.013	-0.018	-0.016	-0.036	0.007	-0.006	1.000

Table 24: *Correlation matrix* $\frac{\text{cov}(\text{p}_\text{i},\text{p}_\text{j})}{\sigma_i\,\sigma j}$ *from a fit to the sum of detector spectra starting at 44.7*μ*s.*

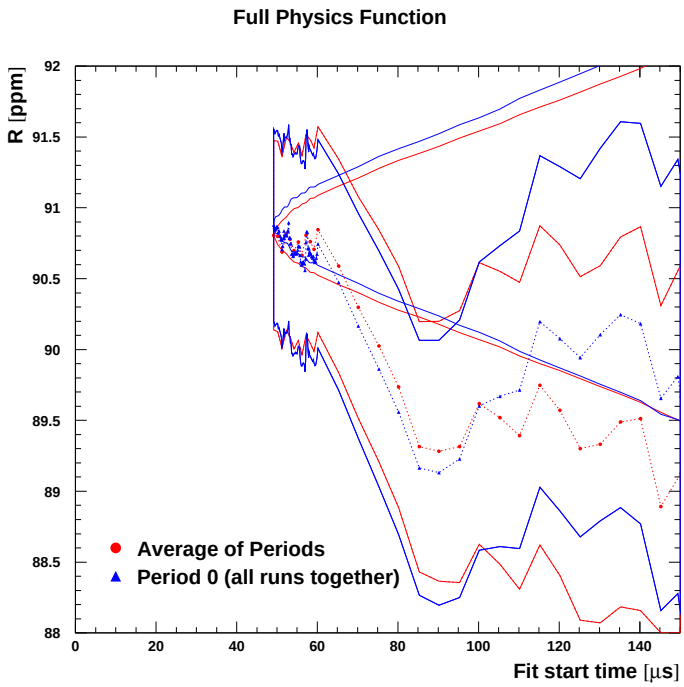

Figure 35: *Comparison between R for the sum and for the average of the run periods.*

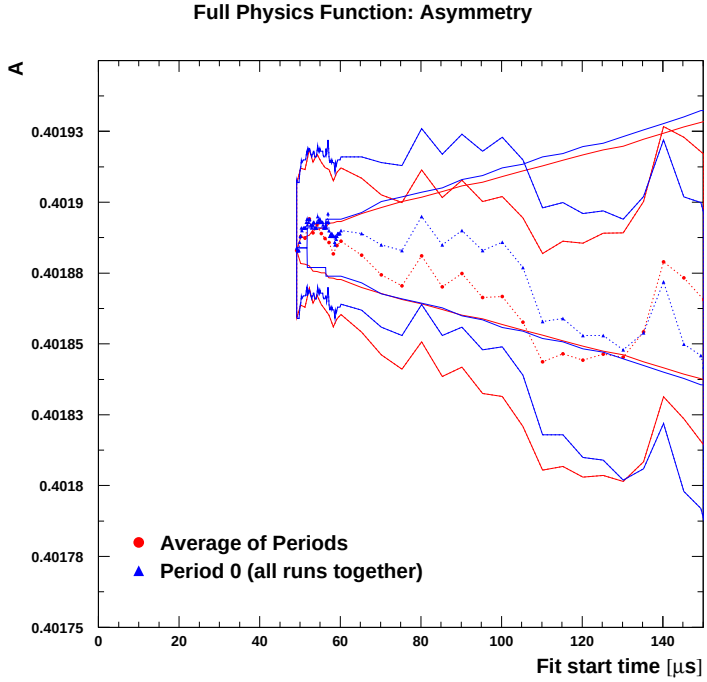

Figure 36: *Comparison between A for the sum and for the average of the run periods.*

The halfring effect that had already been reduced by inclusion of the asymmetry modulation is mostly eliminated when also the phase modulation is fitted for, see Figure 37. This figure also shows that the kink in R at 90 μs originates from the first half of the ring. Interestingly, that half is much more affected by gain instablilities than the second.

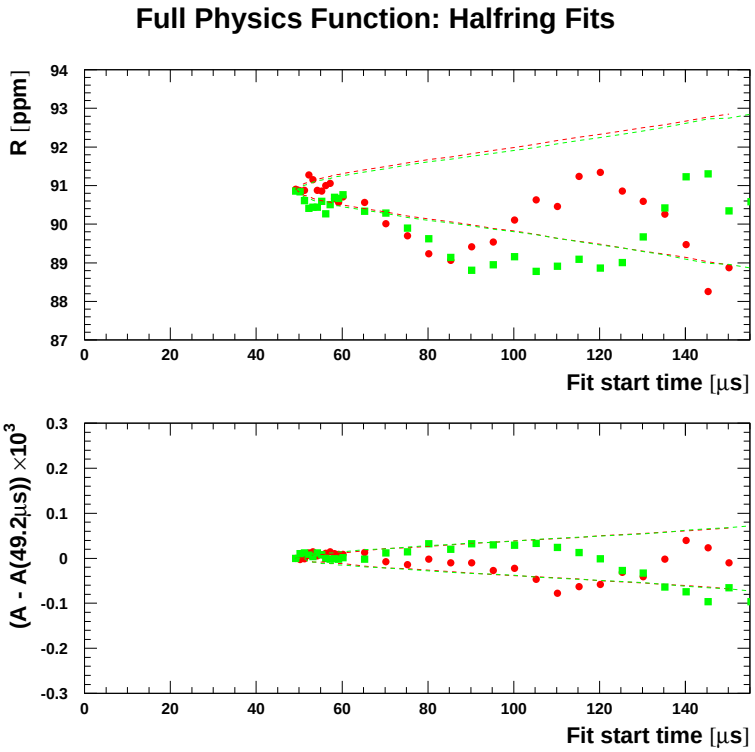

Figure 37: *Fit results for R and A in the two halves of the ring. This figure is for Period 0 (all runs).*

Start time scans for the other parameters and for the different run periods are shown in Appendix C.1. Appendix C.2 shows them for the first and second half of the ring.

Period	Sum of all detectors	First half	Second half	Average of the halves
1a	92.8084 ± 2.3488	95.1462 ± 3.3822	90.6102 ± 3.2667	92.7994 ± 2.3497
1b	82.4620 ± 1.8307	84.5341 ± 2.6382	80.3633 ± 2.5606	82.3865 ± 1.8374
2+3	92.3487 ± 0.9058	91.5398 ± 1.3060	93.1210 ± 1.2576	92.3603 ± 0.9059
4	91.2631 ± 1.3615	91.1703 ± 1.9677	91.1720 ± 1.9095	91.1712 ± 1.3703
Avr.	90.8061 ± 0.6685	90.8084 ± 0.9642	90.7653 ± 0.9314	90.7861 ± 0.6699
0	90.8792 ± 0.6779	90.9037 ± 0.9783	90.8563 ± 0.9423	90.8791 ± 0.6787
|0 - avr.|	0.0731 ± 0.1125	0.0953 ± 0.1655	0.0910 ± 0.1429	0.0930 ± 0.1089

Table 25: *R for the sum of all detectors and for the two half rings; all runs were added. The fits included the g-2 phase modulation. Its envelope was assumed to be the acceptance CBO envelope. The start time was 49.2 μs.*

Like for the two other fit functions we verify the consistency of the four run periods by calculating the pseudo-a_μ (Figure 38). Fitting the pseudo-a_μ values to a constant yields χ^2 /dof = 1.77 / 3.

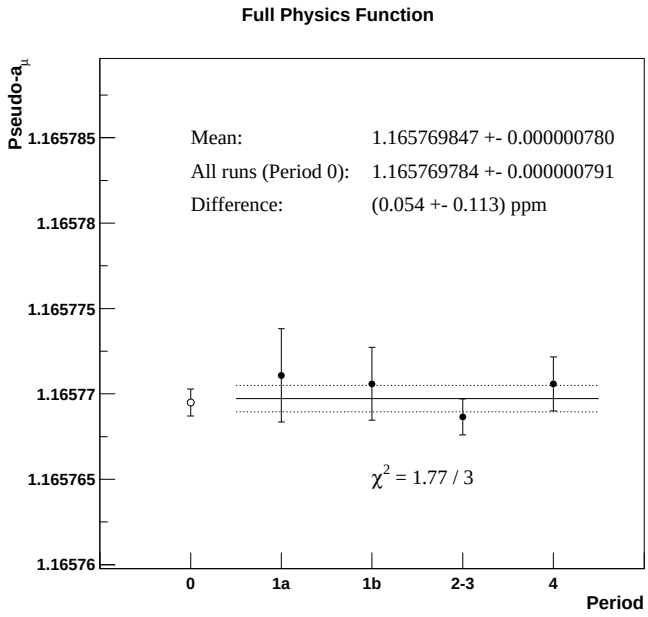

Figure 38: *Pseudo-a_μ versus run period. These numbers contain an offset in ω_p and a global scale factor.*

The run-period consistency check for the CBO parameters was done like with the previous functions. The vector sum for the phase modulation was calculated like in Eq. (37), but with the weights N_p replaced by $N_p\,A_p\,\sin\phi_{a,p}\,\phi_{a,p}$, as can be seen by expanding the phase modulation in the physics function.

Period	$A_{\rm CBO}\times 10^3$	$\phi_{\rm CBO}$	$A_{\rm Rob}\times 10^3$	$\phi_{\rm Rob}$	$A_{\rm Jim}\times 10^3$	$\phi_{\rm Jim}$
1a	2.86 ± 0.16	2.33 ± 0.08	0.53 ± 0.53	3.82 ± 1.00	0.29 ± 0.19	3.61 ± 0.65
1b	4.68 ± 0.15	0.33 ± 0.04	0.48 ± 0.53	3.30 ± 1.08	0.28 ± 0.18	4.98 ± 0.65
2+3	3.89 ± 0.07	5.84 ± 0.03	0.48 ± 0.26	3.99 ± 0.55	0.15 ± 0.09	6.04 ± 0.62
4	3.72 ± 0.10	5.73 ± 0.04	0.56 ± 0.34	3.65 ± 0.61	0.11 ± 0.12	2.36 ± 1.14
vec. sum	3.32 ± 0.06	5.96 ± 0.02	0.49 ± 0.18	3.81 ± 0.38	0.07 ± 0.06	5.60 ± 0.87
0	3.21 ± 0.05	5.95 ± 0.02	0.50 ± 0.19	4.04 ± 0.38	0.13 ± 0.06	5.92 ± 0.50

Table 26: *CBO parameters from fits to the sum of all detectors. The envelope of the phase modulation was assumed to be the same as for the acceptance CBO.*

The agreement between $A_{\rm Jim}$ from Period 0 and the vector sum is not good. This shows that the fitted phase modulation parameters suffer from other systematic effects.

Fits to the Individual Detectors

The fit results for individual detectors at a start time of 49.2 μs are shown in the figures of Appendix C.3.

With the full physics function, R versus detector is constant: the normalised χ^2 does not improve from the constant line to the sine wave (cf. Tables 27 and 28). Furthermore, the halfring amplitude (0.60 ± 0.96) ppm is consistent with zero. There is no disagreement between the centroid value R_0 and the average $\langle R \rangle$ any more (Table 28).

Period	$\langle R \rangle$	χ^2/ndof (fit to a constant)
1a	92.8948 ± 2.3460	24.5 / 21
1b	82.3735 ± 1.8295	20.8 / 21
2+3	92.4421 ± 0.9039	29.0 / 21
4	91.3265 ± 1.3594	15.9 / 21
avr.	90.8703 ± 0.6673	
0	90.8737 ± 0.6765	19.9 / 21
|0 - avr.|	0.0034 ± 0.1112	

Table 27: *Average R from the individual detector fits, for the different run periods with a start time of 49.2 μs. Detectors 2 and 20 were excluded. The full physics function was used.*

Period	R_0	A_{Rc}	A_{Rs}	$\sqrt{A_{Rc}^2 + A_{Rs}^2}$	χ^2/ndof
1a	92.8600 ± 2.3495	-0.8706 ± 3.3119	-0.2989 ± 3.3320	0.9205 ± 3.3140	24.4 / 19
1b	82.2922 ± 1.8325	-2.4730 ± 2.5847	2.1701 ± 2.5968	3.2902 ± 2.5900	19.2 / 19
2+3	92.4294 ± 0.9053	0.0011 ± 1.2756	-1.0642 ± 1.2840	1.0642 ± 1.2840	28.3 / 19
4	91.3461 ± 1.3615	0.1627 ± 1.9187	1.1454 ± 1.9312	1.1569 ± 1.9310	15.6 / 19
avr.	90.8547 ± 0.6684	-0.3591 ± 0.9419	-0.0391 ± 0.9479	0.3612 ± 0.9420	
0	90.8504 ± 0.6776	-0.6032 ± 0.9551	-0.0248 ± 0.9614	0.6037 ± 0.9551	19.5 / 19
|0 - avr.|	0.0043 ± 0.1113	0.2441 ± 0.1582	0.0143 ± 0.1605	0.2425 ± 0.1576	

Table 28: *R versus detector fitted with a sine + cosine function. The individual detector spectra were fitted with the full physics function. The start time was 49.2 μs. Detectors 2 and 20 were excluded.*

Period	$\langle R \rangle - R_0$
1a	+0.0348 ± 0.1282
1b	+0.0813 ± 0.1048
2+3	+0.0127 ± 0.0503
4	-0.0196 ± 0.0756
0	+0.0233 ± 0.0386

Table 29: *Difference between fitting R versus detector to a constant and to a wave (Tables 27 and 28).*

In Table 30 we give the average CBO amplitudes and the CBO vector sums.

Period	$\langle A_{\rm CBO}\rangle \times 10^3$	$\langle A_{\rm Rob}\rangle \times 10^3$	$\langle A_{\rm Jim}\rangle \times 10^3$	$\langle \phi_{\rm Rob} - \phi_{\rm CBO}\rangle$	$\langle \phi_{\rm Jim} - \phi_{\rm CBO}\rangle$
1a	10.25 ± 0.16	4.14 ± 0.53	1.31 ± 0.19	0.05 ± 0.12	0.71 ± 0.13
1b	18.45 ± 0.15	5.53 ± 0.53	1.50 ± 0.18	6.09 ± 0.09	2.00 ± 0.08
2+3	15.47 ± 0.07	4.08 ± 0.26	0.86 ± 0.09	6.14 ± 0.06	1.84 ± 0.09
4	14.07 ± 0.10	3.47 ± 0.34	0.85 ± 0.12	6.09 ± 0.09	1.36 ± 0.13
0	12.60 ± 0.05	3.29 ± 0.19	0.69 ± 0.06	6.11 ± 0.05	2.10 ± 0.09

Period	vector sum over all detectors					
	$A_{\rm CBO} \times 10^3$	$\phi_{\rm CBO}$	$A_{\rm Rob} \times 10^3$	$\phi_{\rm Rob}$	$A_{\rm Jim} \times 10^3$	$\phi_{\rm Jim}$
1a	2.86 ± 0.16	2.31 ± 0.05	0.55 ± 0.53	3.63 ± 0.97	0.28 ± 0.19	3.57 ± 0.68
1b	4.68 ± 0.16	0.33 ± 0.04	0.34 ± 0.58	3.10 ± 1.56	0.29 ± 0.18	5.05 ± 0.68
2+3	3.88 ± 0.07	5.84 ± 0.02	0.38 ± 0.26	4.27 ± 0.68	0.15 ± 0.09	5.88 ± 0.61
4	3.71 ± 0.10	5.72 ± 0.03	0.48 ± 0.34	3.82 ± 0.71	0.11 ± 0.12	2.61 ± 1.14
vec. sum	3.32 ± 0.05	5.95 ± 0.02	0.38 ± 0.19	3.97 ± 0.48	0.08 ± 0.06	5.40 ± 0.78
0	3.21 ± 0.05	5.95 ± 0.02	0.43 ± 0.19	4.27 ± 0.44	0.14 ± 0.06	5.87 ± 0.49

Table 30: *Upper table: CBO parameters from fits to the individual detectors, averaged over all detectors. Lower Table: coherent sum of the CBO parameters over all detectors. The results should be consistent with the fit parameters obtained from the summed spectra (cf. Table 26).*

Again, average amplitude and vector sum of the main CBO are not affected by the inclusion of the phase modulation term (cf. Tables 22 and 30). The same holds for the asymmetry modulation.

The phase modulation vector sum over all detectors reproduces the result from the fit to the sum of detectors (Table 26) rather well: For $A_{\rm Jim}$ we get $(0.14 \pm 0.06) \times 10^{-3}$ vs. $(0.13 \pm 0.06) \times 10^{-3}$. This is in fact better than for the asymmetry modulation.

Comparison between Fits to the Sum and the Average of Individual Fits

For the full physics function both the average $\langle R\rangle$ and the centroid value R_0 from the individual detector fits agree well with the result from the fit to the sum of detectors.

Period	$\lvert\langle R\rangle - R_{\rm sum}\rvert$	$\lvert R_0 - R_{\rm sum}\rvert$
1a	0.0864 ± 0.1147	0.0516 ± 0.0574
1b	0.0885 ± 0.0663	0.1698 ± 0.0812
2+3	0.0934 ± 0.0586	0.0807 ± 0.0301
4	0.0634 ± 0.0756	0.0830 ± 0.0000
0	0.0055 ± 0.04354	0.0288 ± 0.0202

Table 31: *Difference between R from fits to the sum of all detector spectra and the averages $\langle R\rangle$ and R_0 from fits to individual detector spectra.*

With the full physics function almost everything is consistent. The main indication for troubles is the poor start-time stability of R with the very prominent kink at $90\,\mu$s. Furthermore, in Section 6.6 we shall see that the systematic error from gain variations is very big, which destroys the otherwise good competitiveness of this fit function.

5.4.5 Time-of-Flight Correction to Individual Pulses

This study attempts to replace the phase modulation term in the fit function by a correction to the individual positron times before filling them into time histograms. The underlying assumption is that the phase modulation by CBO is mainly caused by the oscillation of the decay positrons' time of flight from the oscillating beam to the detector.

The time of flight

$$dt = p_1 + p_2 \mathrm{e}^{-\frac{t}{110\,\mu\mathrm{s}}} \cos(\omega_{\mathrm{CBO}} t + \phi_{\mathrm{CBO}} + p_3) \tag{39}$$

for a positron detected at the time t was obtained from a simulation [8]. The time spectra were then filled with $t - dt$. The CBO frequency was chosen according to the run period (Section 2). The CBO phase was taken from fits to the spectra of the individual detectors. The parameters p_1, p_2 and p_3 depend on the detector and the pulse energy:

- Non-kicker detectors:

Energy range	p_1 [ns]	p_2 [ns]
2.0 - 2.2 GeV	8.3	0.12
2.2 - 2.4 GeV	9.4	0.14
2.4 - 2.6 GeV	10.5	0.21
2.6 - 2.8 GeV	11.7	0.23
2.8 GeV - ∞	13.6	0.28

  $p_3 = 1.6$ rad

- Kicker detectors (7, 8, 9, 10):

Energy range	p_1 [ns]	p_2 [ns]
2.0 - 2.2 GeV	7.8	0.09
2.2 - 2.4 GeV	8.8	0.12
2.4 - 2.6 GeV	9.8	0.17
2.6 - 2.8 GeV	10.8	0.19
2.8 GeV - ∞	12.4	0.25

  $p_3 = 0.6$ rad

Then the time spectra were fitted with the physics function without phase modulation because the latter should be taken care of by the correction at filling time. For this study no distinction between run periods was made.

To separate the effects from the non-wiggling time-of-flight component p_1 and the wiggling component p_2, we also tried the correction with p_2 having the wrong sign (-). The difference between the fit results for the correct and the wrong sign for p_2 will show the impact of the CBO-oscillating component of the time of flight.

The following paragraphs will show the results of the study for the sum of detectors and for the average of fits to the individual spectra. Note that this study has been done at an earlier stage of the analysis with a fit start time of 44.7 μs which necessitates an additional, exponential term (5 μs life time) accounting for residual slow effects. Therefore the numerical values of R should not be directly compared with those reported in other sections although they are not inconsistent.

Fits to the Sum of Detectors

Table 32 shows that the time-of-flight correction does lead to a change in R, but this

	Fit with physics function without phase modulation			full physics funct.
	no TOF corr.	with TOF corr.	with TOF corr. (wrong sign for p_2)	no TOF corr.
R (all det.)	90.76 ± 0.62	90.93 ± 0.62	90.92 ± 0.62	90.95 ± 0.65
R (first half)	90.91 ± 0.89	91.15 ± 0.88	91.13 ± 0.88	90.95 ± 0.94
R (second half)	90.63 ± 0.86	90.72 ± 0.85	90.72 ± 0.85	90.95 ± 0.91

Table 32: *Fit results with and without time-of-flight correction for a fit start time of 44.7 μs.*

change is mainly due to the non-oscillating component of the time of flight since flipping the sign of the wiggling part p_2 has very little impact.

Fits to Individual Detectors

Table 33 shows that the time-of-flight correction does not reduce the half-ring effect

	Fit with physics function without phase modulation			full physics funct.
	no TOF corr.	with TOF corr.	with TOF corr. (wrong sign for p_2)	no TOF corr.
χ^2 (fit to const.)	29.66 / 21	29.74 / 21	29.70 / 21	21.21 / 21
χ^2 (fit to wave)	23.83 / 19	23.22 / 19	23.26 / 19	20.97 / 19
$\langle R \rangle$	90.72 ± 0.62	90.88 ± 0.61	90.88 ± 0.61	90.98 ± 0.65
R_0	90.63 ± 0.62	90.80 ± 0.61	90.79 ± 0.61	90.95 ± 0.65
A_{Rc}	-2.08 ± 0.87	-2.18 ± 0.86	-2.17 ± 0.86	-0.45 ± 0.92
A_{Rs}	-0.29 ± 0.88	-0.25 ± 0.87	-0.26 ± 0.87	-0.07 ± 0.93
$\sqrt{A_{Rc}^2 + A_{Rs}^2}$	2.10 ± 0.87	2.19 ± 0.86	2.19 ± 0.86	0.45 ± 0.92
$\langle A_{\mathrm{CBO}} \rangle \times 10^3$	12.75 ± 0.05	12.78 ± 0.05	12.78 ± 0.05	12.68 ± 0.05
$\langle A_{\mathrm{Rob}} \rangle \times 10^3$	2.34 ± 0.18	2.34 ± 0.17	2.34 ± 0.17	2.58 ± 0.17

Table 33: *Fit results with and without time-of-flight correction for a fit start time of 44.7 μs. R versus detector was fitted to a constant $\langle R \rangle$ and the function $R(d) = R_0 + A_{Rc} \cos(2\pi \frac{d}{24}) + A_{Rs} \sin(2\pi \frac{d}{24})$.*

whereas fitting with the full physics function eliminates it.

Apparently the oscillation of the time of flight with the CBO is not the only source of the g-2 phase modulation. Applying a time-of-flight correction before filling the time spectra is not an adequate substitute for fitting the full physics function.

5.4.6 Comparison of Fit Results with Different Functions

Period	1999 Func.	Physics Func. without Phase Modulation	Physics Func. with Phase Modulation
1a	92.2437 ± 2.2939	92.3638 ± 2.3189	92.8084 ± 2.3488
1b	81.5497 ± 1.7222	81.8476 ± 1.7693	82.4620 ± 1.8307
2+3	92.0583 ± 0.8177	92.2853 ± 0.8537	92.3487 ± 0.9058
4	91.0478 ± 1.2680	91.4369 ± 1.3087	91.2631 ± 1.3615
0	90.5646 ± 0.6142	90.7789 ± 0.6406	90.8792 ± 0.6779

Table 34: *Comparison of R from fits with the three functions studied. These numbers represent fits to the sum of all detectors starting at 49.2 μs.*

Period	1999 Func.	Physics Func. without Phase Modulation	Physics Func. with Phase Modulation
1a	0.9881	0.9881	0.9880
1b	0.9900	0.9902	0.9901
2+3	1.0046	1.0046	1.0043
4	1.0361	1.0345	1.0348
0	1.0130	1.0112	1.0106

Table 35: *Comparison of χ^2 from fits with the three functions studied. These numbers represent fits to the sum of all detectors starting at 49.2 μs. In all cases the statistical error amounts to 0.0234.*

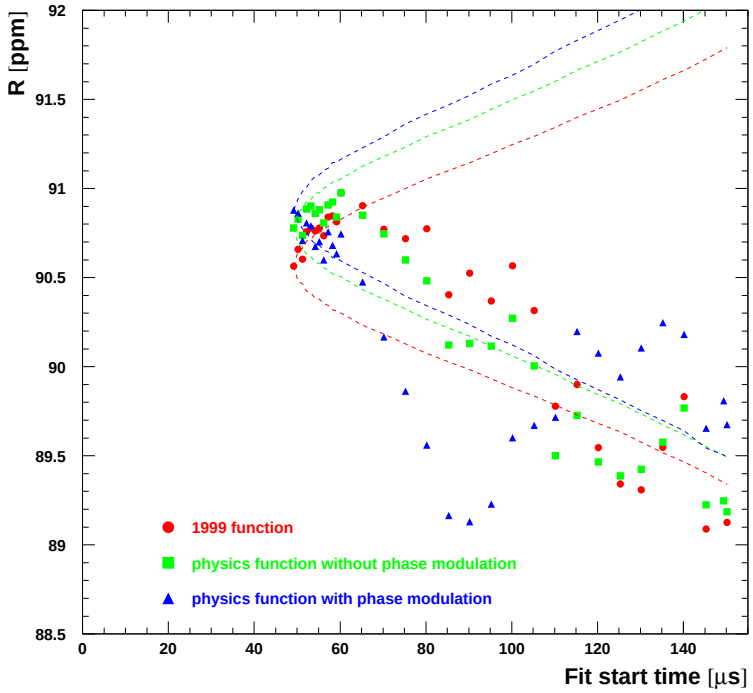

Figure 39: *Start-time scans for the three fit functions studied.*

6 Systematic Errors at 49.2 μs Fit Start Time

6.1 Main (Acceptance) CBO

In [19] a simulation is presented where an additive CBO perturbation with an amplitude of 0.01 was introduced in the data. Ignoring this term in the fit leads to phase pulling in R with an amplitude of 18 ppm at a fit start time $t = 0$ or $18\,\text{ppm} \times \text{e}^{-49.2/120} = 11.9\,\text{ppm}$ at 49.2 μs. If – more realistically – a multiplicative CBO term is used in the simulation and then ignored in the fit, the phase pulling amplitude is reduced by a factor 10 to about 1.2 ppm, corresponding to an RMS error of $1.2\,\text{ppm} / \sqrt{2} = 0.8\,\text{ppm}$. From our fits to the sum of detector spectra with a start time of 49.2 μs we obtain $A_{\text{CBO}} = 0.0032$ (see Tables 10, 18 and 26) instead of the 0.010 assumed in the simulation. This brings the error from completely ignoring the main CBO down to $0.8\,\text{ppm} \times 0.0032 / 0.010 = 0.28\,\text{ppm}$. However, we do fit for the CBO, and the systematic error is determined by the amount of remnant CBO that the fit doesn't take care of. The fraction of left-over CBO can be determined from the factor by which the CBO peak in a Fourier spectrum of fit residuals is reduced when the CBO term is included in the fit function. To enhance the sensitivity of the study to CBO effects we align the time spectra of the individual detectors such that the CBO phases are equal. Thus we avoid cancellation around the ring when the individual spectra are added. Figure 40 shows the result.

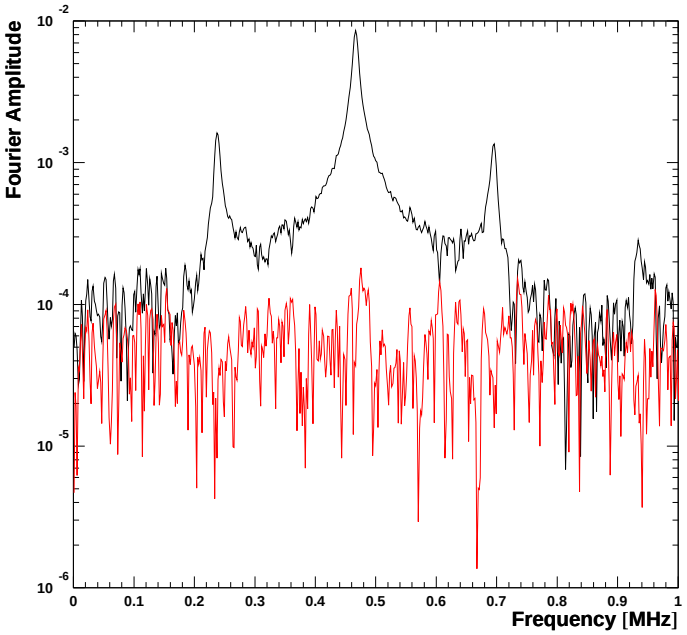

Figure 40: *Residual Fourier spectrum of CBO-aligned data after fits with the (5 parameter + muon loss) function (black) and with the full physics function (red).*

To quantify the CBO peak in the spectrum we average the amplitude in the range [0.3 MHz, 0.6 MHz] and find:

- CBO not fitted: average signal $= 0.989 \times 10^{-3}$
- CBO fitted: average signal $= 0.055 \times 10^{-3}$. It is compatible with the background level

of 0.051×10^{-3} (averaged over the intervals [0, 0.15 MHz] and [0.8 MHz, 0.9 MHz]) and therefore an upper limit for the left-over CBO signal.

This yields a reduction factor of 18 due to fitting, and hence a systematic error of 0.28 ppm / 18 = 0.015 ppm.

We shall now look in more detail at potential error sources in our parameterisation of the CBO functional form:

- The decay time τ_{decay} of the CBO frequency due to the exponential quadrupole voltage droop. From the hardware specifications this time constant is expected to be of the order 200 ms.

- The parameters τ_{rise} and A_{rise} describing the rise of the CBO frequency at the end of scraping. This term is only important at early start times up to about 30 μs. From the quadrupole instrumentation τ_{rise} is known to be around 5 μs which was confirmed by an FSD measurement of the beam centroid at the end of scraping [9]. A manual χ^2 scan with a fit start time of 23 μs found an optimum at $\tau_{\text{rise}} = (4.7 \pm 0.3)$ μs.

  A_{rise} was determined using the fiber harps. From the ratio of CBO frequencies with and without scraping one obtained [10] $A_{\text{rise}} = 1 - \frac{416\,\text{kHz}}{472\,\text{kHz}} = 0.12$. A manual χ^2 scan with a fit start time of 23 μs found an optimum at $A_{\text{rise}} = 0.13 \pm 0.03$.

  With our standard start time of 49.2 μs a manual scan of τ_{rise} between 1 and 10 μs, and A_{rise} between 0.05 and 0.2 resulted in R variations of less than 10^{-4} ppm. We don't show the numerical details of this study because it does not even have "romantic" [21] value.

- The CBO envelope.

- In the start-time scans for the parameter f_{CBO} in Period 0 there is a drop after 100 μs, irrespective of the fit function used (see Appendices A.1, B.1, C.1). This behaviour has nothing to do with the 140 ms droop of f_{CBO} as this is explicitely included in the fit function. The drop after 100 μs does not occur in the individual run periods and seems to have its origin in the mixing of run periods with different CBO frequencies. This raises the question what happens if f_{CBO} is fixed in the fit. We do not favour fixing significant parameters artificially because it only hides their physical evolution in a cosmetic way. Nevertheless we have investigated how the start-time dependence of R changes if f_{CBO} is fixed. The difference graph in Figure 41 shows a tendency similar to the drop of f_{CBO}, but the size of the effect is smaller than the statistically allowed 1 σ deviation.

- The systematic error due to mixing run periods with different CBO frequencies is not separately addressed in this section. Since it is the main source of the difference between the fit result for Period 0 and the weighted average of the results for the sub-periods, it is absorbed in the "analysis-method specific" error treated in Section 6.11.1.

The studies of the CBO frequency droop and the CBO envelope will be treated for each of the three fit functions studied.

The systematic effect of τ_{decay} on R is studied with a manual χ^2 scan. The upper plots in Figures 42 to 44 show that the sensitivity of χ^2 to the tiny effect under study is much better for CBO-phase aligned data. The total change of R within the $\pm 1\sigma$ interval – defined by the increase of the unnormalised χ^2 by 1 with respect to the minimum – amounts only to 0.006 ppm for the 1999-style function and for the physics function without phase

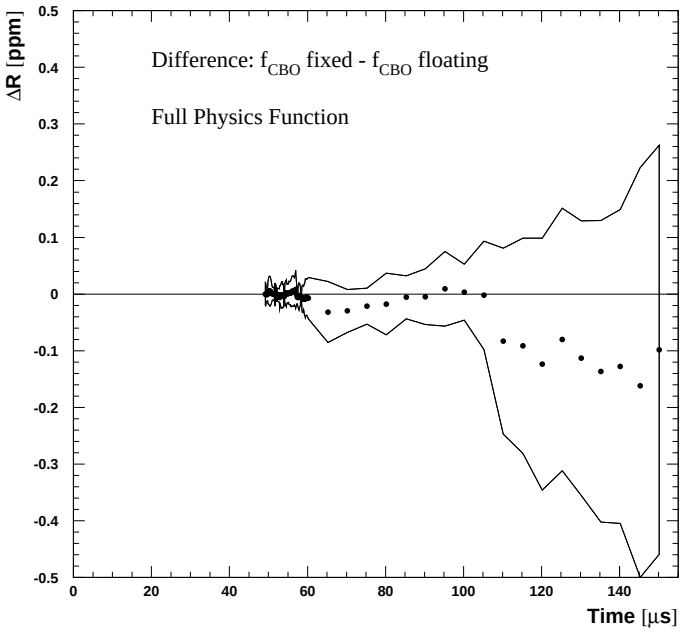

Figure 41: *Difference between the fit results for R with fixed or free f_{CBO} parameter. The error band was calculated as* $\sqrt{|\sigma^2_{\mathrm{fixed}} - \sigma^2_{\mathrm{free}}|}$.

modulation, and to 0.008 ppm for the full physics function. The systematic errors on R are given by 1/2 of these values.

The same principle is used for studying the impact of uncertainties in the CBO envelope. We approximate the empirical envelope by an exponential and manually vary the life time (Figures 45 to 47). The resulting systematic errors on R are 0.003 ppm for the 1999-style function and for the physics function without phase modulation, and 0.002 ppm for the full physics function.

For the total systematic error due to the main CBO it does not make any difference whether we add the errors from τ_{decay} and from the envelope linearly or in quadrature to the 0.015 ppm from the residual CBO. With two digits after the decimal point the result is always 0.02 ppm.

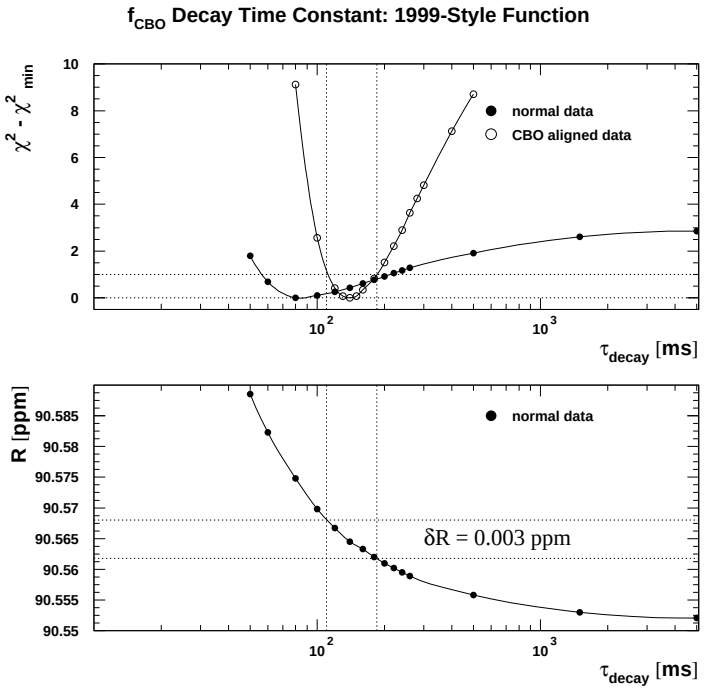

Figure 42: *Influence of the CBO frequency decay time on χ^2 and R with the 1999-style function (sum of detectors).*

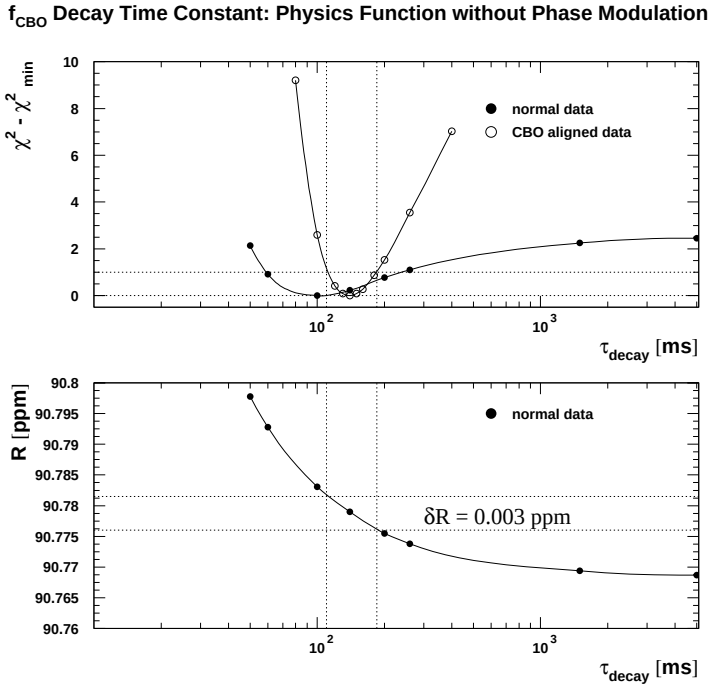

Figure 43: *Influence of the CBO frequency decay time on χ^2 and R with the physics function without phase modulation (sum of detectors).*

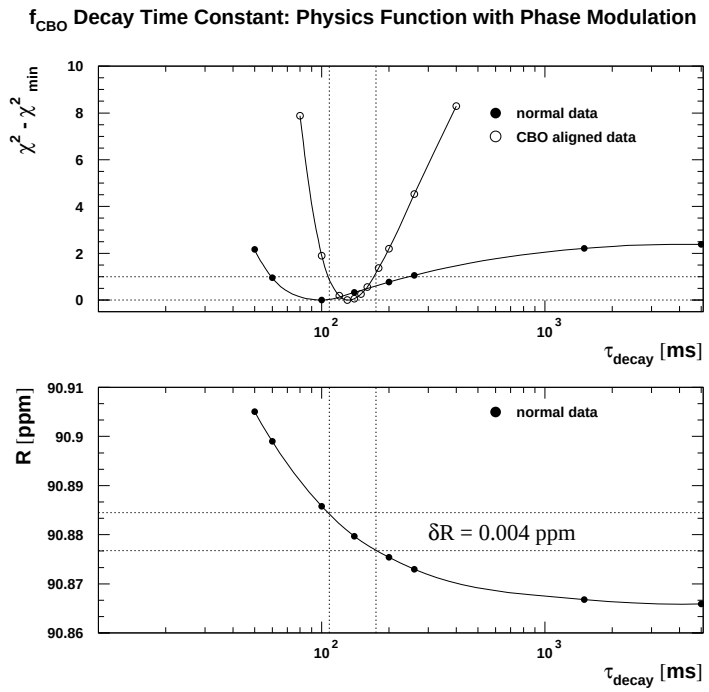

Figure 44: *Influence of the CBO frequency decay time on χ^2 and R with the full physics function including phase modulation (sum of detectors).*

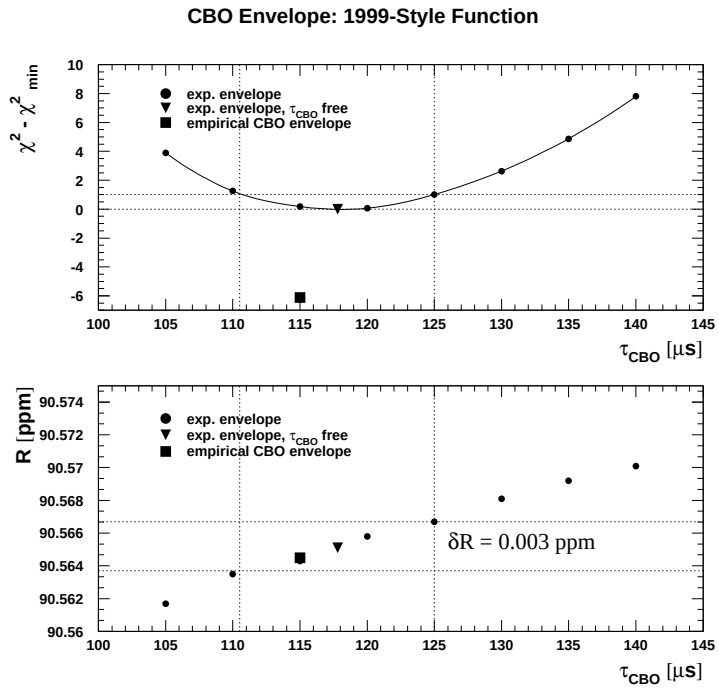

Figure 45: *Influence of the acceptance CBO lifetime on χ^2 and R with the 1999-style function (sum of detectors). The square markers for the empirical CBO envelope are plotted at its approximate life time of 115 μs.*

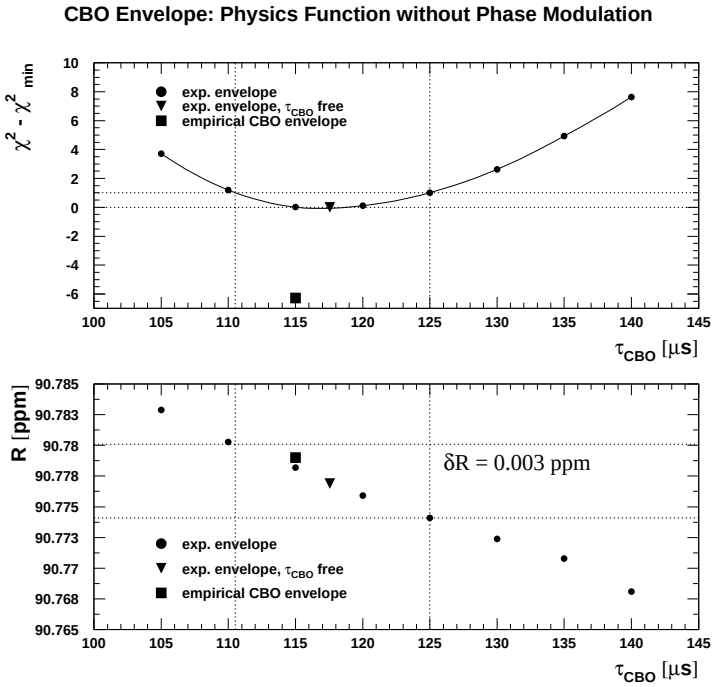

Figure 46: *Influence of the acceptance CBO lifetime on χ^2 and R for the physics function without phase modulation.*

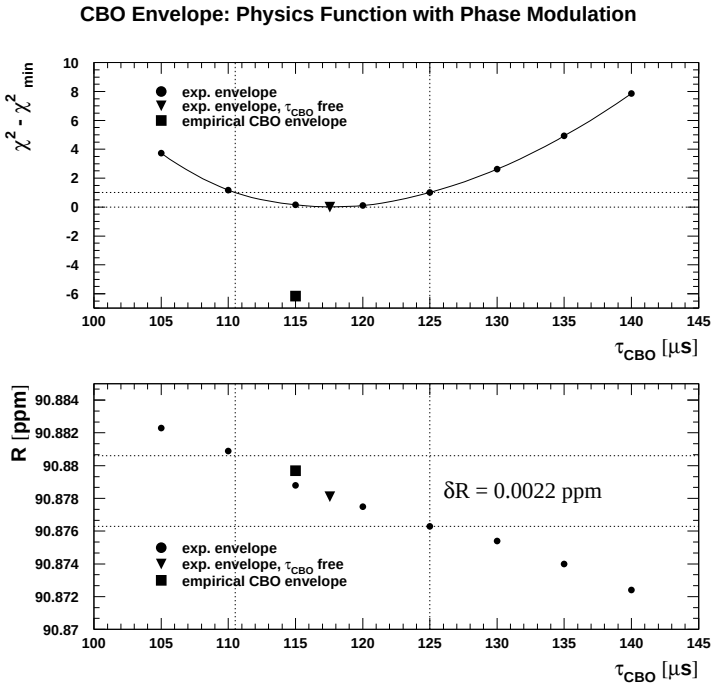

Figure 47: *Influence of the acceptance CBO lifetime on χ^2 and R for the physics function with phase modulation.*

6.2 Acceptance Double CBO

In the 1999-style function the acceptance double CBO is completely ignored. To determine the systematic error due to this omission we exceptionally switch the DCBO term on. The difference in R between the fits with and without DCBO exhibits a clear phase pulling with a frequency consistent with $f_{\mathrm{DCBO}} - f_a = 703\,\mathrm{kHz}$ or a period of $1.42\,\mu\mathrm{s}$ (Figure 48).

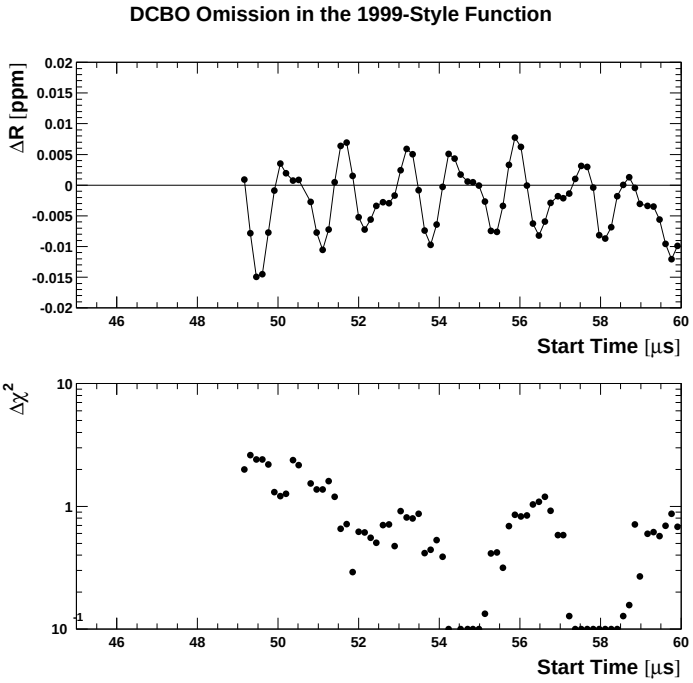

Figure 48: *Phase pulling due to ignoring the acceptance DCBO in the 1999-style function. The upper graph shows the difference $R_{without\ DCBO} - R_{with\ DCBO}$; the lower graph shows the analogous difference for the unnormalised χ^2.*

The peak-to-peak amplitude of the phase pulling around $50\,\mu\mathrm{s}$ is about 0.02 ppm corresponding to an rms error of $0.02\,\mathrm{ppm}/(2\sqrt{2}) = 0.007\,\mathrm{ppm}$. Since the fit with DCBO used g^2_{CBO} as DCBO envelope, the uncertainty of this envelope should also be translated into an error contribution to R. This study is shown in Figure 49. First a manual χ^2 optimisation as a function of the exponential life time τ_{DCBO} is performed, and then the dependence of R on this life time is determined. For enhanced sensitivity it is advantageous to use CBO-phase aligned data. The square of the empirical CBO envelope that is used for the regular parametrisation of the DCBO has an approximate exponential life time of $55\,\mu\mathrm{s}$. The respective values of χ^2 and R are plotted at that life time value; they fit rather well onto the curves for the exponential envelope. The variation of R within the $1\,\sigma$ interval is 0.0013 ppm, i.e. negligible compared to the error from omitting the DCBO.

The total DCBO error for the 1999-style function will be reported as 0.01 ppm.

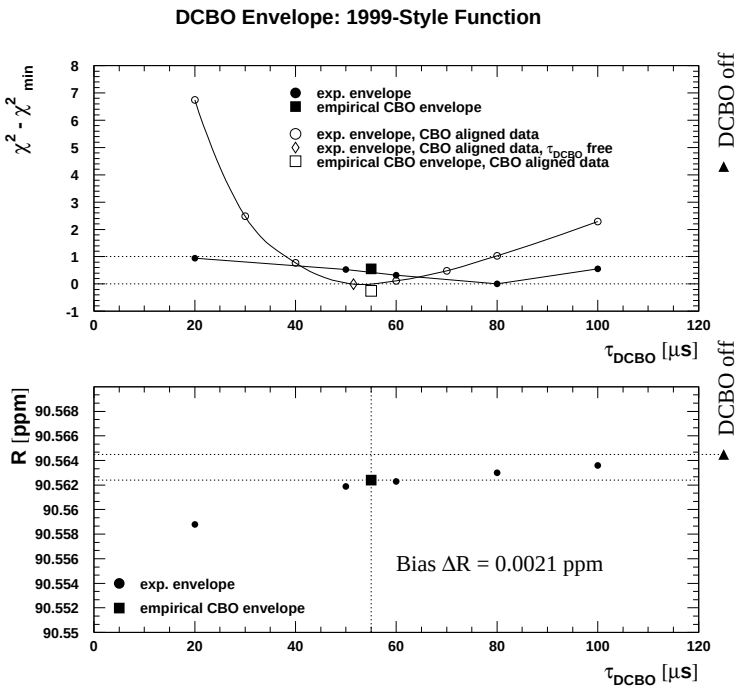

Figure 49: *Study of the systematic error due to uncertainties in the DCBO envelope. The fit start time was 49.2 μs.*

For the two physics functions (with and without phase modulation) only the envelope systematics needs to be investigated. This is done as explained above. The results are shown in Figures 50 and 51.

The resulting systematic errors – 0.0007 ppm without and 0.0015 ppm with phase modulation – are negligible.

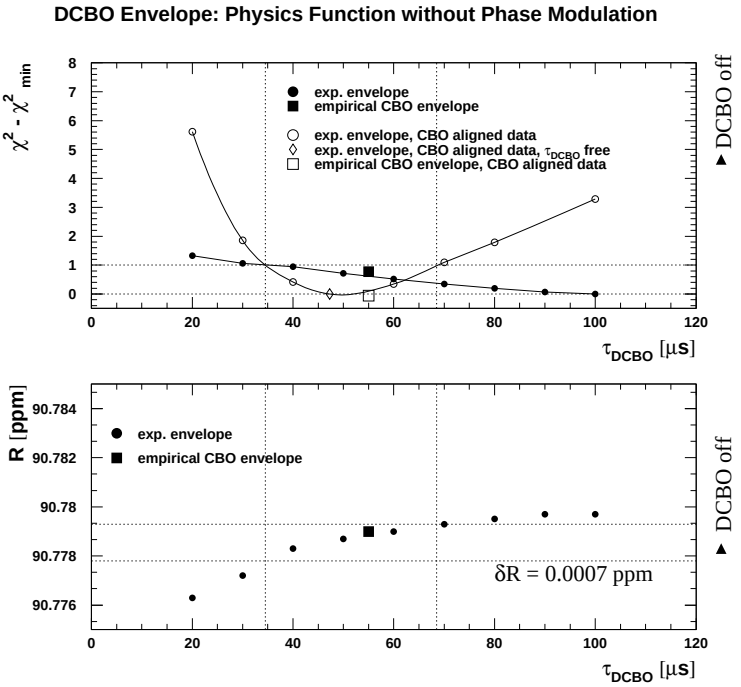

Figure 50: *Optimisation of the acceptance DCBO life time and its impact on R for the physics function without phase modulation. The systematic error* $\delta R = 0.0007\,ppm$ *is obtained from* $\chi^2(\tau_{\mathrm{DCBO}})$ *for CBO-phase aligned data and* $R(\tau_{\mathrm{DCBO}})$ *for normal data.*

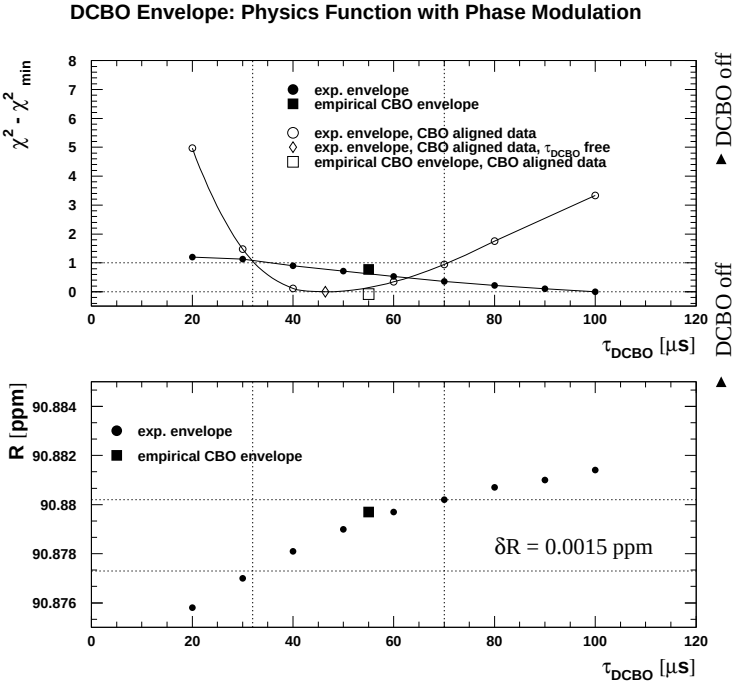

Figure 51: *Optimisation of the acceptance DCBO life time and its impact on R for the physics function with phase modulation. The systematic error* $\delta R = 0.0014\,ppm$ *is obtained from* $\chi^2(\tau_{\mathrm{DCBO}})$ *for CBO-phase aligned data and* $R(\tau_{\mathrm{DCBO}})$ *for normal data.*

6.3 Asymmetry and Phase CBO – Half-Ring Effect

6.3.1 1999-Style Function

The 1999-style function completely ignores both asymmetry and phase modulation by CBO. The resulting systematic error is estimated using Yannis' simulation [19] of the shift of R for a given amplitude of the left CBO side-band $f_{\rm CBO} - f_a$.

In his simulation Yannis adds the left sideband function

$$N_-(t) = N_0\, \mathrm{e}^{-\frac{t}{\tau}}\, A_-\, \mathrm{e}^{-\frac{t}{120\,\mu\mathrm{s}}}\, \cos[(\omega_{\rm CBO} - \omega_a)t + \phi_-] \tag{40}$$

For a left side-band amplitude $A_- = 0.01$ Yannis obtains a phase-pulling amplitude of 74 ppm in R at a start time $t = 0$. At our start time $t = 49.2\,\mu$s this corresponds to an rms systematic error

$$\delta R = 74\,\mathrm{ppm} \times \mathrm{e}^{-49.2/120}/\sqrt{2} \times \frac{A_-}{0.01} = 35\,\mathrm{ppm} \times \frac{A_-}{0.01} \tag{41}$$

We now have to determine the amplitude A_- of the left side-band for the sum of the spectra of all detectors around the ring. An expansion of the physics function (6) for small $A_{\rm Rob}$ and $A_{\rm Jim}$ (see [22]) gives two contributions to the left CBO side-band:

- From the asymmetry modulation:

$$N_{-,\rm Rob}(t) = N_0\, \mathrm{e}^{-\frac{t}{\tau}}\, \frac{1}{2}\, A\, A_{\rm Rob}\, \mathrm{e}^{-\frac{t}{120\,\mu\mathrm{s}}}\, \cos[(\omega_{\rm CBO} - \omega_a)t + \phi_{\rm Rob} - \phi_a] \tag{42}$$

  if we neglect the time dependence of the CBO frequency and approximate the CBO envelope by an exponential with $120\,\mu$s life time. Comparing (42) with (40) we find

$$A_{-,\rm Rob} = \frac{1}{2}\, A\, A_{\rm Rob} \tag{43}$$

- From the phase modulation:

$$N_{-,\rm Jim}(t) = N_0\, \mathrm{e}^{-\frac{t}{\tau}}\, \frac{1}{2}\, A\, A_{\rm Jim}\, \phi_a\, \mathrm{e}^{-\frac{t}{120\,\mu\mathrm{s}}}\, \cos[(\omega_{\rm CBO} - \omega_a)t + \phi_{\rm Jim} - \phi_a - \frac{\pi}{2}] \tag{44}$$

  Comparing (44) with (40) we find

$$A_{-,\rm Jim} = \frac{1}{2}\, A\, A_{\rm Jim}\, \phi_a \tag{45}$$

The combined left side-band term from asymmetry and phase modulation is

$$\begin{aligned} N_-(t) = N_0\, \mathrm{e}^{-\frac{t}{\tau}}\, \mathrm{e}^{-\frac{t}{120\,\mu\mathrm{s}}} \quad & \{A_{-,\rm Rob}\, \cos[(\omega_{\rm CBO} - \omega_a)t + \phi_{\rm Rob} - \phi_a] \\ & + A_{-,\rm Jim}\, \cos[(\omega_{\rm CBO} - \omega_a)t + \phi_{\rm Jim} - \phi_a - \tfrac{\pi}{2}]\} \quad . \end{aligned} \tag{46}$$

The oscillating term in the curly braces has an amplitude A_- given by

$$\begin{aligned} A_-^2 &= [A_{-,\rm Rob}\cos(\phi_{\rm Rob} - \phi_a) + A_{-,\rm Jim}\cos(\phi_{\rm Jim} - \phi_a - \frac{\pi}{2})]^2 \\ &+ [A_{-,\rm Rob}\sin(\phi_{\rm Rob} - \phi_a) + A_{-,\rm Jim}\sin(\phi_{\rm Jim} - \phi_a - \frac{\pi}{2})]^2 \\ &= A_{-,\rm Rob}^2 + A_{-,\rm Jim}^2 + 2\, A_{-,\rm Rob}\, A_{-,\rm Jim}\cos(\phi_{\rm Jim} - \phi_{\rm Rob} - \frac{\pi}{2}) \quad . \end{aligned} \tag{47}$$

The phase difference $\phi_{\mathrm{Jim}} - \phi_{\mathrm{Rob}} - \frac{\pi}{2}$ is known from the fits to individual detectors. From the values of $\langle \phi_{\mathrm{Rob}} - \phi_{\mathrm{CBO}} \rangle$ and $\langle \phi_{\mathrm{Jim}} - \phi_{\mathrm{CBO}} \rangle$ listed in Table 30 (upper block, Period 0) we get

$$\phi_{\mathrm{Jim}} - \phi_{\mathrm{Rob}} - \frac{\pi}{2} = 0.70 \pm 0.10 \quad \text{and hence} \quad \cos(\phi_{\mathrm{Jim}} - \phi_{\mathrm{Rob}} - \frac{\pi}{2}) = 0.76 \pm 0.06 \quad . \tag{48}$$

If both effects cancel by the same factor and mechanism then this phase difference is preserved after cancellation in the "summarized" spectrum. From the lower block of Table 30 follows:

$$\phi_{\mathrm{Jim}} - \phi_{\mathrm{Rob}} - \frac{\pi}{2} = 0.00 \pm 0.66 \tag{49}$$

The phase differences 0.70 rad and 0.00 rad before and after cancellation are almost consistent within the statistical $1\,\sigma$ error of 0.66 rad. We should also bear in mind that we have to expect a big systematic contribution to the error of the phase after cancellation because each of the 22 individual asymmetry and phase modulation vectors suffers from strong correlations with effects that influence the asymmetry. The two modulation effects may be affected differently by such correlations which would yield basically arbitrary phases after cancellation. Therefore it is difficult to make any statement about consistency or inconsistency of the two phase differences. Hence we shall evaluate the halfring systematics under two different assumptions:

- The cancellation mechanisms and factors of asymmetry and phase modulation are equal and their phase relation is preserved.
- The cancellation factors are different and the phase relation after cancellation is arbitrary, i.e. the expectation value of $\cos(\phi_{\mathrm{Jim}} - \phi_{\mathrm{Rob}} - \frac{\pi}{2})$ is 0.

For determining the cancellation factors or equivalently the amplitudes A_{Rob} and A_{Jim} for the sum of detectors (after cancellation) we take different approaches:

a. A_{Rob} and A_{Jim} directly from the fit to the sum of detector spectra

Table 26 (Period 0) gives the values

$$A_{\mathrm{Rob}} = (0.50 \pm 0.19) \times 10^{-3} \tag{50}$$

$$A_{\mathrm{Jim}} = (0.13 \pm 0.06) \times 10^{-3} \quad . \tag{51}$$

Comparing these amplitudes for the detector sum with the corresponding average amplitudes for the individual detectors (Table 30, upper block, Period 0), one finds that by adding all detectors around the ring the asymmetry modulation cancels by a factor $1/(6.6 \pm 2.9)$ and the phase modulation by $1/(5.3 \pm 2.3)$.

Using Eq. (43) and (45) and the values $A = 0.40188 \pm 0.00003$ and $\phi_a = 2.9676 \pm 0.0001$, we find

$$A_{-,\mathrm{Rob}} = (0.10 \pm 0.04) \times 10^{-3} \tag{52}$$

$$A_{-,\mathrm{Jim}} = (0.078 \pm 0.036) \times 10^{-3} \quad . \tag{53}$$

Taking directly these amplitudes for calculating the left side-band amplitude implies the assumption of different cancellation factors and hence an arbitrary phase relation for the two vectors after cancellation. With Eq. (47) and $\cos(\phi_{\mathrm{Jim}} - \phi_{\mathrm{Rob}} - \frac{\pi}{2}) = 0$ we obtain the combined left side-band amplitude

$$A_- = (0.127 \pm 0.039) \times 10^{-3} \quad , \tag{54}$$

corresponding to a systematic error

$$\delta R = (0.44 \pm 0.14)\text{ppm} \quad . \tag{55}$$

A similar result follows from using the vector sums of A_{Rob} and A_{Jim} from fits to the individual detectors (Table 30, lower block, Period 0) instead of the results from the fit to the sum of detectors:

$$\delta R_{\text{vectorsum}} = (0.42 \pm 0.14)\text{ppm} \quad . \tag{56}$$

Alternatively we can assume equal cancellation mechanisms for asymmetry and phase modulation with an average cancellation factor of $1/(5.8 \pm 1.8)$. In this model we need to take the phase difference (48). This leads to a combined left side-band amplitude

$$A_{-} = (0.173 \pm 0.039) \times 10^{-3} \quad , \tag{57}$$

or a systematic error

$$\delta R = (0.61 \pm 0.17)\text{ppm} \quad . \tag{58}$$

All these direct methods have the drawback that they rely on the fit parameters A_{Rob}, ϕ_{Rob}, A_{Jim}, ϕ_{Jim} which correlate strongly with the asymmetry (see correlation matrix in Table 24) which is affected by badly controlled effects like gain variations and unsubtracted pileup. By using δR from (55) and assigning separate systematic errors to pileup and gain variations, we may cover some fundamental effects twice.

b. Imperfect cancellation of asymmetry and phase modulation purely due to the missing detectors

In this approach we take the position that the amplitudes A_{Rob} and A_{Jim} are consistent with being constant as a function of detector, and that the phases ϕ_{Rob} and ϕ_{Jim} change linearly by $2\,\pi$ around the ring [15]. If there were 24 equal and equidistant detectors, all CBO effects would vectorially cancel. However, in reality the detectors 2 and 20 are missing. Their relative angle being $\pi/2$, the residual amplitudes $A_{\text{Rob/Jim,sum}}$ for the sum of the 22 detectors are

$$A_{\text{Rob/Jim,sum}} = A_{\text{Rob/Jim,indiv}} \frac{\sqrt{2}}{22} \quad , \tag{59}$$

corresponding to a cancellation factor of $\frac{\sqrt{2}}{22} = 1/15.6 = 0.065$. Applying this factor to the average amplitudes $\langle A_{\text{Rob/Jim}} \rangle$ yields

$$A_{\text{Rob,sum}} = (0.21 \pm 0.01) \times 10^{-3} \tag{60}$$

$$A_{\text{Jim,sum}} = (0.044 \pm 0.004) \times 10^{-3} \tag{61}$$

and hence a systematic error

$$\delta R = (0.22 \pm 0.06)\text{ppm} \quad . \tag{62}$$

This estimate is by more than a factor 2 lower than the one obtained in approach a.

How valid is the underlying assumption of detector independent asymmetry and phase modulations? Fitting A_{Rob} versus detector with a constant results in a χ^2 of 39 / 21 (probability = 1 %). The analogous result for A_{Jim} is $\chi^2 = 28/21$ (probability = 14 %). A fit of ϕ_{Rob} versus detector with a linear function with slope $-\frac{2\pi}{24}$ gives $\chi^2 = 62/21$ (probability = 6 $\times 10^{-6}$); the same for ϕ_{Jim} gives $\chi^2 = 33/21$ (probability = 5 %). At

least for the asymmetry modulation these fit qualities are rather poor, suggesting that the detectors deviate from their expected behaviour by more the statistical uncertainty. However, given that these parameters are influenced by gain variations and pileup, the fit results can be misleading. From the fits to the data we cannot draw a clear conclusion about the real cancellation factors. We can only consider (62) as a lower limit on δR.

Very recently another piece of information became available which confirms our suspicions about the validity of the geometrical cancellation hypothesis. R. Carey's full g-2 simulation [8] attained a statistical uncertainty of 1.08 ppm. The fit results for his Monte-Carlo data are shown in Appendix E. The amplitudes of asymmetry and phase modulation averaged over all detectors are given in Table 36 along with the χ^2 of their fits to constants.

	$\langle A_{\mathrm{Rob}}\rangle[10^{-3}]$	$\chi^2_{\langle A_{\mathrm{Rob}}\rangle}$	$\langle A_{\mathrm{Jim}}\phi_a\rangle$[mrad]	$\chi^2_{\langle A_{\mathrm{Jim}}\phi_a\rangle}$
Monte-Carlo	3.8 ± 0.3	45 / 23	1.9 ± 0.3	14 / 23
Data	3.3 ± 0.2	39 / 21	2.1 ± 0.2	28 / 21

Table 36: *Comparison of average asymmetry and phase modulation amplitude between data and Monte-Carlo. Also shown are the χ^2 obtained by fitting the amplitudes as a function of detector to constants.*

The amplitudes are consistent between Monte-Carlo and data within $1.4\,\sigma$. The incompatibility of $A_{\mathrm{Rob}}(d)$ with a constant is similarly strong. Clearly, we should not use the geometrical cancellation factor.

c. Using information from CBO variations of the average energy

H. Deng presented an independent access to the cancellation of the asymmetry modulation [23]. The origin of this effect lies in oscillations of the average energy with the CBO frequency.

Every g-2 period is divided into 8 time slices. Then the average energy versus time is determined in 8 sets, each of them using every 8th time slice. Thus, all bins of a given set have a constant g-2 phase. Then for each set the sensitivity factor between energy scale change and average energy is determined in the usual way. The resulting energy scale variation with time shows a clear CBO signature. Now Fourier spectra are constructed in two ways:

1. The energy-scale-versus-time histograms for the individual detectors are Fourier-analysed, then the Fourier amplitudes are added up.

2. The energy-scale-versus-time histograms for the individual detectors are first added (in the time domain), then the sum is Fourier-analysed.

The Fourier amplitude at the CBO frequency is proportional to the CBO oscillation amplitude of the average energy. Since the asymmetry modulation by CBO is a small perturbation less than

$$\Delta A(49\,\mu\mathrm{s}) = 2\,A\,A_{\mathrm{Rob}}\,g_{\mathrm{CBO}}(49\,\mu\mathrm{s}) \approx 2\times 0.4\times 3.3\times 10^{-3}\times \mathrm{e}^{-49/120} = 1.75\times 10^{-3} \quad (63)$$

as compared to the average asymmetry of 0.4, the relation between average energy and average asymmetry can be considered in linear approximation within the narrow modulation range. Therefore, the Fourier amplitude of the average energy can be assumed to be

proportional to A_{Rob}, and the ratio between the amplitudes in spectrum (1) and spectrum (2) is the cancellation factor for the asymmetry modulation.

Huaizhang's result for the cancellation factor is 1 / 9.3. This leads to an asymmetry modulation amplitude of

$$A_{\mathrm{Rob,sum}} = (0.35 \pm 0.02) \times 10^{-3} \tag{64}$$

for the sum of detectors. It is currently not entirely clear whether the phase modulation arises from the same mechanism. It is likely that the modulation of the average energy of detected pulses translates into a phase modulation via the energy dependence of the g-2 phase. In that case the cancellation factor of 1 / 9.3 holds for the phase modulation, too. The combination of both modulation vectors would then proceed via Eq. (47) with a phase difference cosine of 0.76. The resulting systematic error would be

$$\delta R = (0.38 \pm 0.12)\mathrm{ppm} \quad . \tag{65}$$

Alternatively, we can take the position that we have no independent access to the cancellation of the phase modulation and therefore have to take the pessimistic result (51) from the direct approach (a) and assume an arbitrary phase relation. We obtain then the systematic error

$$\delta R = (0.39 \pm 0.12)\mathrm{ppm} \quad . \tag{66}$$

We regard this result as the most realistic for the asymmetry modulation and as the safest for the phase modulation. It will be used for our systematic error table.

6.3.2 Physics Function without Phase Modulation

Including the asymmetry modulation into the fit function removes about 50 % of the half-ring effect. For the rest of it a systematic error has to be assigned. Furthermore, there is an error contribution from the uncertainty of the envelope of the asymmetry modulation.

The error due to the left-over half-ring effect will again be determined via Eq. (41) using the left side-band amplitude from Eq. (47). The residual asymmetry modulation amplitude A_{Rob} can be set to 0 because the effect is fitted for. A possible imperfection in the fit result for A_{Rob} and its effect on R is automatically accounted for by the increased statistical error. The only potential physical origin of a systematically wrong A_{Rob} is insufficient knowledge of the envelope which will be addressed below.

For A_{Jim} either the value from Eq. (51) corresponding to a cancellation factor of 1 / 5.3 or a value based on the cancellation factor of 1 / 9.3 from the average-energy modulation can be chosen. In the two cases we find

$$A_- = A_{-,\mathrm{Jim}} = (0.078 \pm 0.036) \times 10^{-3} \quad \text{or} \tag{67}$$

$$A_- = A_{-,\mathrm{Jim}} = (0.044 \pm 0.021) \times 10^{-3} \quad . \tag{68}$$

The results for the systematic errors obtained via Eq. (41) are

$$\delta R_{A_-} = (0.27 \pm 0.13)\,\mathrm{ppm} \quad \text{or} \tag{69}$$

$$\delta R_{A_-} = (0.15 \pm 0.07)\,\mathrm{ppm} \quad . \tag{70}$$

To be conservative, we select the first value.

To determine the systematic error from the uncertainty of the envelope of the asymmetry modulation, the envelope is approximated by an exponential, and a manual χ^2 scan over its life time τ_{Rob} is performed (Figure 52). To enhance the sensitivity of χ^2 to CBO effects, this study is done with CBO time-aligned data. The 1-sigma interval of τ_{Rob} is

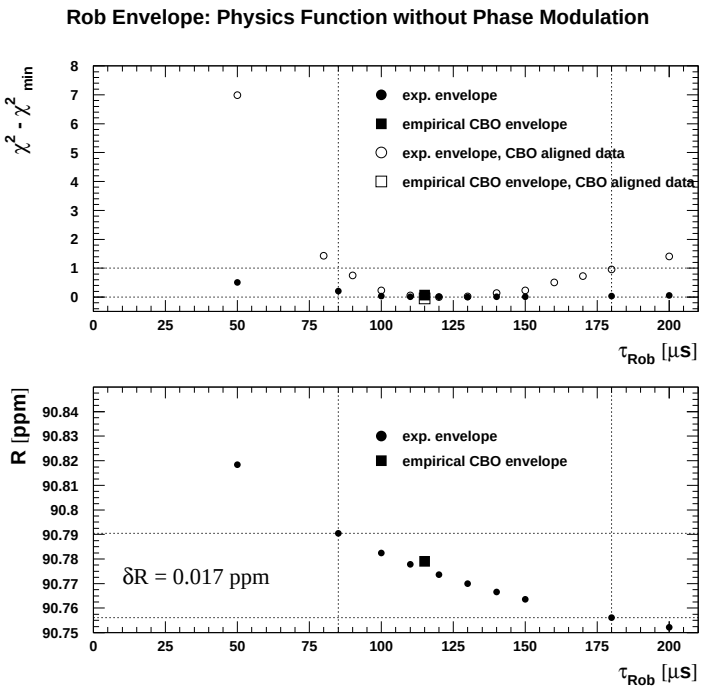

Figure 52: *Optimisation of the asymmetry CBO life time τ_{Rob} and its impact on R for the physics function without phase modulation. The systematic error $\delta R = 0.017\,ppm$ is obtained from $\chi^2(\tau_{\mathrm{Rob}})$ for CBO-phase aligned data and $R(\tau_{\mathrm{Rob}})$ for normal data.*

limited by 85 μs and 180 μs where χ^2 increases by 1 as compared to its minimum. In this interval R changes by 0.034 ppm, so the systematic error is

$$\delta R_{\tau_{\mathrm{Rob}}} = 0.017\,\mathrm{ppm} \quad . \tag{71}$$

For combining the partial errors from Eq. (69) and (71) we conservatively make use of the "angle" (48) between asymmetry and phase modulation:

$$\delta R_{\mathrm{halfring}} = \sqrt{0.27^2 + 0.017^2 + 2 \times 0.27 \times 0.017 \times 0.76}\,\mathrm{ppm} = 0.28\,\mathrm{ppm} \quad . \tag{72}$$

6.3.3 Full Physics Function

In the full physics function both asymmetry and phase modulation are taken into account. Systematic error sources are the envelopes of these effects.

Their uncertainties are evaluated like in the previous section (see Figures 53 and 54). From the asymmetry modulation envelope one gets an error of 0.025 ppm. In the case of the phase modulation envelope, the life time of the empirical envelope which was used for the final fits of the analysis lies at the lower edge of the $1\,\sigma$ interval of τ_{Jim}. One could now argue that our result for R has a bias and should be corrected to the value corresponding to the optimum τ_{Jim}. However, there is physical motivation for using the same CBO envelope for all three CBO effects because they are all caused by the same beam movements, and we prefer not to choose the χ^2 minimum from the τ_{Jim} scan. Instead, we give the full variation of R over the $1\,\sigma$ interval as a conservative systematic error, i.e. 0.09 ppm. Another way would be to report the asymmetric error (+0.01 -0.08) ppm, which however is difficult to combine with the other errors.

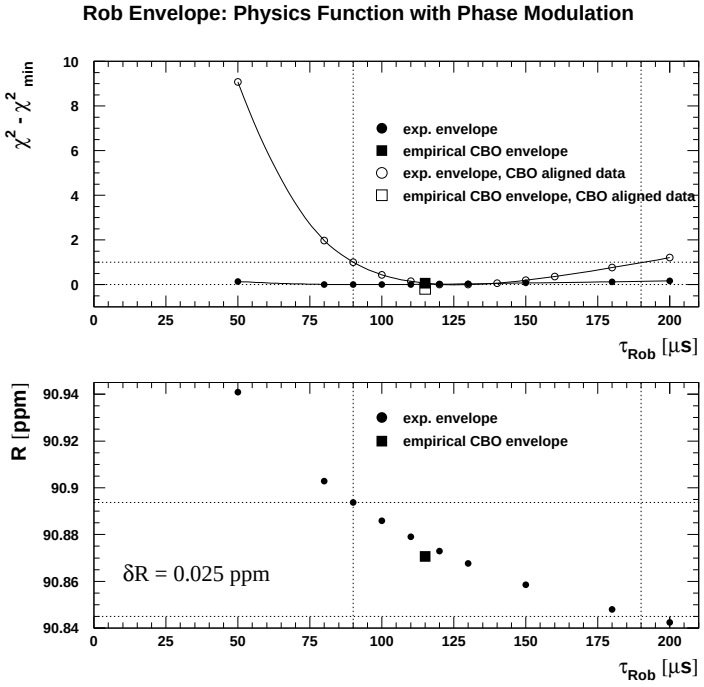

Figure 53: *Optimisation of the asymmetry CBO life time τ_{Rob} and its impact on R for the full physics function including phase modulation. The systematic error $\delta R = 0.025$ ppm is obtained from $\chi^2(\tau_{\mathrm{Rob}})$ for CBO-phase aligned data and $R(\tau_{\mathrm{Rob}})$ for normal data.*

The total systematic error due to the asymmetry and phase modulation is computed like in Eq. (72):

$$\delta R_{\mathrm{halfring}} = \sqrt{0.025^2 + 0.09^2 + 2 \times 0.025 \times 0.09 \times 0.76}\,\mathrm{ppm} = 0.11\,\mathrm{ppm} \quad . \tag{73}$$

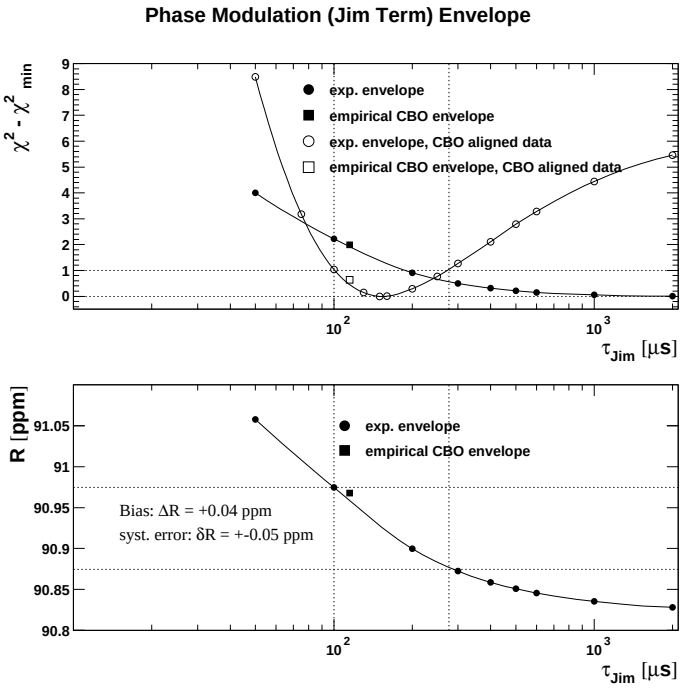

Figure 54: *Dependence of χ^2 and R on the phase modulation lifetime if the envelope is approximated by an exponential. The fit start time was 44.7 μs. The sum of all detector spectra was fitted. The open circles represent the acceptance CBO envelope which has a life-time of about 115 μs if approximated by an exponential.*

6.4 Vertical Oscillation and Waist

To investigate the short-lived effects of the vertical beam oscillation and waist we first identify the phase pulling at very early start times due to omission of these terms from the fit function. The difference between the R results from fits with and without the vertical waist (Figure 55) exhibits a phase pulling with a frequency around $f_{\mathrm{VW}} - f_a = 1520\,\mathrm{kHz}$ ($T \approx 6.6\,\mu\mathrm{s}$) and an amplitude of about 0.05 ppm at start times between $23\,\mu$s and $32\,\mu$s. At our standard start times around $49\,\mu$s it has decayed to about 0.03 ppm. Note however that this first study was done with the set of detectors that are available at $23\,\mu$s, i.e. the detectors (2), 3, 4, 5, 6, 8 are missing. Thus, the cancellation of the VW around the ring is very incomplete. To get the relevant phase pulling amplitude, we repeat the study between $45\,\mu$s and $50\,\mu$s for our usual set of detectors (only 2 and 20 missing); see Figure 56. The phase pulling amplitude is reduced to about 0.008 ppm corresponding to a systematic error of $0.008\,\mathrm{ppm} / \sqrt{2} = 0.006\,\mathrm{ppm}$.

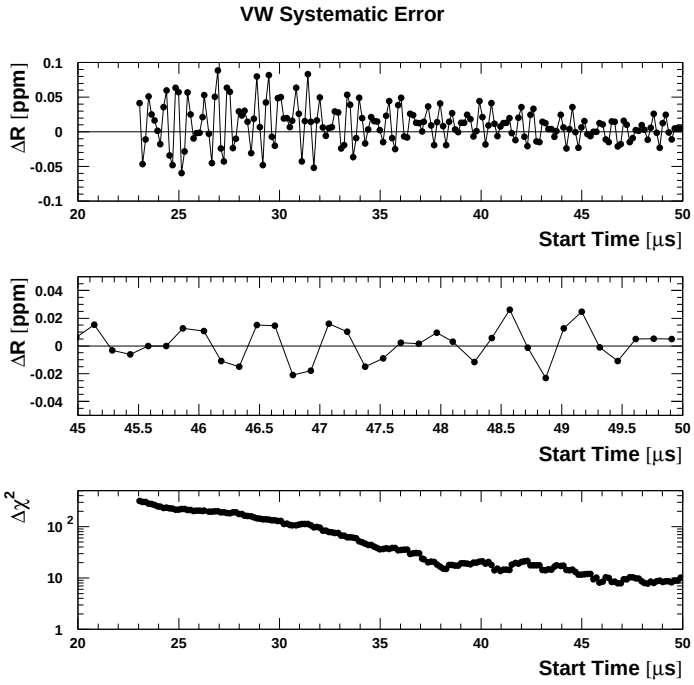

Figure 55: *Systematic effect from omitting the vertical waist in the fit function. The two upper plots show the R-difference between start-time scans using the physics function without and with the vertical waist term. The lowest plot shows the difference in the absolute χ^2. For this study only the detectors that are available at 23 μs were used (i.e. five detectors are missing).*

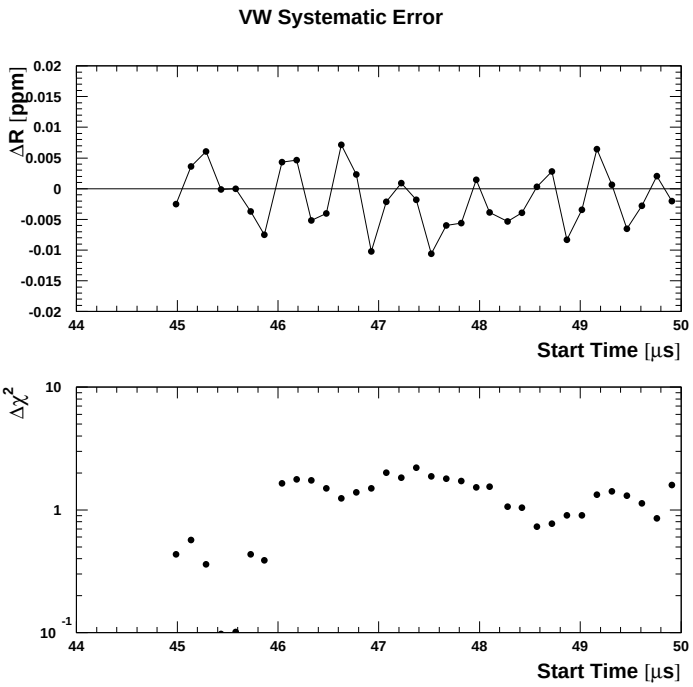

Figure 56: *Like Figure 55 but with all detectors except 2 and 20, and only for start times later than 45 μs. The lower effect on R is due to better cancellation around the ring for this more complete set of detectors.*

The impact of omitting the VO is investigate in the same way as the one of the VW. The phase pulling at very early times for the early detectors is shown in Figure 57 whereas the phase pulling for the full detector set between 45 μs and 50 μs is shown in Figure 58. Again we find an amplitude of about 0.008 ppm or a systematic error of 0.006 ppm.

For the combination of VW and VO the systematic error is 0.01 ppm for both linear and quadratic addition if we round off after the second digit.

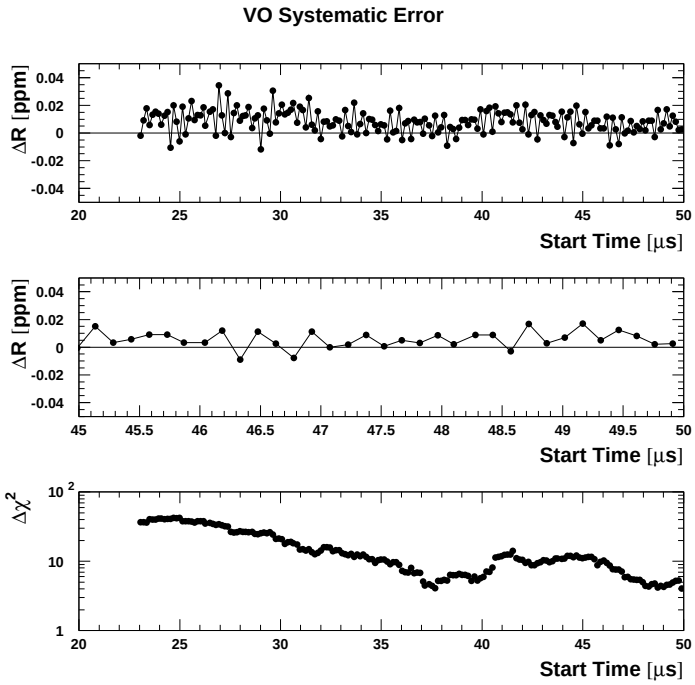

Figure 57: *Systematic effect from omitting the vertical oscillation in the fit function. The two upper plots show the R-difference between start-time scans using the physics function without and with the vertical oscillation term. The lowest plot shows the difference in the absolute χ^2. For this study only the detectors that are available at 23 μs were used.*

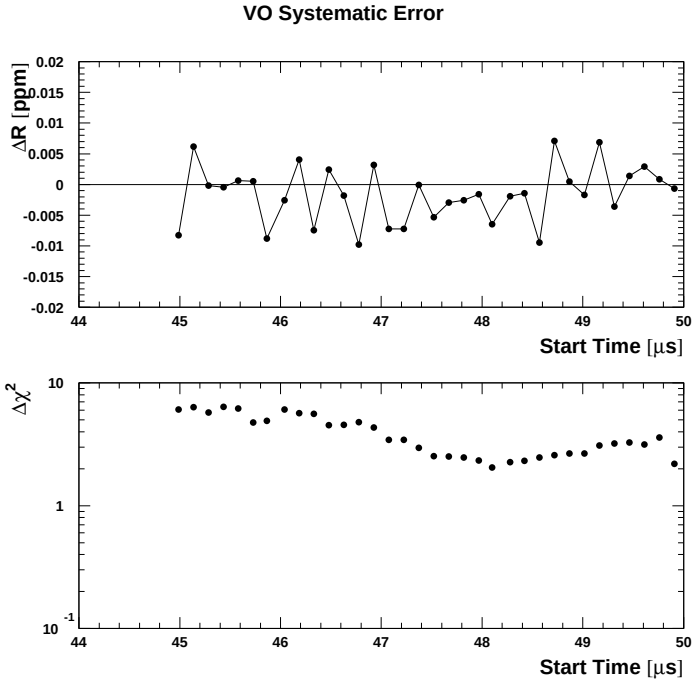

Figure 58: *Like Figure 57 but with all detectors except 2 and 20, and only for start times later than 45 μs.*

6.5 Residual Pileup

To obtain an estimate for the systematic error due to left-over pileup, two steps are needed: first the fraction of residual pileup has to be determined, then its influence on R. For the first step there are different possible approaches:

a. From comparison of early and late energy spectra.

b. By optimising a pileup multiplier in order to match the average energies with and without an upper energy cut above the maximum single-pulse energy of 3.2 GeV. For perfect pileup subtraction the energy spectrum would have no entries above this cut.

c. χ^2 minimisation: introduce pileup multipliers λ and fit the spectrum $N - \lambda \cdot (D - S1 - S2)$ for different values of λ and look for the least χ^2.

6.5.1 Early-to-Late Evolution of the Energy Spectrum

Obtaining the fraction of unsubtracted pileup from the comparison of early and late energy spectra is an old concept; see e.g. [12].

Let us denote the non-pileup subtracted energy spectrum at the time t by $N(t)$, the constructed pileup energy spectrum by $P(t) = D(t) - S1(t) - S2(t)$ and the pileup subtracted energy spectrum by $S(t)$. Due to limitations of the subtraction method, both $P(t)$ and $S(t)$ are imperfect. Their true counterparts will be called $\tilde{P}(t)$ and $\tilde{S}(t)$. The unsubtracted spectrum can be decomposed as

$$N(t) = \tilde{S}(t) + \tilde{P}(t) \tag{74}$$

At a later time $t + \Delta t$ we have

$$N(t+\Delta t) = \tilde{S}(t+\Delta t) + \tilde{P}(t+\Delta t) = \tilde{S}(t)\,\mathrm{e}^{-\Delta t/\tau} + \tilde{P}(t)\,\mathrm{e}^{-2\Delta t/\tau} \tag{75}$$

Now the late spectrum is scaled by the decay factor $\mathrm{e}^{\Delta t/\tau}$ and subtracted from the early spectrum:

$$N(t) - \mathrm{e}^{\Delta t/\tau}\,N(t+\Delta t) = \tilde{P}(t) - \mathrm{e}^{-\Delta t/\tau}\,\tilde{P}(t) = \tilde{P}(t)[1 - \mathrm{e}^{-\Delta t/\tau}] \tag{76}$$

Hence the pileup at the early time t is given by

$$\tilde{P}(t) = \frac{N(t) - \mathrm{e}^{\Delta t/\tau}\,N(t+\Delta t)}{1 - \mathrm{e}^{-\Delta t/\tau}} \tag{77}$$

The inefficiency in the pileup subtraction can be written as

$$\begin{aligned} 1 - \eta(t) &\equiv 1 - \frac{P(t)}{\tilde{P}(t)} = 1 - \frac{P(t)[1 - \mathrm{e}^{-\Delta t/\tau}]}{N(t) - \mathrm{e}^{\Delta t/\tau}\,N(t+\Delta t)} \\ &= \frac{[N(t) - P(t)] - \mathrm{e}^{\Delta t/\tau}[N(t+\Delta t) - P(t+\Delta t)]}{N(t) - \mathrm{e}^{\Delta t/\tau}\,N(t+\Delta t)} \end{aligned} \tag{78}$$

For the early spectrum the time slice [49.2; 66.7] μs was used. The time interval for the late energy spectrum was varied for the purpose of an additional consistency check. For the choice of this interval the bin boundaries 66.7, 75.6, 97.3, 123.5, 149.6, 202.0, 315.6, 450.0 and 600.0 μs were available.

The upper plots in Figure 59 show an early and a late energy spectrum for N and P for the sum of all detectors and run periods. Since the pileup spectrum has a zero crossing

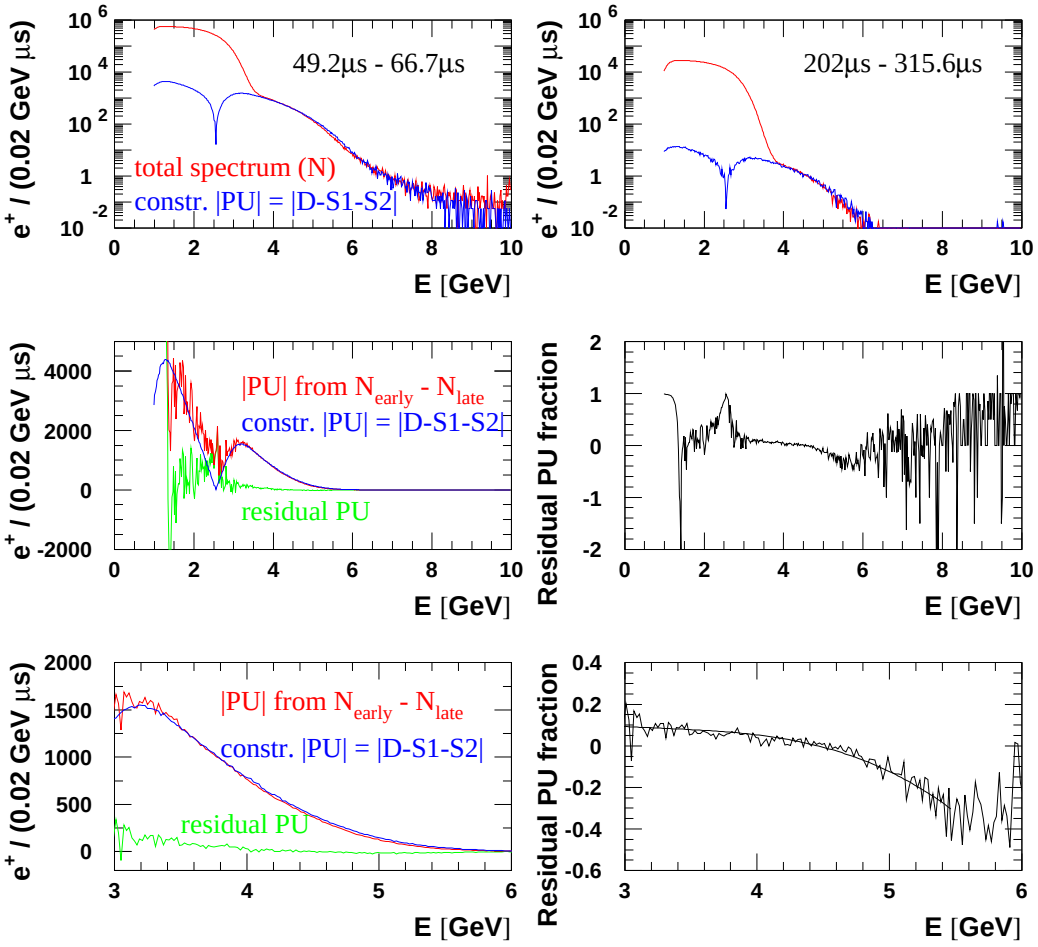

Figure 59: *Determination of the residual pileup fraction using the evolution of the energy spectrum from the time bin [49.2 µs; 66.7 µs] to [202.0 µs; 315.6 µs].*

around 2.6 GeV, the modulus is drawn to avoid conflicts with the logarithmic scale. The middle and lower left-hand graphs compare the constructed pileup spectrum $|D - S1 - S2|$ with the one determined according to Eq. (78). The difference is the residual pileup which is also shown. The middle and lower right-hand plots show the residual pileup fraction. The lower part of the figure zooms into the sub-range from 3 to 6 GeV where this method is reliable. Below 3 GeV the pileup spectrum tends towards the 2.6 GeV zero crossing where the uncertainties are big. To obtain a quantitative estimate of the residual pileup fraction, the lower right-hand graph is fitted with a third-order polynomial to smoothen out fluctuations. Then the function obtained from this fit is averaged over energies from 3.0 GeV to 5.5 GeV. At higher energies the statistics become poor. As weight for this mean the energy spectrum is chosen in order to emphasize the lower energy part where we have most data. Another interesting feature is the zero-crossing of the residual pileup fraction near 4.5 GeV. It suggests that at very high energies we oversubtract pileup. Because of

this zero-crossing several different averages were tried and compared:

- the simple linear mean: $\int_{3.0\,\mathrm{GeV}}^{5.5\,\mathrm{GeV}} dE \frac{dN}{dE}(1-\eta(E))$
- the linear mean of the modulus: $\int_{3.0\,\mathrm{GeV}}^{5.5\,\mathrm{GeV}} dE \frac{dN}{dE}|1-\eta(E)|$
- the square-root of the quadratic mean: $\sqrt{\int_{3.0\,\mathrm{GeV}}^{5.5\,\mathrm{GeV}} dE \frac{dN}{dE}(1-\eta(E))^2}$

Figure 60 shows these three means as a function of the centre of the late time slice. The differences are small because the weights emphasize the flat portion just above 3 GeV.

In any case, quoting 6.9 % residual pileup is a safe estimate.

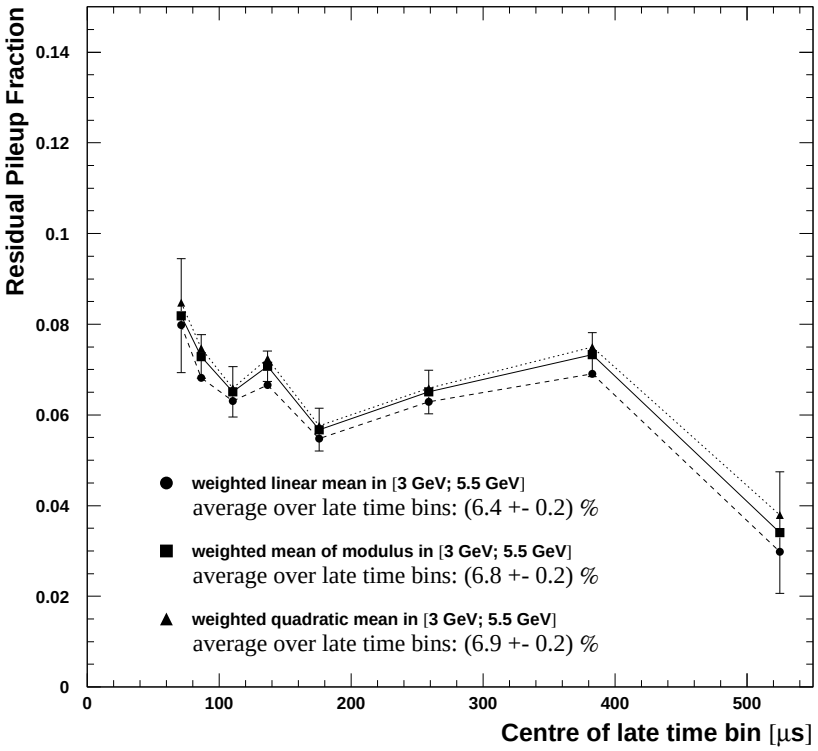

Figure 60: *Residual pileup fraction in the energy range 3.0 GeV - 5.5 GeV from the early-to-late evolution of the energy spectrum as a function of the late time bin. Error bars are only shown for the mean of the modulus. The others have the same size.*

6.5.2 Matching Average Energies with and without Energy Cut

If there were no pileup, the average energies without upper energy cut and with an upper cut above the maximum single-pulse energy of 3.2 GeV would be the same. Any difference in the average energies with and without cut shows that there is unsubtracted pileup above the cut. One can now optimise a pileup multiplier such that this difference vanishes.

Let us define the normalised energy variation with time by

$$\zeta(t) \equiv \frac{\langle E\rangle(t)}{\langle E\rangle(200\,\mu\mathrm{s})} \quad , \tag{79}$$

as illustrated by Figure 61. Furthermore, we define the difference ratio

$$\rho(t) \equiv \frac{\zeta_{\text{no cut}}(t) - \zeta_{\text{cut}}(t)}{\zeta_{\text{no PUS}}(t) - 1} \tag{80}$$

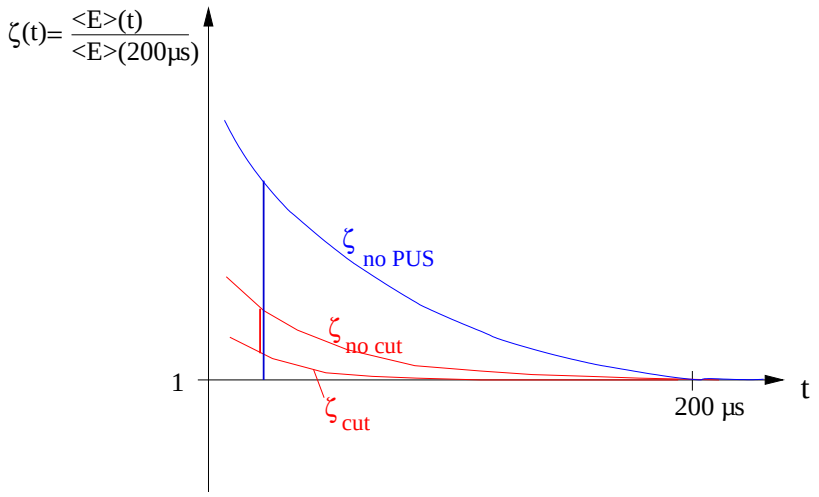

Figure 61: *Variations of the average energy with time for three cases: without pileup subtraction ("no PUS"); with pileup subtraction and without upper energy cut ("no cut"); with pileup subtraction and with upper energy cut ("cut"). The function $\rho(t)$ in Eq. (80) is the ratio between the red and the blue vertical line. Note that the difference between ζ_{cut} and $\zeta_{no\ cut}$ is strongly exaggerated.*

The time variation of the average energy without pileup subtraction is dominated by pileup, not by gain effects. If now the difference $\zeta_{\text{no cut}} - \zeta_{\text{cut}}$ between the average energies with and without cut is due to pileup, then it will be proportional to $\zeta_{\text{no PUS}}(t) - 1$, or in other words, $\rho(t)$ will be constant. This hypothesis was tested on the data for different upper energy cuts. Figure 62 shows $\rho(t)$ for two example detectors and the cuts 3.2 GeV and 3.4 GeV.

For detector 1, $\rho(t)$ is flat for both cuts. Detector 7 however still has its characteristic gain wiggle if the cut is set at 3.2 GeV. For higher cuts it disappears. Apparently, with the 3.2 GeV cut there are still many single pulses left which is not surprising given the 10 % energy resolution smearing out the end-point of the energy spectrum. To isolate pileup, a higher cut has to be chosen. It turned out that 3.4 GeV is adequate in all cases. For each detector $\rho(t)$ was fitted to a constant line in the range from 50 μs to 100 μs. The levels are shown in Figure 63 for a cut at 3.4 GeV.

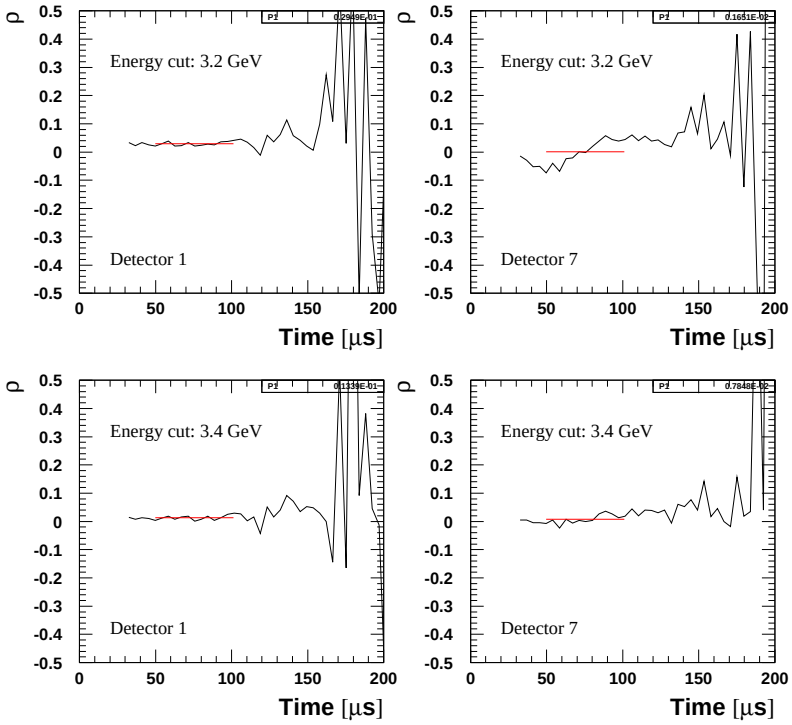

Figure 62: $\rho(t)$ *for two different energy cuts and two detectors. Constant lines were fitted between* $50\,\mu s$ *and* $100\,\mu s$.

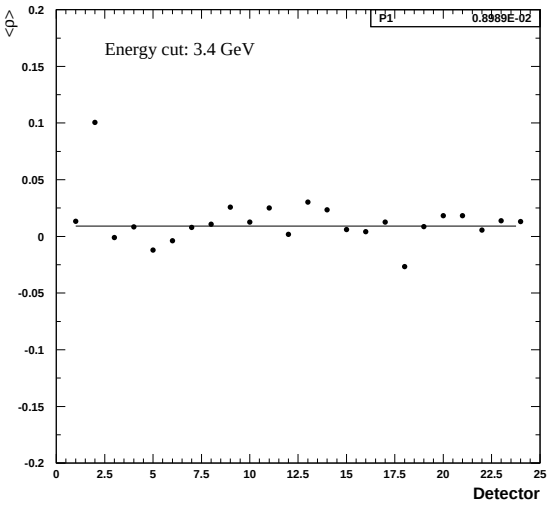

Figure 63: $\langle\rho(t)\rangle$ *versus detector, as obtained from fits like in Figure 62.*

At this point, pileup multipliers λ are introduced individually for all detectors. They are chosen such that $\langle\rho(t)\rangle = 0$. Figure 64 shows the distribution of λ-values for the 22 detectors, again for an energy cut at 3.4 GeV.

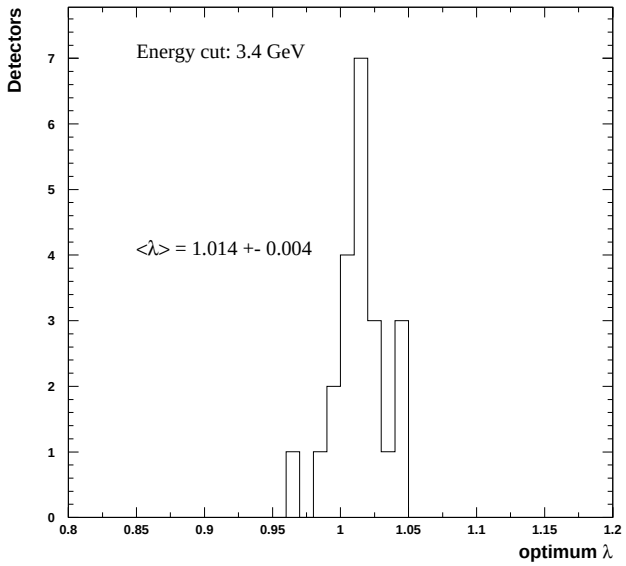

Figure 64: *Distribution of pileup multipliers needed to make $\langle\rho(t)\rangle = 0$ for each individual detector.*

The average multiplier of 1.014 means that – integrated over energies above 3.4 GeV – 1.4 % of the pileup was left over by the pileup subtraction procedure.

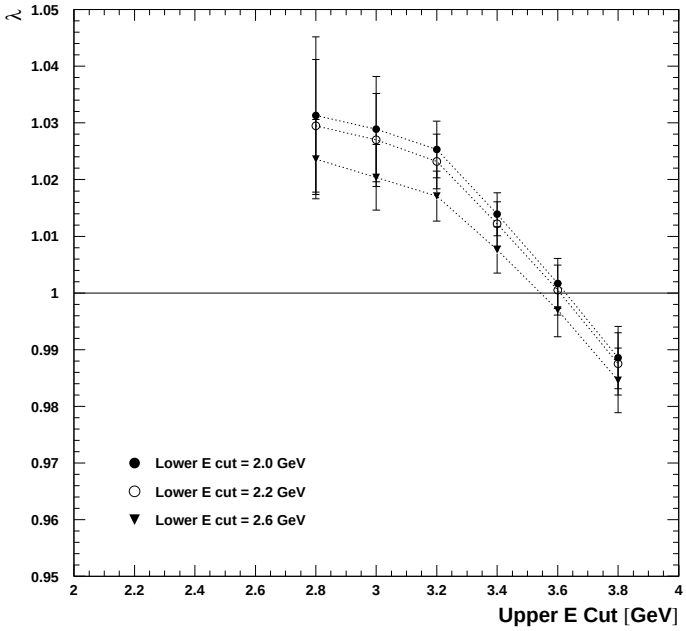

Figure 65: *Average optimum pileup multiplier as a function of the upper energy cut for different lower energy cuts.*

The early-to-late energy study in Section 6.5.1 had given strong indication for an energy-dependent pileup subtraction efficiency. To verify this result qualitatively with the present method, the procedure described above was repeated for several different upper energy cuts. Figure 65 shows that $\langle\lambda\rangle$ crosses 1 around 3.6 GeV, i.e. the residual pileup fraction has a zero-crossing at that cut energy, or in other words, for very high energies too much pileup is subtracted. This was also the finding of the earlier study.

Since below 3.2 GeV the energy spectrum is dominated by single pulses, the points at 2.8 GeV and 3.0 GeV are not meaningful for our purposes. From the range between 3.2 GeV and 3.8 GeV we can conclude that pileup subtraction works at the level of ±3 %. Unfortunately no additional energy bins above 3.8 GeV were made, and we cannot predict the evolution of the graph beyond that point. Therefore quantitative statements cannot be given. We should however bear in mind that for practical relevance the residual pileup fraction should be weighted with the energy spectrum which gives higher importance to the values at lower energies.

As an additional test, also the lower energy cut (usually 2.0 GeV) was varied. Any dependence on this lower cut must have its origin in effects other than pileup. Thus this test gives an idea about the reliability of this method. In the figure we see that there is indeed a dependence at the 1 % level for an upper cut of 3.4 GeV, but it improves for increasing upper cuts where the contamination by single pulses decreases.

6.5.3 χ^2 Minimisation with Pileup Multipliers

The method of χ^2 minimisation with respect to a pileup multiplier λ is only used as an additional check of the order of magnitude of the residual pileup. Its accuracy suffers from correlations between λ and other effects acting on the asymmetry like gain variations and the half-ring effect.

The results shown in Figures 66 to 68 suggest residual pileup of

- (-5.8 ± 3.9) % if the 1999-style function is used for the fit,
- (-3.7 ± 4.4) % if the physics function without phase modulation is used,
- $(+0.5 \pm 5.1)$ % if the full physics function is used.

These values don't coincide with the results from the other studies but they confirm that pileup subtraction is good within at most ± 10 %.

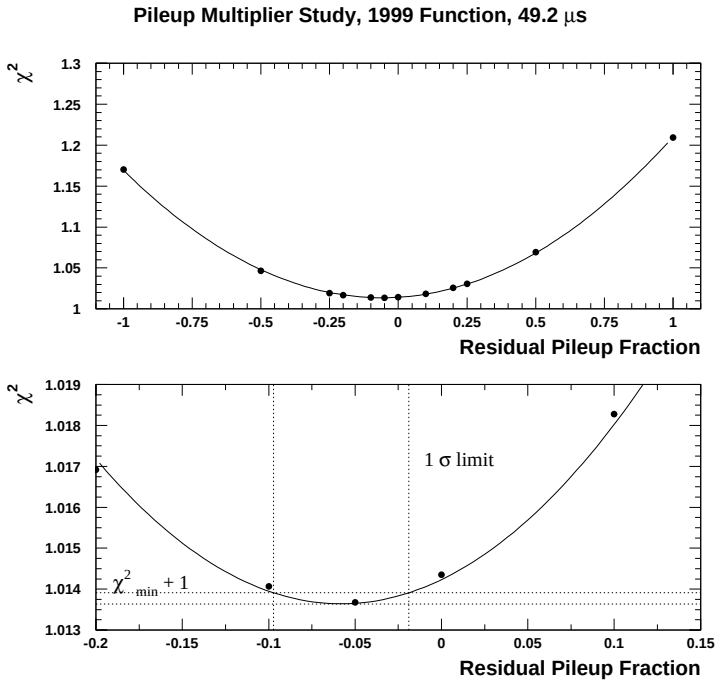

Figure 66: *Reduced χ^2 as a function of the fraction of unsubtracted pileup.*

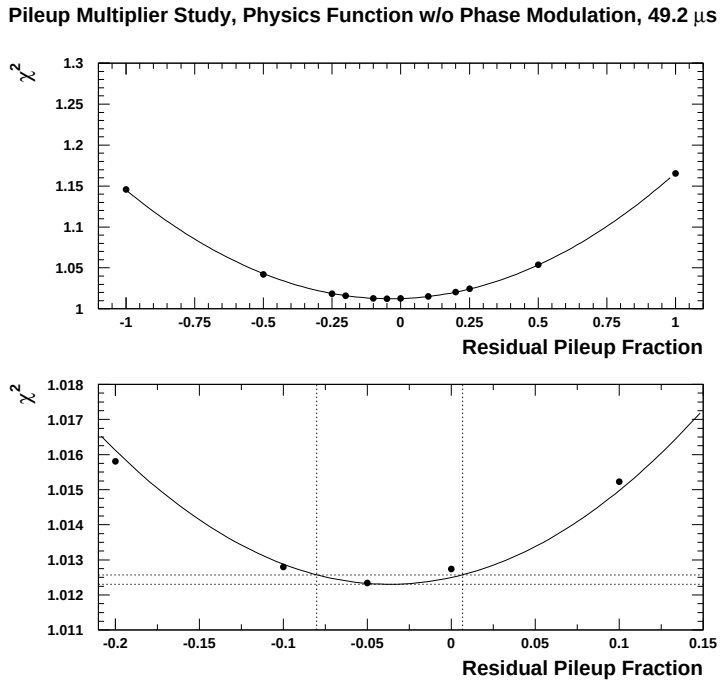

Figure 67: *Reduced χ^2 as a function of the fraction of unsubtracted pileup.*

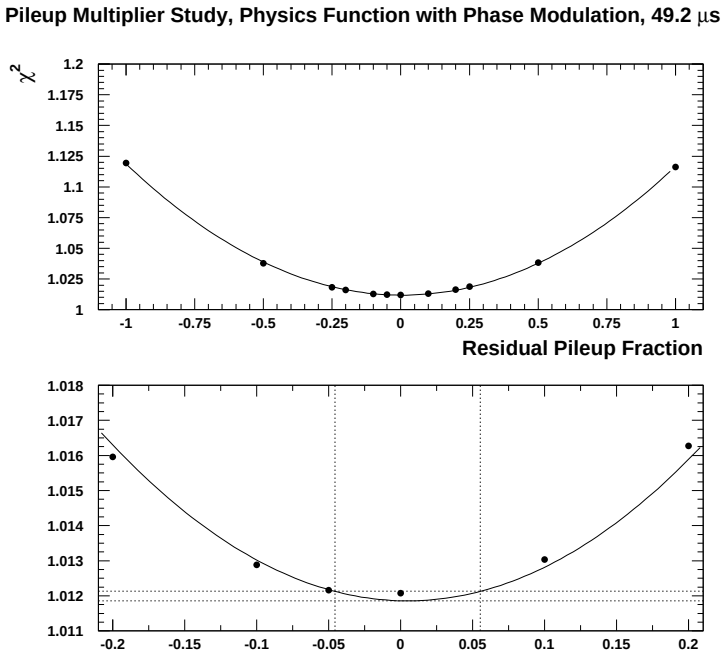

Figure 68: *Reduced χ^2 as a function of the fraction of unsubtracted pileup.*

6.5.4 Influence of Residual Pileup on R

Figures 69 to 71 show the dependence of R on the fraction of residual pileup. Using the most pessimistic residual pileup fraction 6.9 % from the early-to-late energy spectrum study (Section 6.5.1) one obtains the following systematic errors:

- 1999-style function: 0.03 ppm
- physics function without phase modulation: 0.01 ppm
- full physics function: 0.06 ppm

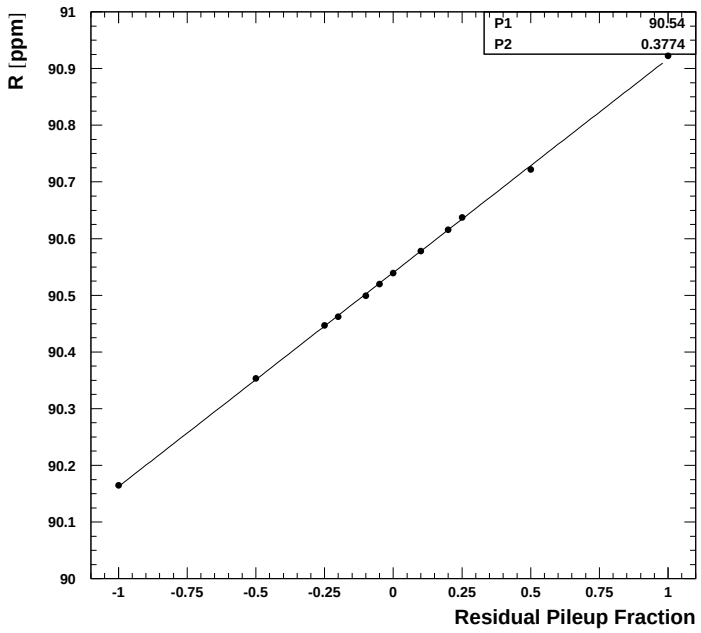

Figure 69: *R as a function of the fraction of unsubtracted pileup for the 1999-style function.*

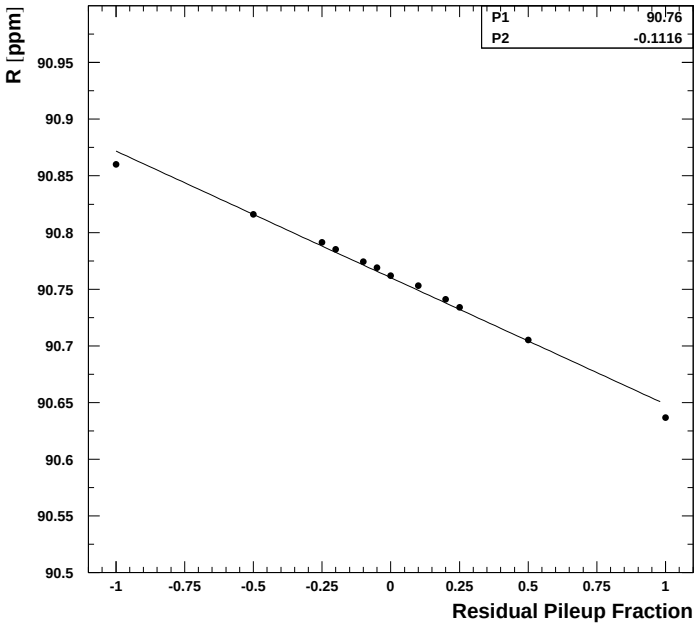

Figure 70: *R as a function of the fraction of unsubtracted pileup for the physics function without phase modulation.*

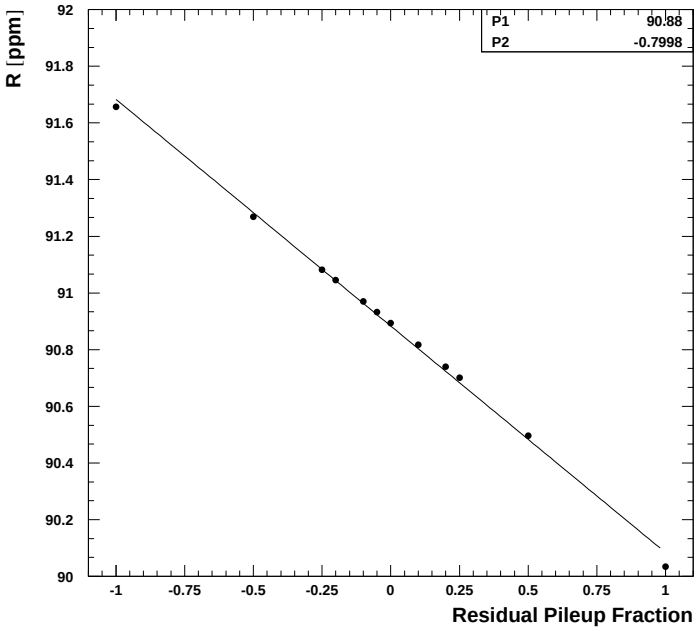

Figure 71: *R as a function of the fraction of unsubtracted pileup for the full physics function.*

6.5.5 Shift in R due to Pileup Phase

Potentially, simple scaling of the artificially constructed pileup does not cover all possible systematic pileup effects because this artificial pileup may have a phase shift with respect to the true pileup. Thus the assumed residual pileup may have a slightly wrong phase and pull R stronger than expected. This problem was studied by Yannis [16] who found a maximum systematic error of 0.2 times the shift in R between the pileup multipliers 0 and 1. For our three functions this leads to the following systematic error contributions:

- 1999-style function: $0.2 \times 0.38\,\text{ppm} = 0.075\,\text{ppm}$.
- physics function without phase modulation: $0.2 \times 0.11\,\text{ppm} = 0.022\,\text{ppm}$.
- full physics function: $0.2 \times 0.80\,\text{ppm} = 0.160\,\text{ppm}$.

Since these new errors come from the phase of the residual pileup vector whereas the errors discussed in the previous sections are caused by its amplitude, the two contributions should be added in quadrature. Hence our total systematic errors from pileup amount to

- 1999-style function: 0.08 ppm.
- physics function without phase modulation: 0.02 ppm.
- full physics function: 0.17 ppm.

6.5.6 Impact of the Error Enhancement by the Constructed Pileup

In Section 5.2 (Eq. (32)) the correction to the error $\sqrt{N_i}$ of the number of entries in a histogram bin was discussed. In that treatment a tacit approximation was made: the factor $X = \frac{D}{S}$ was averaged over a g-2 period and thus assumed to be non-wiggling which is not strictly correct. To investigate whether this approximation has any influence on the result for R, we replaced the constant X by

$$X(t) = X_0[1 + A_X \cos(\omega_a t + \phi_a + \Delta\phi_X)] \tag{81}$$

The X-asymmetry A_X was varied between 0 and 0.5, and the relative phase $\Delta\phi_X$ between 0 and $2\,\pi$. The result of the study is not even worthwhile to report quantitatively: the maximum variation in R was $9{\times}10^{-6}$ ppm. The statistical error $\sigma(R)$ changed slightly more: up to $6{\times}10^{-5}$ ppm.

Another test was to remove the error correction entirely by setting X to 0. The changes in R are given in Table 37.

	1999 Function	Physics Func. without Phase Modulation	Physics Func. with Phase Modulation
ΔR [ppm]	0.0005	0.0020	0.0063

Table 37: *Effect of the error enhancement by the constructed pileup: the values shown are the differences in R between fits with and without error correction.*

These values are small and correspond to the very unlikely case of a 100 % mistake in our understanding of the error enhancement.

6.5.7 Impact of the Correction for Lost Doubles due to the High Thresholds

At last we investigate the systematic error from the lost-pileup correction applied to the doubles spectrum: Potential error sources are the over- or under-estimation of the fraction of lost pileup, and the exponential life time of the doubles spectrum obtained by a fit and used for the correction (see Section 4.4).

The first mentioned issue is addressed by applying different multiples of the doubles correction, 1 being the standard case. Figure 72 shows that a 100 % error in the correction would lead to the systematic errors listed in Table 38.

	1999 Function	Physics Func. without Phase Modulation	Physics Func. with Phase Modulation
ΔR [ppm]	0.0030 ± 0.0000	0.0059 ± 0.0000	0.0184 ± 0.0116

Table 38: *Effect of the correction for missing double pulses due to the high threshold. The values shown are the differences in R between fits with corrected and to the uncorrected pileup spectra.*

Adding these errors quadratically to the ones for residual pileup does not change the result down to the second digit. Furthermore, a 100 % error is very unlikely.

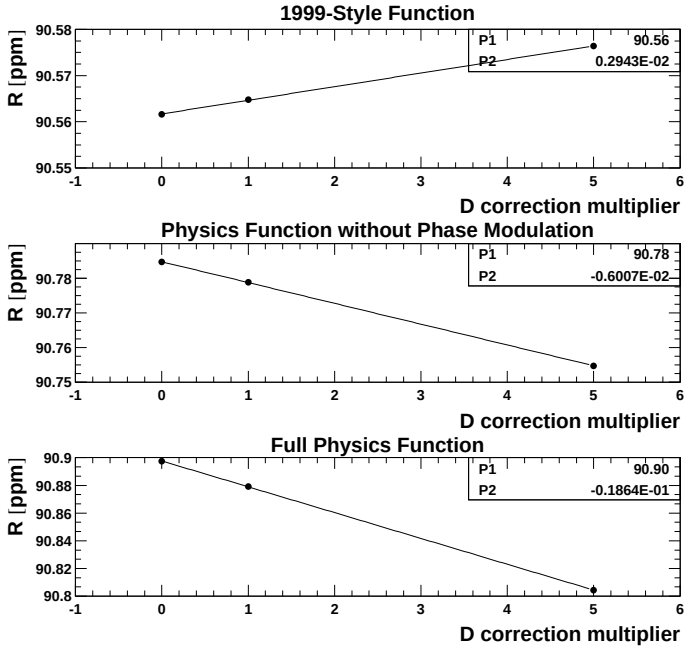

Figure 72: *Effect of the correction for missing double pulses due to the high hardware thresholds. Multiples of the correction (see Section 4.4) were applied to the doubles spectrum. The standard fits were done with a multiplier of 1.*

The second (non-) issue to be discussed here is the life time of the doubles spectrum used for the lost-pileup correction. For this purpose this life time was varied by ±10 μs (as compared with a sub-μs uncertainty returned by the fit to the doubles spectrum). The results are given in Table 72. They are all below 0.01 ppm.

τ_{Dcorr}	1999 Function	Physics Func. without Phase Modulation	Physics Func. with Phase Modulation
$22\,\mu$s	90.5633 ± 0.6143	90.7782 ± 0.6406	90.8795 ± 0.6779
from fit ($\sim 32\,\mu$s)	90.5646 ± 0.6143	90.7788 ± 0.6406	90.8791 ± 0.6779
$42\,\mu$s	90.5649 ± 0.6143	90.7828 ± 0.6406	90.8878 ± 0.6779

Table 39: *Effect of the life time used for the missing doubles correction.*

6.6 Gain Changes

6.6.1 Conventional Gain Correction without Upper Energy Cut

The first step of the study is to determine the average pulse energy as a function of time for all detectors individually. The average energy varies dominantly over a g-2 cycle but has also a CBO frequency component. We neglect the latter and only remove the variation with ω_a by histogramming the average energy in time bins with the width of a g-2 period. A more correct procedure correcting also for the CBO dependence was proposed by H. Deng [23] and may be pursued in the future.

Without a lower energy cut, a relative gain change $\Delta g \equiv \Delta G/G$ would translate into an equal change in the observed average energy $\Delta E/E$. Since we subject our pulses to an energy cut of 2 GeV, the relation

$$\frac{\Delta E}{E} = a\frac{\Delta G}{G} = a\,\Delta g \tag{82}$$

needs to be calibrated [20]. For this purpose we apply scale factors $1 + \Delta g_1 = 0.995$ and $1 + \Delta g_2 = 1.005$ to all pulse energies and determine the modified average energies $E_1(t)$ and $E_2(t)$. Then we can calculate the sensitivity factor a as

$$a(t) = \frac{E_2(t) - E_1(t)}{E_0(t)\,(\Delta g_2 - \Delta g_1)} \quad . \tag{83}$$

Detector	a	Detector	a
1	0.4642 ± 0.0004	13	0.4551 ± 0.0004
2	0.4598 ± 0.0005	14	0.4492 ± 0.0004
3	0.4478 ± 0.0005	15	0.4592 ± 0.0004
4	0.4584 ± 0.0005	16	0.4352 ± 0.0004
5	0.4556 ± 0.0005	17	0.4548 ± 0.0004
6	0.4426 ± 0.0005	18	0.4396 ± 0.0004
7	0.4189 ± 0.0005	19	0.4455 ± 0.0004
8	0.4079 ± 0.0005	20	0.3543 ± 0.0006
9	0.4232 ± 0.0005	21	0.4454 ± 0.0004
10	0.4498 ± 0.0004	22	0.4311 ± 0.0004
11	0.4537 ± 0.0004	23	0.4343 ± 0.0004
12	0.4387 ± 0.0004	24	0.4318 ± 0.0004

Table 40: *Sensitivity factors for the relation between relative gain change and average energy change for a lower energy cut of 2 GeV.*

If the relation between gain change and average energy is linear, $a(t)$ should not depend on the time. In Appendix D.1, $a(t)$ is shown for all detectors. Fits to constant lines are superimposed. The resulting sensitivity factors are given in Table 40.

Figure 73 shows the gain $G(t)$ relative to the reference time 200 μs, as obtained from the average energy and the sensitivity factor. The corresponding results for the two half rings are displayed in Figure 74.

Gain variation plots for the individual run periods and detectors can be found in Appendix D.2.

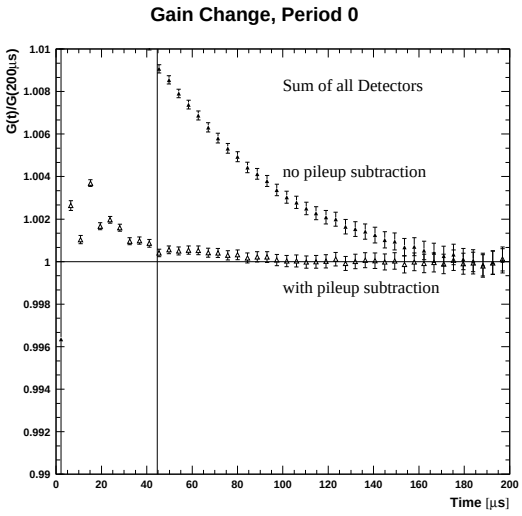

Figure 73: *Gain versus time for all runs and all detectors together.*

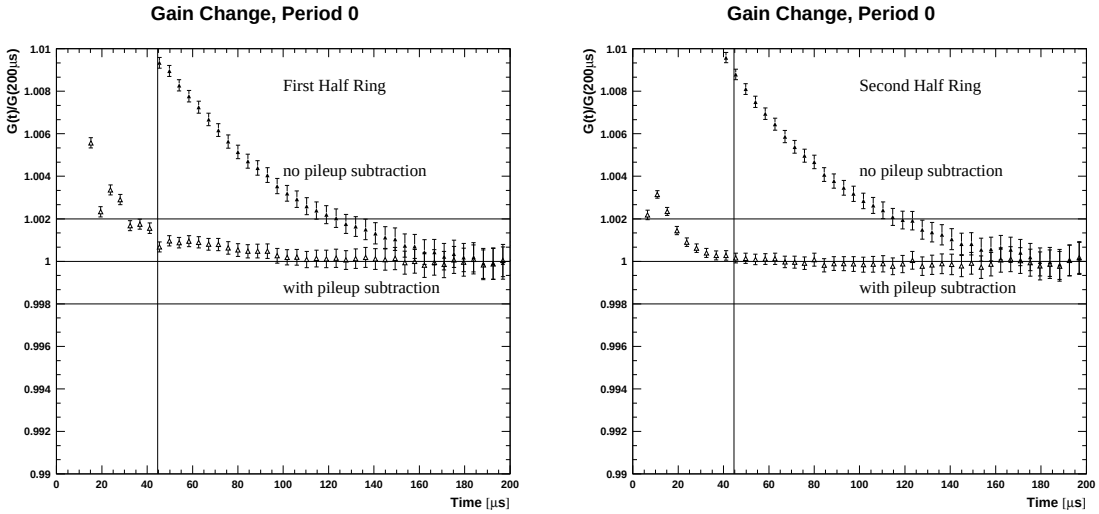

Figure 74: *Gain versus time for the two half rings (all runs together).*

Using an empirical parametrisation of $\Delta g(t)$ for each individual detector, a gain correction factor $1/(1+\Delta g)$ can be applied to the pulse energies before filling the time spectra.

Fit results after application of the gain correction are shown in Appendix D.3. The main observations in a comparison with the results from non-corrected data are (see Table 41):

- χ^2 deteriorates, mainly with the 1999-style function;
- the asymmetry stability deteriorates.

Apparently this gain correction does not work as well as it should. A possible reason is that imperfections in the pileup subtraction cause a part of the average energy variations. But then they are treated as gain variations which is wrong and can affect the asymmetry. Indeed, in Section 6.5 about residual pileup we have seen subtraction inefficiencies at very high energies causing differences between average energies with and without upper energy cut.

		1999 Function	Physics Func. without Phase Modulation	Physics Func. with Phase Modulation
χ^2	raw	1.013	1.011	1.011
	corr.	1.026	1.019	1.013
ΔA $[10^{-4}]$	raw	1.0	0.9	0.6
	corr.	2.4	2.2	1.8

Table 41: *Comparison of χ^2 at a start time of 49.2 μs and the peak-to-peak variation of the asymmetry for data without and with conventional gain correction.*

Another fault of the standard gain correction technique is the negligence of CBO effects. However, Fred has shown in a meeting that this effect should be very small.

Because of these problems we have decided not to apply a gain correction to the data used for the standard fits.

6.6.2 Artificial Enhancement of Gain Variations without Upper Energy Cut

To improve the handle on the influence of gain changes on the ω_a fit results, artificially enhanced gain variations were introduced. This was done by creating time spectra based on manipulated pulse energies, i.e. modified effective energy thresholds. The energy of a pulse detected at a time t was multiplied by a factor

$$\kappa_g(t) \equiv \frac{1 + \xi \Delta g(t)}{1 + \Delta g(t)} \quad , \tag{84}$$

where the gain multiplier ξ was a fixed coefficient. The value $\xi = 1$ corresponds to untreated energies. For this study, the values $\xi = 5$ and $\xi = 10$ were used. These choices magnify the gain changes which are present in the data by a factor 5 or 10. The case $\xi = 0$ (i.e. corrected energy scale, ideally no gain changes left), was already discussed in the previous section.

Note that the use of the experimental gain variations $\Delta g(t)$ for obtaining a systematic error estimate is based on the confidence that the average energies provide a sufficient knowledge about the magnitude of the gain variations, even though this knowledge is not precise enough for obtaining satisfactory fit results after a gain correction. Since the observed average energy variations are partly due to residual pileup, the present systematic error estimate for gain effects will contain a pileup contribution and hence be conservative.

Fit results for the four values of ξ and our three fit functions are shown in Figures 75 to 77. The upper plots show a strong phase pulling in the cases $\xi = 5$ and $\xi = 10$. In the lower plots the R-difference with respect to $\xi = 0$ for a start time of 49.2 μs is drawn as a function of ξ. The sytematic error estimate from this approach was chosen to be either R at $\xi = 0$ or the value of a linear fit at $\xi = 0$, whichever was greater. The results are:

- 1999-style function: δR =0.04 ppm;
- physics function without phase modulation: δR =0.13 ppm;
- full physics function: δR =0.35 ppm.

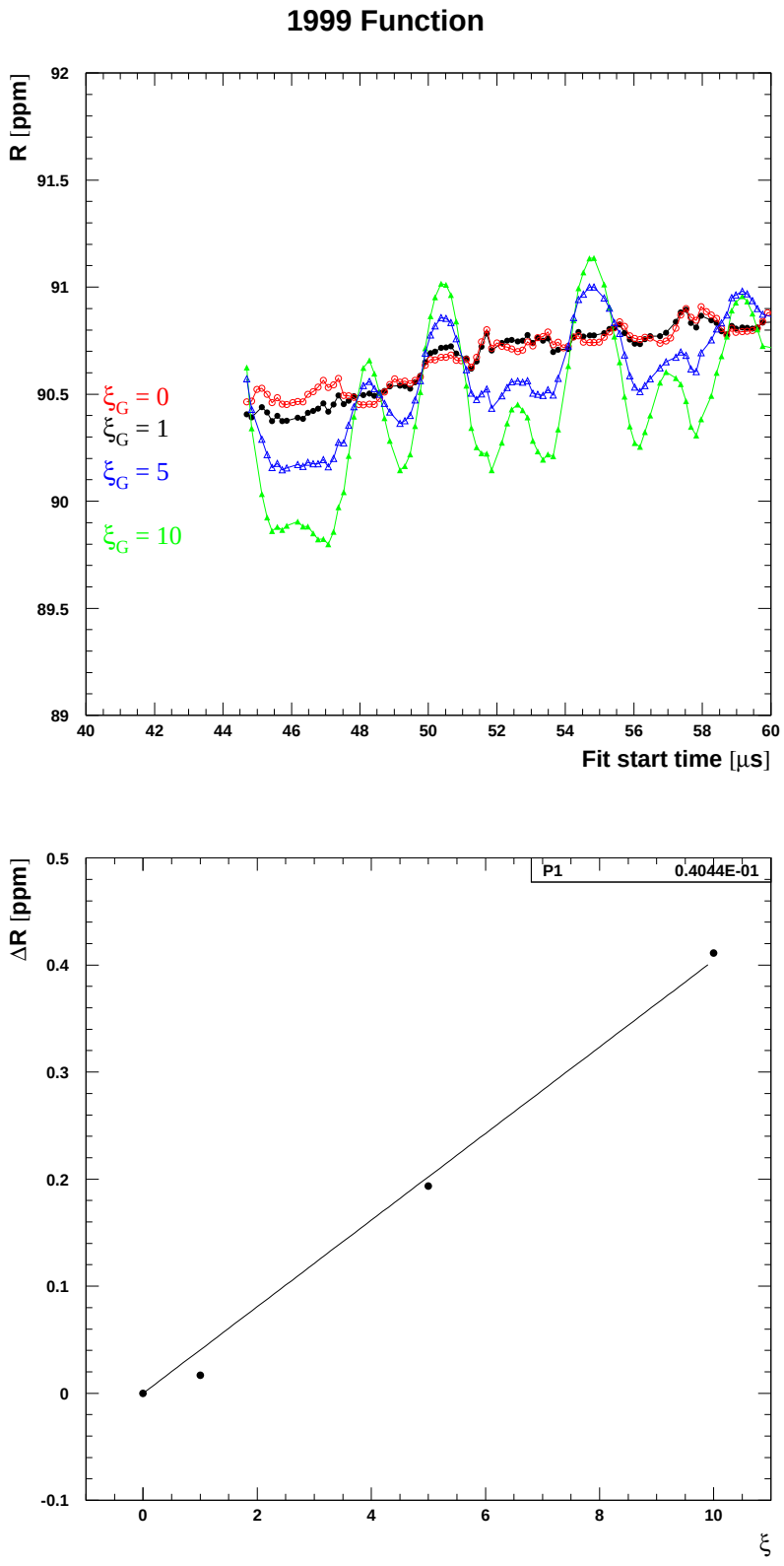

Figure 75: *Study of gain correction and artificial gain change. The linear fit in the lower plot was forced through the point (0, 0).*

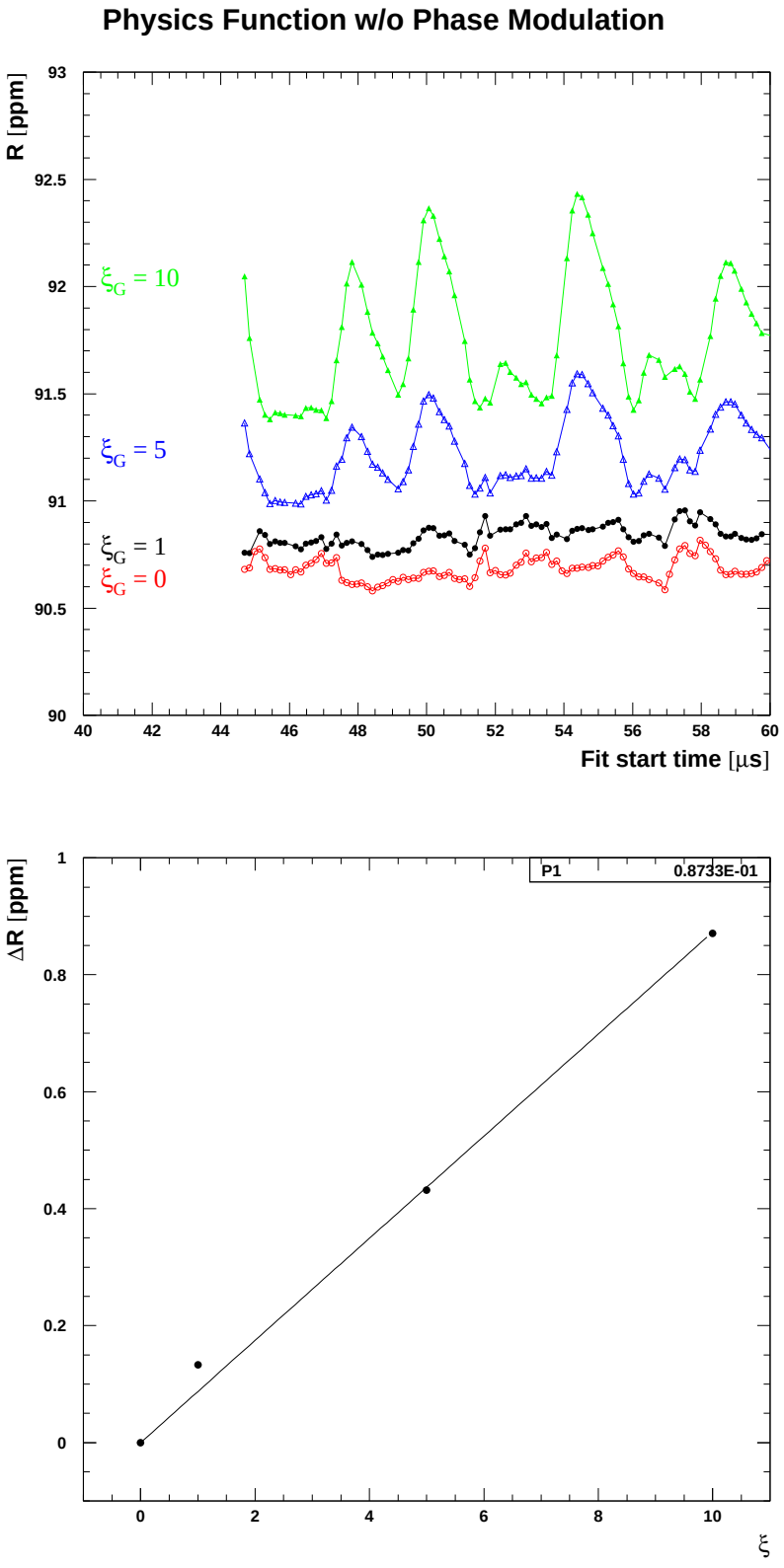

Figure 76: *Study of gain correction and artificial gain change.*

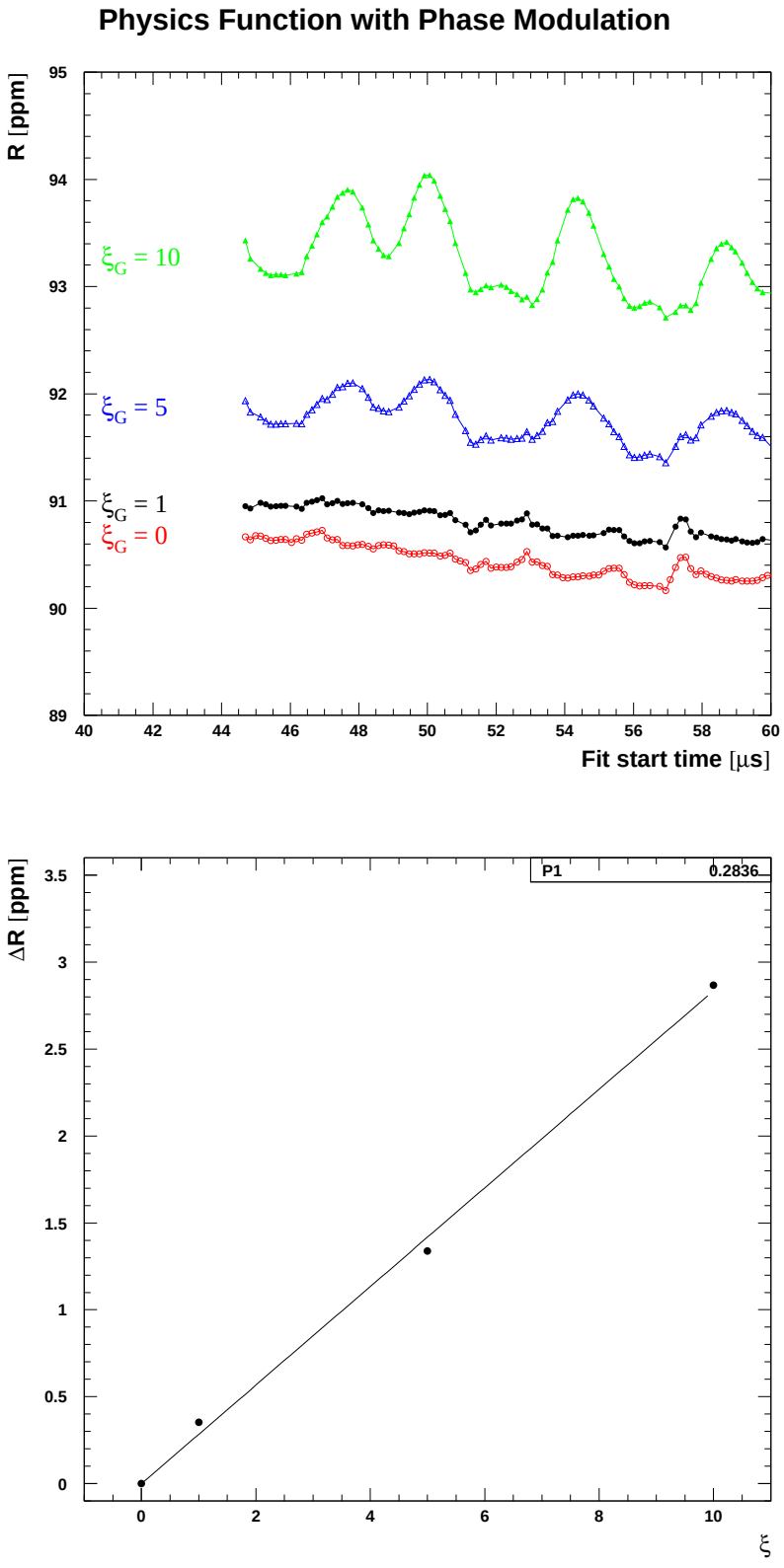

Figure 77: *Study of gain correction and artificial gain change.*

6.6.3 Gain Studies with Upper Energy Cut

The same gain correction as described in Section 6.6.1 was applied to data with an upper energy cut at 3.2 GeV. Figure 78 shows the relative gain changes for the sum of all detectors and the two half rings. Individual detectors are given in Figures 159 and 160.

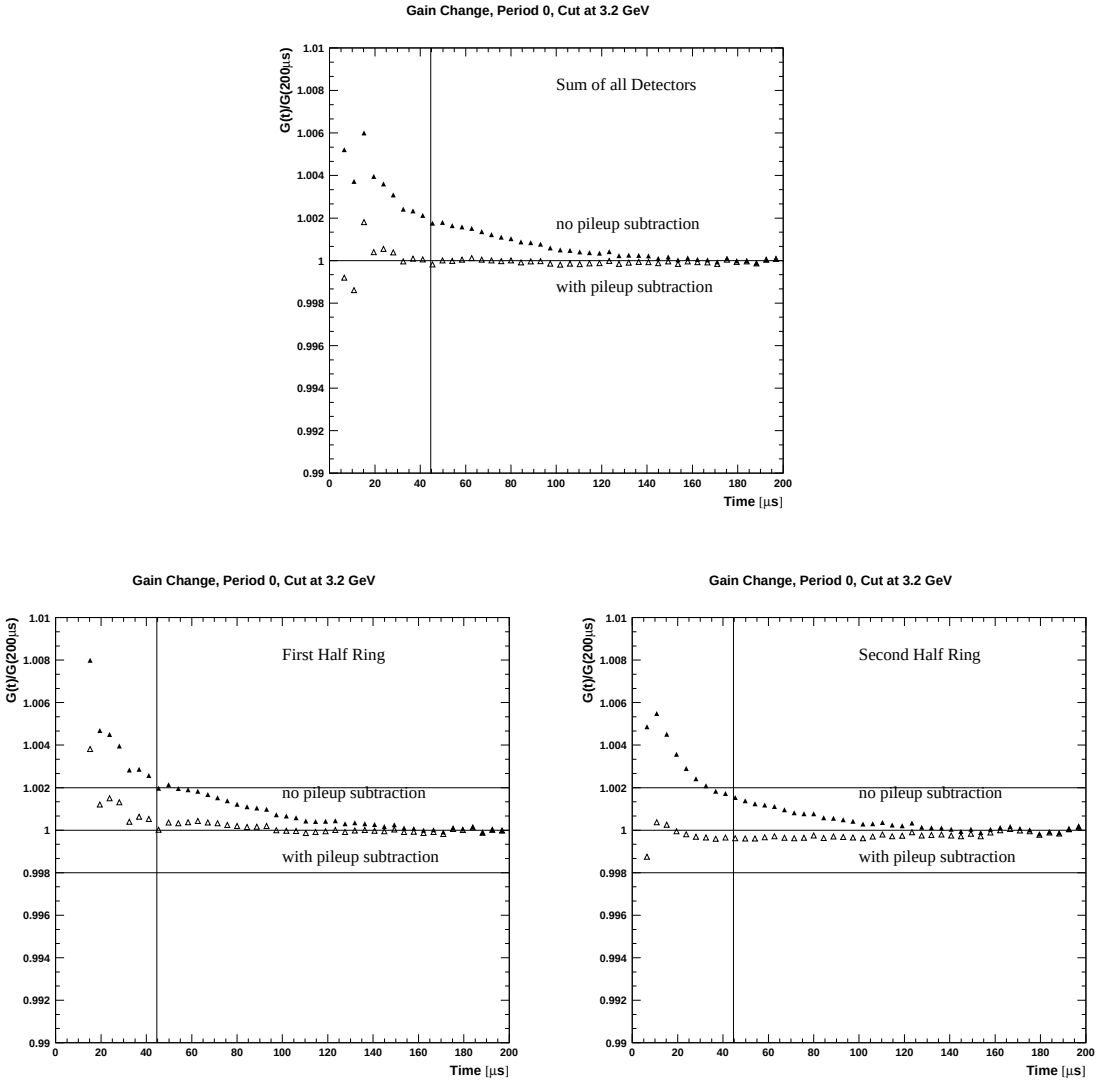

Figure 78: *Gain versus time for all detectors and the two half rings.*

The fit results analogous to those in Table 41 are given in Table 42. We notice that with the cut χ^2 does not deteriorate any more but even slightly improves. The asymmetry stability still suffers from the gain correction, but far less than without energy cut. The big effect of this cut above the energy endpoint for single pulses confirms the suspicion that the main reason for the failure of the conventional gain correction is pileup.

It is worthwhile to note that the energy cut by itself – i.e. without gain correction – does not change R significantly (Table 43).

The influence of the gain correction on the fit result with energy cut is shown in Figures 79 to 81. Like in the study without energy cut, also data with an artificial gain variation $\xi = 10$ were fitted. The changes in R are about 2 times smaller than without upper energy cut. Also, the second frequency component (CBO or double g-2) which was

		1999 Function	Physics Func. without Phase Modulation	Physics Func. with Phase Modulation
χ^2	raw	1.0102	1.0081	1.0071
	corr.	1.0097	1.0072	1.0053
ΔA $[10^{-4}]$	raw	1.1	0.86	0.48
	corr.	1.2	0.96	0.54

Table 42: *Comparison of χ^2 at a start time of 49.2 μs and the peak-to-peak variation of the asymmetry for data without and with gain correction with an upper energy cut at 3.2 GeV.*

	1999 Function	Physics Func. without Phase Modulation	Physics Func. with Phase Modulation
$R_{\text{without cut}}$	90.5646 ± 0.6142	90.7789 ± 0.6406	90.8792 ± 0.6779
$R_{\text{with cut}}$	90.5866 ± 0.6137	90.7994 ± 0.6402	90.8869 ± 0.6781
$R_{\text{with cut}} - R_{\text{without cut}}$	0.0220 ± 0.0248	0.0205 ± 0.0226	0.0077 ± 0.0165

Table 43: *Comparison of R with and without energy cut at 3.2 GeV for a start time of 49.2 μs. In both cases no gain correction was applied.*

very prominent in the phase pulling without energy cut has almost vanished. In the light of the strong effect of the energy cut whose primary action consists basically in eliminating high-energy pileup, it becomes more likely that the second phase-pulling component was $2f_a$ caused by pileup.

One could now take the position that the systematic error determined without energy cut is too pessimistic because it is contaminated by pileup contributions, and that the real systematic error from gain variations follows from the study with energy cut. In that case we would obtain more favourable values:

- 1999-style function: δR =0.02 ppm;
- physics function without phase modulation: δR =0.08 ppm;
- full physics function: δR =0.18 ppm.

However, since all the other systematic studies were done without energy cut it does not seem safe to choose the new, more agressive values as systematic errors.

For now we shall therefore keep the conservative results from Section 6.6.2. Before drawing the final conclusion on the gain systematics we shall shed light on this problem from another perspective: the start-time instablity of the asymmetry.

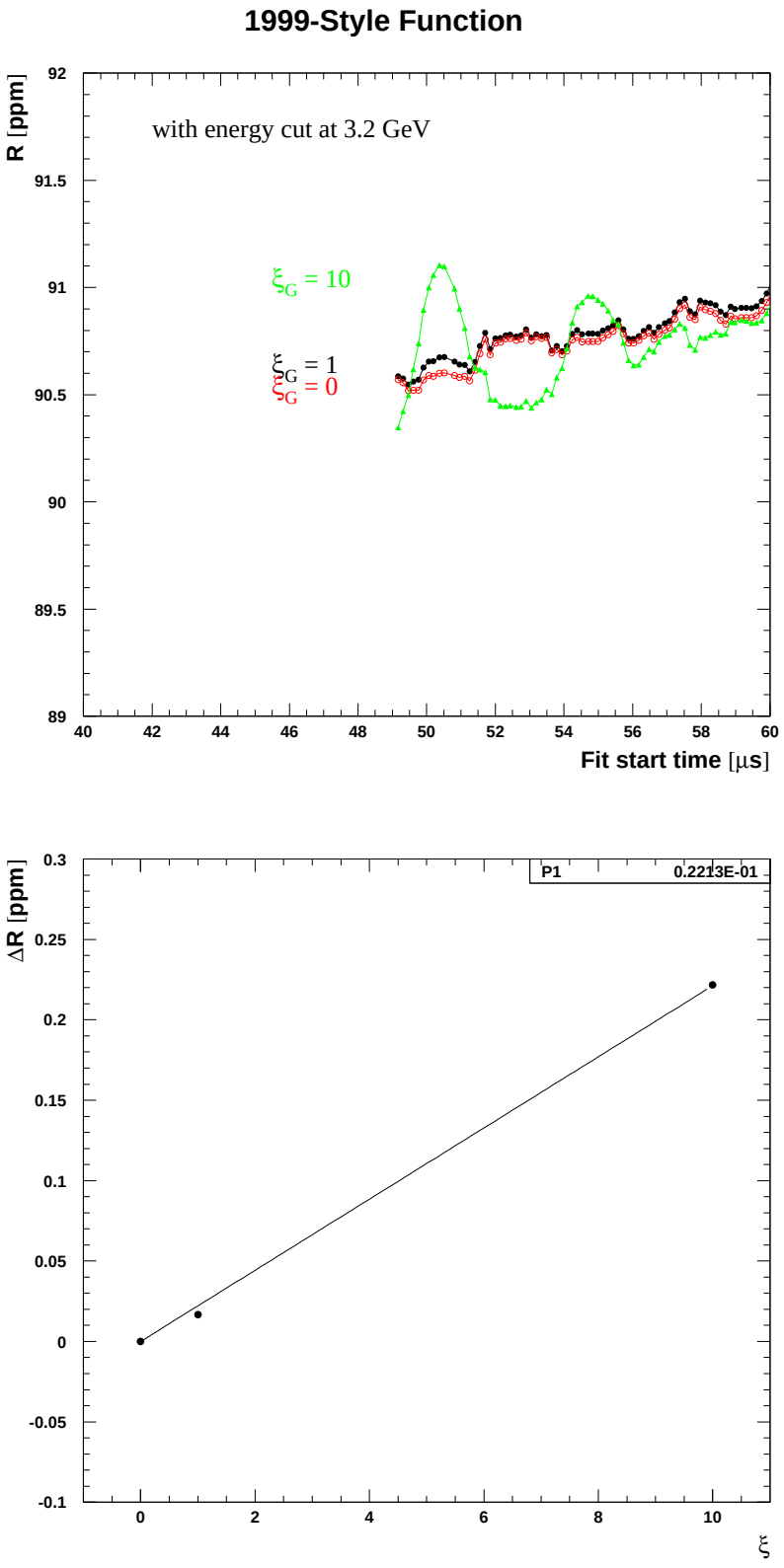

Figure 79: *Study of gain correction and artificial gain change with an upper energy cut at 3.2 GeV.*

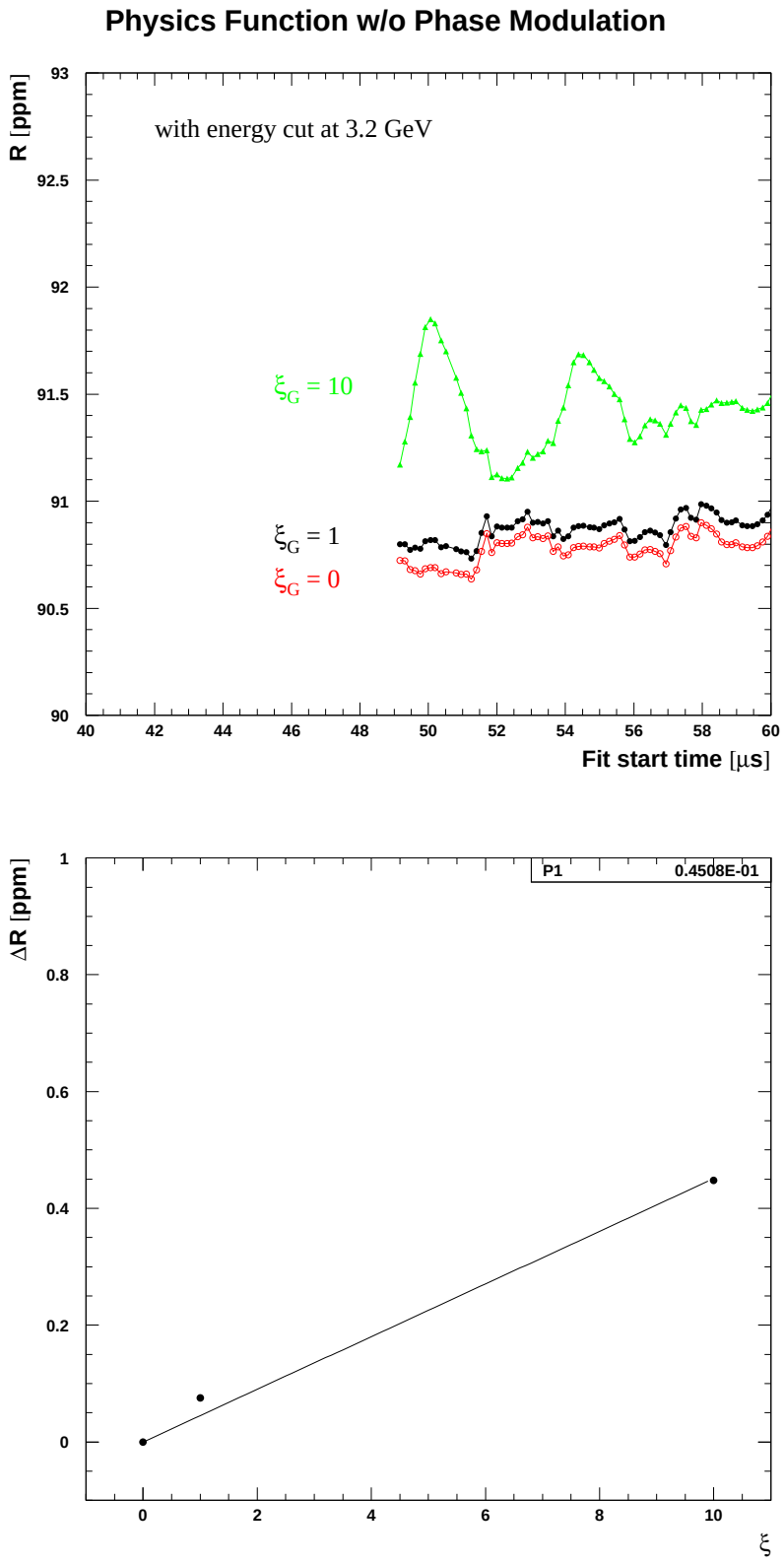

Figure 80: *Study of gain correction and artificial gain change with an upper energy cut at 3.2 GeV.*

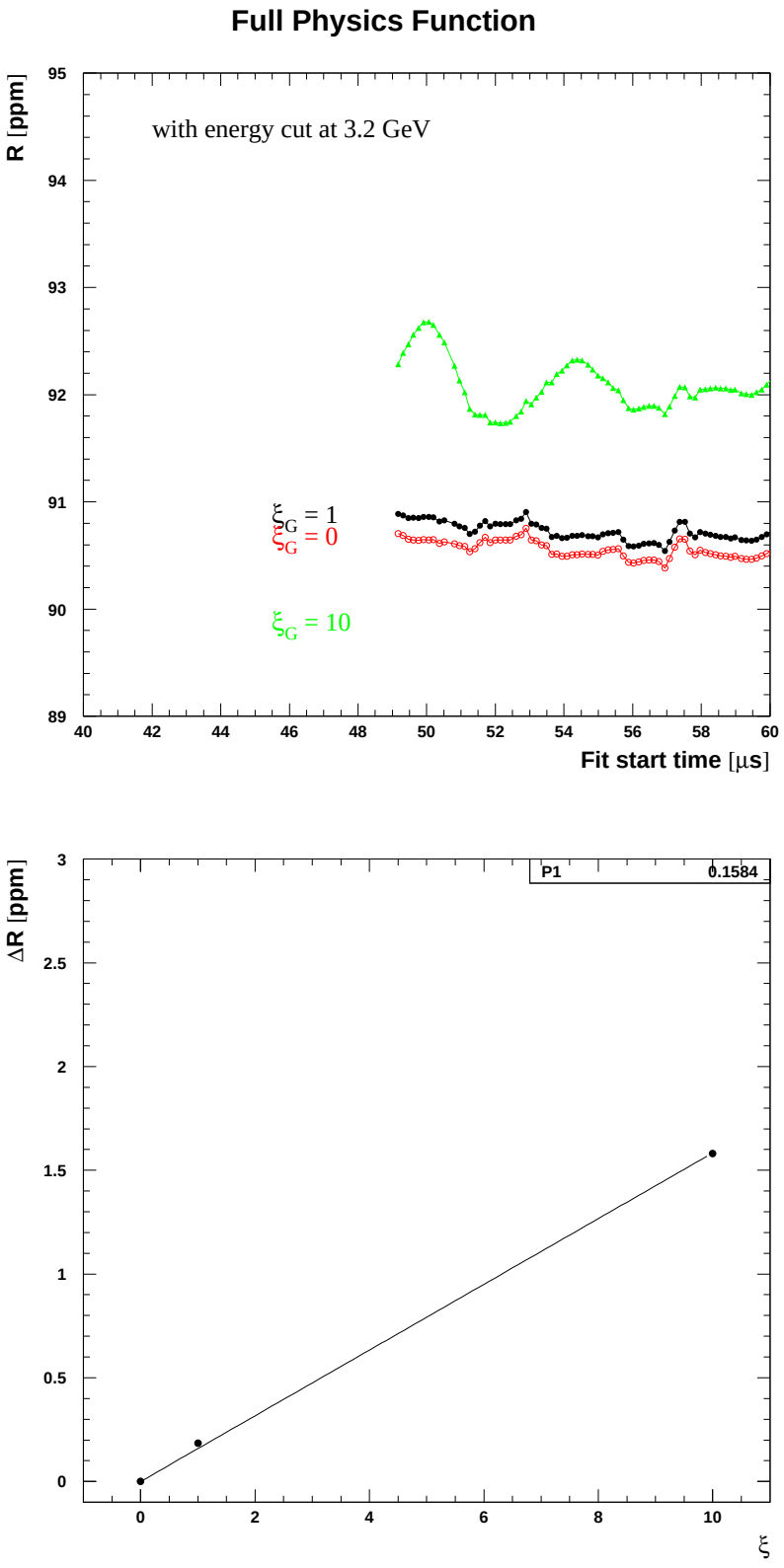

Figure 81: *Study of gain correction and artificial gain change with an upper energy cut at 3.2 GeV.*

6.7 Systematic Error from the Asymmetry Instability

Instabilities in start-time scans for the asymmetry can be caused either by gain variations or by unseen pileup involving pulses below 250 MeV. Although the latter would cause a rise of the asymmetry with time rather than a droop as observed in the fit results, we shall conservatively develop systematic error estimates for both assumptions on the origin of the instability. The two estimates will be added in quadrature despite being aware of double-counting a part of the underlying physical effects.

These studies are based on Figure 26 for the 1999-style function. We do not use the results from fits with the physics functions (Figures 31 and 36) because the terms for asymmetry and phase modulation by CBO strongly correlate with A and potentially compensate a part of the asymmetry instability. Using the estimates from the 1999-style function yields the most conservative result.

6.7.1 Interpretation as Gain Variation

Gain variations are not only visible from the average energy as a function of time, but also translate into an start-time instability of the asymmetry.

According to Bill [17], a true[1] asymmetry change $\Delta A = 0.0001$ corresponds to a relative gain change $\Delta g = 0.01\,\%$. Thus the observed gain change of $\Delta g \approx 0.04\,\%$ at $50\,\mu$s for the sum of all detectors (Figure 73) is expected to cause a true asymmetry change of $\Delta A \approx 0.0004$.

From a simulation Yannis learnt that an explicit linear asymmetry change from $\Delta A(50\,\mu\text{s}) = 0.0006$ to $\Delta A(100\,\mu\text{s}) = 0$ causes a measured $\Delta A'(50\,\mu\text{s}) = 0.00015$ in a start-time scan for fits with the 1999-style function. The corresponding variation of R in the same start-time scan was found to be

- ≈ 0 ppm for the 1999-style function;
- 0.5 ppm for the physics function without phase modulation;
- 1 ppm for the full physics function.

Scaling these simulation results to the $\Delta A \approx 0.0004$ obtained from $\Delta g \approx 0.04\,\%$, we expect an (asymmetry vs. start-time) instability $\Delta A' \approx 0.0001$ which is exactly what we see in Figure 26. Furthermore, we expect the following peak-to-peak changes ΔR or systematic errors δR:

- $\Delta R = 0$ ppm for the 1999-style function;
- $\Delta R = 0.33$ ppm or $\delta R = 0.33\,\text{ppm}/2 = 0.17$ ppm for the physics function without phase modulation.
- $\Delta R = 0.67$ ppm or $\delta R = 0.67\,\text{ppm}/2 = 0.34$ ppm for the full physics function.

The new estimates for the physics functions are very close to the ones obtained from the observed average energies in conjunction with fits of time spectra based on artificially modified gain variations (Section 6.6.2). For the final error table we choose the most pessimistic estimates. For the 1999-style function it is the old value 0.04 ppm because the new study did not see any effect. For the physics function without phase modulation the larger estimate is 0.17 ppm from the present study. For the full physics function the old value 0.35 ppm is slightly bigger.

[1] Here, an explicit asymmetry variation in the data is meant, not the result of a fit assuming constant asymmetry.

6.7.2 Interpretation as Unseen Pileup

The estimate of an upper limit on the systematic error from unseen pileup is done along the lines of [18] for the sum of all detectors and all runs.

1999-Style Function

With the 1999 function, the asymmetry shows a peak-to-peak variation $\delta A = 0.00010$ (Figure 26). We take the full value as systematic error on A which is very conservative.

As shown in [18], the sensitivity of ϕ to unseen pileup is at most 0.19 times the sensitivity of A. This gives a maximum systematic error contribution of $\delta\phi \leq 0.19 \times 0.00010 = 1.9 \times 10^{-5}$ for the phase, which is 0.17 times the statistical error $\sigma(\phi) = 1.1 \times 10^{-4}$. Since R is strongly correlated with the phase, the contribution of this effect to the systematic error on R is again about 0.17 times the statistical error:

$$\frac{\delta R}{R} \approx \frac{\sigma(R)}{R}\frac{\delta\phi}{\sigma(\phi)} = 0.61\,\text{ppm} \times 0.17 = 0.1\,\text{ppm} \tag{85}$$

Physics Function without Phase Modulation

Following the same procedure as for the 1999 function and using the asymmetry peak-to-peak variation $\delta A = 0.00009$ (Figure 31) one finds a systematic error of $\delta\phi \leq 0.19 \times 0.00009 = 1.72 \times 10^{-5}$ on the phase. With the statistical error $\sigma(\phi) = 1.2 \times 10^{-4}$ we obtain

$$\frac{\delta R}{R} \approx \frac{\sigma(R)}{R}\frac{\delta\phi}{\sigma(\phi)} = 0.64\,\text{ppm} \times 0.14 = 0.09\,\text{ppm} \quad . \tag{86}$$

This value suggest a smaller systematic error than for the 1999 function. However, since unseen pileup affects the g-2 phase already at pulse level, it is unsafe to believe that using a more sophisticated fit function leads to a smaller systematic error than using the 1999 function. From the correlation matrix (Table 16) we know that the asymmetry is rather strongly correlated with the parameters A_{Rob} and ϕ_{Rob} of the asymmetry modulation. The pileup effect on A may be partially cancelled by some other effect picked up via this correlation. Therefore, to be conservative, we take the larger value 0.1 ppm from the 1999 function as systematic error for the physics function without phase modulation.

Full Physics Function

The same procedure as for the two other functions yields $\delta A = 0.00006$ (Figure 36), and hence $\delta\phi \leq 0.19 \times 0.00006 = 1.04 \times 10^{-5}$. With the statistical error $\sigma(\phi) = 1.3 \times 10^{-4}$ we obtain

$$\frac{\delta R}{R} \approx \frac{\sigma(R)}{R}\frac{\delta\phi}{\sigma(\phi)} = 0.68\,\text{ppm} \times 0.088 = 0.06\,\text{ppm} \tag{87}$$

In the full physics function A correlates not only with A_{Rob} and ϕ_{Rob} but also with A_{Jim} (Table 24), which further reduces the reliability of the asymmetry for the purpose of this pileup study. Therefore, we use once again the larger value 0.1 ppm from the 1999 function.

6.8 Muon losses and Other Slow Effects

In this section we investigate the systematic error from the combined function for muon losses and residual slow effects. For the functional form see Section 5.1.4. Figure 82 shows that the rse term contributes only a very small modification to the shape of the slow function $g_{\rm slow}(t)$ which is dominated by the muon loss function $g_{\rm loss}(t)$. Nevertheless, the muon loss function alone does not provide a sufficient description of the slow variation of the positron time spectrum, as reflected by χ^2 (around 1.2 without rse term) and by the phase pulling with an amplitude of 0.6 ppm at 46 μs and 0.4 ppm at 50 μs if the rse term is not included (see Figure 83).

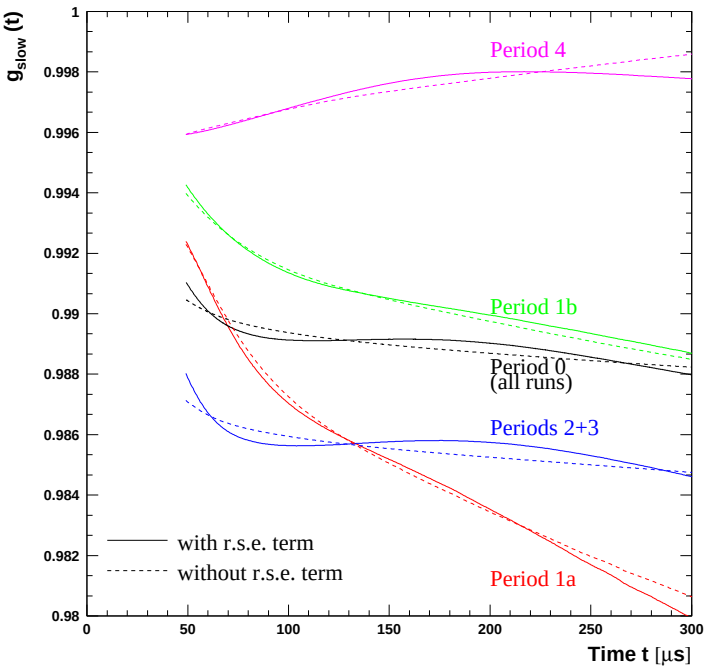

Figure 82: *Continuous lines: functional form of the combined slow effects $g_{\rm slow}(t)$ for the different run periods. The parameters were obtained from the fits. The graphs shown here represent the 1999-style function. They are indistinguishable from the graphs for the two other functions, as one can see from the almost identical parameter values given in Tables 45 to 44. Dashed line: function $\frac{N_0^{no\ rse}}{N_0^{with\ rse}} g_{\rm slow}(t)$ determined by the fit if only the muon loss term is included, i.e. A_{rse} is fixed to 0.*

The parameters of $g_{\rm slow}(t)$ for the three fit functions and all the run periods are listed in Tables 44 to 46. We notice that the values are almost independent of the fit function. Furthermore, their orders of magnitude agree from period to period. Note also that without rse term the "loss amplitude" in Period 4 has an unphysical negative value. This happens because between Periods 3 and 4 the radial magnetic field was changed in order to optimise scraping which almost eliminated muon losses at later times. Hence in Period 4 the slow function is dominated by the rse term which requires a positive slope.

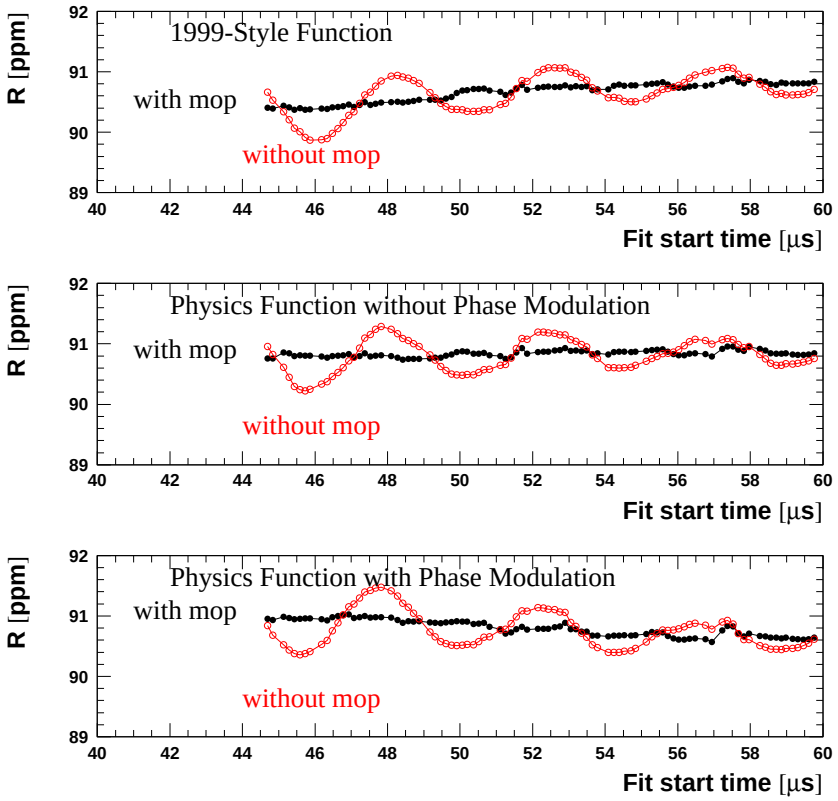

Figure 83: *Phase pulling if the empirical term describing residual slow effects ("mop") is not included in the fit. The muon loss term however is included; the loss amplitude* A_{loss} *is a free parameter.*

Period	1999 Function	Physics Func. without Phase Modulation	Physics Func. with Phase Modulation
1a	0.0203 ± 0.0018	0.0203 ± 0.0018	0.0204 ± 0.0018
	(0.0151 ± 0.0004)	(0.0151 ± 0.0003)	(0.0152 ± 0.0003)
1b	0.0113 ± 0.0013	0.0113 ± 0.0013	0.0114 ± 0.0013
	(0.0087 ± 0.0003)	(0.0087 ± 0.0003)	(0.0087 ± 0.0003)
23	0.0155 ± 0.0008	0.0155 ± 0.0008	0.0155 ± 0.0008
	(0.0047 ± 0.0002)	(0.0047 ± 0.0002)	(0.0047 ± 0.0002)
4	0.0022 ± 0.0014	0.0022 ± 0.0014	0.0022 ± 0.0014
	(-0.0036 ± 0.0002)	(-0.0036 ± 0.0002)	(-0.0036 ± 0.0002)
0	0.0120 ± 0.0006	0.0120 ± 0.0006	0.0120 ± 0.0006
	(0.0040 ± 0.0001)	(0.0040 ± 0.0001)	(0.0040 ± 0.0001)

Table 44: *Fitted muon loss amplitude* A_{loss} *for the different run periods and fit functions and a start time of 49.2 μs. The values in brackets are obtained if* A_{rse} *is fixed to 0, i.e. if the residual slow effects are not included in the fit.*

Period	1999 Function	Physics Func. without Phase Modulation	Physics Func. with Phase Modulation
1a	0.00391 ± 0.00132	0.00392 ± 0.00132	0.00396 ± 0.00132
1b	0.00181 ± 0.00073	0.00183 ± 0.00073	0.00186 ± 0.00074
23	0.00512 ± 0.00034	0.00512 ± 0.00034	0.00512 ± 0.00034
4	0.00410 ± 0.00099	0.00410 ± 0.00099	0.00409 ± 0.00099
0	0.00425 ± 0.00030	0.00425 ± 0.00030	0.00425 ± 0.00030

Table 45: *Values of the parameter $A_{\rm rse}$ for the different run periods and fit functions. They were obtained from fits with a start time of 49.2 μs.*

Period	1999 Function	Physics Func. without Phase Modulation	Physics Func. with Phase Modulation
1a	113.73 ± 9.40	113.81 ± 9.38	114.08 ± 9.33
1b	171.33 ± 36.43	171.14 ± 35.94	170.75 ± 35.05
23	134.12 ± 3.44	134.12 ± 3.44	134.11 ± 3.44
4	122.84 ± 7.53	122.84 ± 7.53	122.74 ± 7.54
0	127.01 ± 2.83	127.01 ± 2.83	127.01 ± 2.83

Table 46: *Values of the parameter $\tau_{\rm rse}$ in μs for the different run periods and fit functions. They were obtained from fits with a start time of 49.2 μs.*

Two contributions to the systematic error will be considered: the impact of uncertainties in the muon loss functional form on R, and the sensitivity of R to variations in the parameters $A_{\rm loss}$, $A_{\rm rse}$ and $\tau_{\rm rse}$.

For the functional form of $g_{\rm loss}$ the muon loss analysis [11] delivered a best estimate, a minimum and a maximum (Figure 84a) which differ in the subtraction of the proton background that is also seen by the FSDs. Using those three loss functions in the fit yields R-values that differ only at the ppb level (Figure 84b).

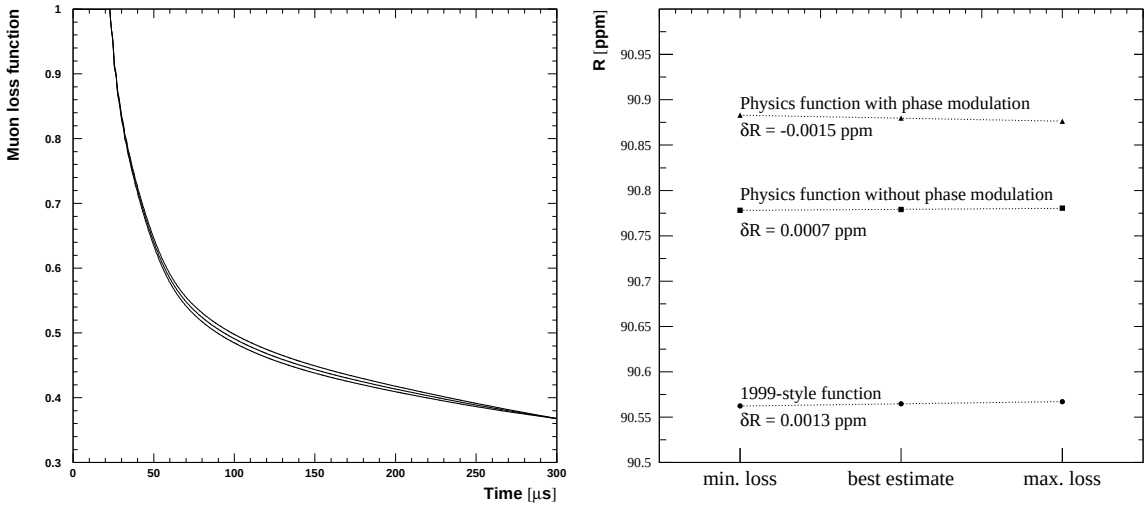

Figure 84: *(a) Best estimate and limits for the muon loss function. (b) Impact of the shape of the muon loss function on R.*

Table 47 shows the correlation submatrix with all rows but only the three columns pertaining to the parameters of g_{slow}. The latter correlate only weakly with R. The lowest 3×3 block shows that the two amplitudes A_{loss} and A_{rse} correlate very strongly whereas the life time τ_{rse} almost decouples from them. Therefore, we shall investigate the impact of the two amplitudes on R in a two-dimensional scan; τ_{rse} on the other hand can be treated separately.

	A_{loss}	A_{rse}	τ_{rse}
N_0	0.994	0.986	0.007
A	-0.034	-0.030	0.009
ϕ_a	0.018	0.015	-0.002
R	**0.013**	**0.012**	**-0.001**
f_{CBO}	0.027	0.023	0.002
A_{CBO}	-0.328	-0.297	0.001
ϕ_{CBO}	-0.036	-0.031	-0.004
A_{Rob}	-0.009	-0.008	0.015
ϕ_{Rob}	-0.029	-0.026	0.022
A_{Jim}	-0.004	-0.004	-0.001
ϕ_{Jim}	-0.054	-0.048	-0.006
A_{DCBO}	0.004	0.003	0.007
ϕ_{DCBO}	0.011	0.010	0.019
A_{loss}	1.000	0.978	0.007
A_{rse}	0.978	1.000	0.006
τ_{rse}	0.007	0.006	1.000

Table 47: *Correlation matrix between the parameters of g_{slow} and all parameters of the full physics function.*

Figures 85, 87 and 89 show the τ_{rse} studies for the 1999-style function and the physics functions without and with phase modulation respectively. Like in several previous sections, the dependence of χ^2 on τ_{rse} is used for determining a 1 σ interval which is then translated into a systematic error interval for R. We find:

- 1999-style function: $\delta R_{\tau_{\text{rse}}} = 0.003\,\text{ppm}$
- physics function without phase modulation: $\delta R_{\tau_{\text{rse}}} = 0.0007\,\text{ppm}$
- full physics function: $\delta R_{\tau_{\text{rse}}} = 0.006\,\text{ppm}$

The same principle is applied to A_{loss} and A_{rse} but in a two-dimensional way: the upper left diagrammes of Figures 86, 88 and 90 represent χ^2 paraboloids on a very coarse grid[2]. Due to the almost 100 % correlation of the two parameters, the independent axes $\mathcal{A}_1$ and $\mathcal{A}_2$ are basically oriented along the diagonals. We now draw the cross-sections of the paraboloid along $\mathcal{A}_1$ and $\mathcal{A}_2$ (upper right graphs of the figures). Along $\mathcal{A}_1$ the evolution of χ^2 is very shallow and results in a wide 1 σ interval. Fortunately, the slope of R along $\mathcal{A}_1$ (lower plots) is also small, and we get a small systematic error along this axis. Along $\mathcal{A}_2$, χ^2 has a narrow minimum which is advantageous, given the steep R evolution along this axis. Again, the systematic error along this axis is small, too. The total systematic error is now given by the quadratic sum of the partial errors along the independent axes.

[2] three-dimensional surface plots were tried but didn't prove to be very clear.

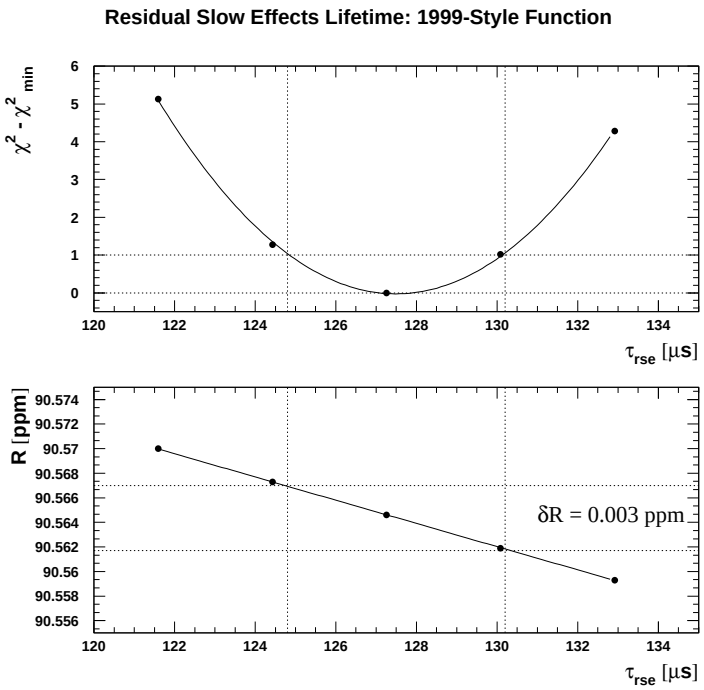

Figure 85: *Systematic error due to the uncertainty in the lifetime of the residual slow effects.*

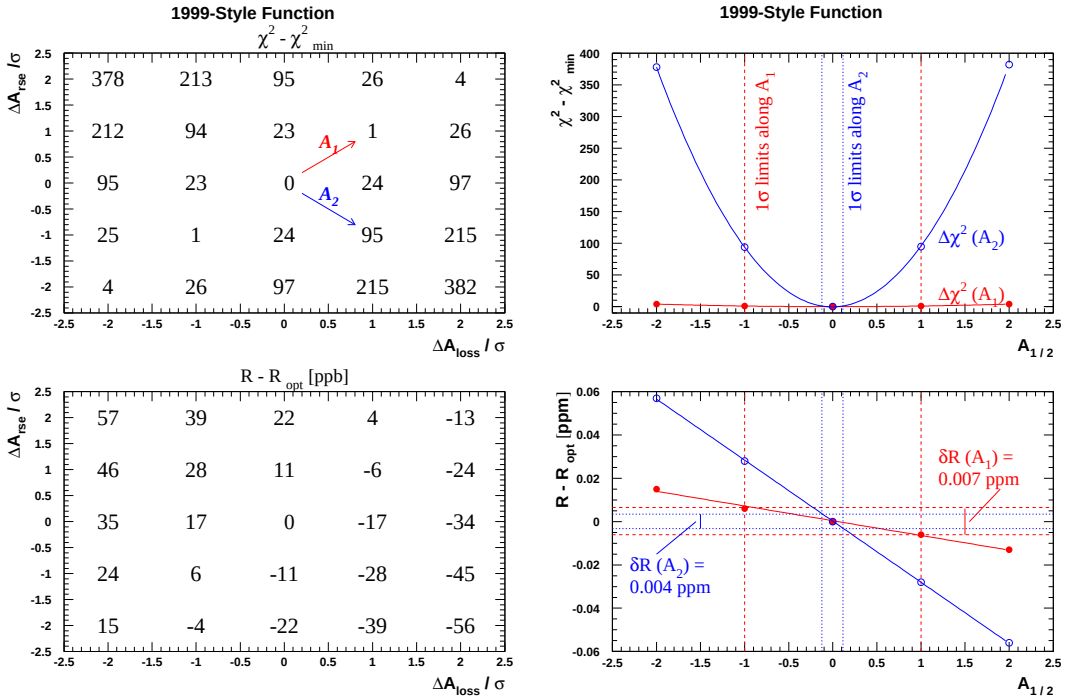

Figure 86: *Systematic error due to the uncertainty in the amplitudes of muon losses and residual slow effects.*

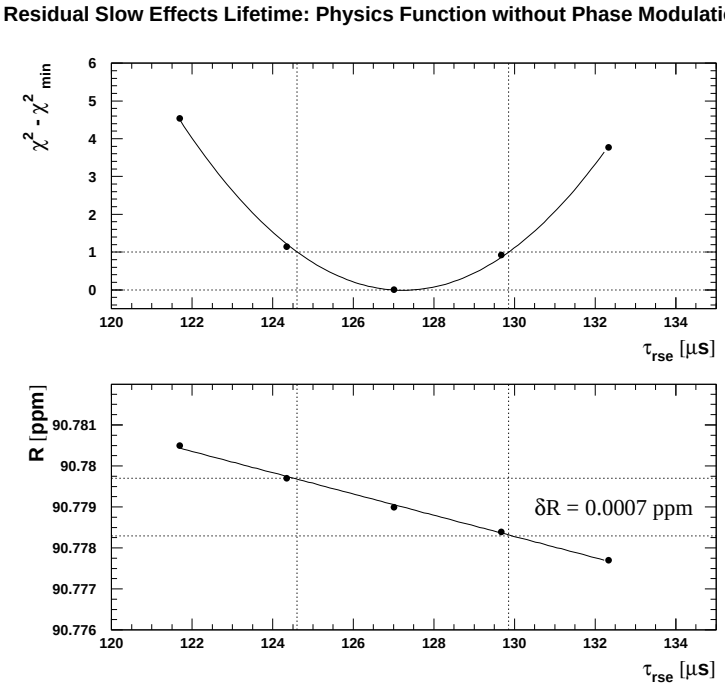

Figure 87: *Systematic error due to the uncertainty in the lifetime of the residual slow effects.*

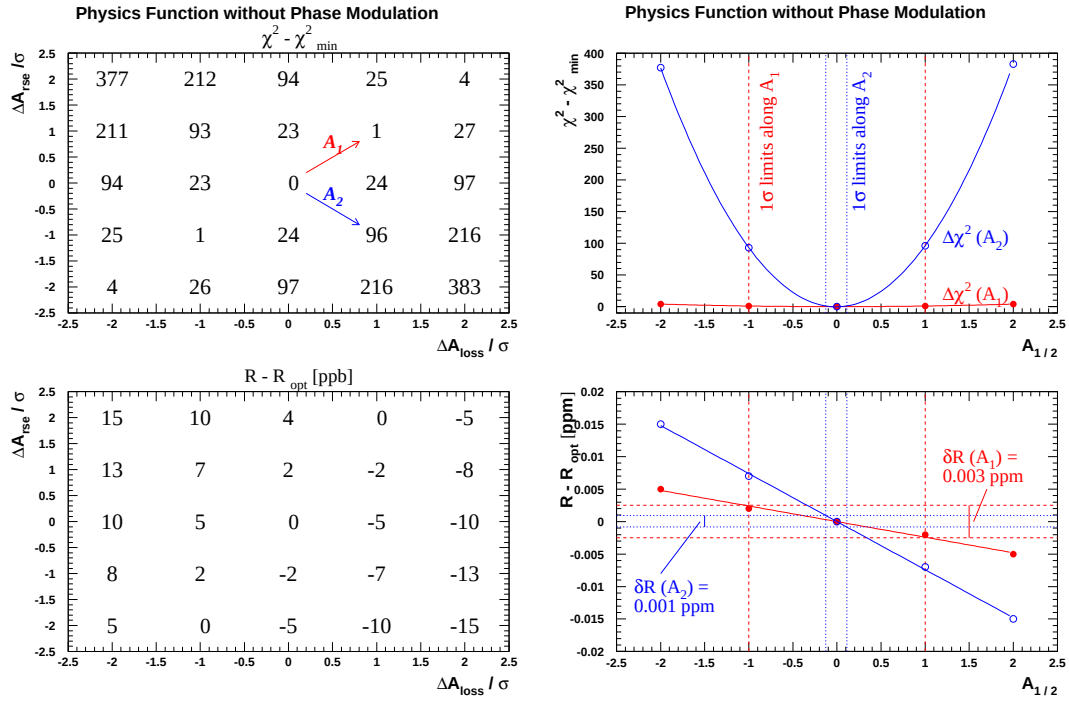

Figure 88: *Systematic error due to the uncertainty in the amplitudes of muon losses and residual slow effects.*

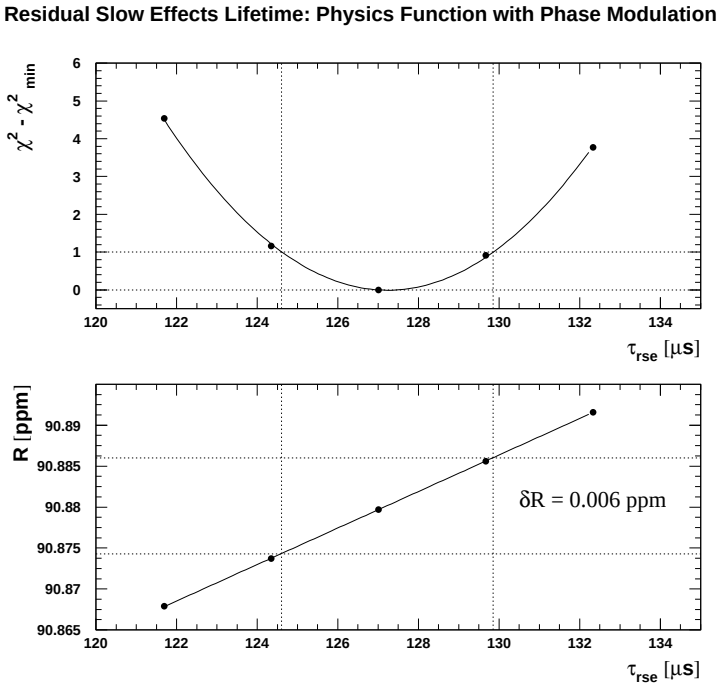

Figure 89: *Systematic error due to the uncertainty in the lifetime of the residual slow effects.*

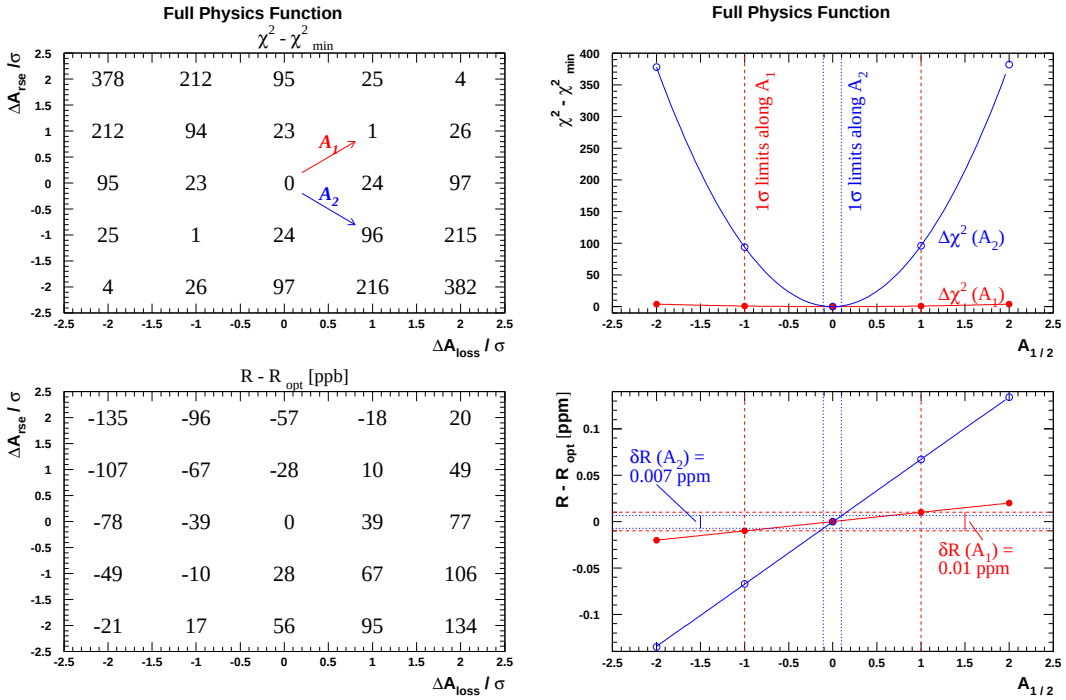

Figure 90: *Systematic error due to the uncertainty in the amplitudes of muon losses and residual slow effects.*

The results are:

- 1999-style function: $\delta R_{\tau_{\rm rse}} = 0.008\,{\rm ppm}$
- physics function without phase modulation: $\delta R_{\tau_{\rm rse}} = 0.003\,{\rm ppm}$
- full physics function: $\delta R_{\tau_{\rm rse}} = 0.007\,{\rm ppm}$

What is the lesson for life that we are taught by this chapter?
Mops are very romantic.

6.9 Binning Effects

Before investigating the impact of the bin width on the fit result for R we need to determine the statistically permissible spread due to filling identical data into histograms with different bin widths. Such a purely statistical effect is to be expected because the events are filled into different bins resulting in fluctuations of the number of entries of a given bin. To study the effect of these fluctuations on the fit result, we generate Monte Carlo data *without* any fast rotation structure which could entail a physical dependence on the bin width. In this way the statistical effect is separated. The function used for generation and fit of the Monte Carlo data was the innocent 5-parameter function. The statistical spread determined by this simulation will be used as an error of possible systematic effects seen in the real data.

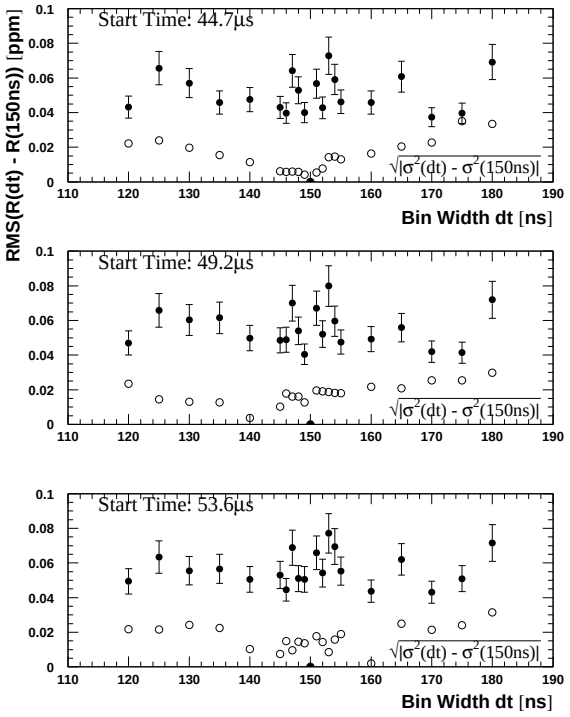

Figure 91: *Monte Carlo study of the statistically allowed variation of the fit result for R due to filling identical data into histograms with different bin widths. The solid markers show the RMS of the distribution of $R_i(dt_{\rm bin}) - R_i(150\,{\rm ns})$ as a function of the bin width $dt_{\rm bin}$ for 24 data sets i. The open markers show the naive error estimate $\sigma(\Delta R(dt_{\rm bin})) \approx \langle\sqrt{|\sigma^2(R(dt_{\rm bin})) - \sigma^2(R(150\,{\rm ns}))|}\rangle$ for comparison.*

In practice, the Monte Carlo study was done in the following way:

- 21 bin widths between 120 ns and 180 ns were chosen.
- For each of them 24 data sets – each with a statistical error of 0.63 ppm – were generated and fitted with the 5-parameter function.
- For each data set i and each bin width dt_{bin} the difference between its fit result $R_i(dt_{\mathrm{bin}})$ and the result for the standard bin width 150 ns is calculated: $\Delta R_i(dt_{\mathrm{bin}}) = R_i(dt_{\mathrm{bin}}) - R_i(150\,\mathrm{ns})$.
- The RMS of the distribution of $\Delta R_i(dt_{\mathrm{bin}})$ is the statistically expected variation of R as a function of the bin width. We find a typical variation of 0.05 ppm. The naive error estimate $\sigma(\Delta R(dt_{\mathrm{bin}})) \stackrel{?}{\approx} \langle\sqrt{|\sigma^2(R(dt_{\mathrm{bin}})) - \sigma^2(R(150\,\mathrm{ns}))|}\rangle$ turns out to be off by a factor 2 - 3.

Now the real data are filled into histograms with different bin widths after randomisation over the cyclotron period of 149.2105 ns. To look for a possible resonance at 149.2105 ns we choose finer bin width steps around this value.

Then these histograms are fitted with our three fit functions. This is done with the start times 44.7 μs, 49.2 μs and 53.6 μs. The results are shown in Figures 92 to 94. In none of the cases there is any evidence for a resonance. As conservative estimates for the systematic error the greater of means or rms of the ΔR distributions for the start time 49.2 μs are chosen. Thus we find:

- 1999-style function: $\delta R = (0.05 \pm 0.05)$ ppm.
- physics function without phase modulation: $\delta R = (0.04 \pm 0.05)$ ppm.
- full physics function: $\delta R = (0.06 \pm 0.05)$ ppm.

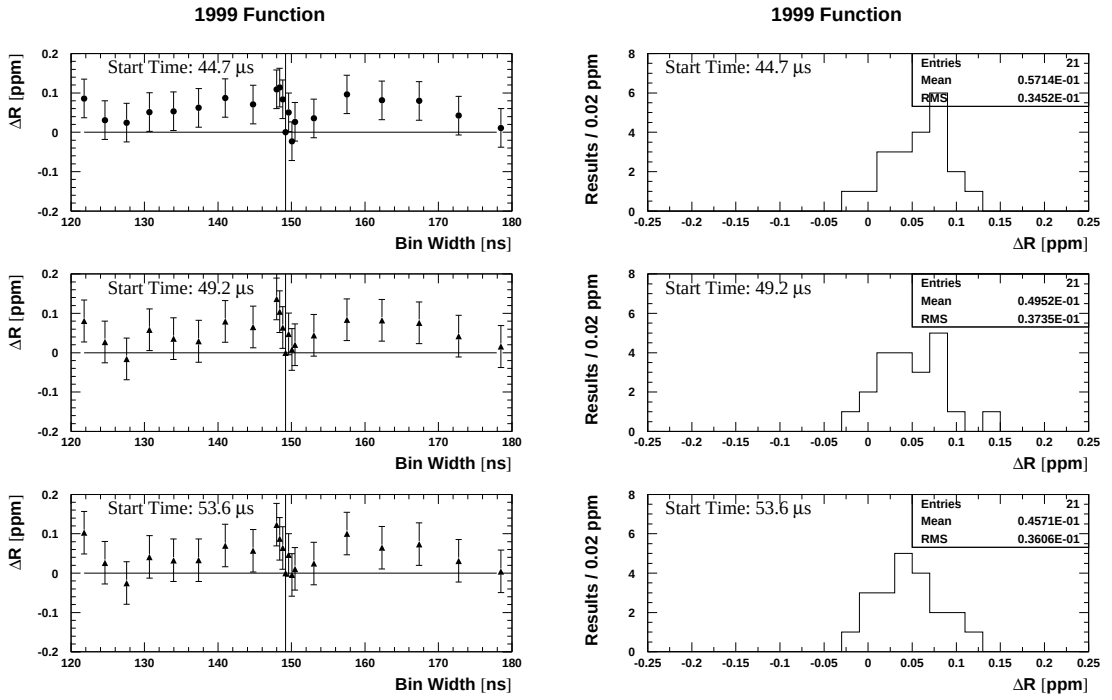

Figure 92: *Left side: Difference between the fit result $R(dt_{\text{bin}})$ for a bin width dt_{bin} and the standard result $R(149.2105\,\text{ns})$. The error bars were taken from a simulation explained in the text and shown in Figure 91. Right side: Projection of Figure 92 on the ΔR axis.*

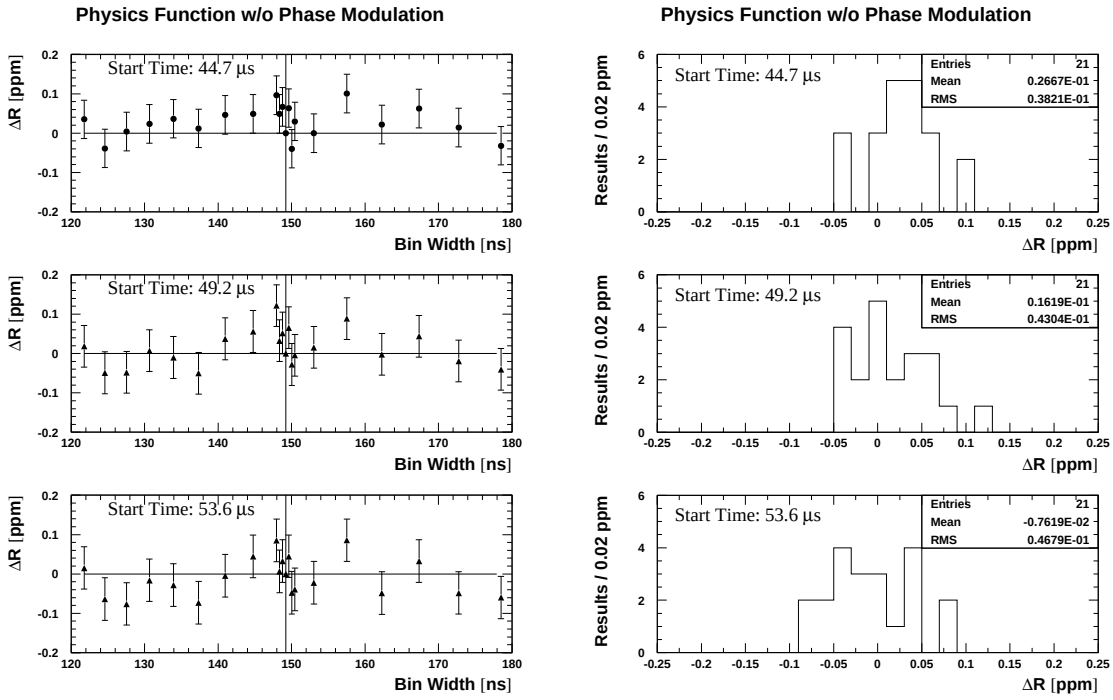

Figure 93: *Left side: Difference between the fit result $R(dt_{\text{bin}})$ for a bin width dt_{bin} and the standard result $R(149.2105\,\text{ns})$. The error bars were taken from the Figure 91. Right side: Projection of Figure 93 on the ΔR axis.*

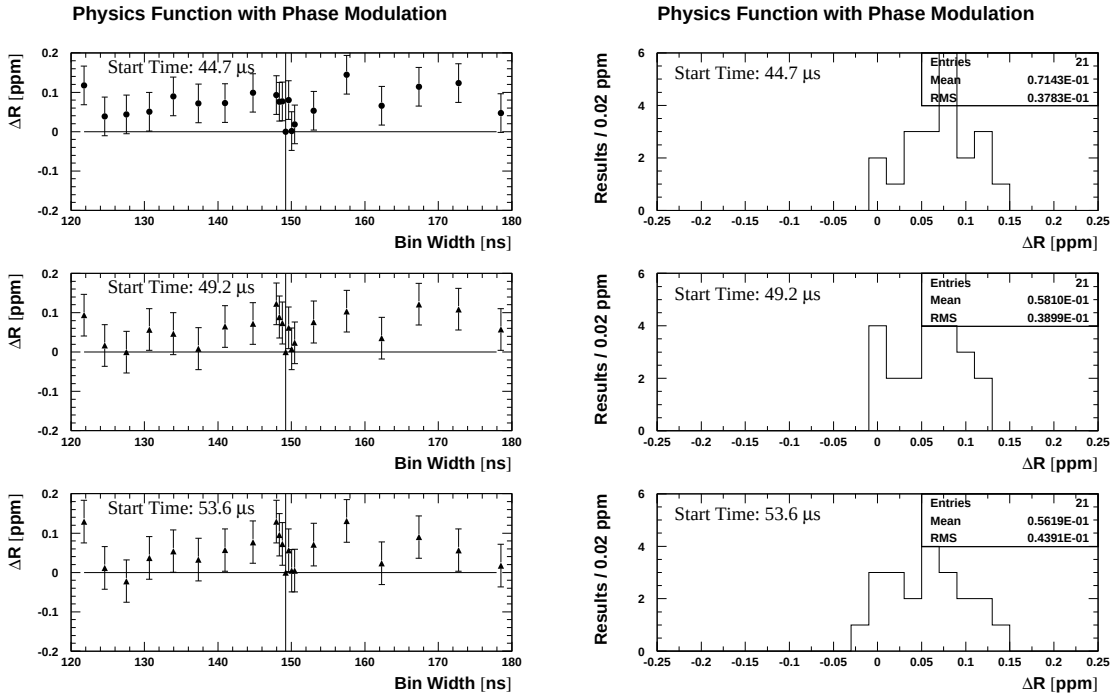

Figure 94: *Left side: Difference between the fit result $R(dt_{\mathrm{bin}})$ for a bin width dt_{bin} and the standard result $R(149.2105\,\mathrm{ns})$. The error bars were taken from the Figure 91. Right side: Projection of Figure 93 on the ΔR axis. The full physics function was used.*

6.10 Randomisation

The time spectra for the full run list (period 0) were randomised with 10 different random seeds but the same randomisation period given by the cyclotron period of 149.2105 ns. Then for each seed the sum of detector spectra was fitted. Figure 95 shows the distributions of R and χ^2. Their means and rms are listed in Table 48.

	1999 Function	Physics Func. without Phase Modulation	Physics Func. with Phase Modulation
$\langle R \rangle$ [ppm]	90.5785 ± 0.6092	90.7563 ± 0.6355	90.8409 ± 0.6730
$rms(R)$ [ppm]	0.0435	0.0691	0.0550
$\langle \chi^2 \rangle$	1.0178	1.0152	1.0136
$rms(\chi^2)$	0.0131	0.0126	0.0132

Table 48: *The effects of randomisation on R and χ^2.*

We also show a start time scan for R with the results of all random seeds combined (Figure 96). For the purpose of comparison we superimpose the scan for the particular seed for which all studies were done up to this point of the report.

The systematic error on the average of the 10 results is given by $\mathrm{rms}(R)/\sqrt{10-1}$.

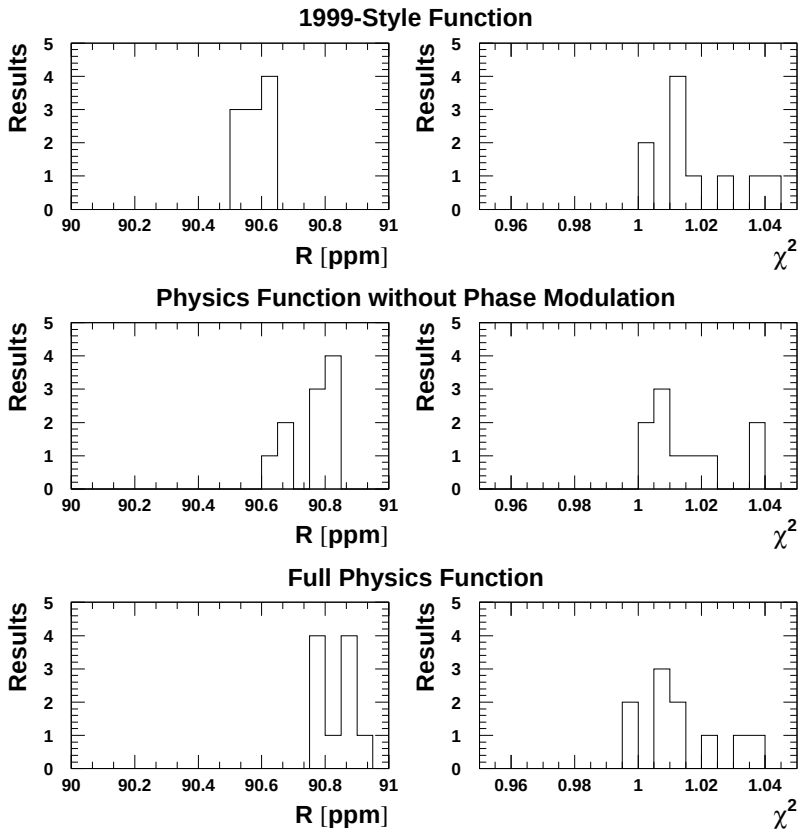

Figure 95: *Distributions of R and χ^2 for the 10 random seeds.*

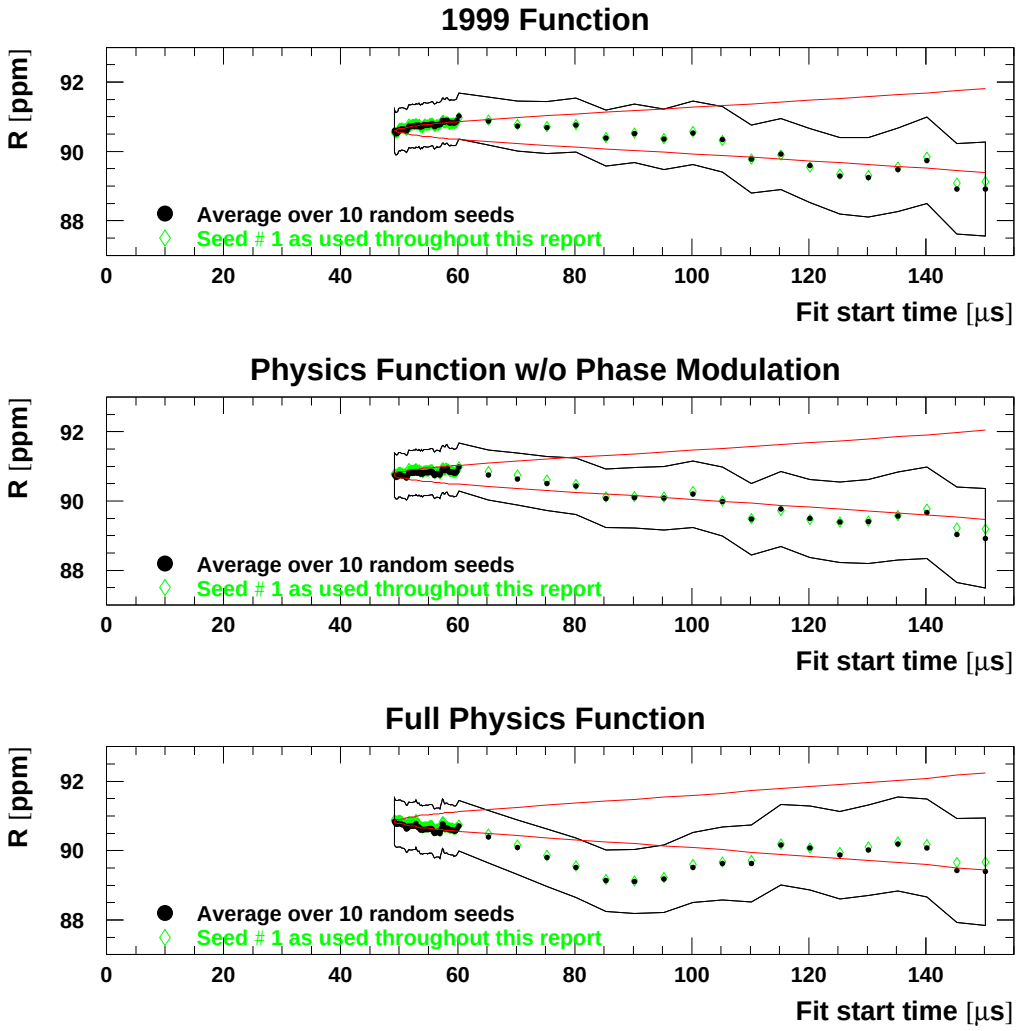

Figure 96: *Start time scans for R averaged over 10 random seeds. For comparison we also plot the result for the particular seed used in the rest of this document.*

6.11 Analysis Method

6.11.1 Run Period Consistency

Differences between fit results for Period 0 (all runs combined) and the weighted average of the individual periods' results are mainly due to the different CBO frequencies in the periods; it was the predominant reason for distinguishing them. These differences are not covered by any other systematic error discussed so far and will enter the final systematic error table as independent errors. In Table 49 we give this comparison for the sum and for the average of the detectors. As final result the maximum of the two values is chosen.

	1999 Function	Physics Func. without Phase Modulation	Physics Func. with Phase Modulation
R_{sum}	0.07 ± 0.03	0.04 ± 0.06	0.07 ± 0.11
$\langle R \rangle$	0.00 ± 0.04	0.04 ± 0.06	0.00 ± 0.11
pseudo-a_μ	0.07 ± 0.03	0.04 ± 0.06	0.05 ± 0.11

Table 49: *Difference [ppm] between the R-value obtained from fitting all runs together and the weighted average of the values from the individual run periods. This is done for fits to the sum of detectors (first row) and for the average over individual detector fits (second row). The third row shows the differences [ppm] between the pseudo-a_μ for Period 0 and the weighted average of the pseudo-a_μ values from the individual periods.*

6.11.2 Fit to the Sum of Spectra and to Individual Detector Spectra

The comparison of results for the sum of detector spectra and the average of individual detector results is only done as an additional consistency check. Differences are mainly caused by improper treatment of the halfring effect and are hence already included in the systematic error from the asymmetry and phase modulation. Therefore, the values listed in Table 50 don't enter the final error table.

	1999 Function	Physics Func. without Phase Modulation	Physics Func. with Phase Modulation
$\lvert R_{\text{sum}} - \langle R \rangle \rvert$	0.07 ± 0.05	0.00 ± 0.04	0.01 ± 0.04

Table 50: *Difference [ppm] between R from fits to the sum of detector spectra and the average over R from individual detector fits.*

7 Summary

The final systematic error balance is given in Table 51.

Effect	1999 Function	Physics Func. without Phase Modul.	Full Physics Function
Acceptance CBO	0.02 ppm	0.02 ppm	0.02 ppm
Acceptance DCBO	0.01 ppm	0.00 ppm	0.00 ppm
Asymmetry and phase CBO (halfring effect)	0.39 ppm	0.28 ppm	0.11 ppm
Vertical oscillation and waist	0.01 ppm	0.01 ppm	0.01 ppm
Run period consistency (mixture of n-values)	0.07 ppm	0.04 ppm	0.07 ppm
Residual pileup	0.08 ppm	0.02 ppm	0.17 ppm
Unseen pileup	0.10 ppm	0.10 ppm	0.10 ppm
Detector gain variations	0.04 ppm	0.17 ppm	0.35 ppm
Muon losses, other slow effects	0.01 ppm	0.00 ppm	0.01 ppm
Binning	0.05 ppm	0.04 ppm	0.06 ppm
Randomisation	0.01 ppm	0.02 ppm	0.02 ppm
AGS Background (*)	0.01 ppm	0.01 ppm	0.01 ppm
Quadratic sum	0.42 ppm	0.35 ppm	0.43 ppm
Linear sum	0.80 ppm	0.71 ppm	0.93 ppm

(*) borrowed from Fred Gray [24].

Table 51: *Systematic errors for a fit start time of 49.2 μs.*

Should the errors in Table 51 be added linearly on in quadrature?
The main correlations are between residual pileup, unseen pileup and gain variations. In the discussion of the systematic error from gain variations we have seen that the latter contains contributions from high-energy pileup. If one tried to take take this correlation into consideration it would reduce rather than increase the total error w.r.t. the quadratic sum. A limit on the error from unseen pileup was determined from the same observable – the asymmetry instability – that also served for one of the estimates for the gain systematics. It is certain that some multiple-counting of the truly underlying physical effect is done here.

The determination of the error from the halfring effect was based on an independent measurement of the cancellation factor and hence does not suffer from correlations with gain.

We conclude that a linear addition would not be justified and that addition in quadrature is already conservative and hence safe.

Final result with quadratic sum of systematic errors:

- 1999-style function: $R = (90.58 \pm \underbrace{0.61 \pm 0.42}_{0.74\,\text{ppm}})\,\text{ppm}$

  with the official offset: $R = 128.39\,\text{ppm}$

- Physics function without phase modulation: $R = (90.76 \pm \underbrace{0.64 \pm 0.35}_{0.73\,\text{ppm}})\,\text{ppm}$

  with the official offset: $R = 128.57\,\text{ppm}$

- Full physics function: $R = (90.84 \pm \underbrace{0.67 \pm 0.40}_{0.78\,\text{ppm}})\,\text{ppm}$

  with the official offset: $R = 128.65\,\text{ppm}$

The preferred result is the one from the physics function without phase modulation. It has the smallest total error.

References

[1] I. Logashenko: FIT Pulse Finding Algorithm, g-2 Note 334, rev. March 1999; Shapes of WFD Pulses and the FIT Pulse Finding Algorithm, g-2 Note 369, September 2000.

[2] E. Sichtermann: Run selection for 2000, presented at offline meetings and available on `http://g2muon:precess@g2pc1.bu.edu/secure/jim/` .

[3] C. Özben: G2off Based ω_a Analysis of g-2, Section 3, analysis report, June 2002.

[4] C. Özben and Y.K. Semertzidis: Eliminating Pileup from the g-2 Data, g-2 Note 365, July 2000.

[5] I. Logashenko: energy dependence of f_L and the g2off dead-time, private communication.

[6] C. Özben, Y.K. Semertzidis: Pileup and Energy Threshold, g-2 Note 397, June 2001.

[7] F. Farley et al.: Estimation of Error in Differential Pileup Subtracted Data, g-2 Note 377, December 2000.

[8] R. Carey: full simulation of CBO effects, presentation at an analysis workshop, spring 2002.

[9] C. Polly: FSD beam centroid, plot in the g-2 logbook, 2000.

[10] O. Rind: CBO frequency with and without scraping from the fiber harps, plot in the g-2 logbook, 2000.

[11] C. Polly: Muon losses for the different run periods, presentation at an analysis workshop, spring 2002.

[12] C. Özben: 1999 ω_a Analysis of g-2, g-2 Note 385, January 2001.

[13] G.D. Lafferty, T.R. Wyatt: Where to Stick Your Data Points: The Treatment of Measurements Within Wide Bins, CERN-PPE/94-72, 1994.

[14] H. Deng: Magnetic field versus run, private communication; see also: H. Deng et al.: Analysis of the Magnetic Field for 2000, draft of a g-2 note, July 2002.

[15] Y.K. Semertzidis: The effect of missing detectors 2, 20; presentation in the BNL-based offline meeting on April 17, 2002.

[16] Y.K. Semertzidis: Shift in R due to pileup phase a.k.a. the "Underwater" effect, draft of a g-2 note, July 2002.

[17] W. Morse: relationship between gain and asymmetry; private communication.

[18] W. Morse: The Low Pulse Height Pile-Down Effect, g-2 Note 373, October 2000.

[19] Y.K. Semertzidis: The Spectrum of χ and Systematic Errors Due to Backgrounds in the 2000 Run Data, g-2 Note 406, January 2002. See remark 3 in Section 4.

[20] A. Steinmetz: The 98 Systematic Error on the g-2 Frequency, g-2 Note 351, November 1999.

[21] "Romantic studies": introduced by C. Özben.

[22] Y.K. Semertzidis: On the Question of the Functional Form of the 2000 Run Data, g-2 Note 403, December 2001.

[23] H. Deng: The Average Energy Change with CBO Frequency, draft of a g-2 note, July 2002.

[24] F. Gray: Energy-binned analysis of the 2000 ω_a data, analysis report, July 2002.

A Fit Results for the 1999-Style Function

A.1 Start Time Scans for the Sum of Detectors

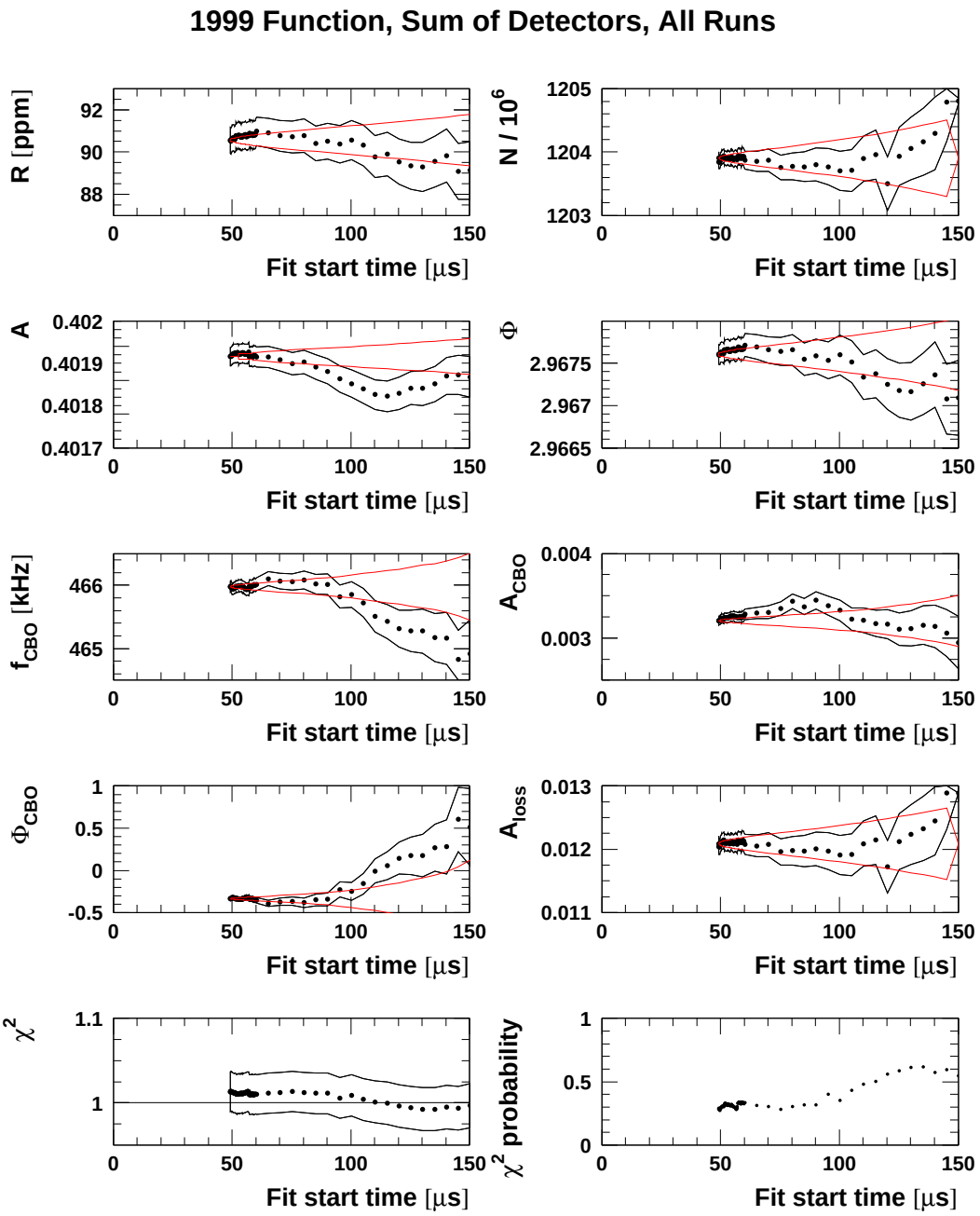

Figure 97: *Start time scan with the 1999-style function for all 2000 data. The muon life time was fixed to 64.407 μs.*

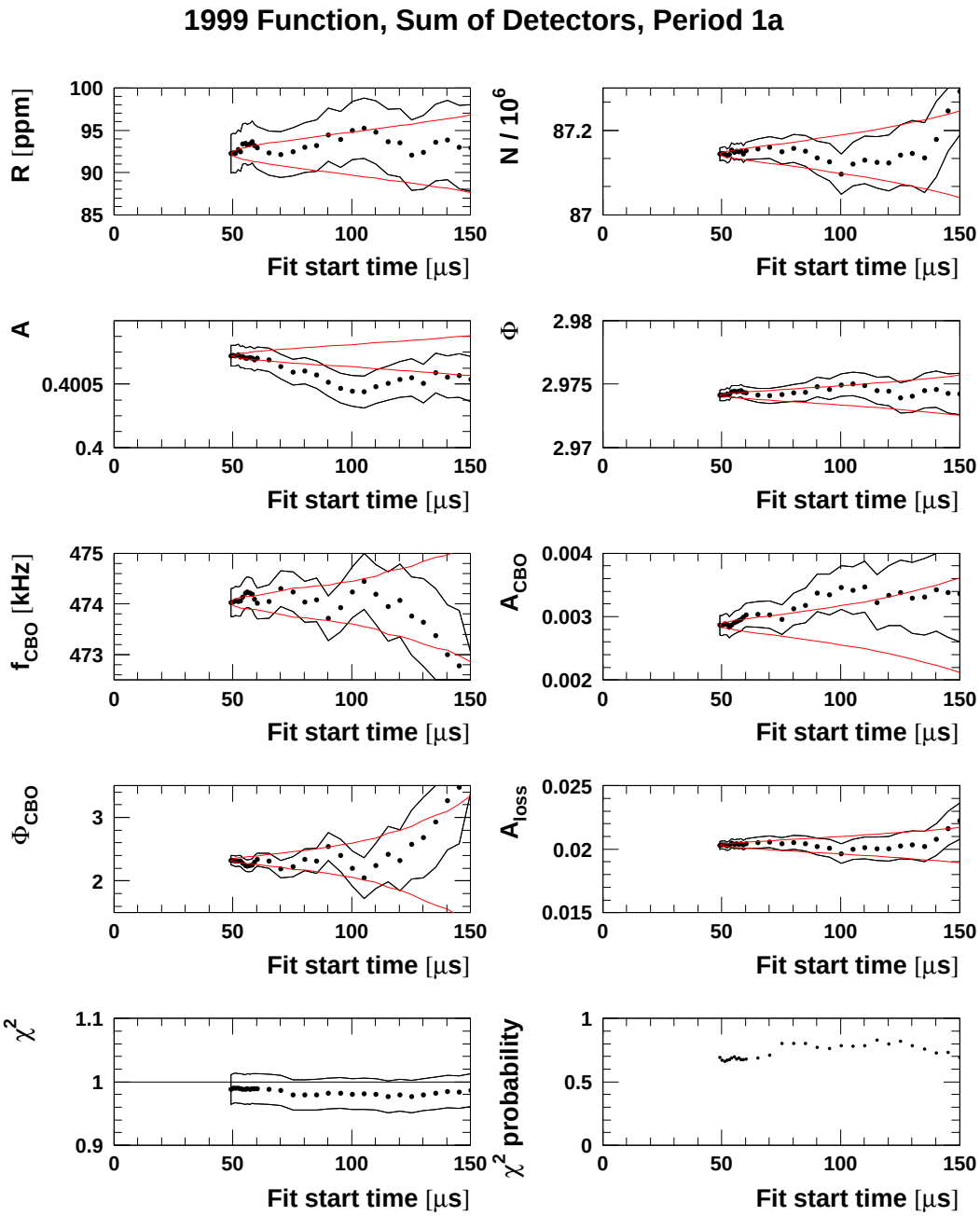

Figure 98: *Start time scan with the 1999-style function for period 1a. The muon life time was fixed to 64.407 μs.*

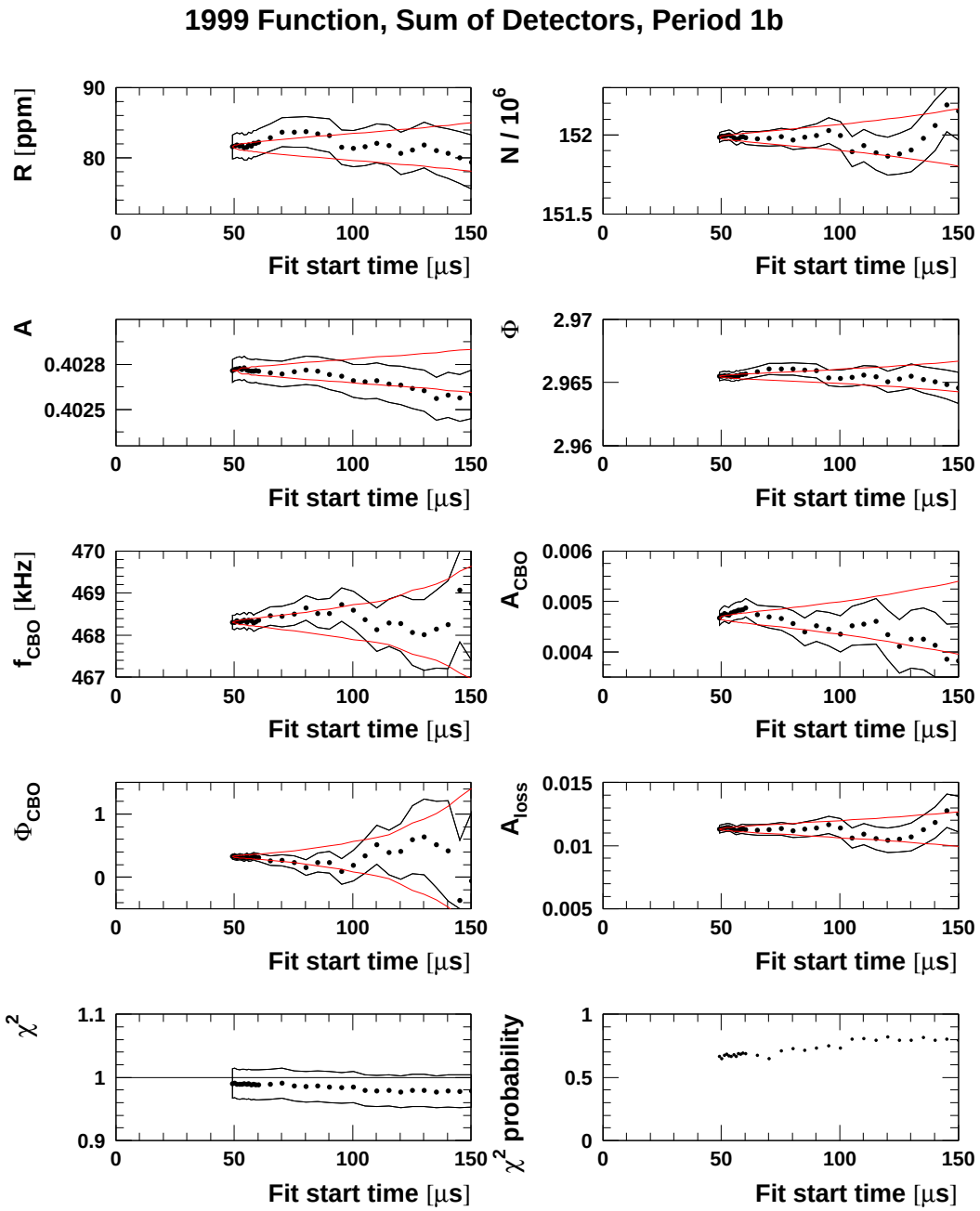

Figure 99: *Start time scan with the 1999-style function for period 1b. The muon life time was fixed to 64.407 μs.*

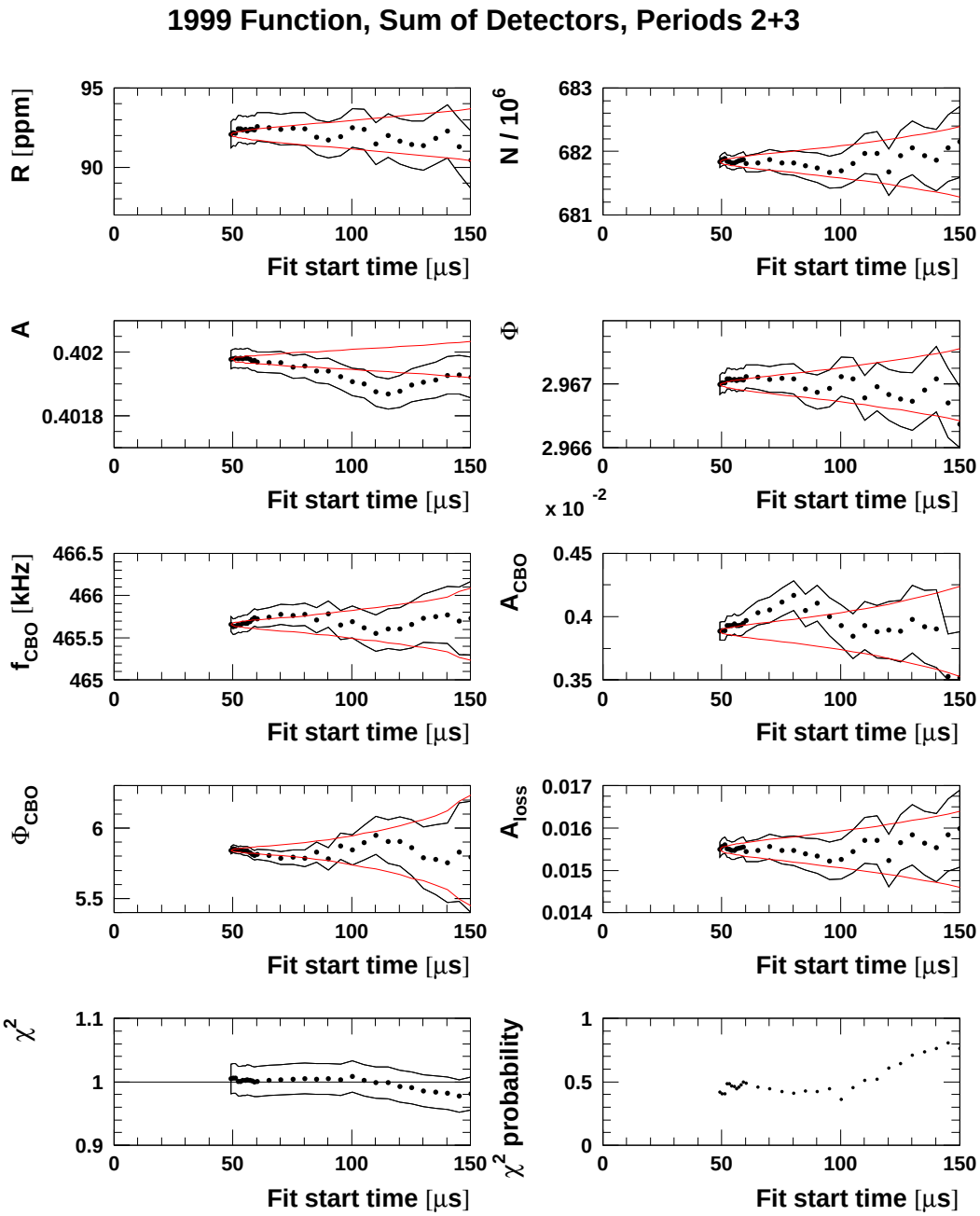

Figure 100: *Start time scan with the 1999-style function for periods 2+3. The muon life time was fixed to 64.407 μs.*

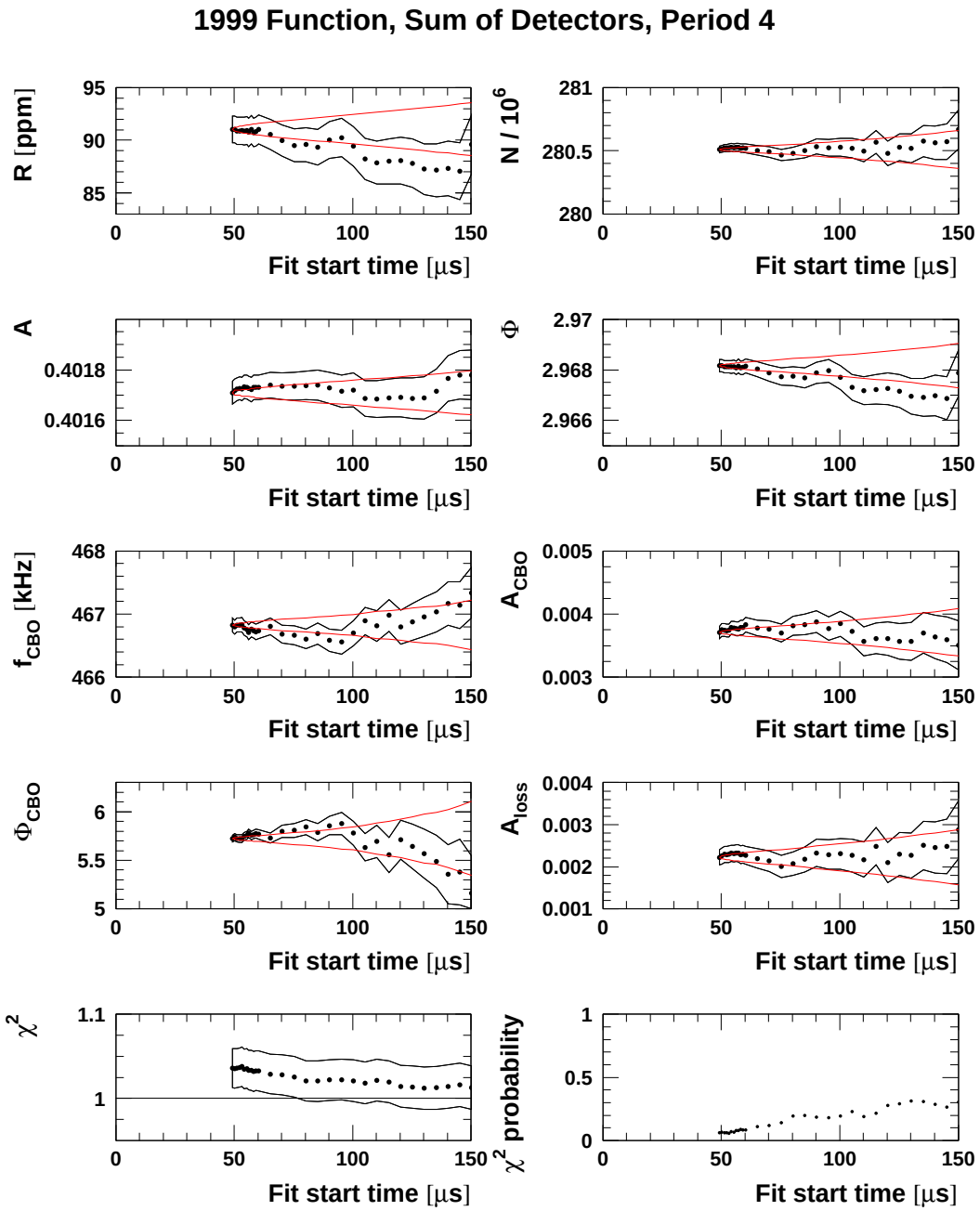

Figure 101: *Start time scan with the 1999-style function for period 4. The muon life time was fixed to 64.407 μs.*

A.2 Start Time Scans for the Two Half Rings

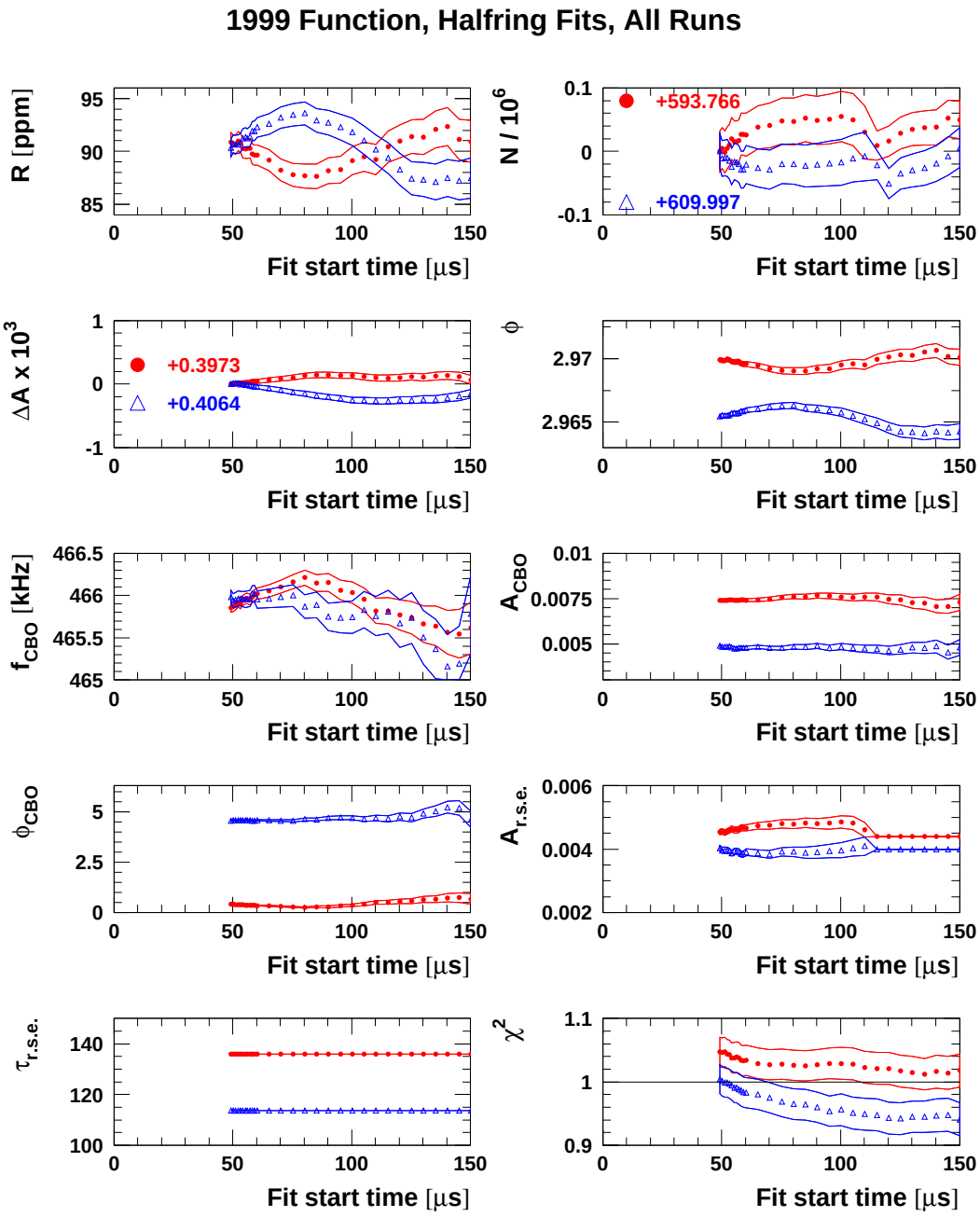

Figure 102: *Start time scan for the two half rings separately (red circles = det. 1-12, blue triangles = det. 13-24) with the 1999-style function for all runs.*

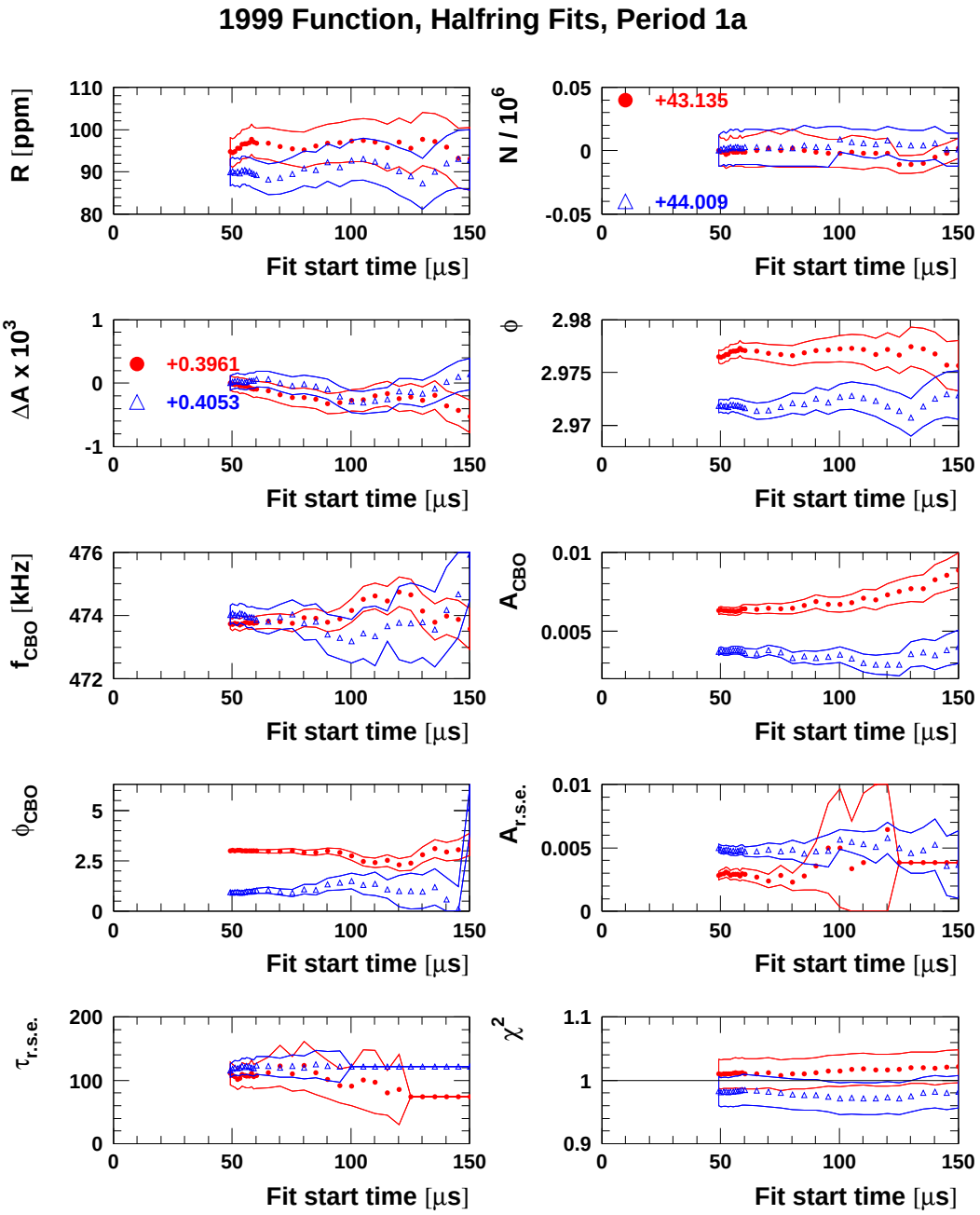

Figure 103: *Start time scan for the two half rings separately (red circles = det. 1-12, blue triangles = det. 13-24) with the 1999-style function for period 1a.*

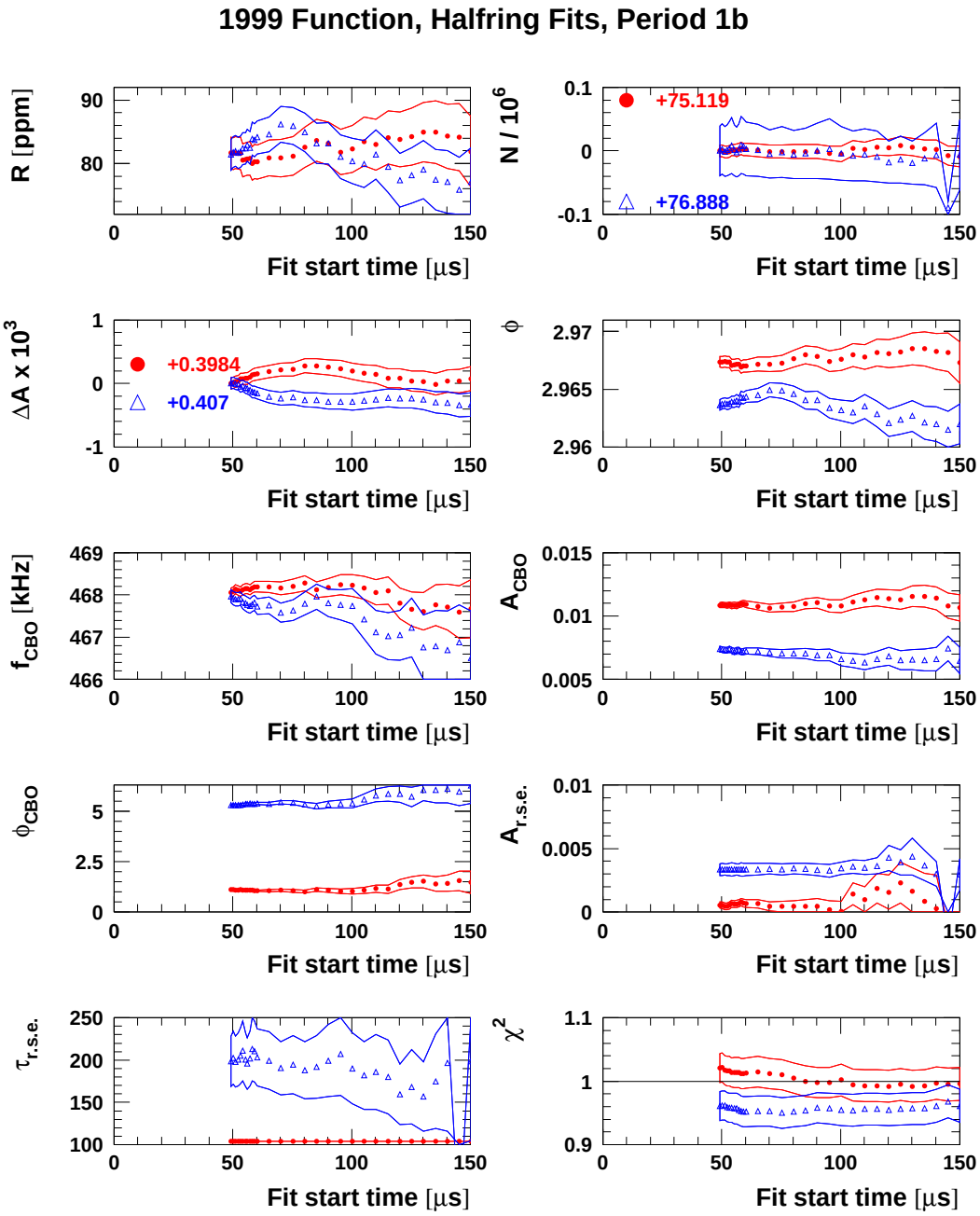

Figure 104: *Start time scan for the two half rings separately (red circles = det. 1-12, blue triangles = det. 13-24) with the 1999-style function for period 1b.*

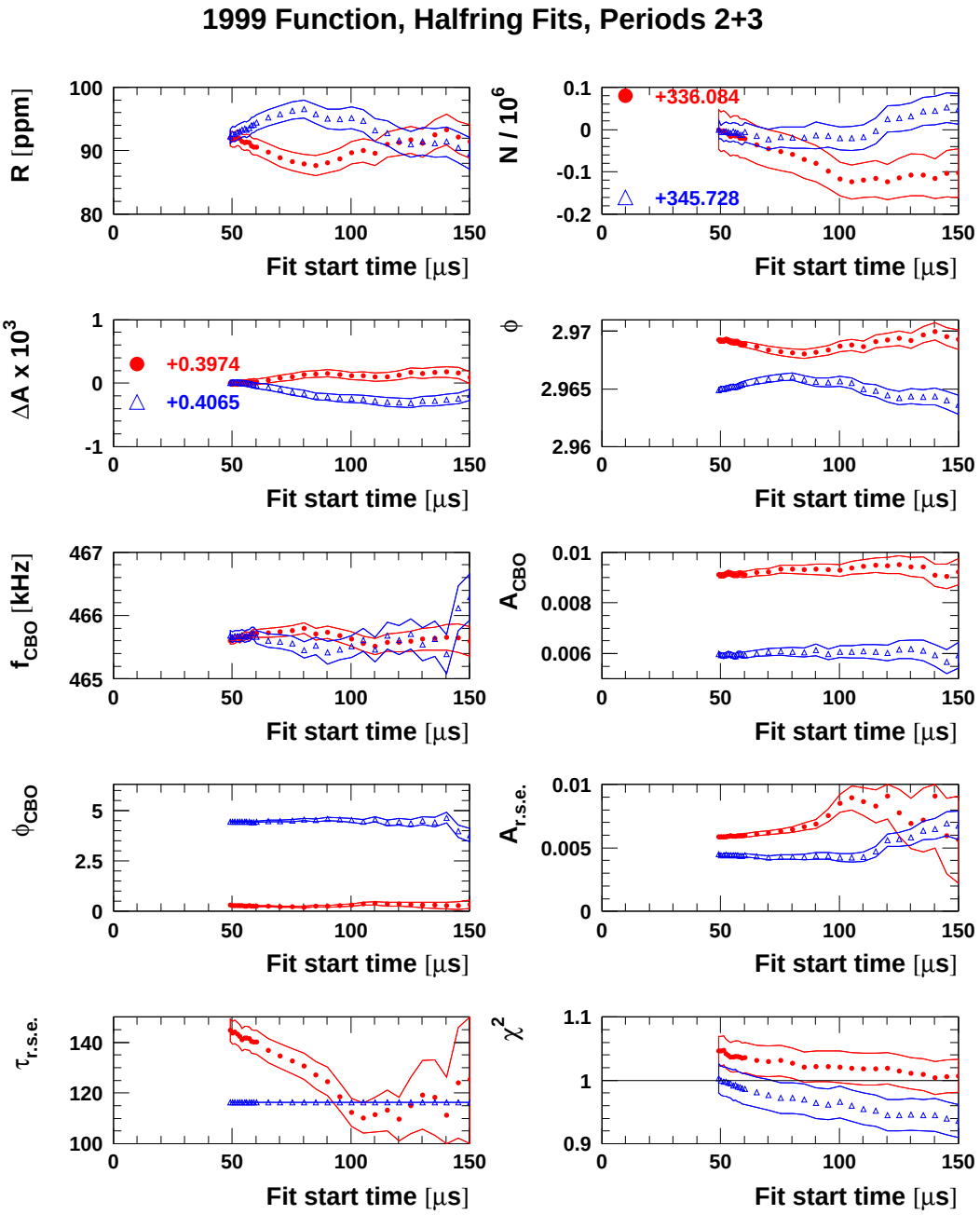

Figure 105: *Start time scan for the two half rings separately (red circles = det. 1-12, blue triangles = det. 13-24) with the 1999-style function for period 23.*

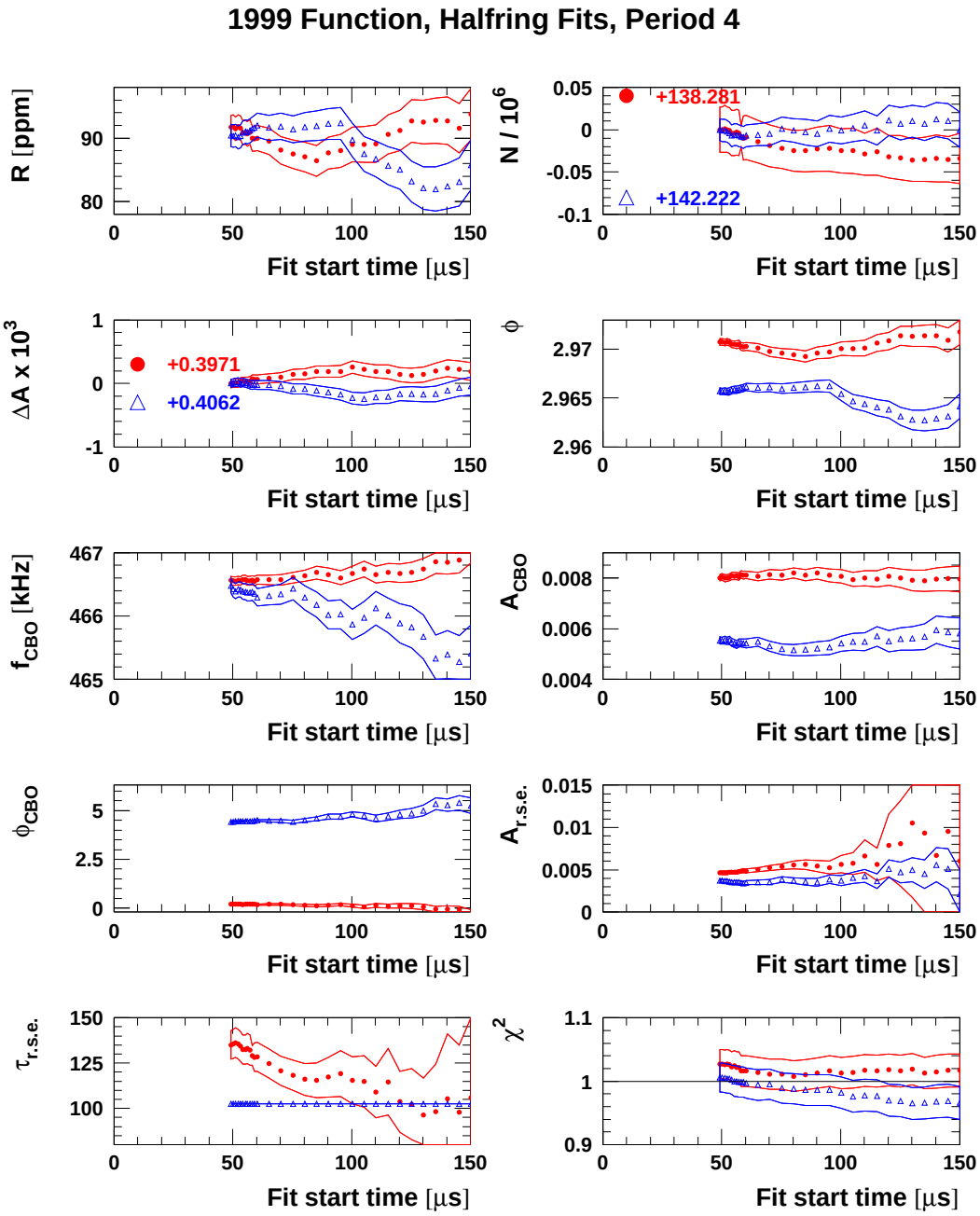

Figure 106: *Start time scan for the two half rings separately (red circles = det. 1-12, blue triangles = det. 13-24) with the 1999-style function for period 4.*

A.3 Individual Detector Fits Starting at 49.2 μs

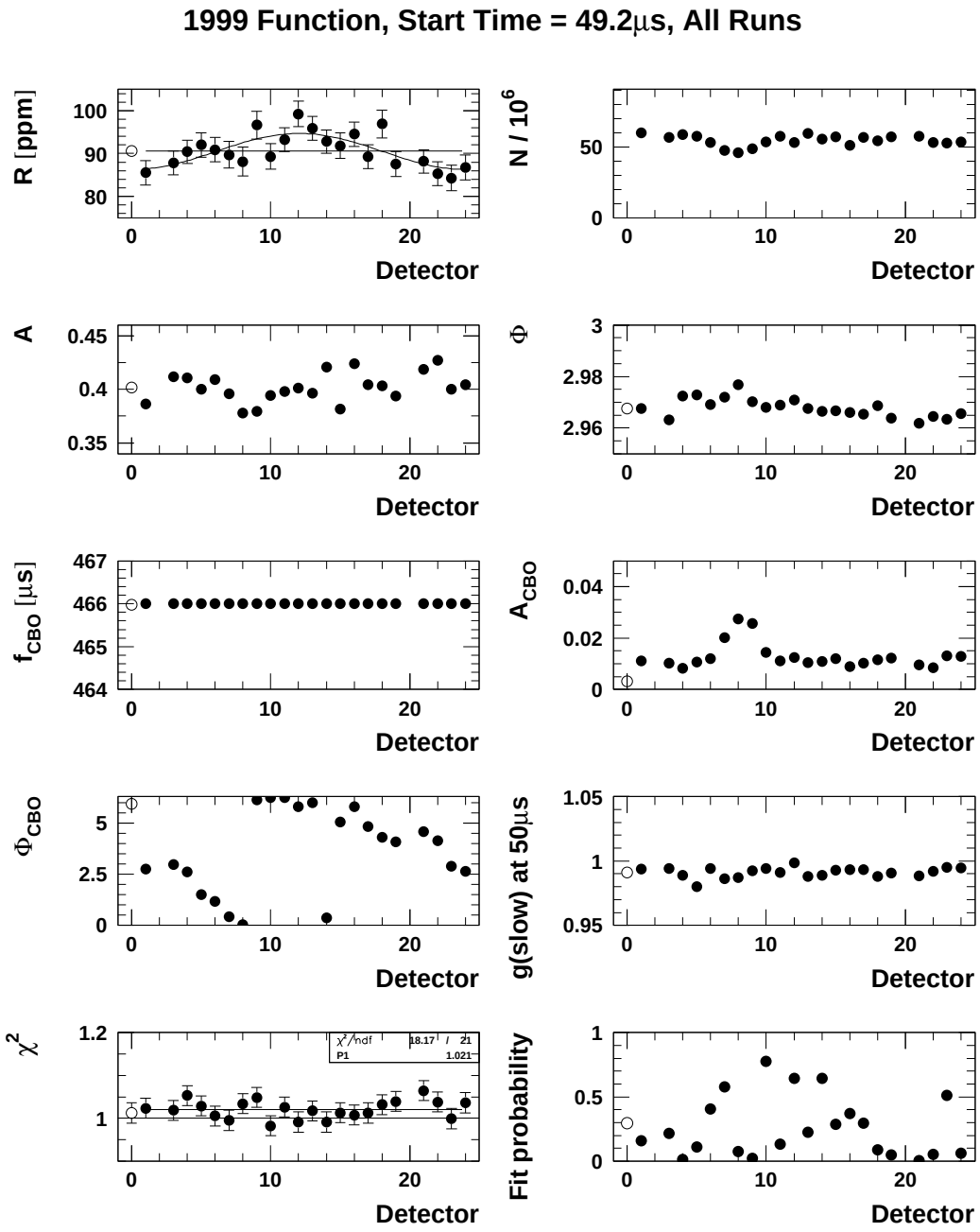

Figure 107: *Fits of individual detector spectra with the 1999-style function for all 2000 data. The muon life time was fixed to 64.407 μs. The open marker at detector 0 represents the fit to the sum.*

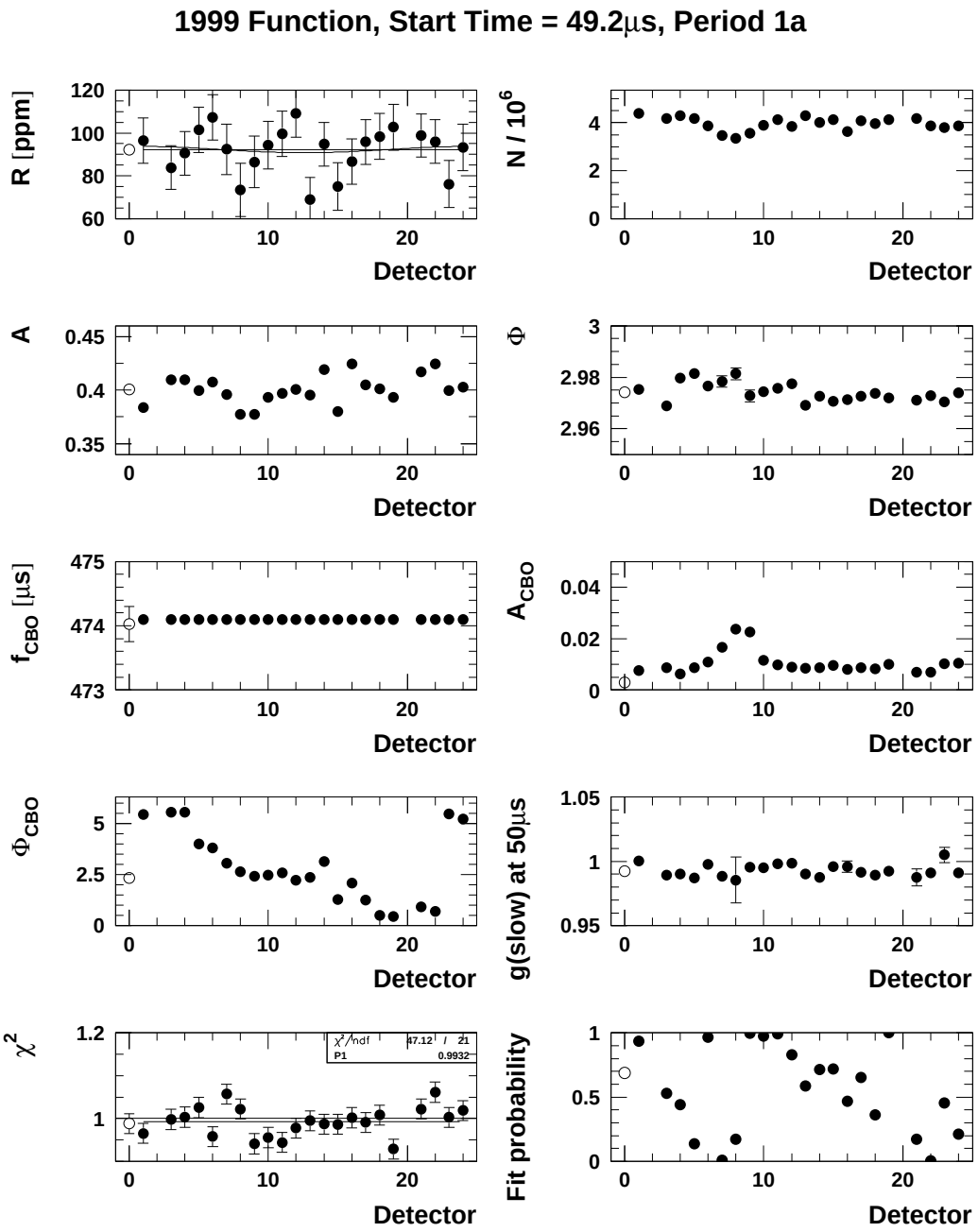

Figure 108: *Fits of individual detector spectra with the 1999-style function for period 1a. The muon life time was fixed to 64.407 μs. The open marker at detector 0 represents the fit to the sum.*

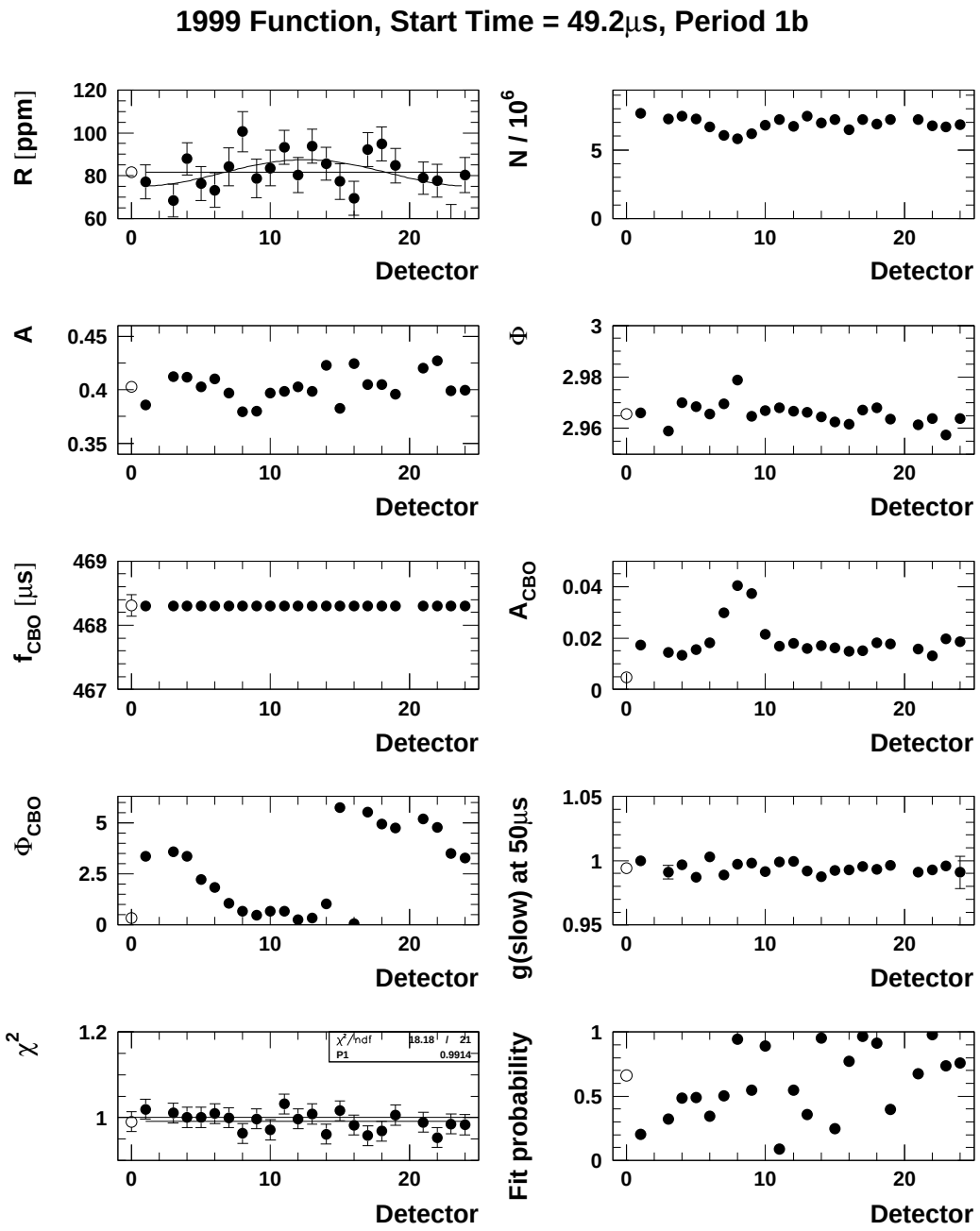

Figure 109: *Fits of individual detector spectra with the 1999-style function for period 1b. The muon life time was fixed to 64.407 μs. The open marker at detector 0 represents the fit to the sum.*

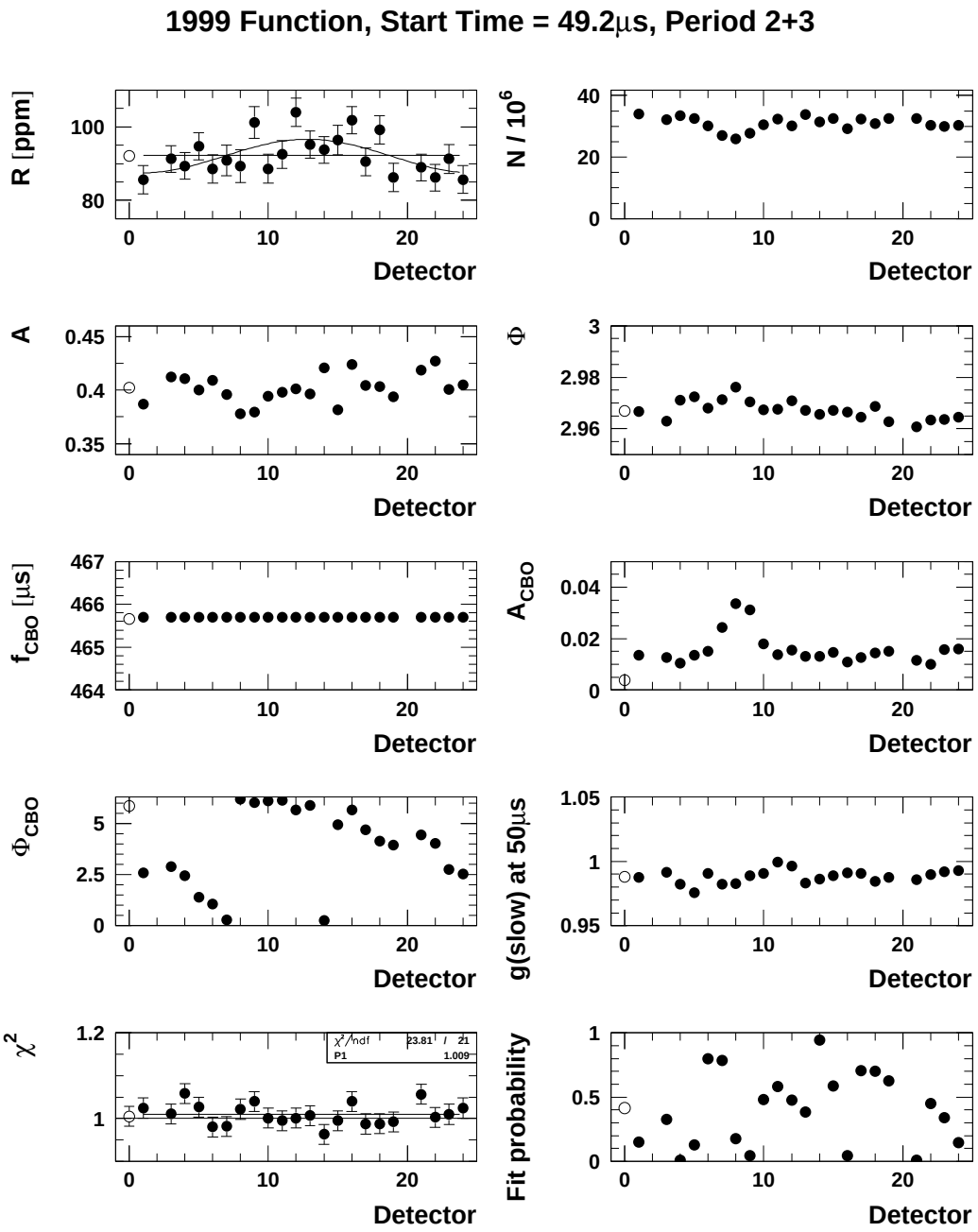

Figure 110: *Fits of individual detector spectra with the 1999-style function for periods 2+3. The muon life time was fixed to 64.407 μs. The open marker at detector 0 represents the fit to the sum.*

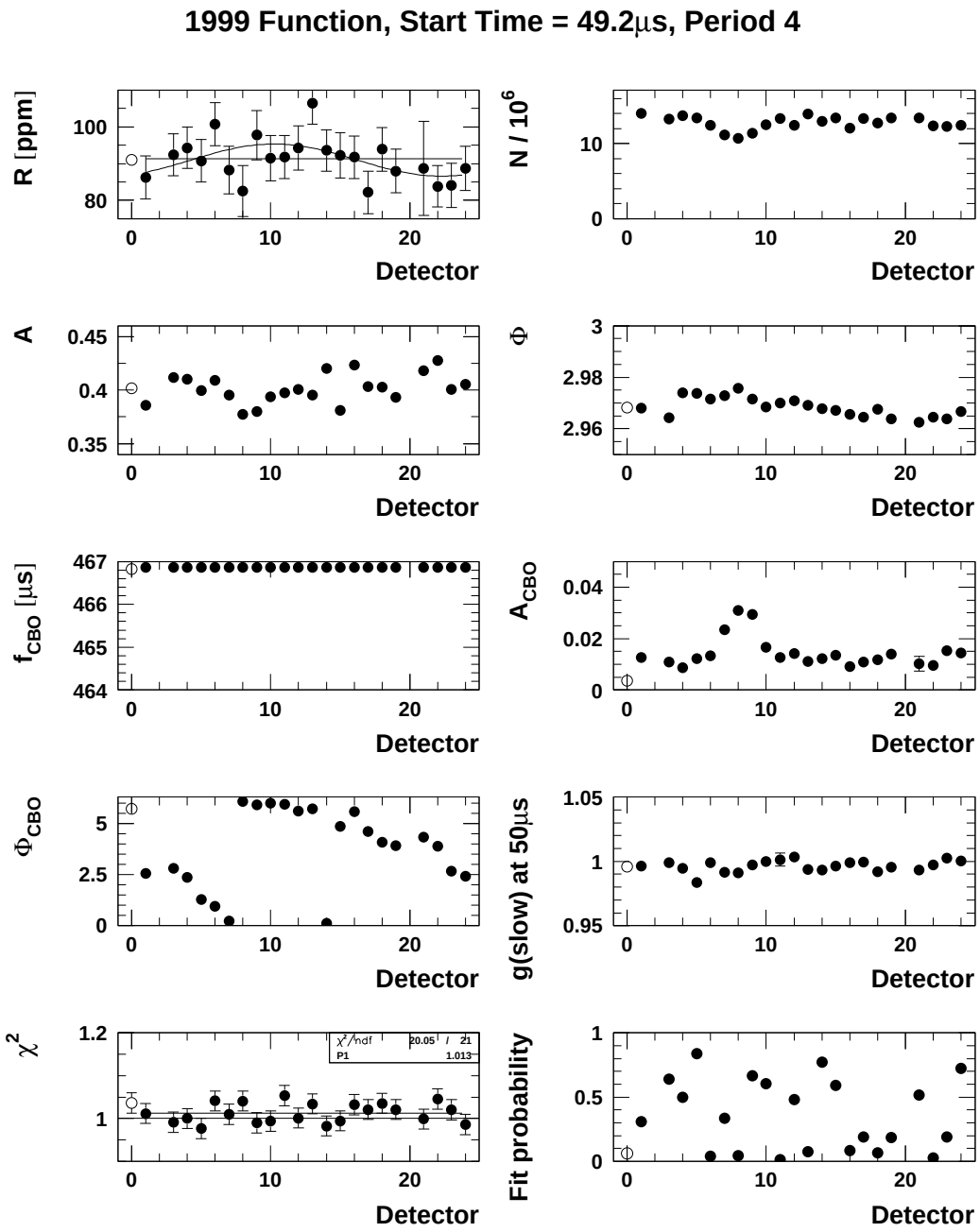

Figure 111: *Fits of individual detector spectra with the 1999-style function for period 4. The muon life time was fixed to 64.407 μs. The open marker at detector 0 represents the fit to the sum.*

B Fit Results for the Physics Function without Phase Modulation

B.1 Start Time Scans for the Sum of Detectors

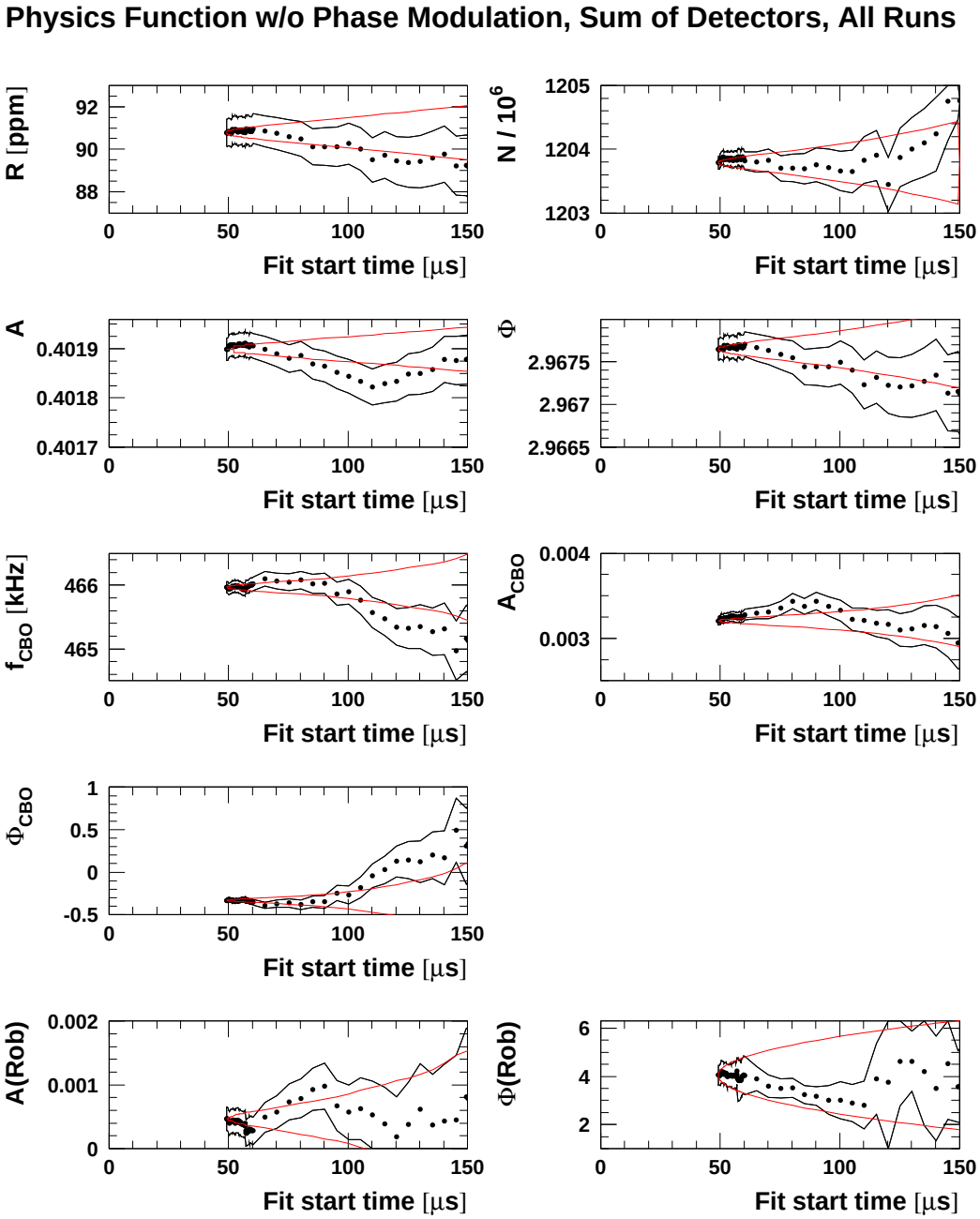

Figure 112: *Start time scan with the physics function for all runs. The g-2 phase modulation (Jim effect) was switched off. The muon life time was fixed to 64.407 μs.*

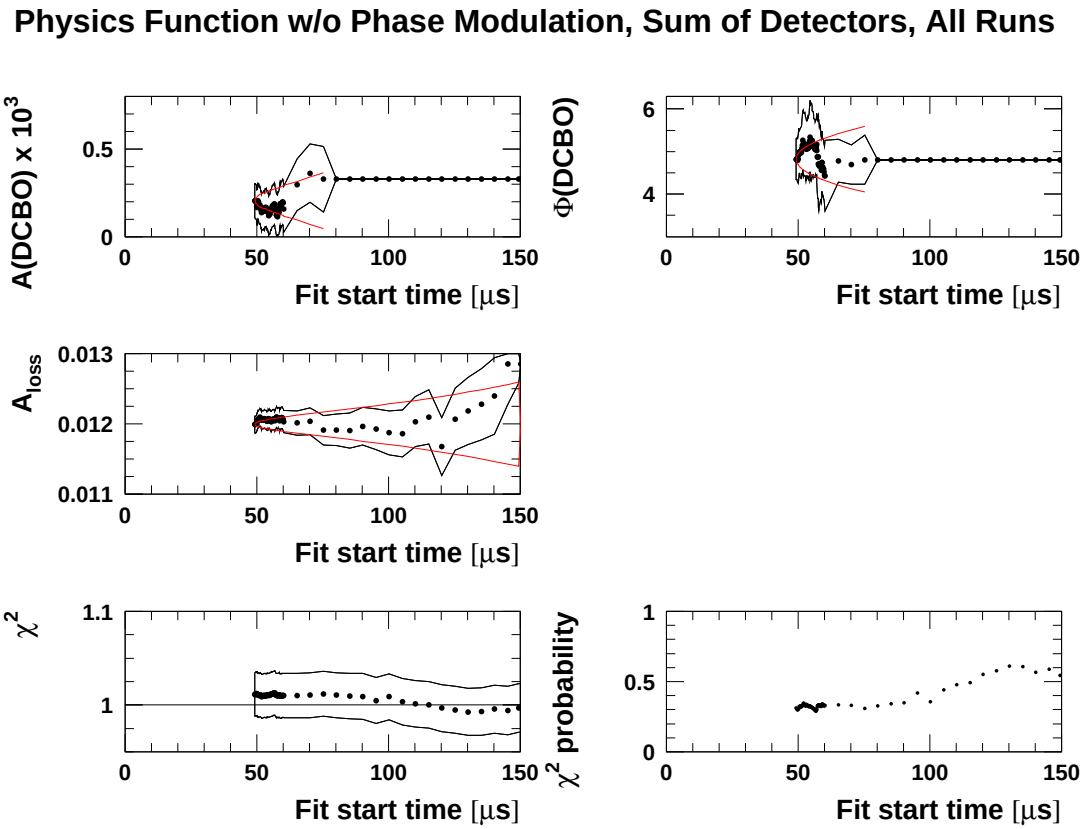
Physics Function w/o Phase Modulation, Sum of Detectors, All Runs
A(DCBO) x 10^3
0.5
0
0
50
100
150
Fit start time [μs]
Φ(DCBO)
6
4
0
50
100
150
Fit start time [μs]
A_loss
0.013
0.012
0.011
0
50
100
150
Fit start time [μs]
χ^2
1.1
1
0
50
100
150
Fit start time [μs]
χ^2 probability
1
0.5
0
0
50
100
150
Fit start time [μs]

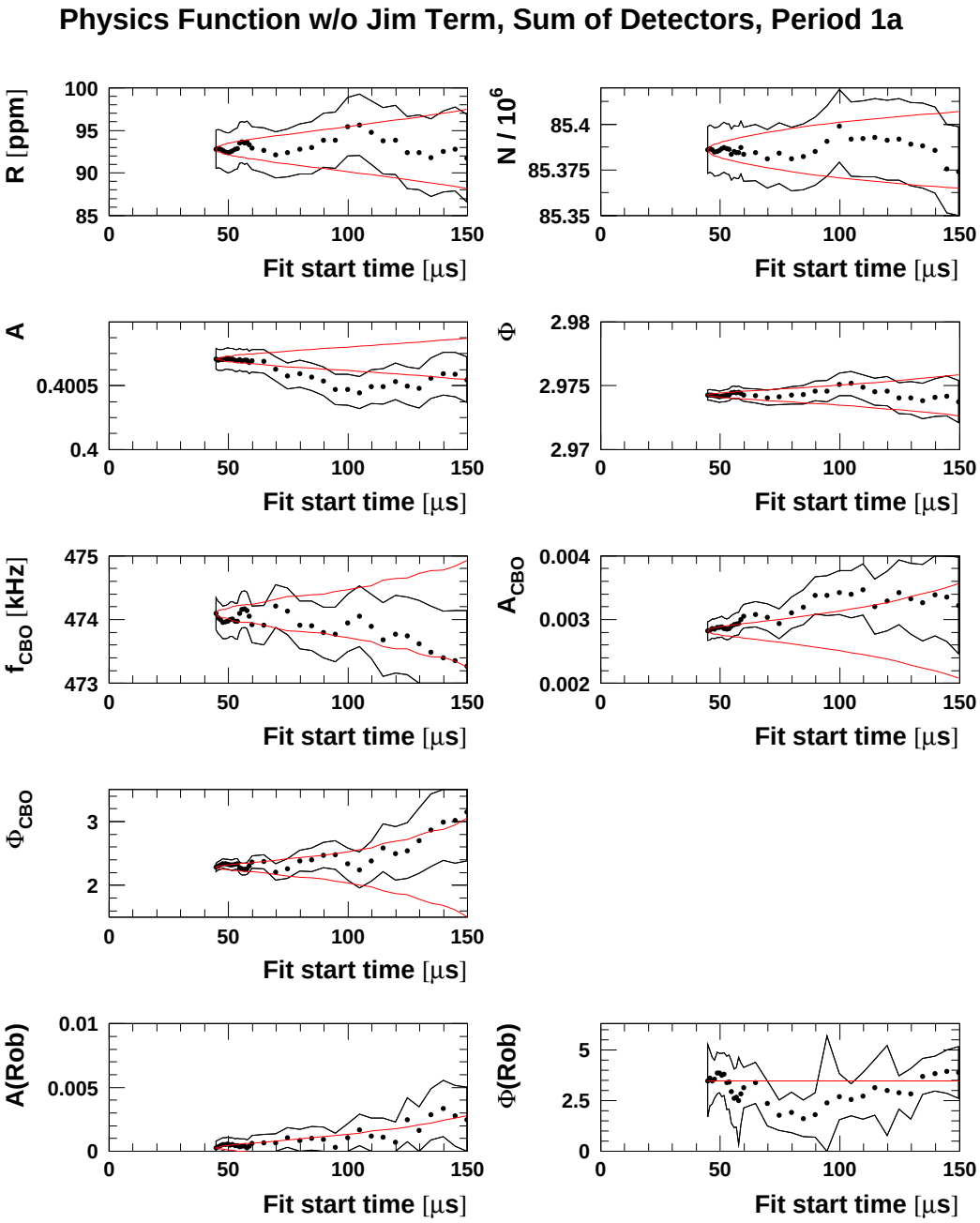

Figure 113: *Start time scan with the physics function for period 1a. The g-2 phase modulation (Jim effect) was switched off.*

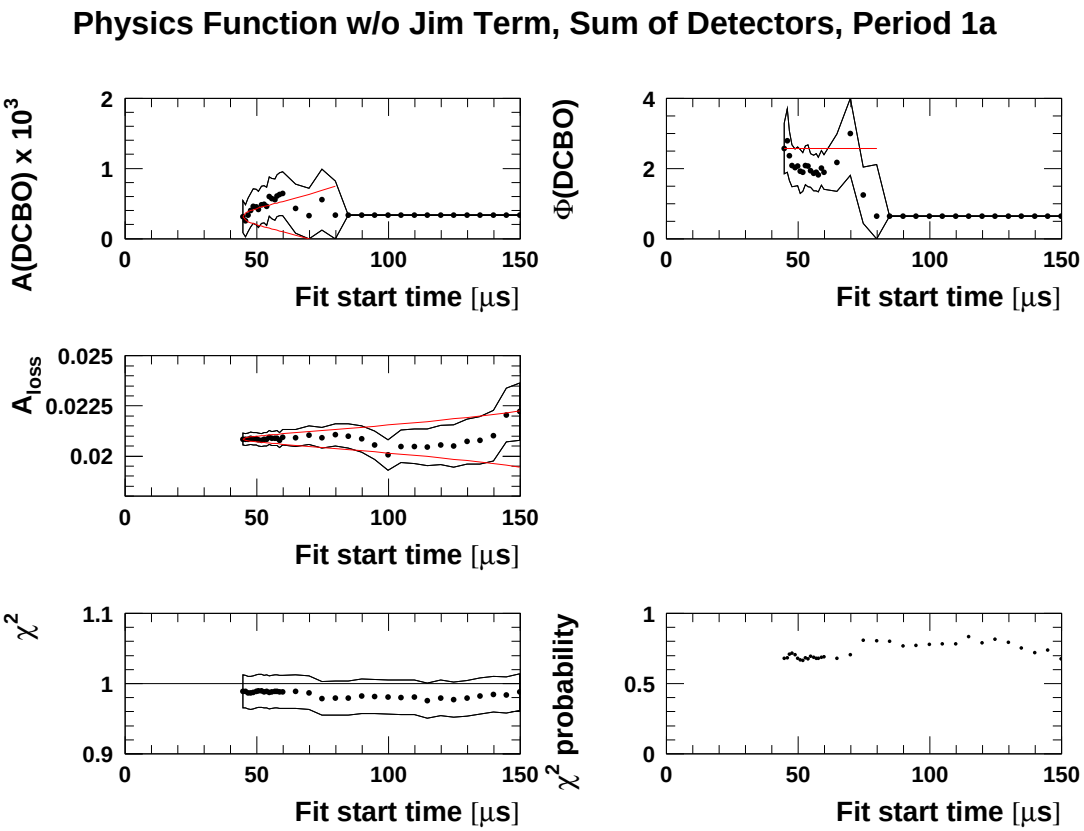
Physics Function w/o Jim Term, Sum of Detectors, Period 1a
A(DCBO) x 10^3
Φ(DCBO)
A_loss
χ^2
χ^2 probability
Fit start time [μs]

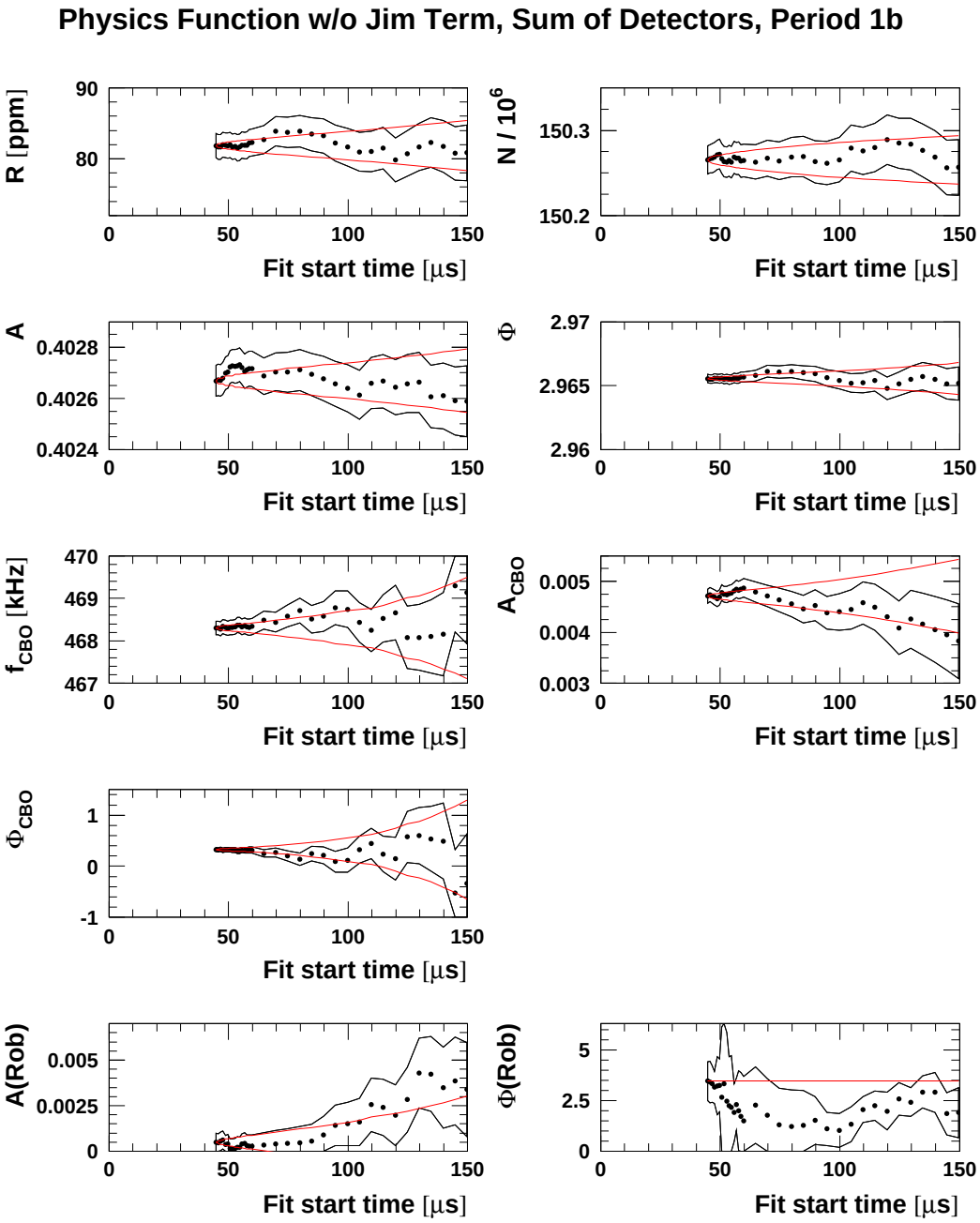

Figure 114: *Start time scan with the physics function for period 1b. The g-2 phase modulation (Jim effect) was switched off.*

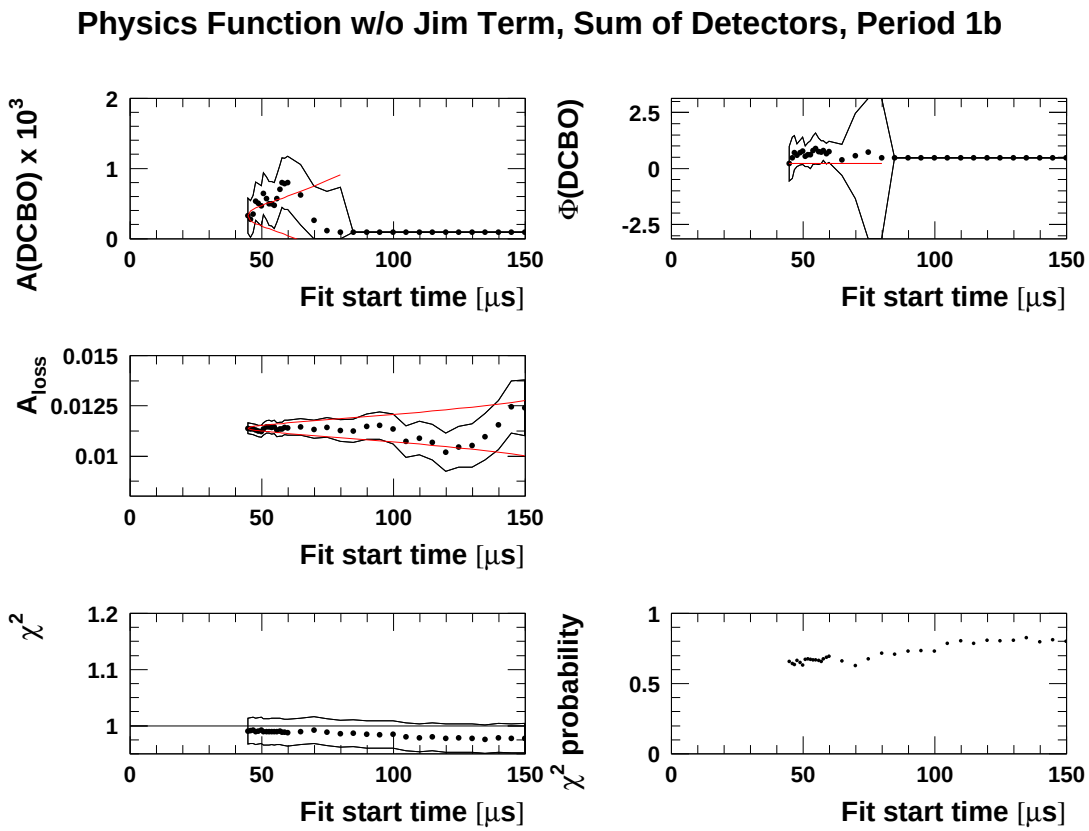
Physics Function w/o Jim Term, Sum of Detectors, Period 1b
A(DCBO) x 10^3
Φ(DCBO)
A_loss
χ^2
χ^2 probability
Fit start time [μs]

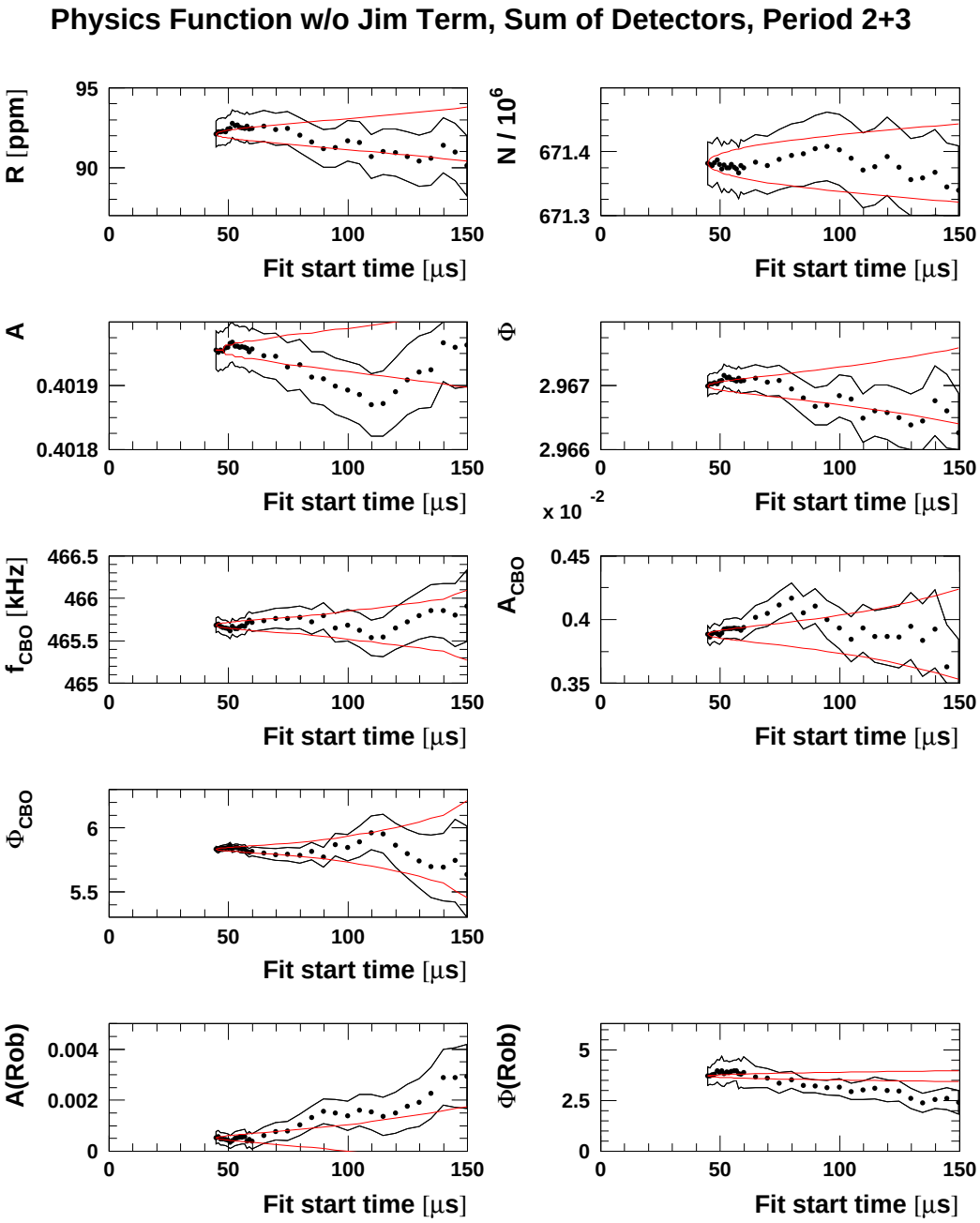

Figure 115: *Start time scan with the physics function for periods 2+3. The g-2 phase modulation (Jim effect) was switched off.*

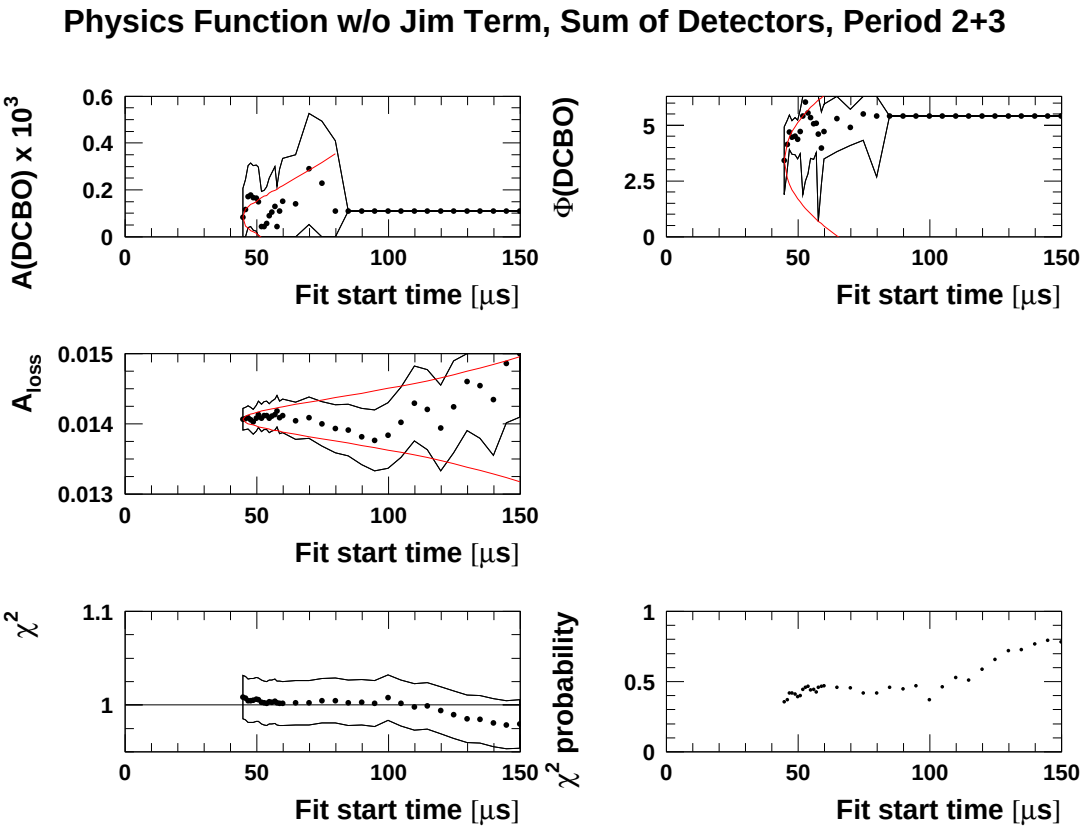
Physics Function w/o Jim Term, Sum of Detectors, Period 2+3
A(DCBO) x 10^3
Φ(DCBO)
A_loss
χ^2
χ^2 probability
Fit start time [μs]

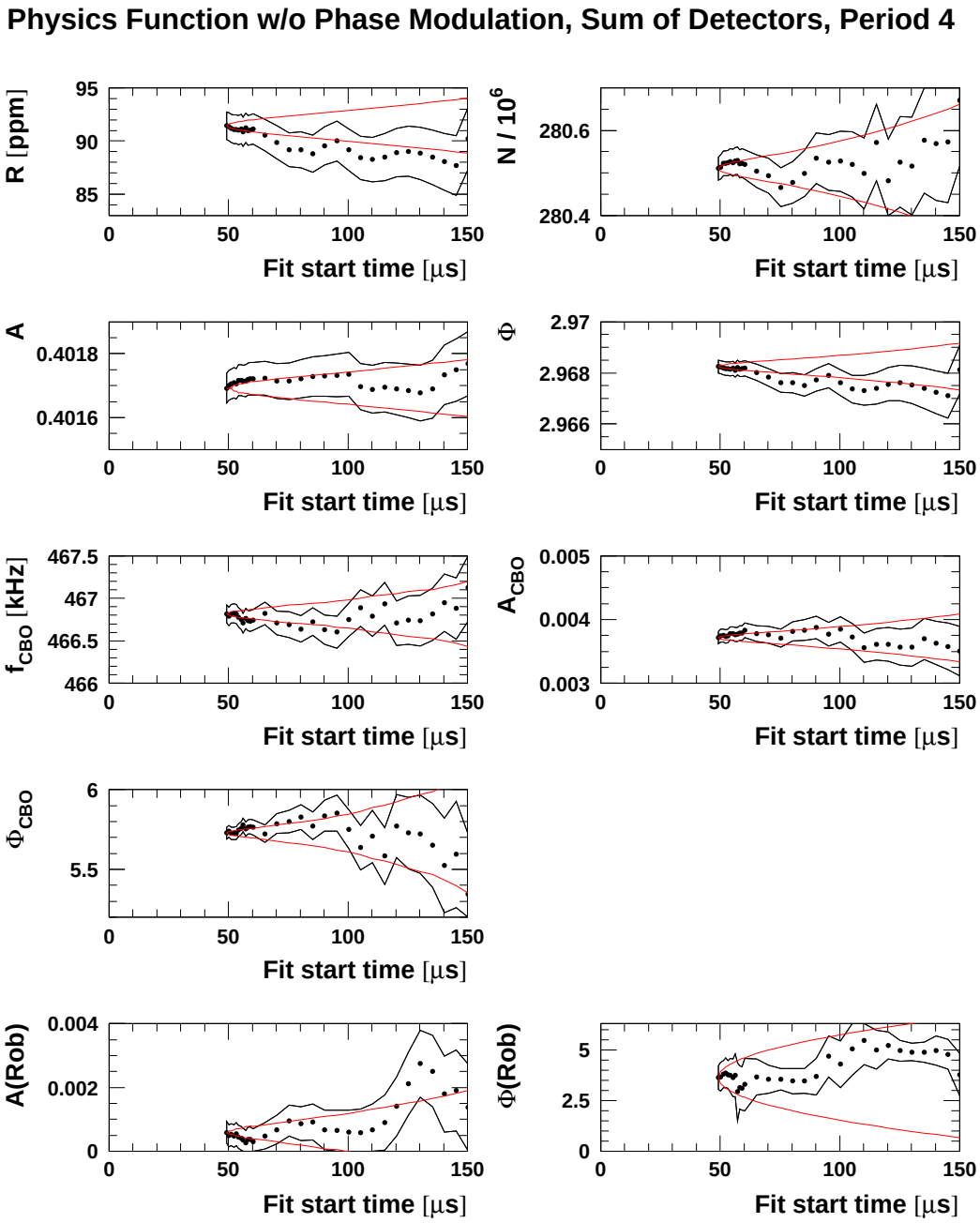

Figure 116: *Start time scan with the physics function for period 4. The g-2 phase modulation (Jim effect) was switched off.*

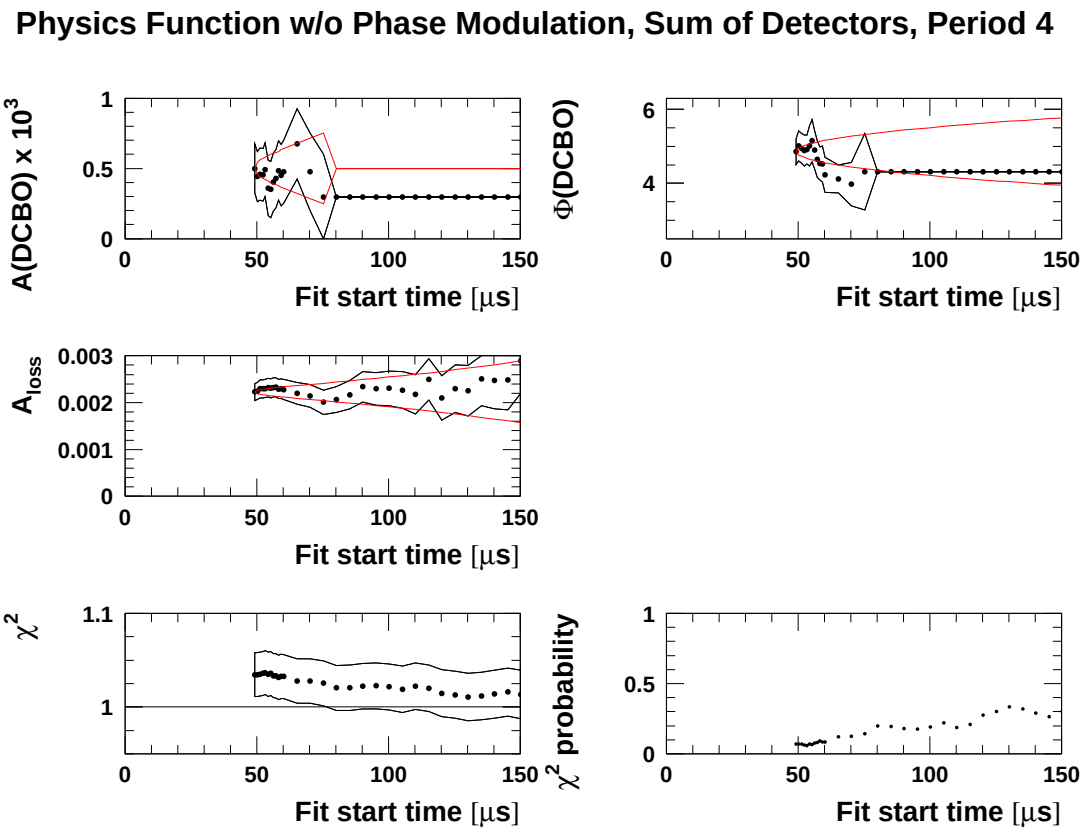
Physics Function w/o Phase Modulation, Sum of Detectors, Period 4
A(DCBO) x 10^3
Φ(DCBO)
A_loss
χ^2
χ^2 probability
Fit start time [μs]

B.2 Start Time Scans for the Two Half Rings

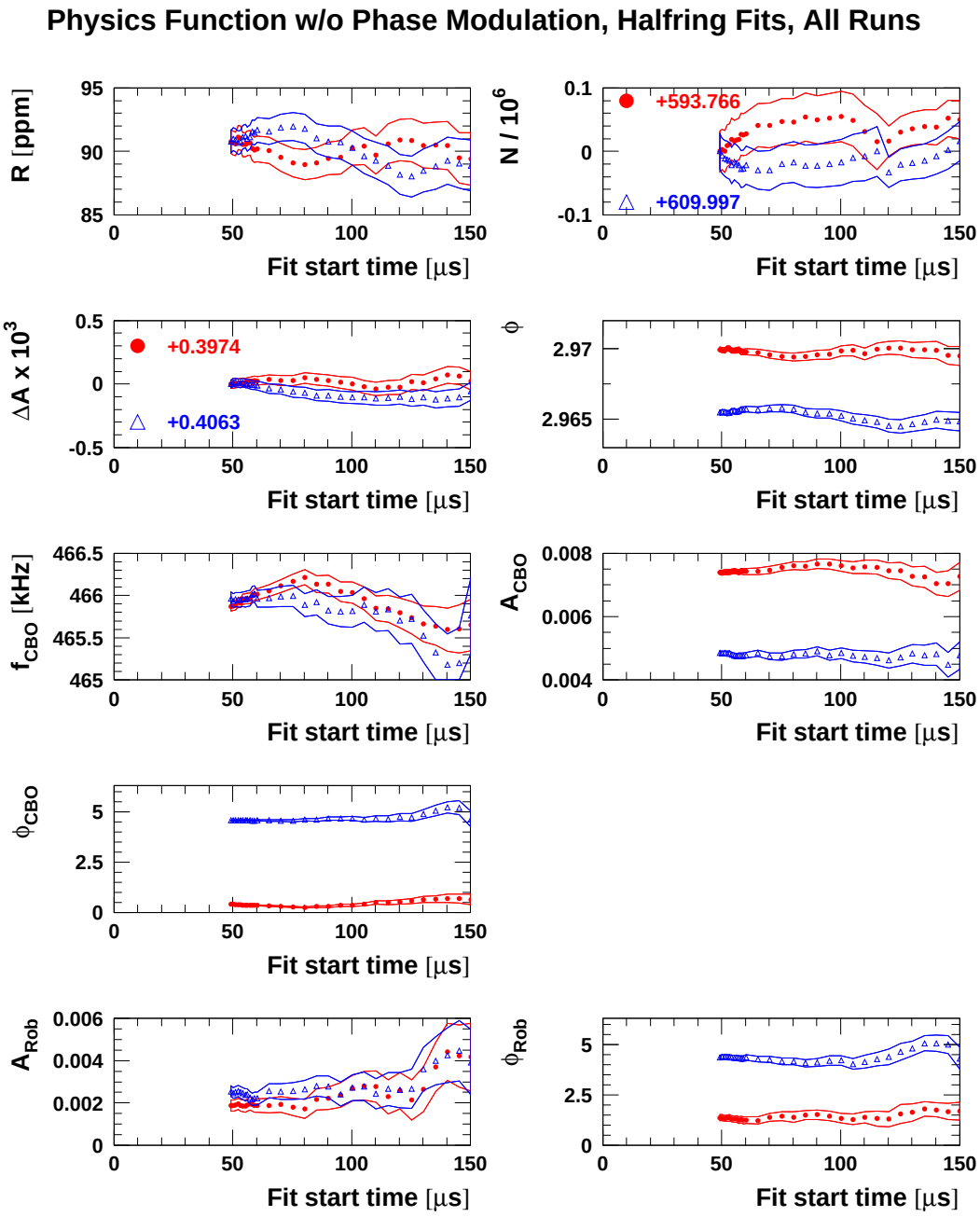

Figure 117: *Start time scan for the two half rings separately (red circles = det. 1-12, blue triangles = det. 13-24) with the physics function for all runs. The g-2 phase modulation (Jim effect) was switched off.*

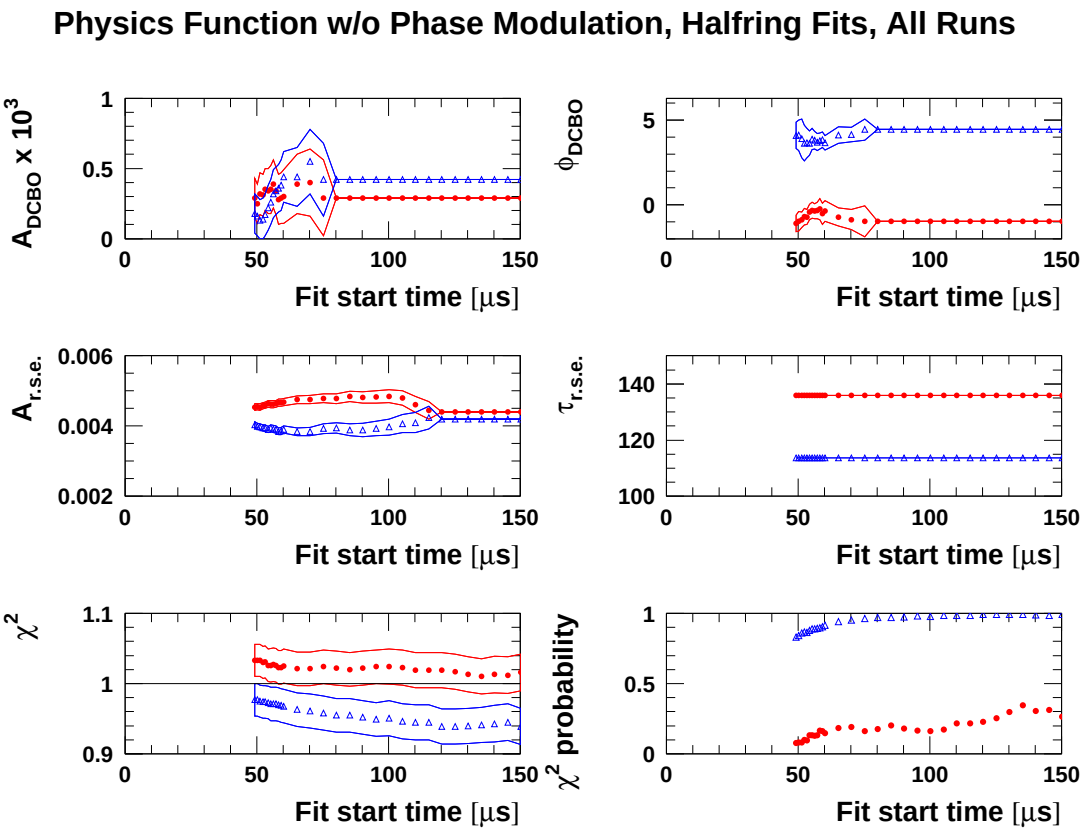
Physics Function w/o Phase Modulation, Halfring Fits, All Runs
A_{DCBO} x 10^3
ϕ_{DCBO}
$A_{r.s.e.}$
$\tau_{r.s.e.}$
χ^2
χ^2 probability
Fit start time [μs]

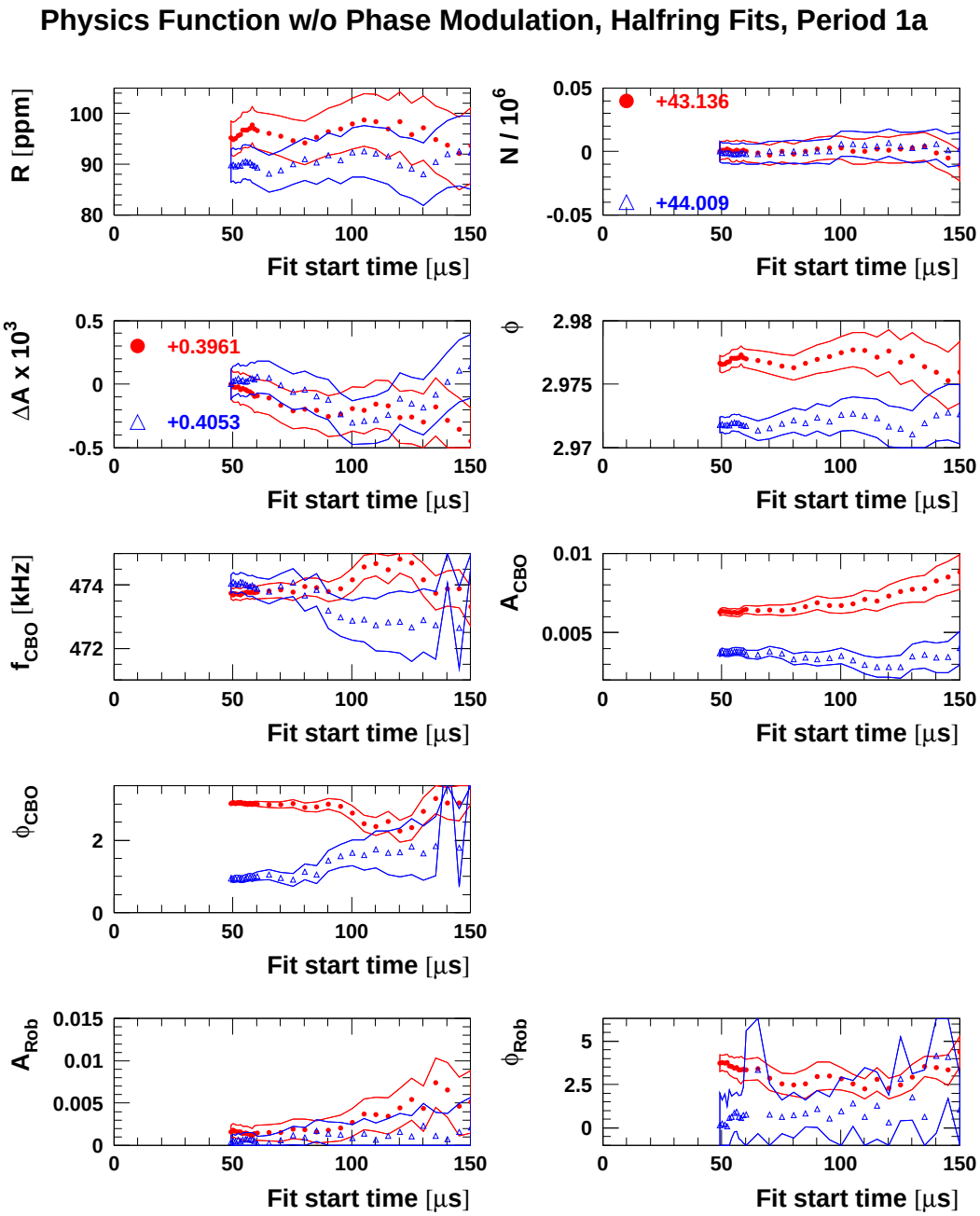

Figure 118: *Start time scan for the two half rings separately (red circles = det. 1-12, blue triangles = det. 13-24) with the physics function for period 1a. The g-2 phase modulation (Jim effect) was switched off.*

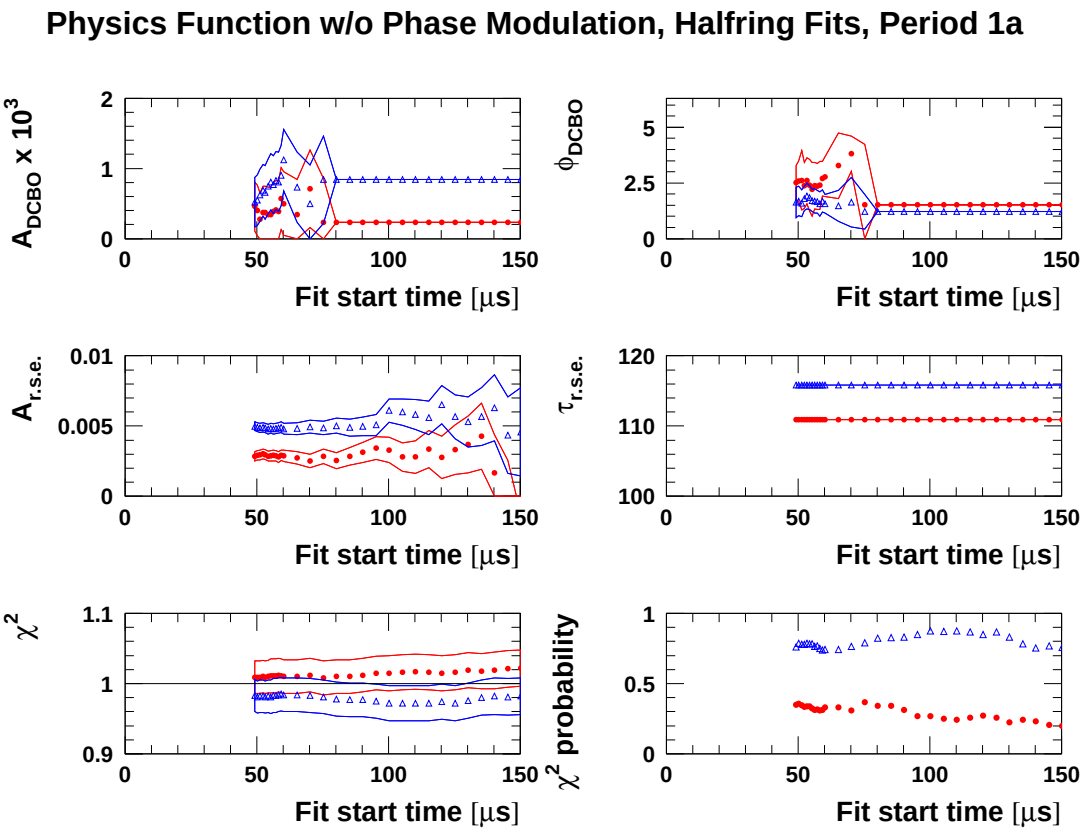
Physics Function w/o Phase Modulation, Halfring Fits, Period 1a
A_{DCBO} x 10^3
ϕ_{DCBO}
$A_{r.s.e.}$
$\tau_{r.s.e.}$
χ^2
χ^2 probability
Fit start time [μs]

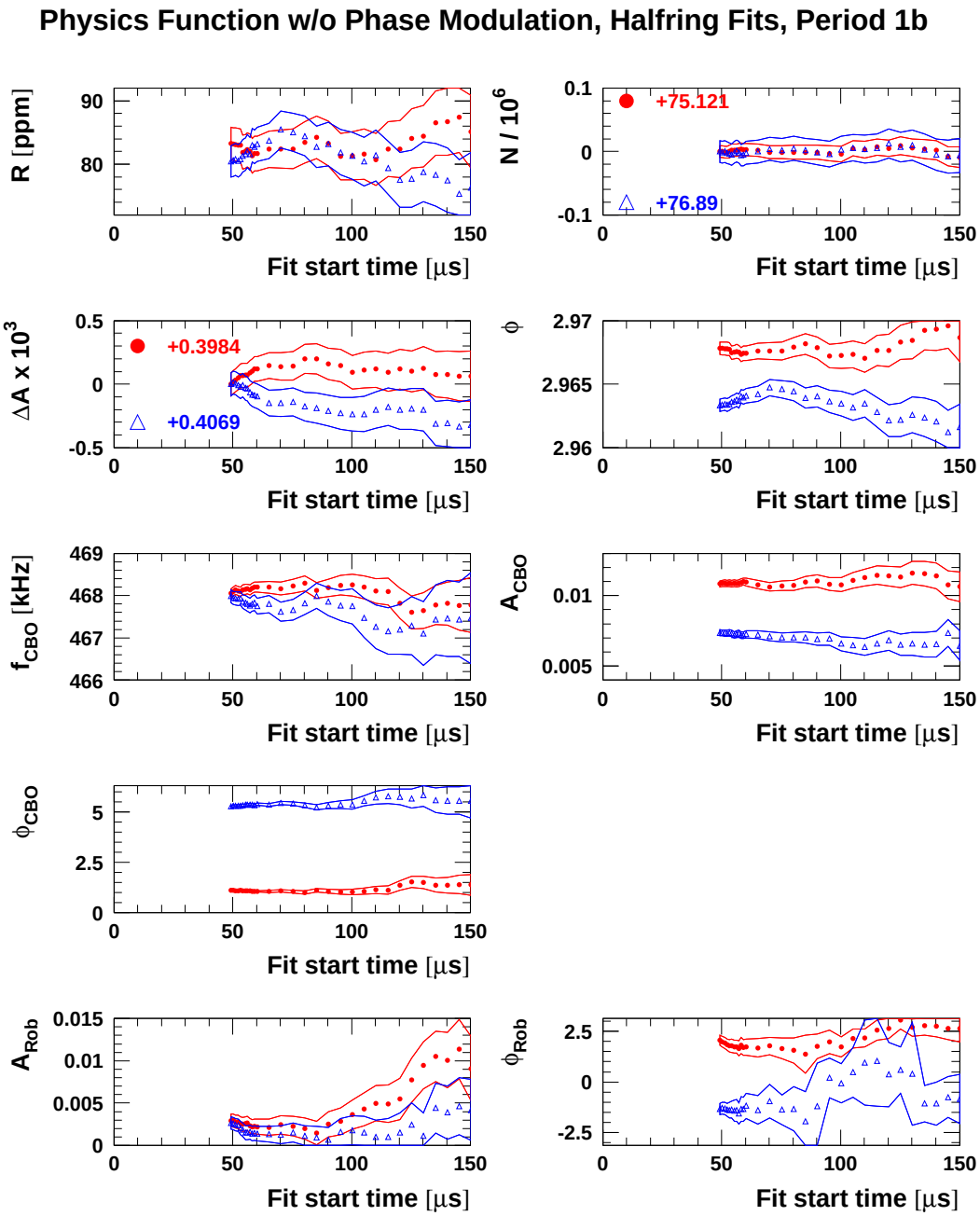

Figure 119: *Start time scan for the two half rings separately (red circles = det. 1-12, blue triangles = det. 13-24) with the physics function for period 1b. The g-2 phase modulation (Jim effect) was switched off.*

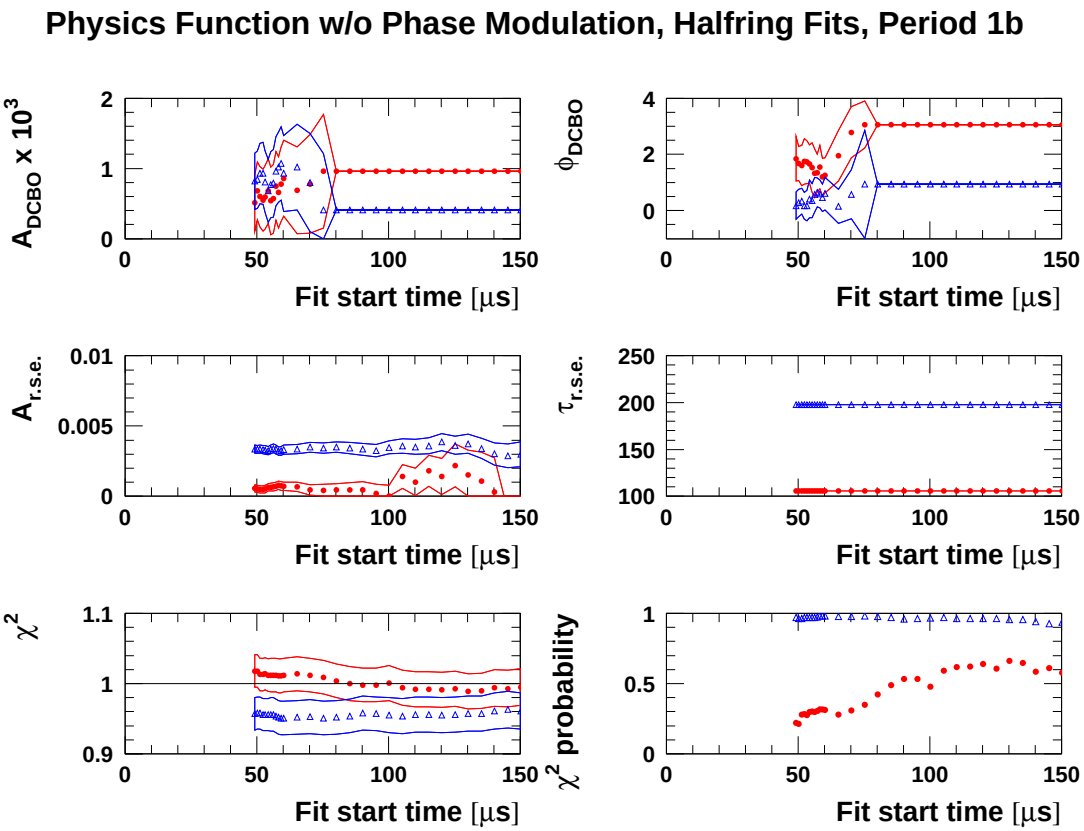
Physics Function w/o Phase Modulation, Halfring Fits, Period 1b
A_{DCBO} x 10^3
ϕ_{DCBO}
$A_{r.s.e.}$
$\tau_{r.s.e.}$
χ^2
χ^2 probability
Fit start time [μs]

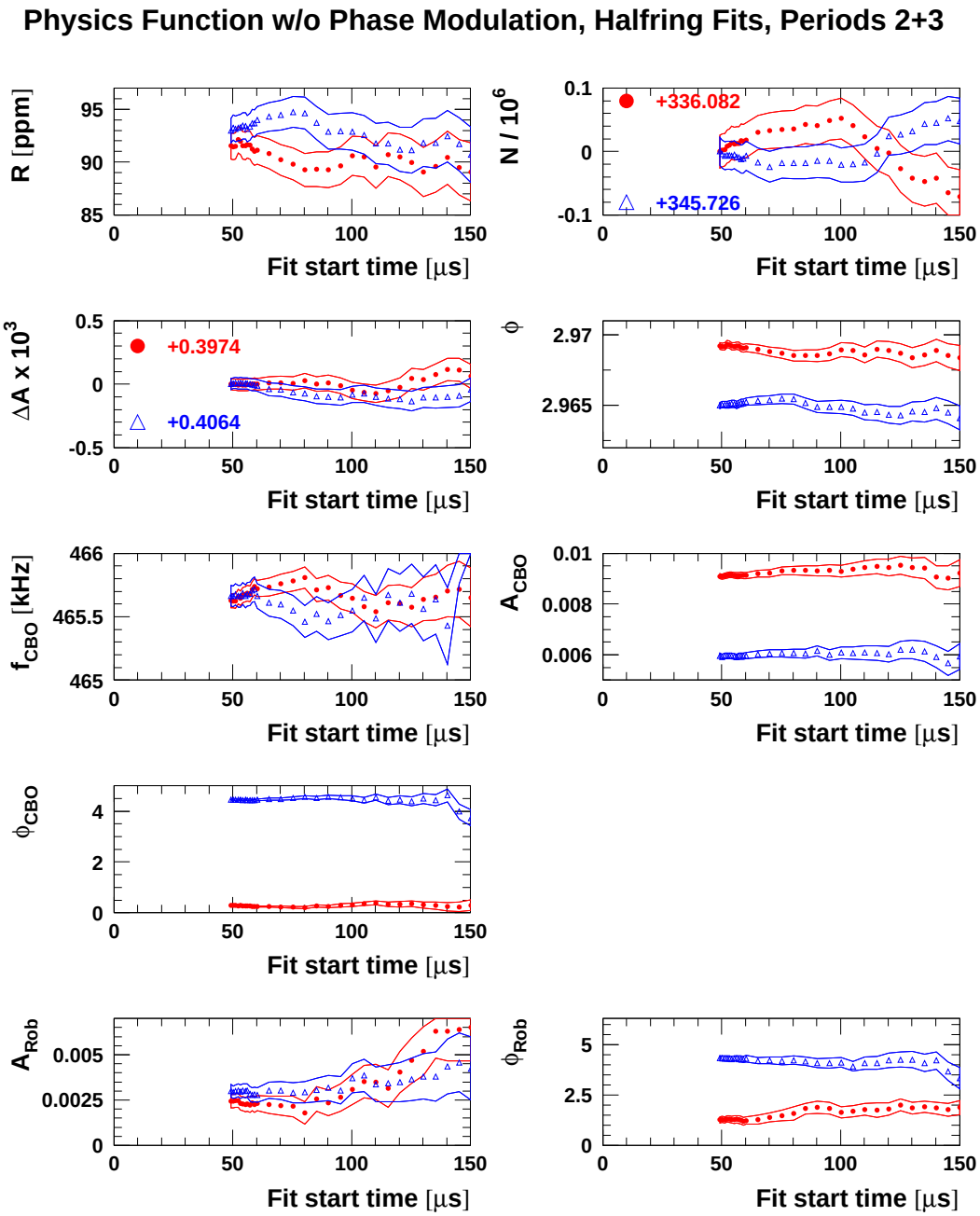

Figure 120: *Start time scan for the two half rings separately (red circles = det. 1-12, blue triangles = det. 13-24) with the physics function for periods 2+3. The g-2 phase modulation (Jim effect) was switched off.*

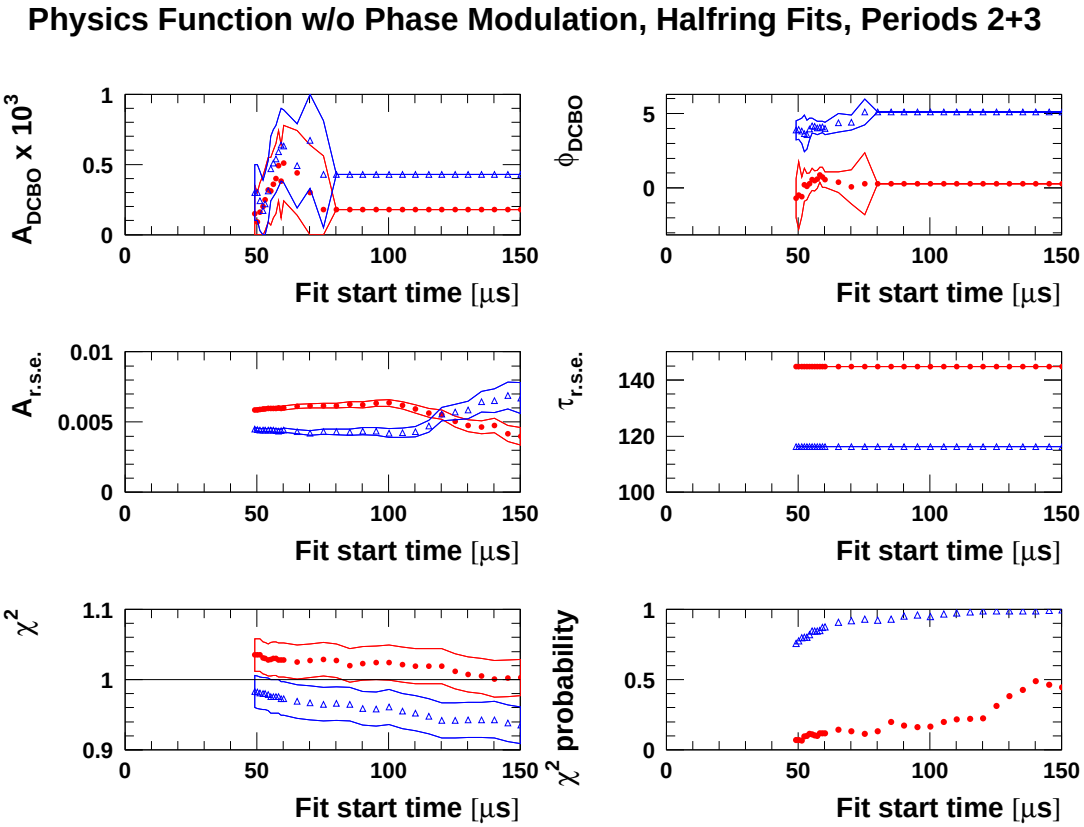
Physics Function w/o Phase Modulation, Halfring Fits, Periods 2+3
A_{DCBO} x 10^3
ϕ_{DCBO}
$A_{r.s.e.}$
$\tau_{r.s.e.}$
χ^2
χ^2 probability
Fit start time [μs]

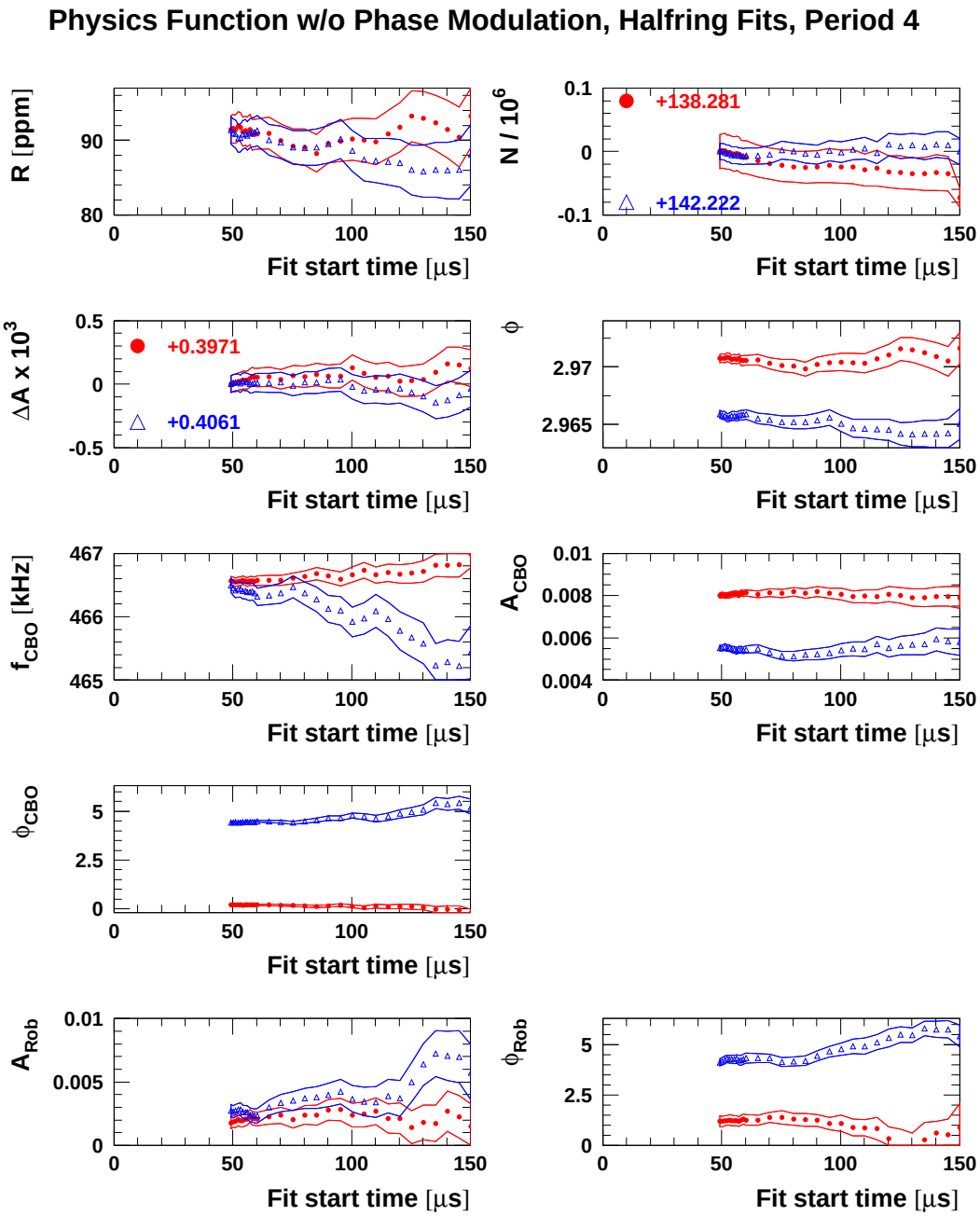

Figure 121: *Start time scan for the two half rings separately (red circles = det. 1-12, blue triangles = det. 13-24) with the physics function for period 4. The g-2 phase modulation (Jim effect) was switched off.*

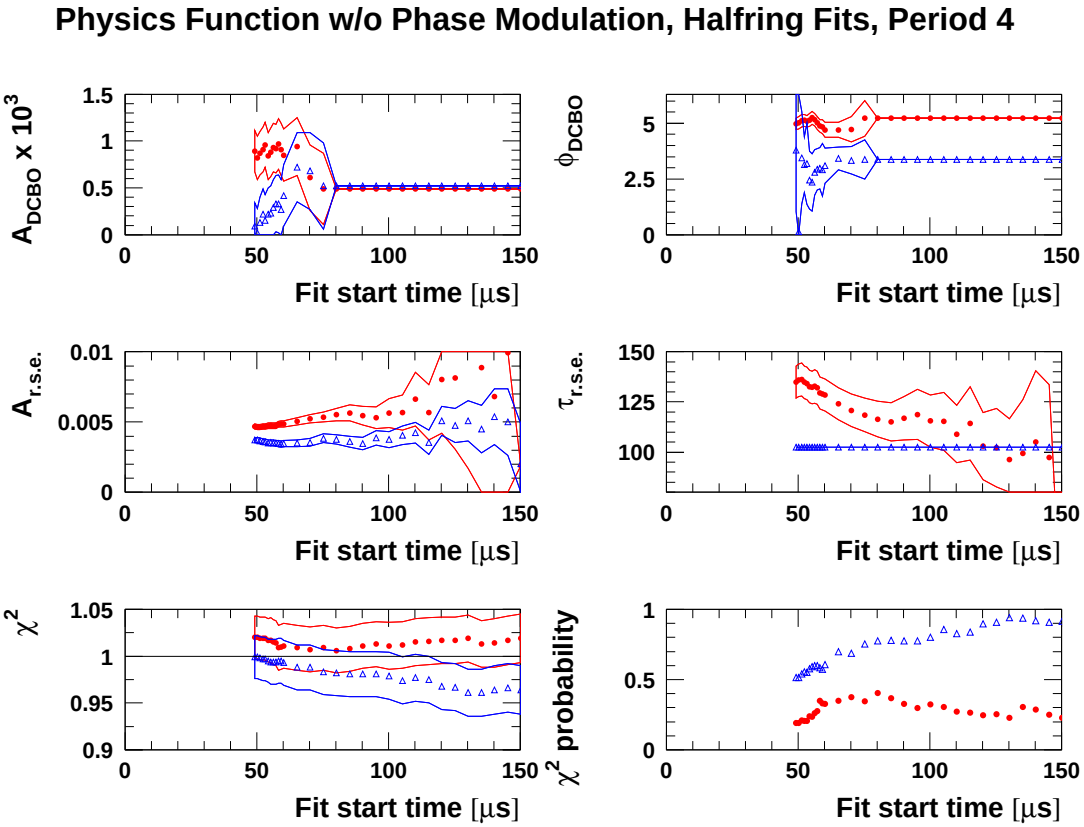
Physics Function w/o Phase Modulation, Halfring Fits, Period 4
A_{DCBO} x 10^3
ϕ_{DCBO}
$A_{r.s.e.}$
$\tau_{r.s.e.}$
χ^2
χ^2 probability
Fit start time [μs]

B.3 Individual Detector Fits Starting at 49.2 μs

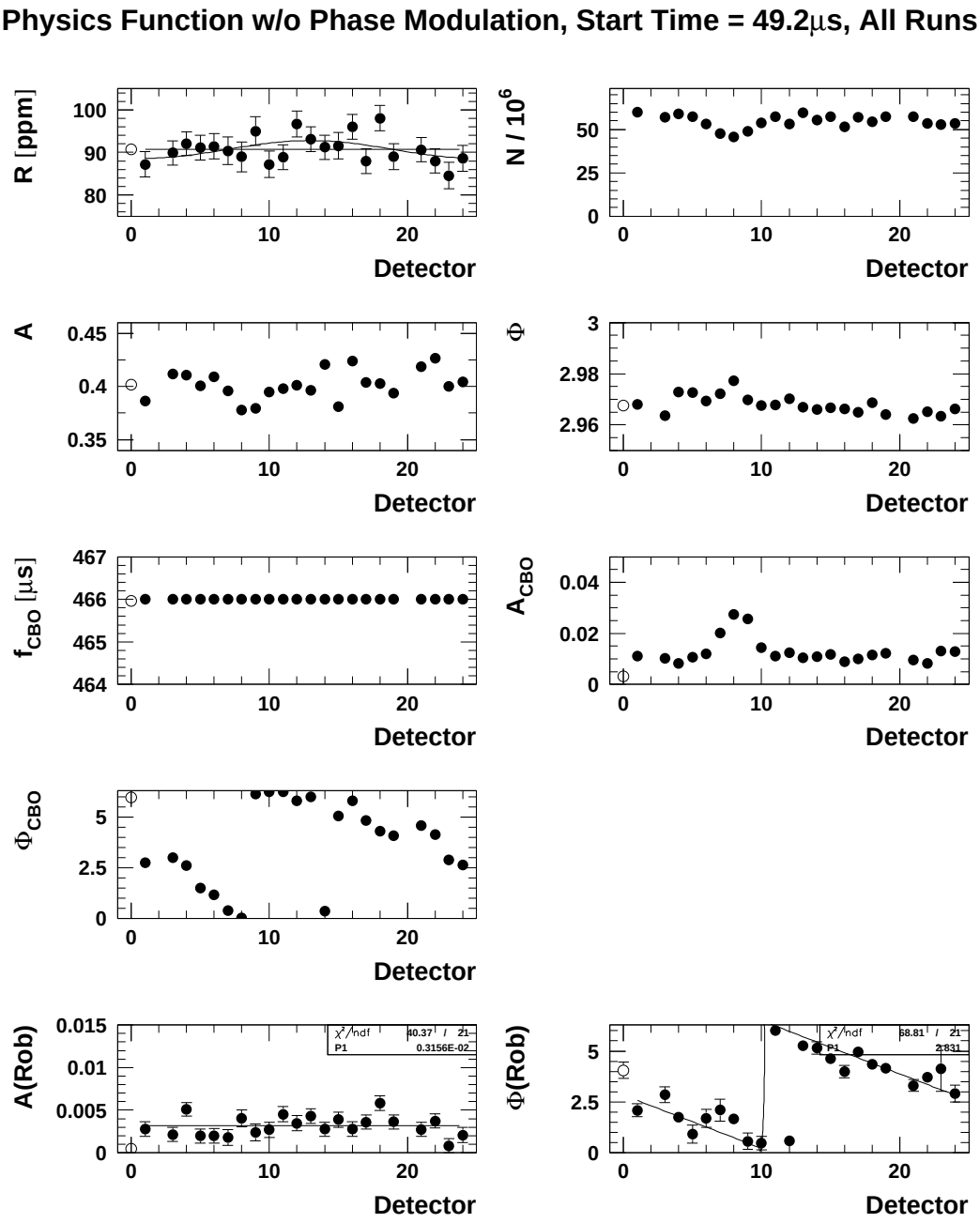

Figure 122: *Fits of individual detector spectra with the physics function for all runs. The g-2 phase modulation (Jim effect) was switched off.*

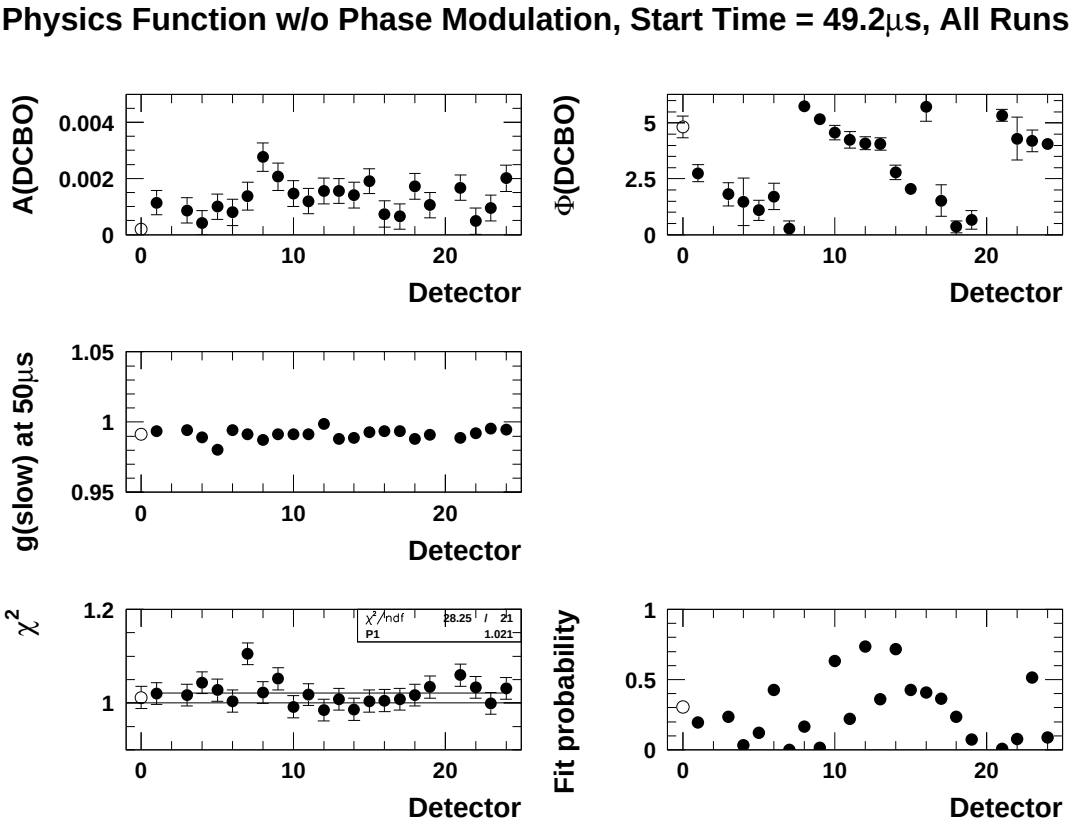
Physics Function w/o Phase Modulation, Start Time = 49.2μs, All Runs
A(DCBO)
0.004
0.002
0
0
10
20
Detector
Φ(DCBO)
5
2.5
0
0
10
20
Detector
g(slow) at 50μs
1.05
1
0.95
0
10
20
Detector
χ²
1.2
1
χ²/ndf 28.25 / 21
P1 1.021
0
10
20
Detector
Fit probability
1
0.5
0
0
10
20
Detector

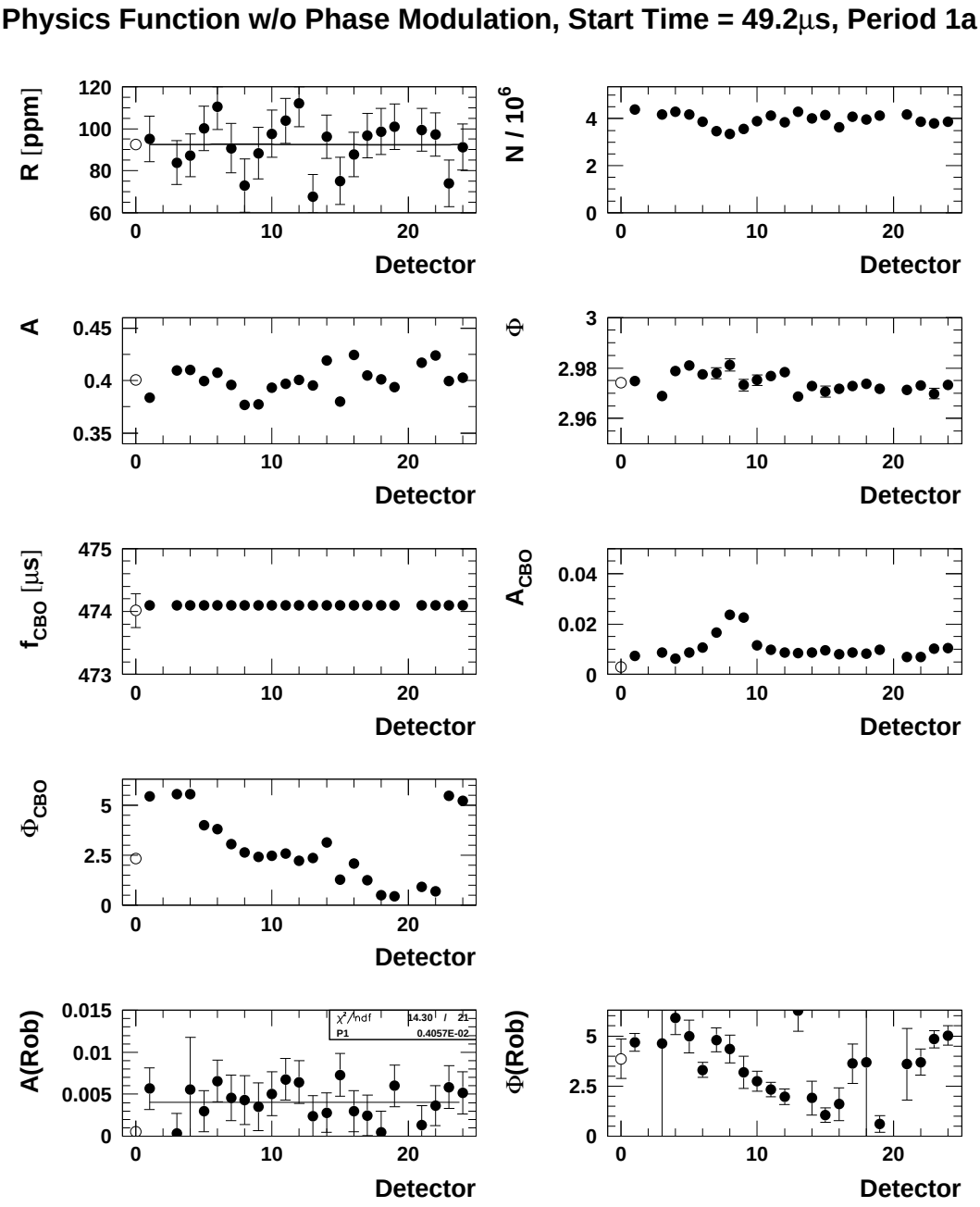

Figure 123: *Fits of individual detector spectra with the physics function for period 1a. The g-2 phase modulation (Jim effect) was switched off.*

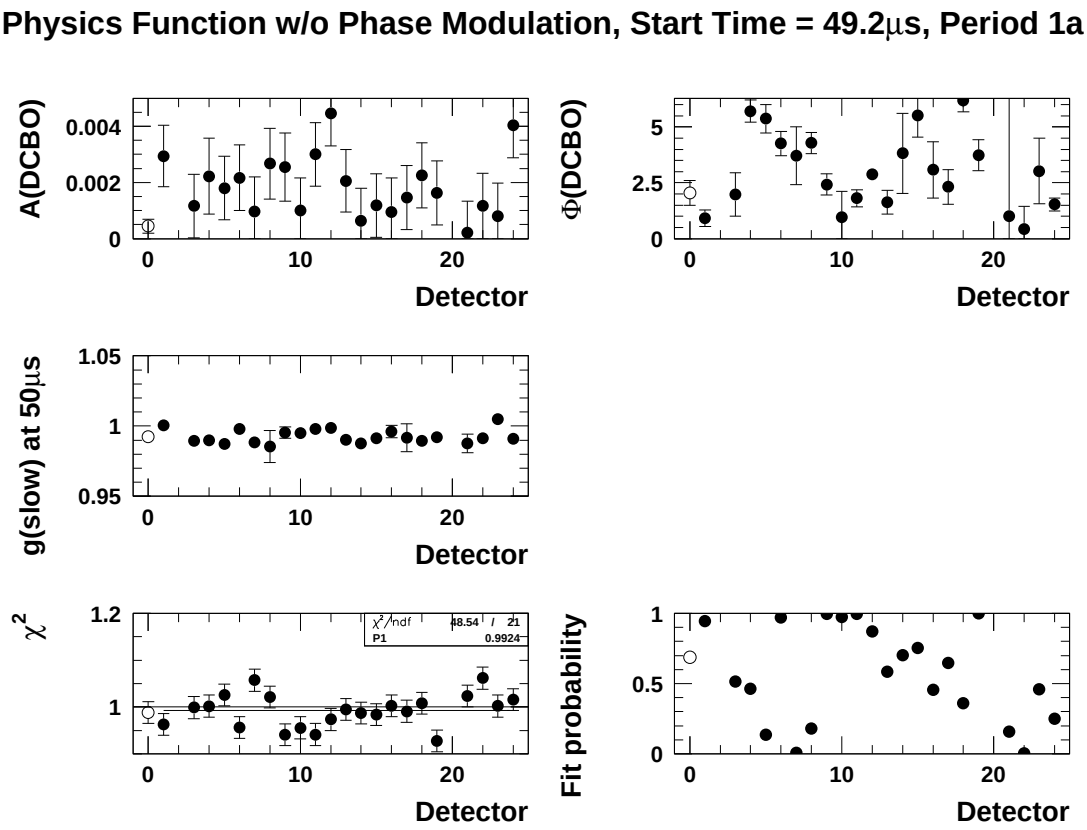
Physics Function w/o Phase Modulation, Start Time = 49.2μs, Period 1a
A(DCBO)
0.004
0.002
0
0
10
20
Detector
Φ(DCBO)
5
2.5
0
0
10
20
Detector
g(slow) at 50μs
1.05
1
0.95
0
10
20
Detector
χ²
1.2
1
χ²/ndf 48.54 / 21
P1 0.9924
0
10
20
Detector
Fit probability
1
0.5
0
0
10
20
Detector

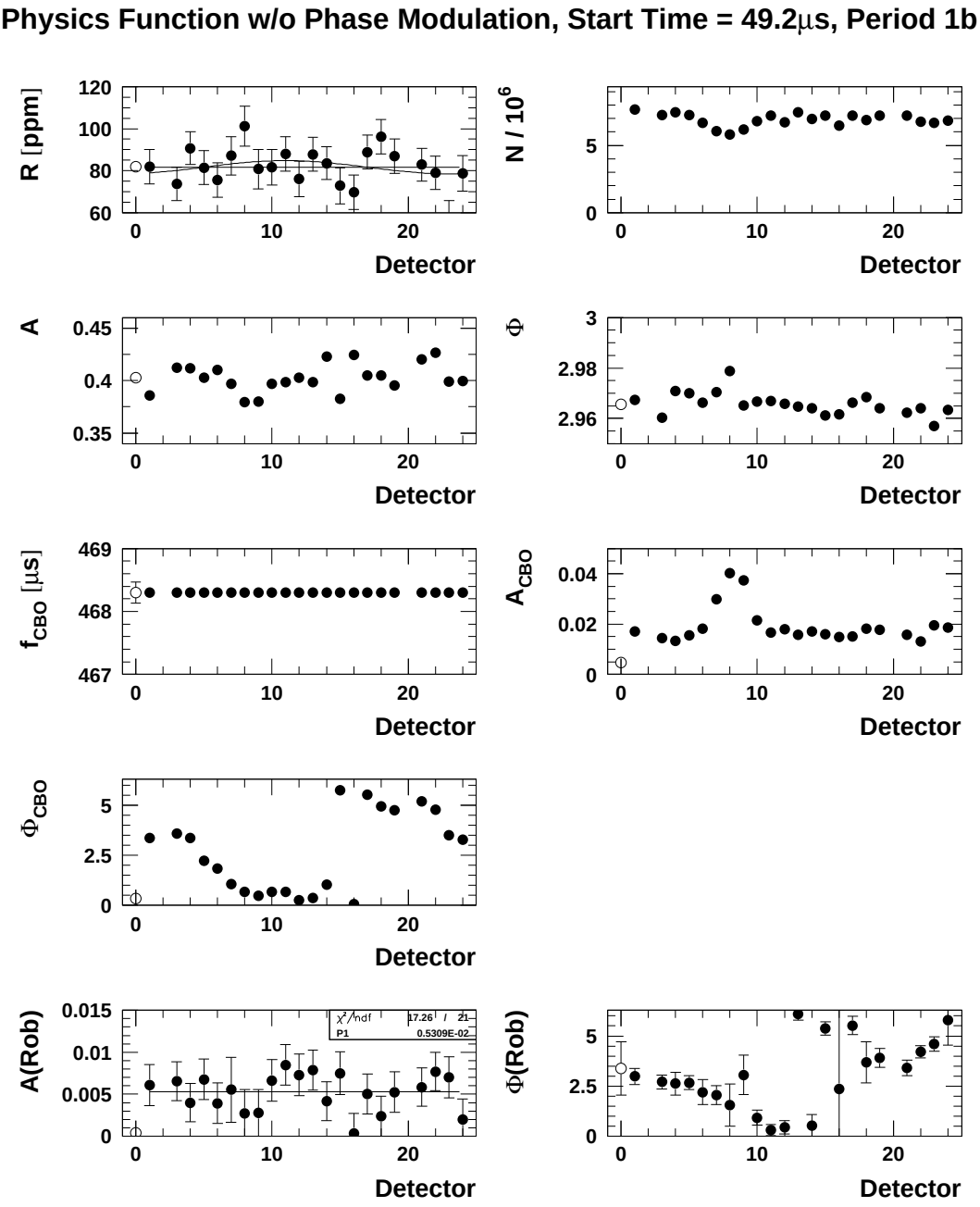

Figure 124: *Fits of individual detector spectra with the physics function for period 1b. The g-2 phase modulation (Jim effect) was switched off.*

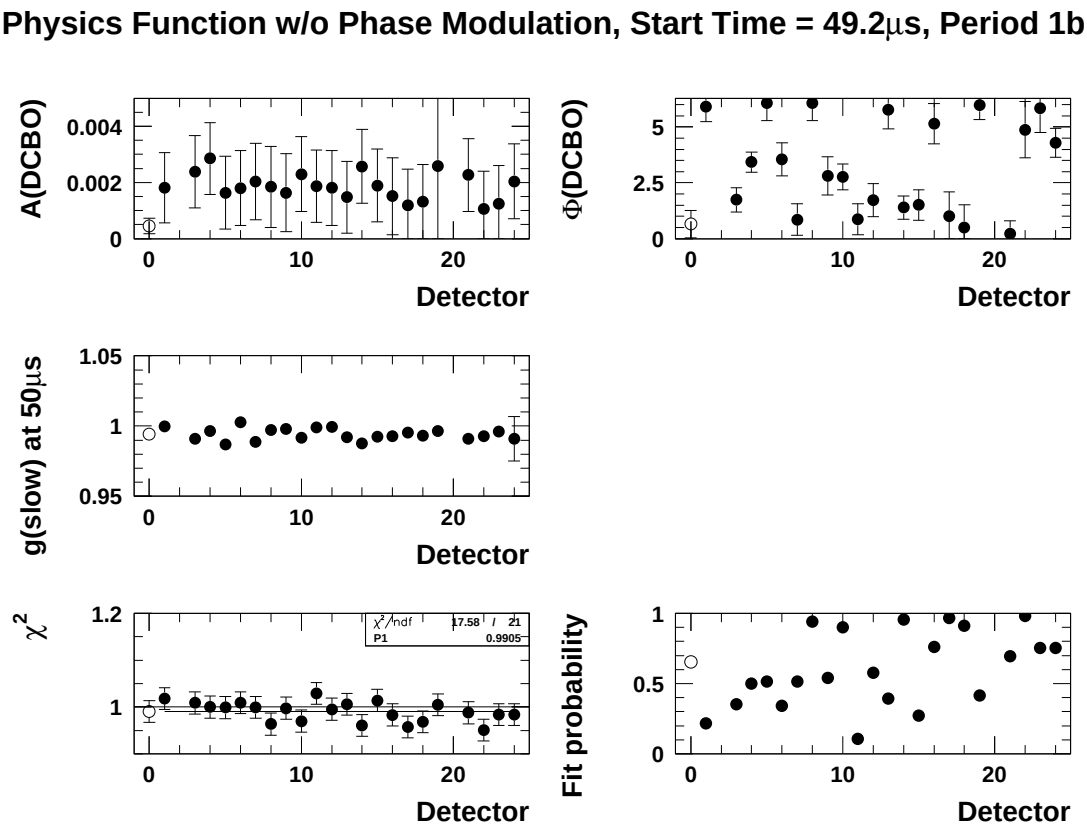
Physics Function w/o Phase Modulation, Start Time = 49.2μs, Period 1b
A(DCBO)
0.004
0.002
0
0
10
20
Detector
Φ(DCBO)
5
2.5
0
0
10
20
Detector
g(slow) at 50μs
1.05
1
0.95
0
10
20
Detector
χ²
1.2
1
χ²/ndf 17.58 / 21
P1 0.9905
0
10
20
Detector
Fit probability
1
0.5
0
0
10
20
Detector

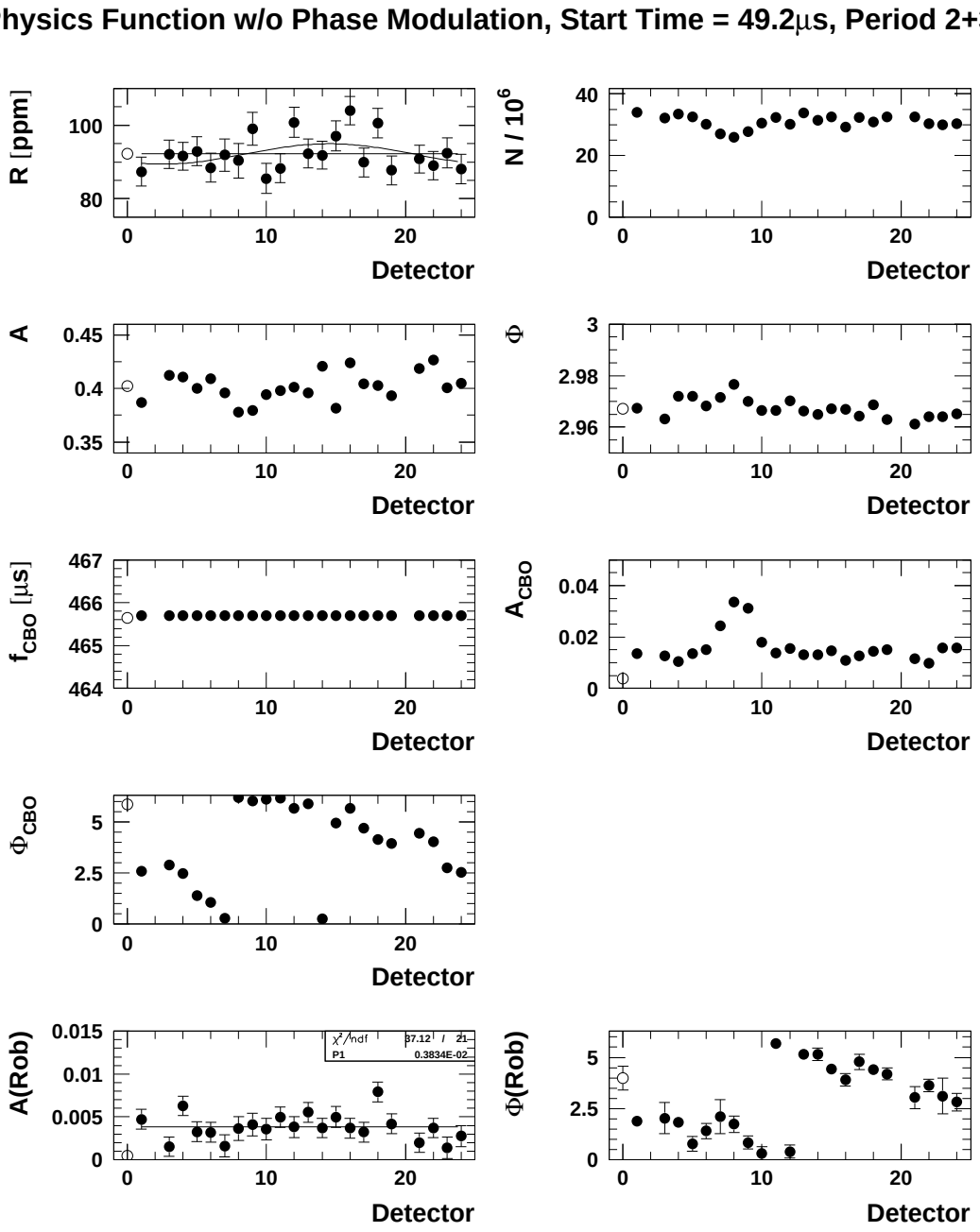

Figure 125: *Fits of individual detector spectra with the physics function for period 23. The g-2 phase modulation (Jim effect) was switched off.*

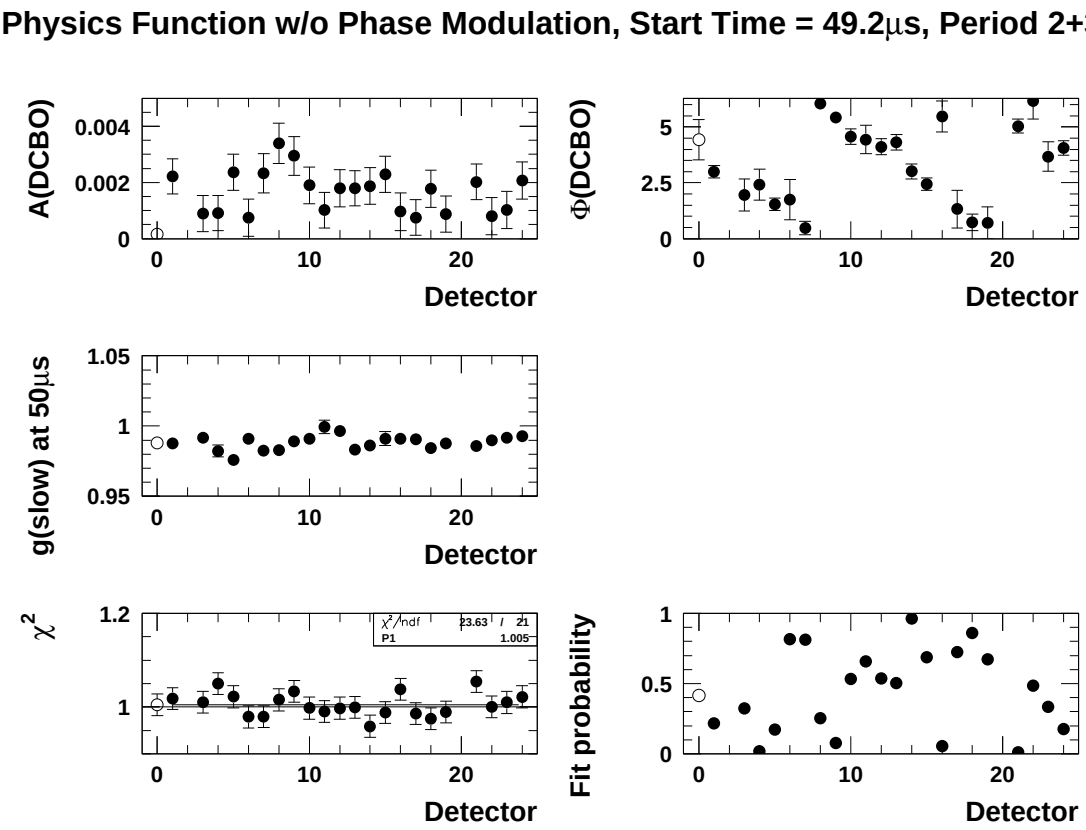
Physics Function w/o Phase Modulation, Start Time = 49.2μs, Period 2+3
A(DCBO)
0.004
0.002
0
0
10
20
Detector
Φ(DCBO)
5
2.5
0
0
10
20
Detector
g(slow) at 50μs
1.05
1
0.95
0
10
20
Detector
χ²
1.2
1
χ²/ndf 23.63 / 21
P1 1.005
0
10
20
Detector
Fit probability
1
0.5
0
0
10
20
Detector

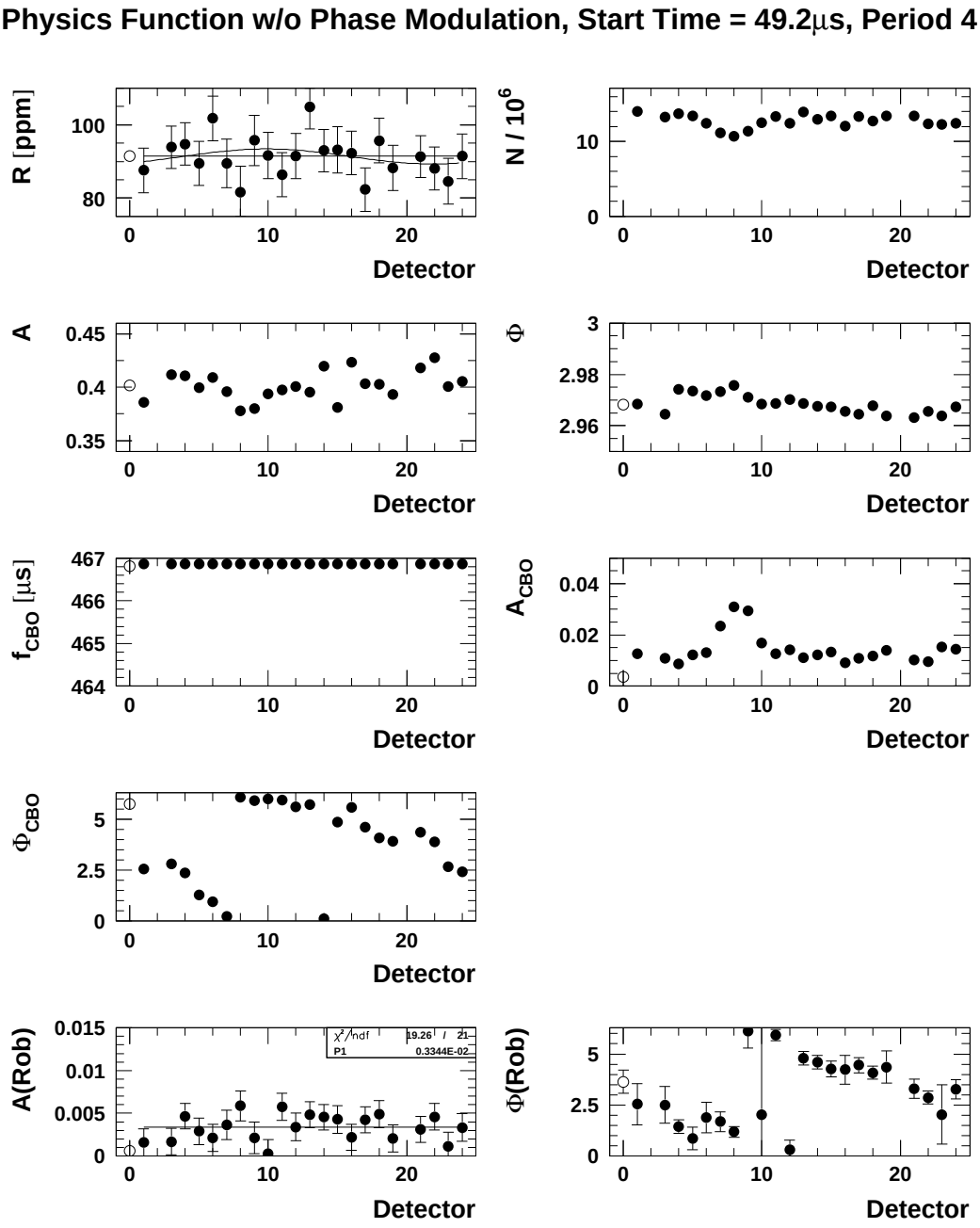

Figure 126: *Fits of individual detector spectra with the physics function for period 4. The g-2 phase modulation (Jim effect) was switched off.*

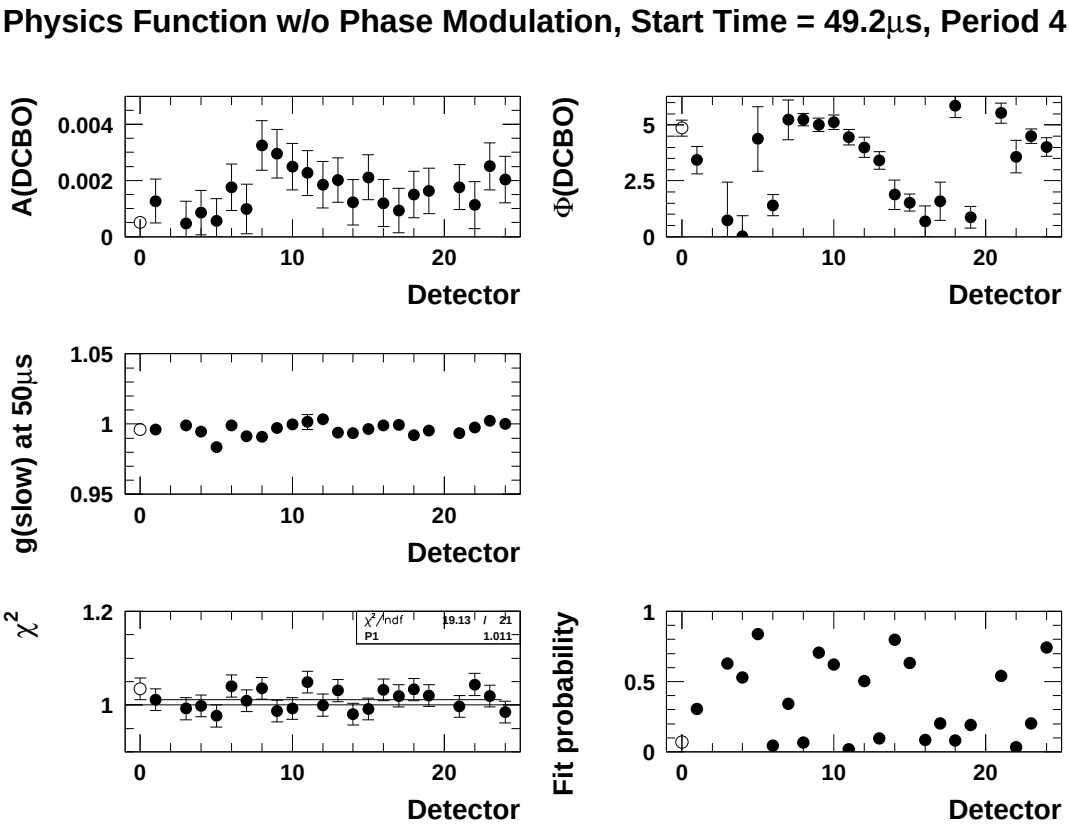
Physics Function w/o Phase Modulation, Start Time = 49.2μs, Period 4
A(DCBO)
0.004
0.002
0
0
10
20
Detector
Φ(DCBO)
5
2.5
0
0
10
20
Detector
g(slow) at 50μs
1.05
1
0.95
0
10
20
Detector
χ²
1.2
1
χ²/ndf 19.13 / 21
P1 1.011
0
10
20
Detector
Fit probability
1
0.5
0
0
10
20
Detector

C Fit Results for the Physics Function including Phase Modulation

C.1 Start Time Scans for the Sum of Detectors

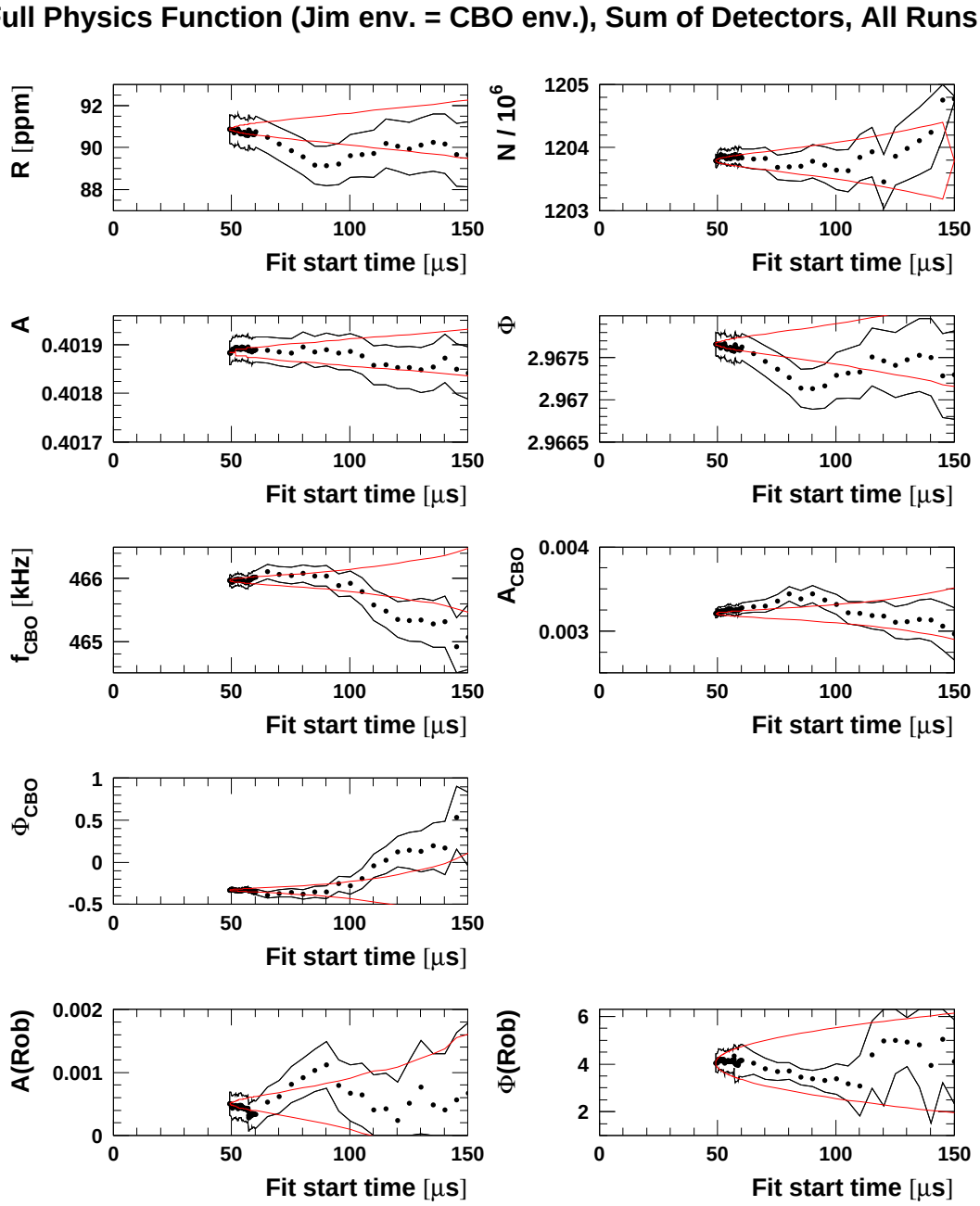

Figure 127: *Start time scan with the physics function for all runs. The phase modulation was assumed to have the same envelope as the acceptance CBO. The muon life time was fixed to 64.407 μs.*

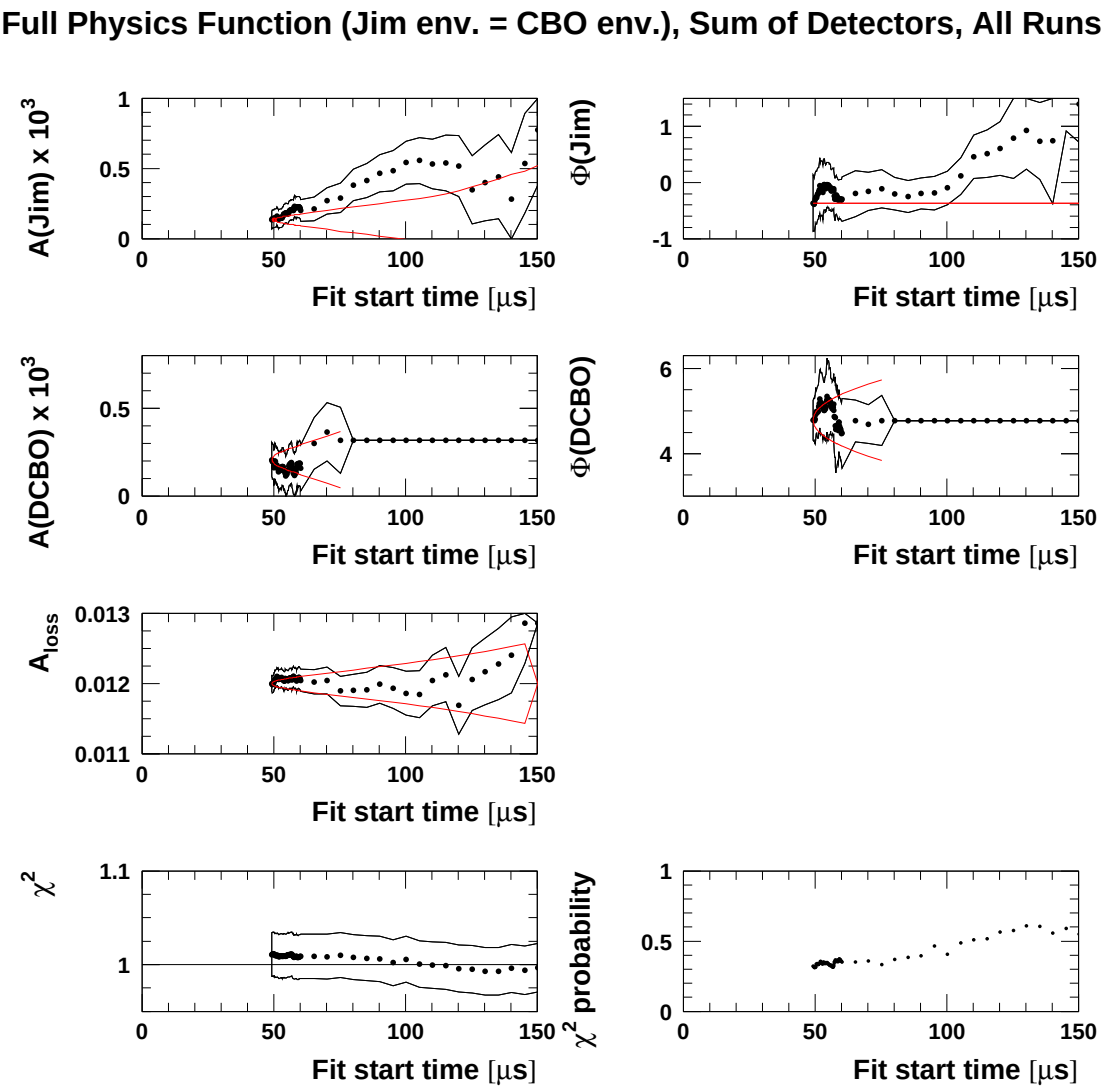
Full Physics Function (Jim env. = CBO env.), Sum of Detectors, All Runs
A(Jim) x 10^3
Φ(Jim)
A(DCBO) x 10^3
Φ(DCBO)
A_loss
χ^2
χ^2 probability
Fit start time [μs]

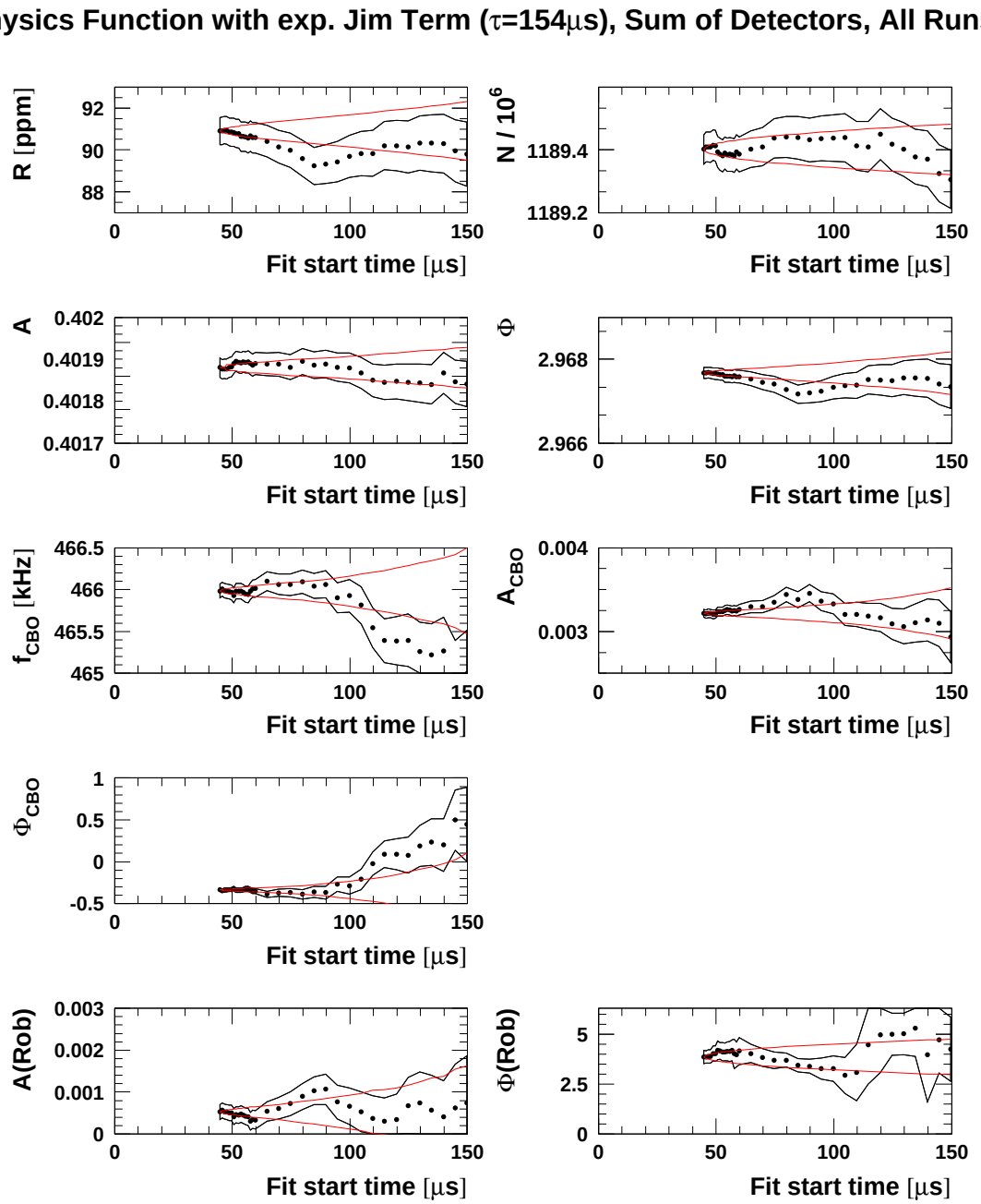

Figure 128: *Start time scan with the physics function for all runs. The phase modulation was assumed to have an exponential envelope with 154 μs life time.*

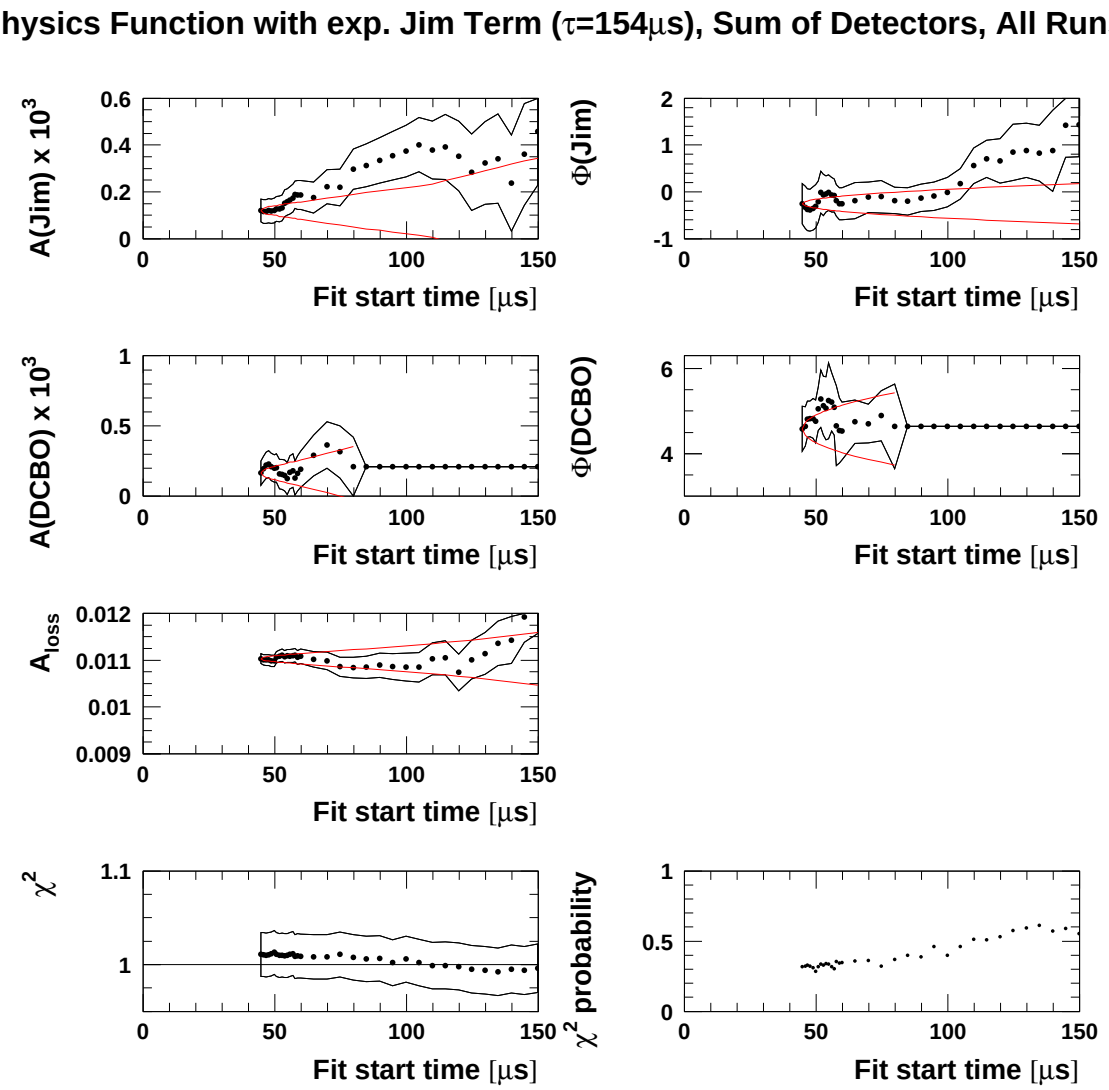
Physics Function with exp. Jim Term (τ=154μs), Sum of Detectors, All Runs
A(Jim) x 10^3
Φ(Jim)
A(DCBO) x 10^3
Φ(DCBO)
A_loss
χ^2
χ^2 probability
Fit start time [μs]

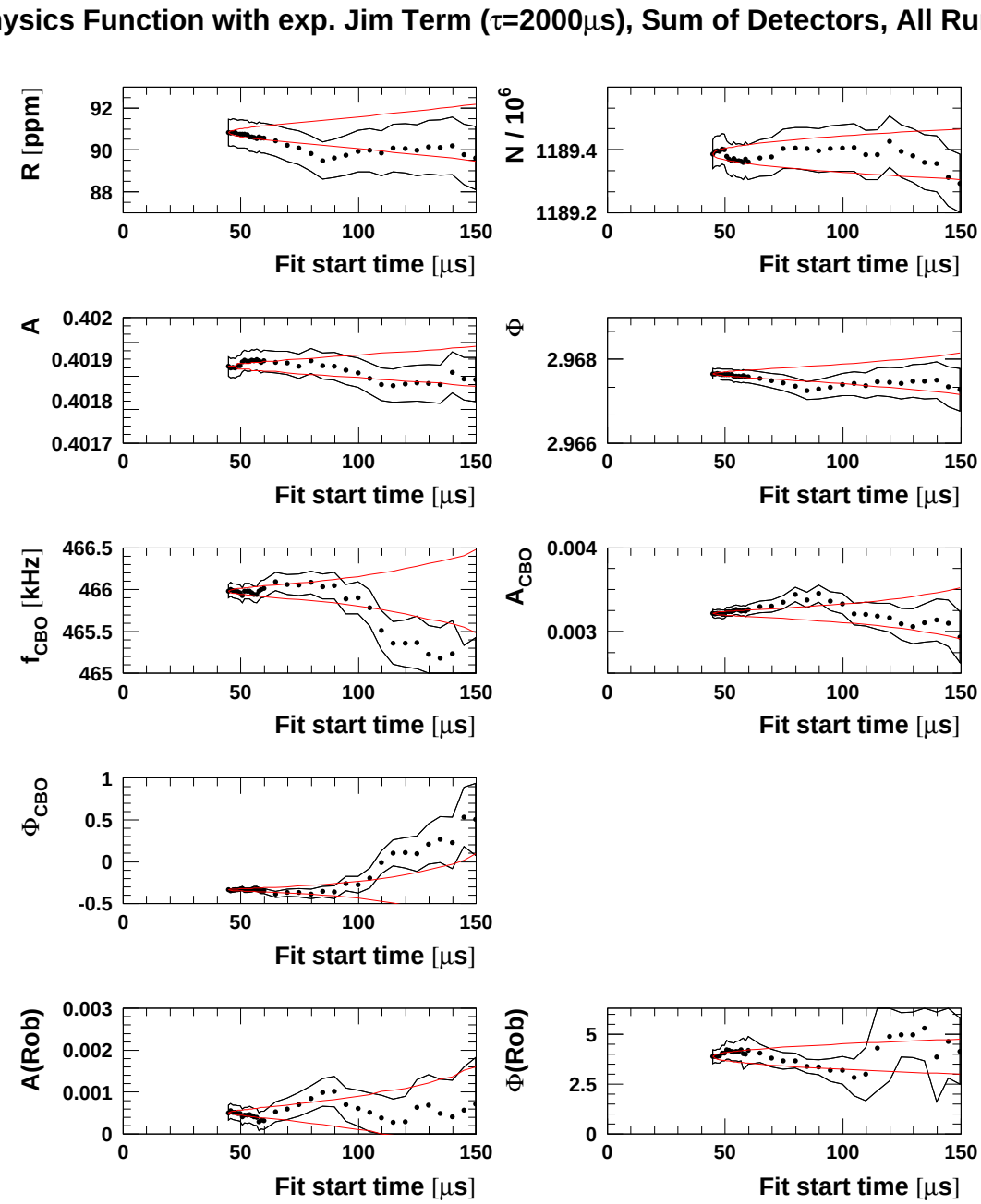

Figure 129: *Start time scan with the physics function for all runs. The phase modulation was assumed to have an exponential envelope with 2000 μs life time.*

Physics Function with exp. Jim Term (τ=2000μs), Sum of Detectors, All Runs

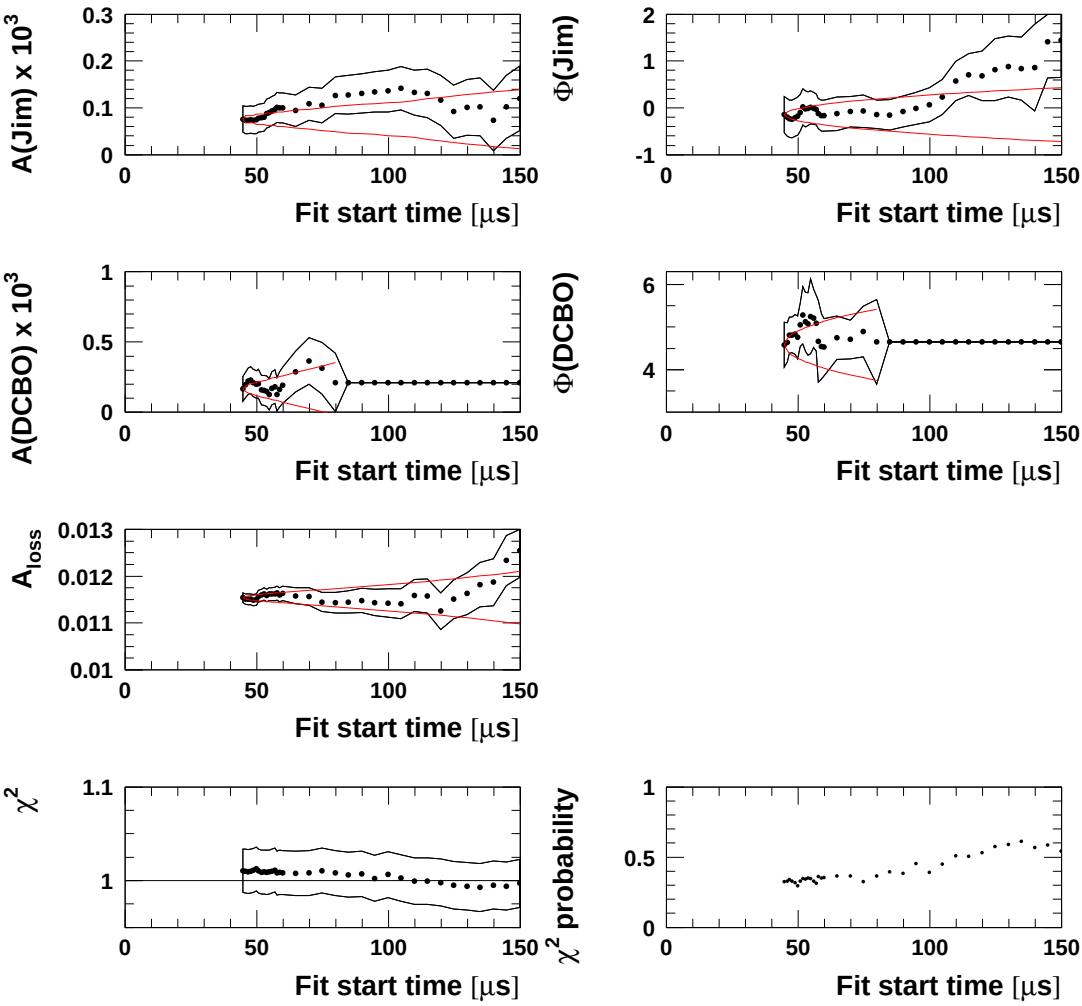

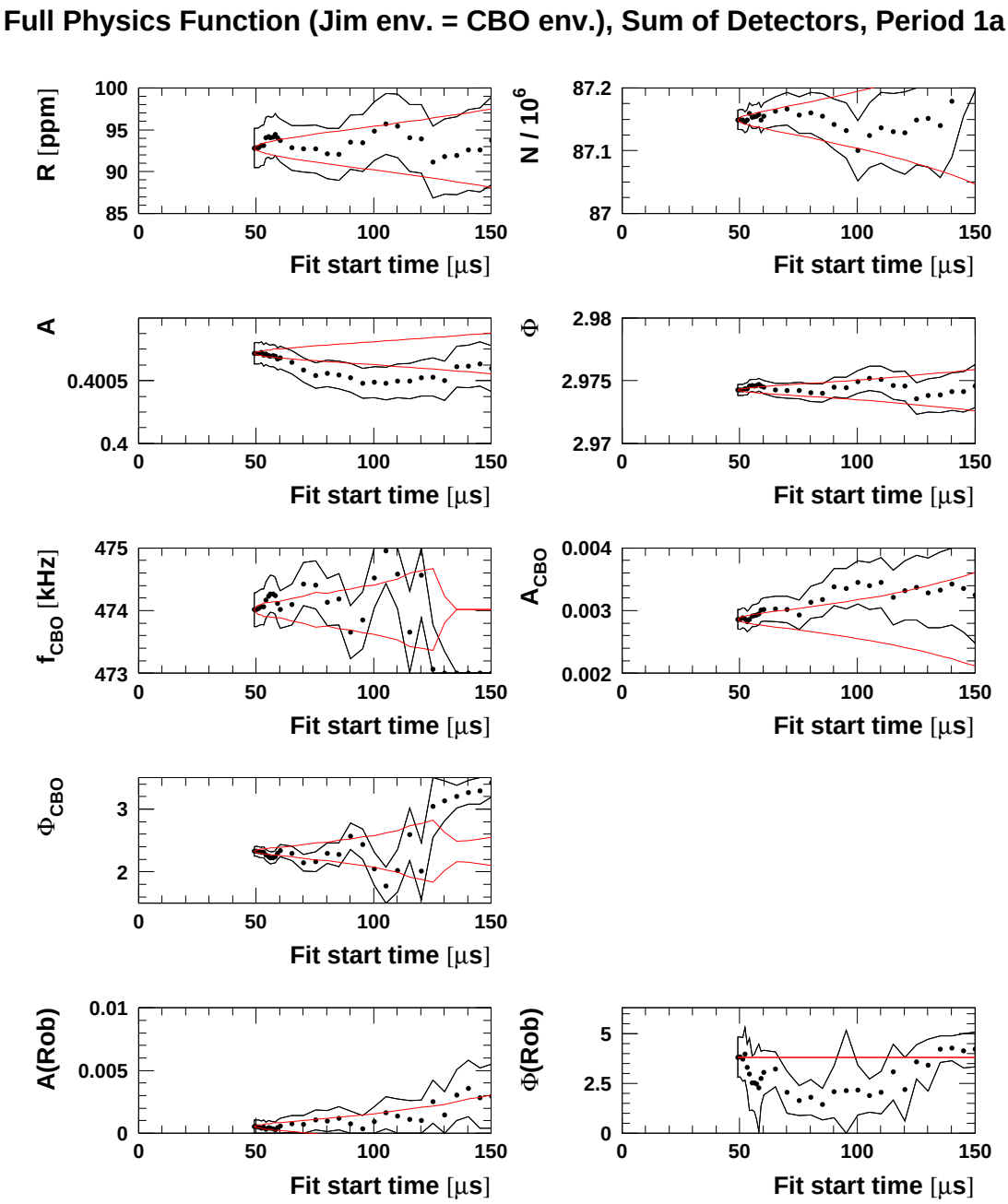

Figure 130: *Start time scan with the physics function for run period 1a. The phase modulation was assumed to have the same envelope as the acceptance CBO. The muon life time was fixed to 64.407 μs.*

Full Physics Function (Jim env. = CBO env.), Sum of Detectors, Period 1a

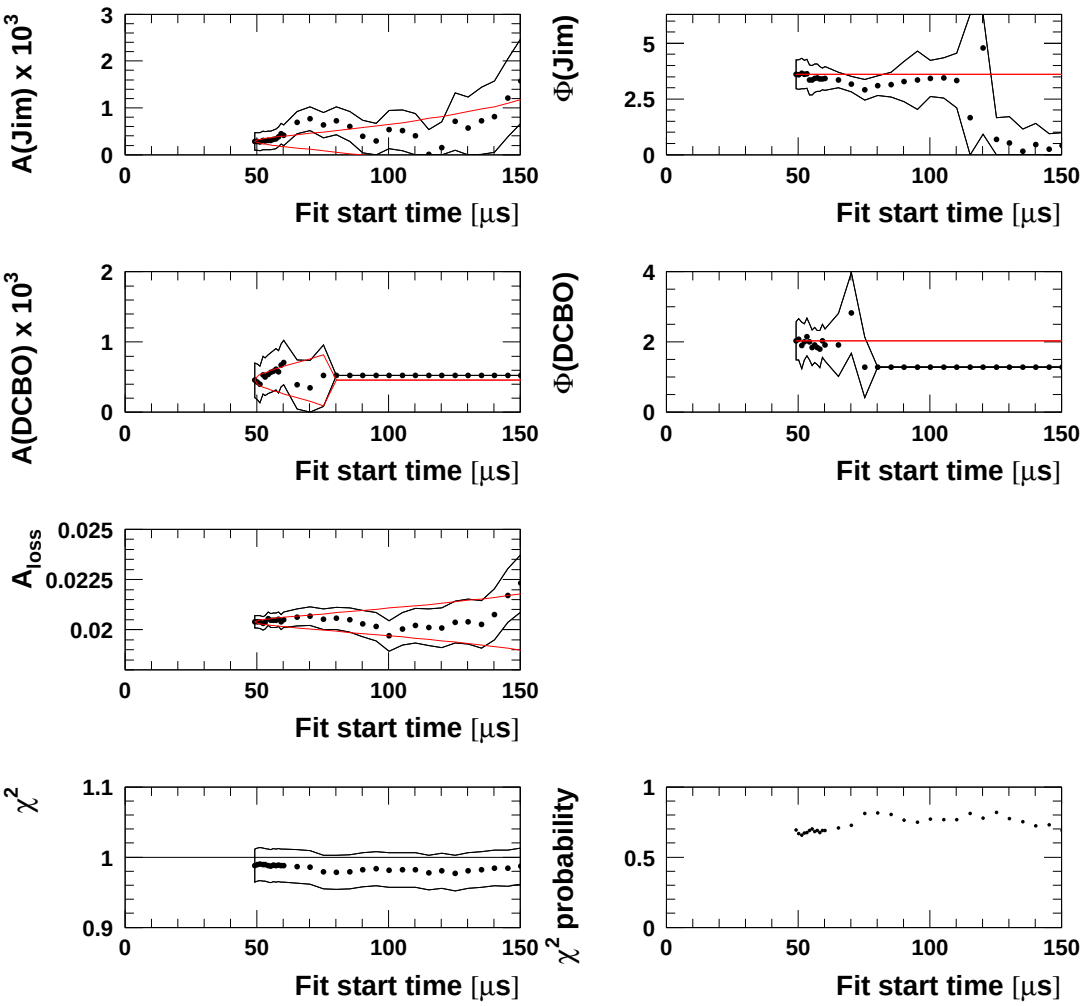

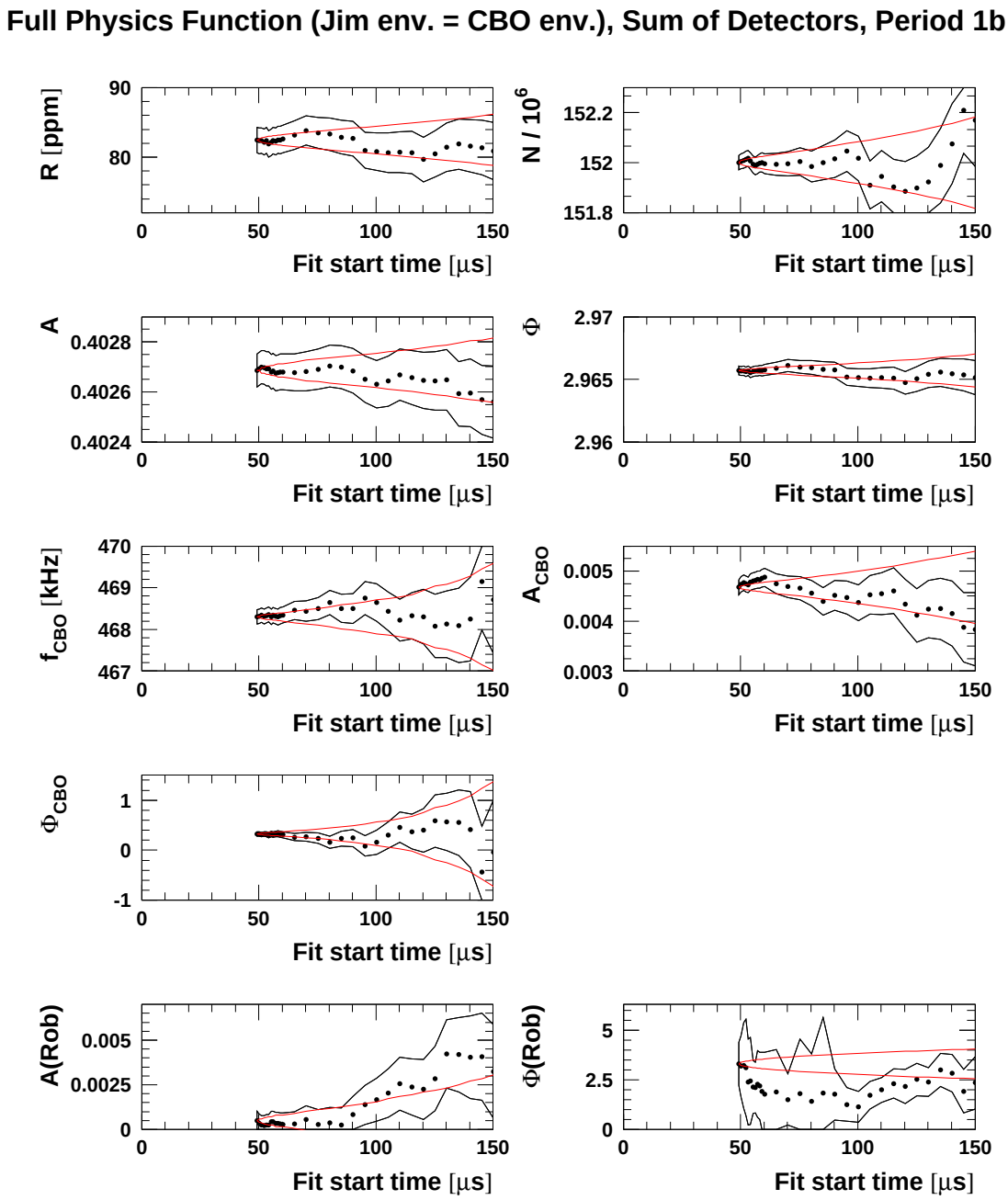

Figure 131: *Start time scan with the physics function for run period 1b. The phase modulation was assumed to have the same envelope as the acceptance CBO. The muon life time was fixed to 64.407 μs.*

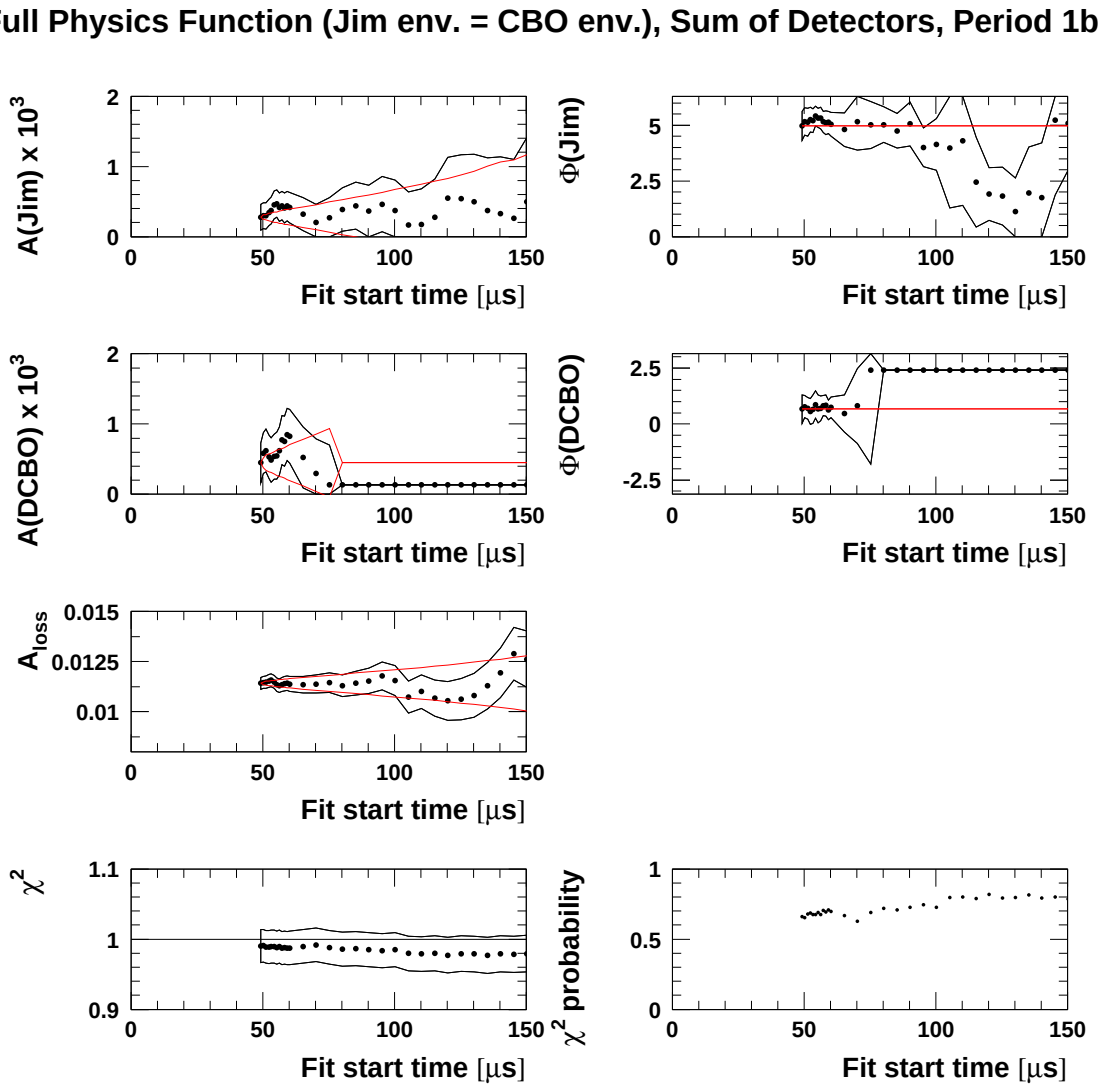
Full Physics Function (Jim env. = CBO env.), Sum of Detectors, Period 1b
A(Jim) x 10^3
Φ(Jim)
A(DCBO) x 10^3
Φ(DCBO)
A_loss
χ^2
χ^2 probability
Fit start time [μs]

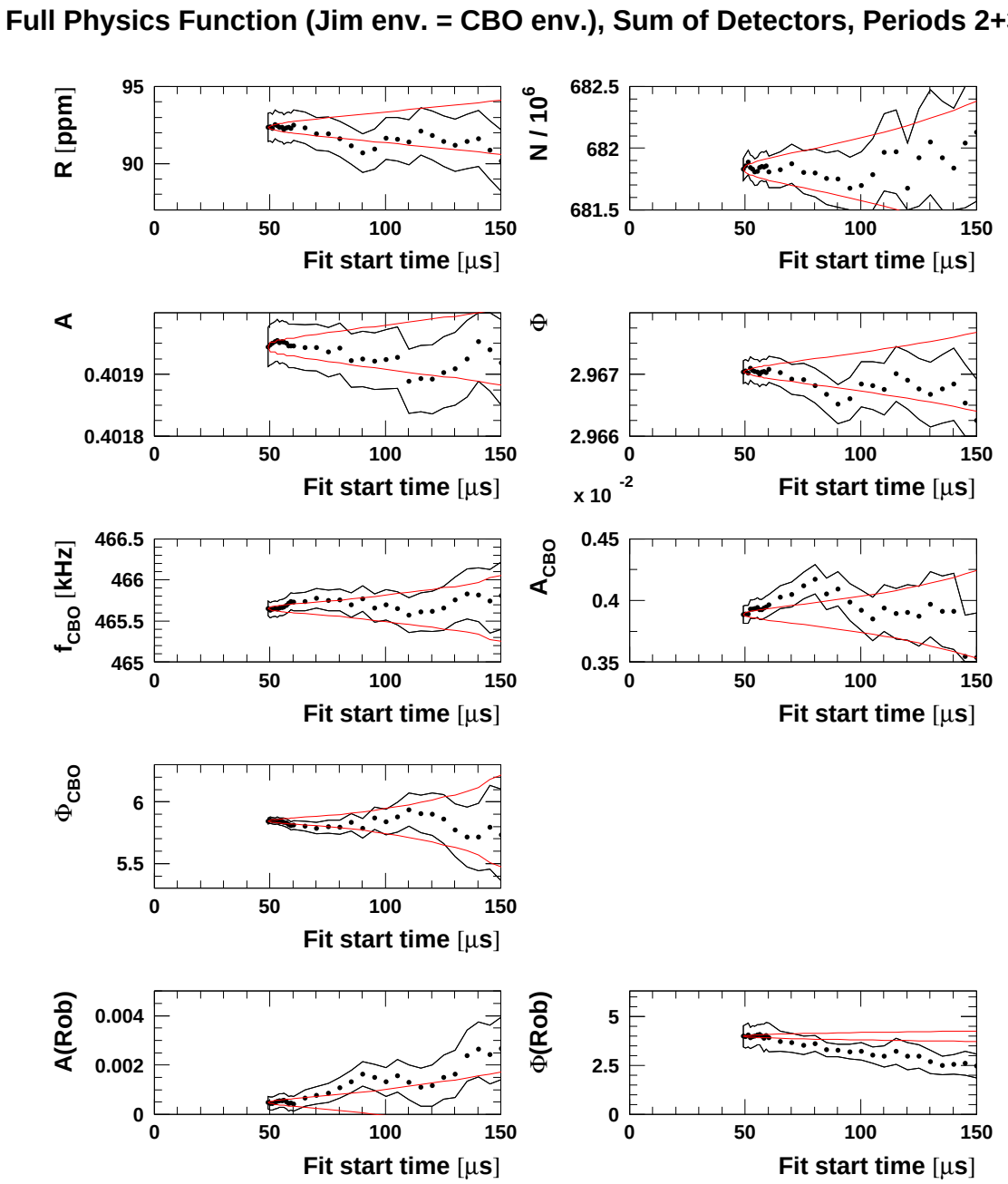

Figure 132: *Start time scan with the physics function for run periods 2+3. The phase modulation was assumed to have the same envelope as the acceptance CBO. The muon life time was fixed to 64.407μs.*

Full Physics Function (Jim env. = CBO env.), Sum of Detectors, Periods 2+3

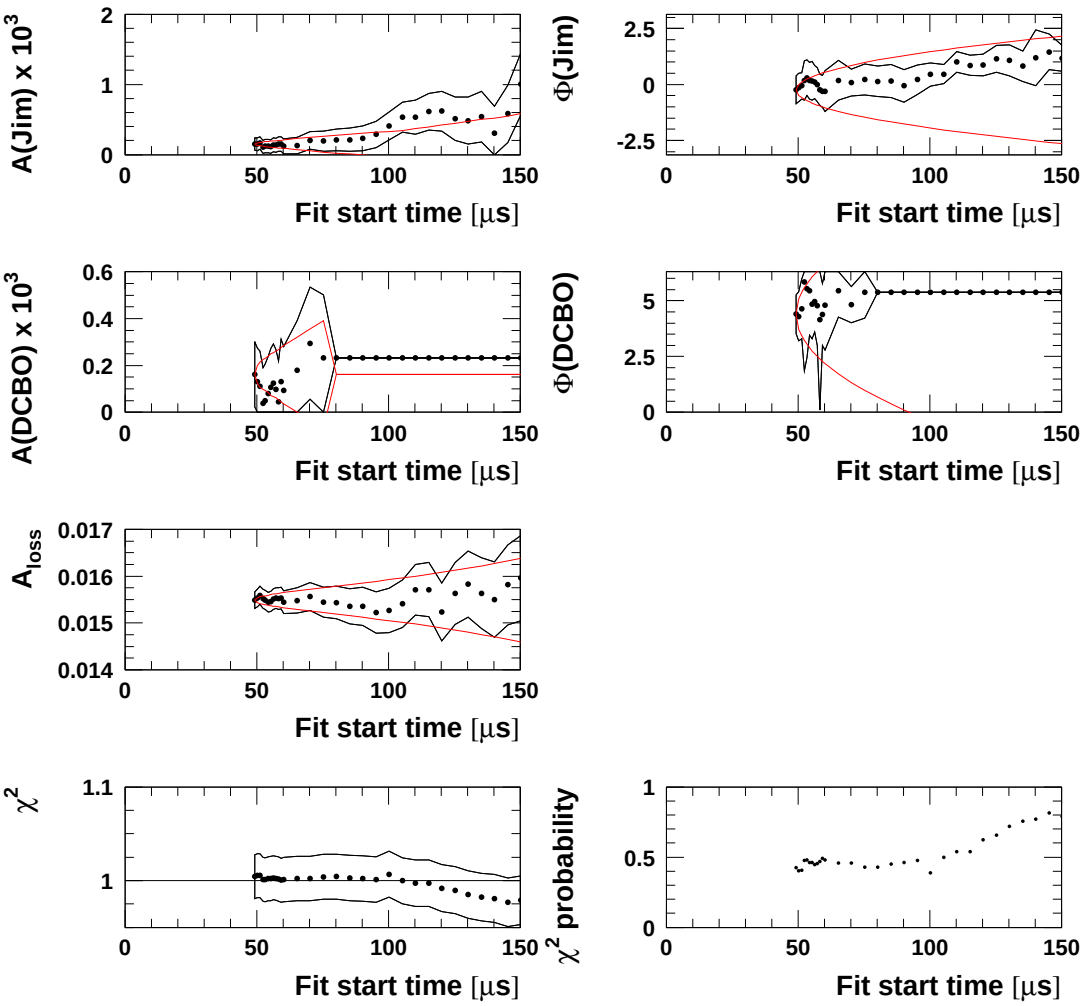

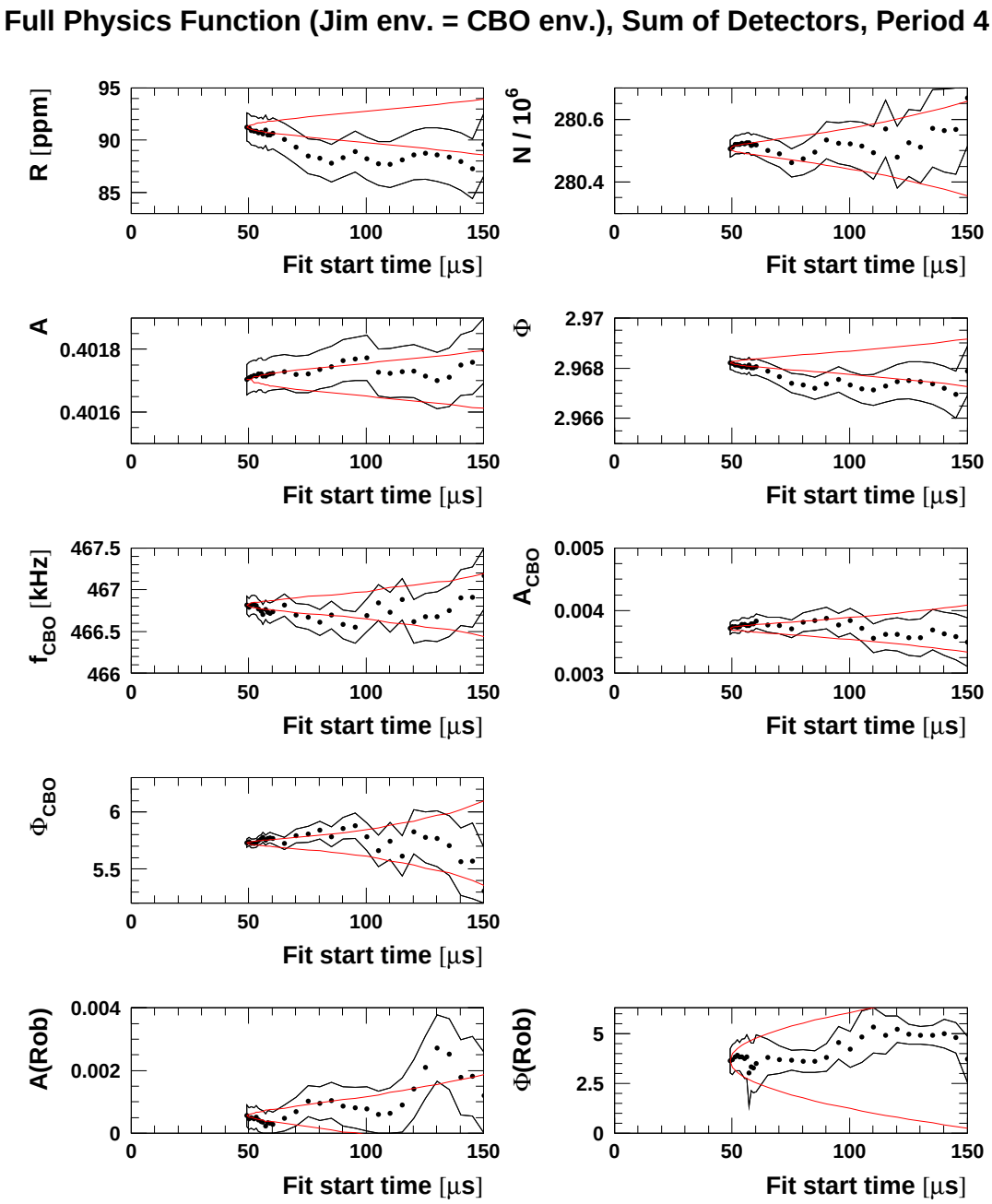

Figure 133: *Start time scan with the physics function for run period 4. The phase modulation was assumed to have the same envelope as the acceptance CBO. The muon life time was fixed to 64.407 μs.*

Full Physics Function (Jim env. = CBO env.), Sum of Detectors, Period 4

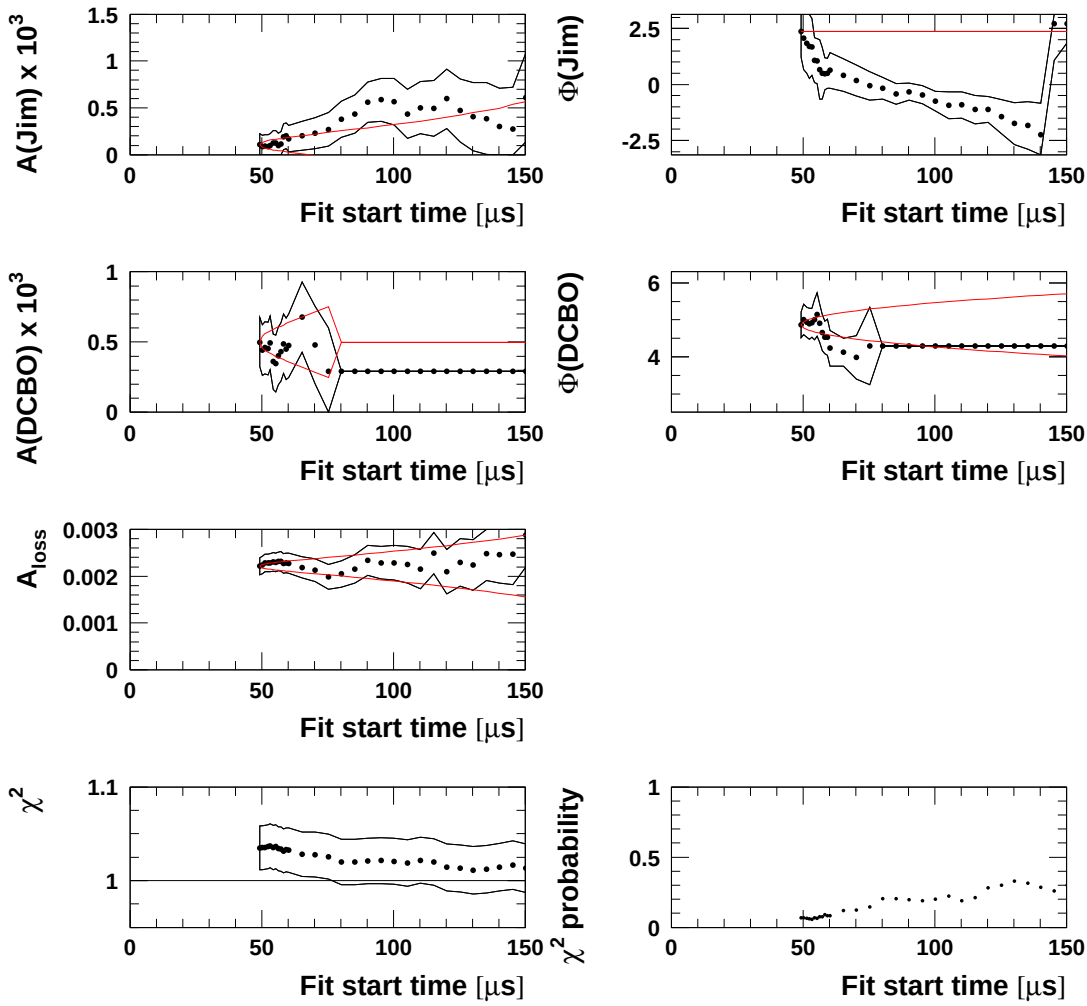

C.2 Start Time Scans for the Two Half Rings

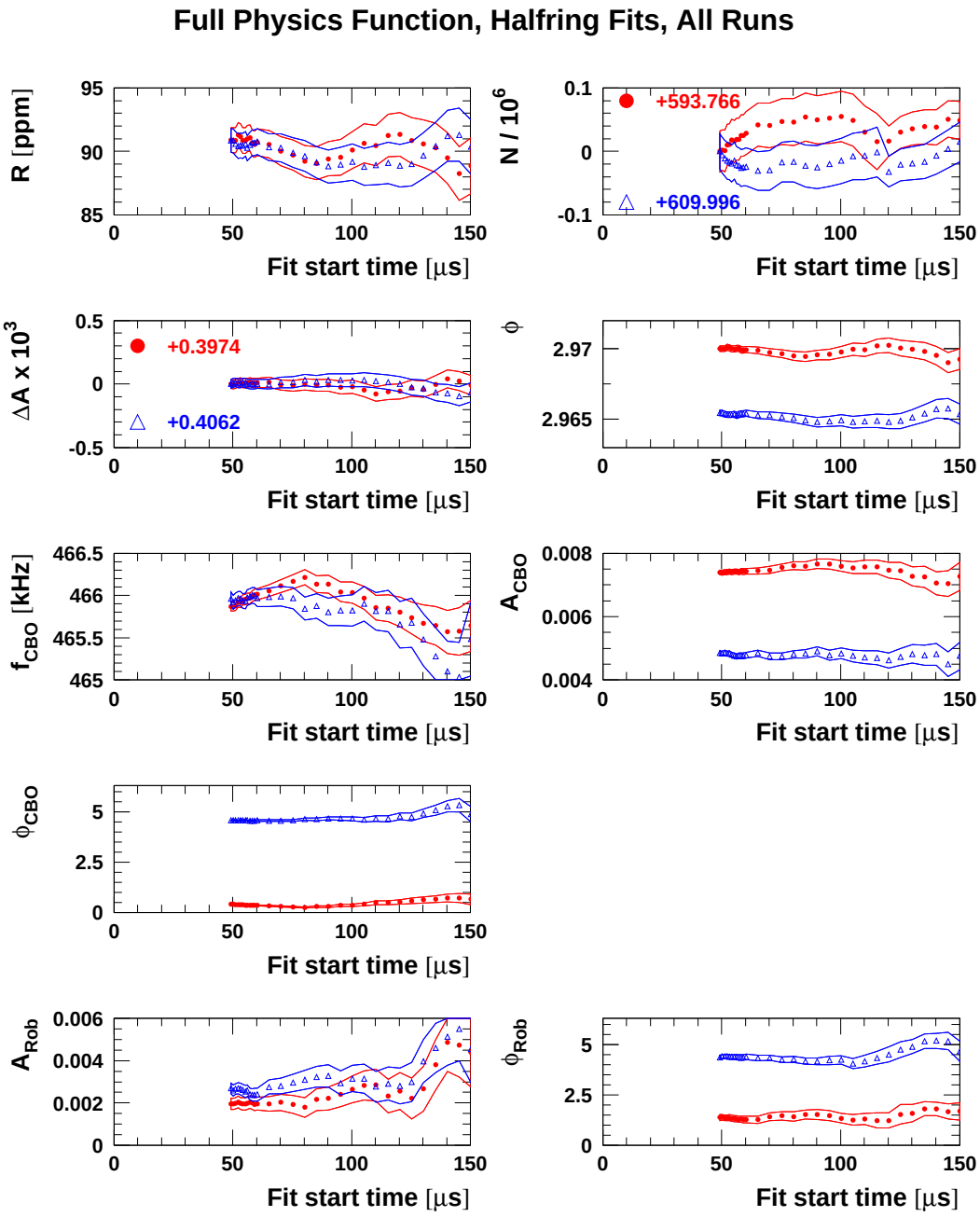

Figure 134: *Start time scan for the two half rings separately (red circles = det. 1-12, blue triangles = det. 13-24) with the physics function for all runs.*

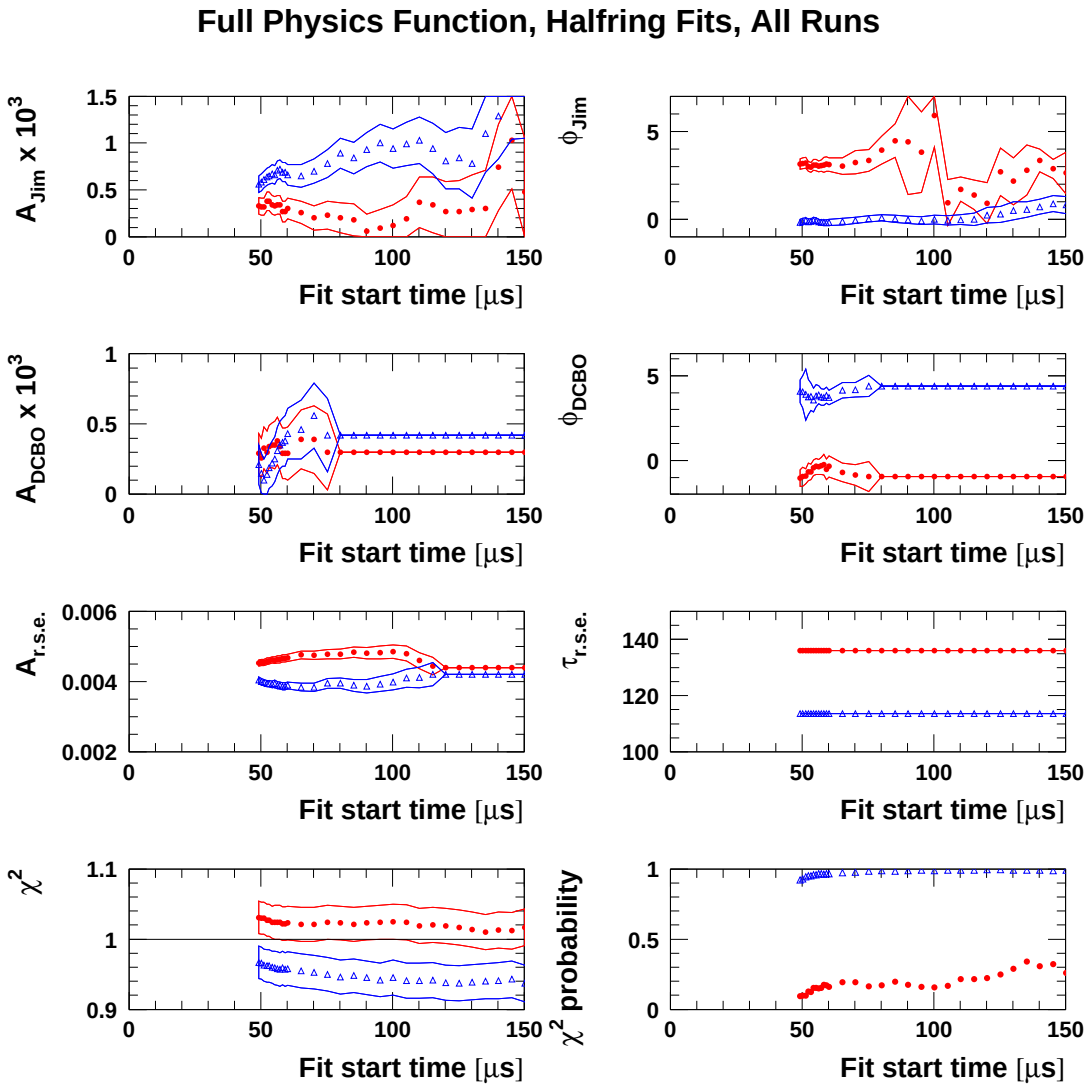
Full Physics Function, Halfring Fits, All Runs
A_{Jim} x 10^3
ϕ_{Jim}
A_{DCBO} x 10^3
ϕ_{DCBO}
$A_{r.s.e.}$
$\tau_{r.s.e.}$
χ^2
χ^2 probability
Fit start time [μs]

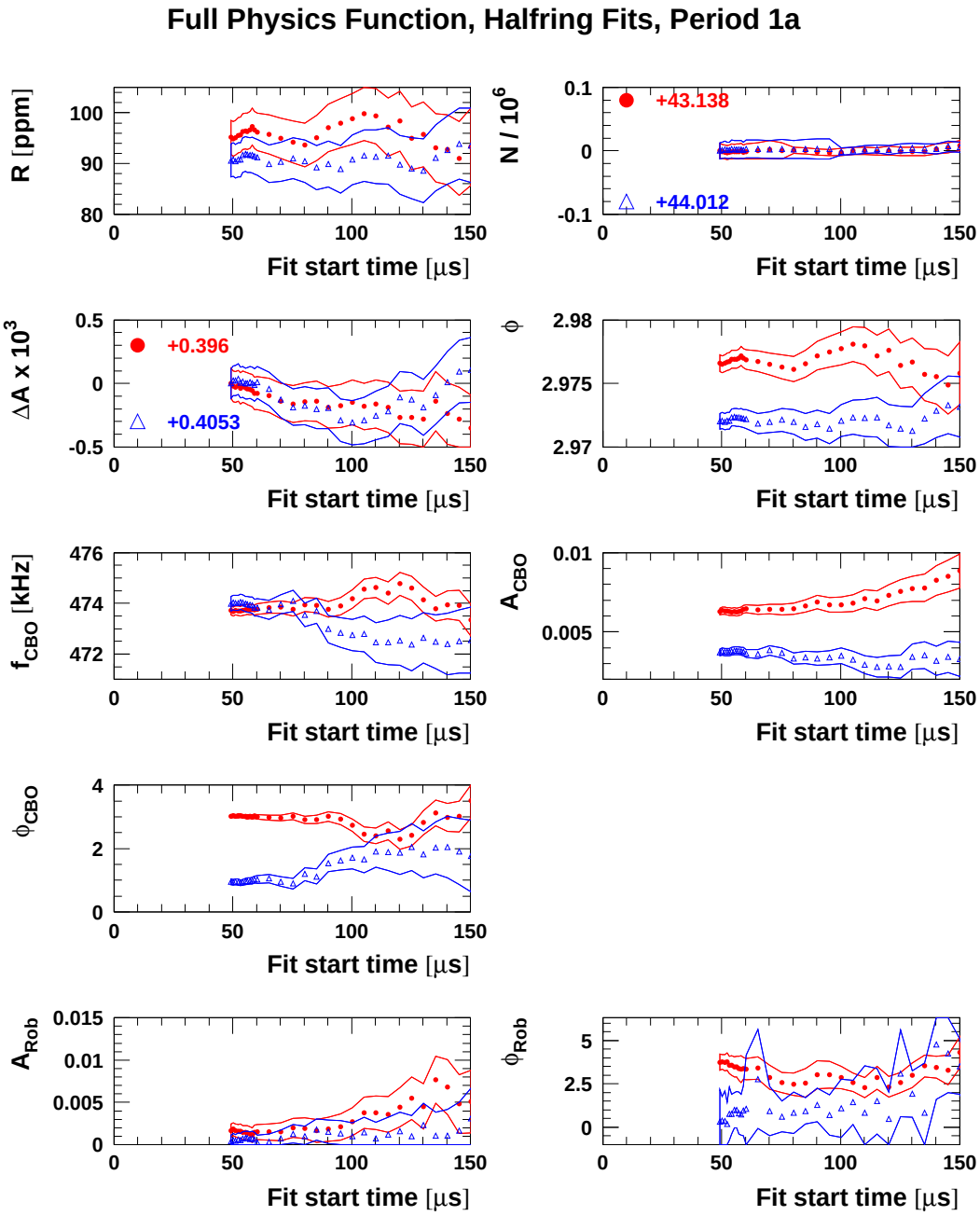

Figure 135: *Start time scan for the two half rings separately (red circles = det. 1-12, blue triangles = det. 13-24) with the physics function for run period 1a.*

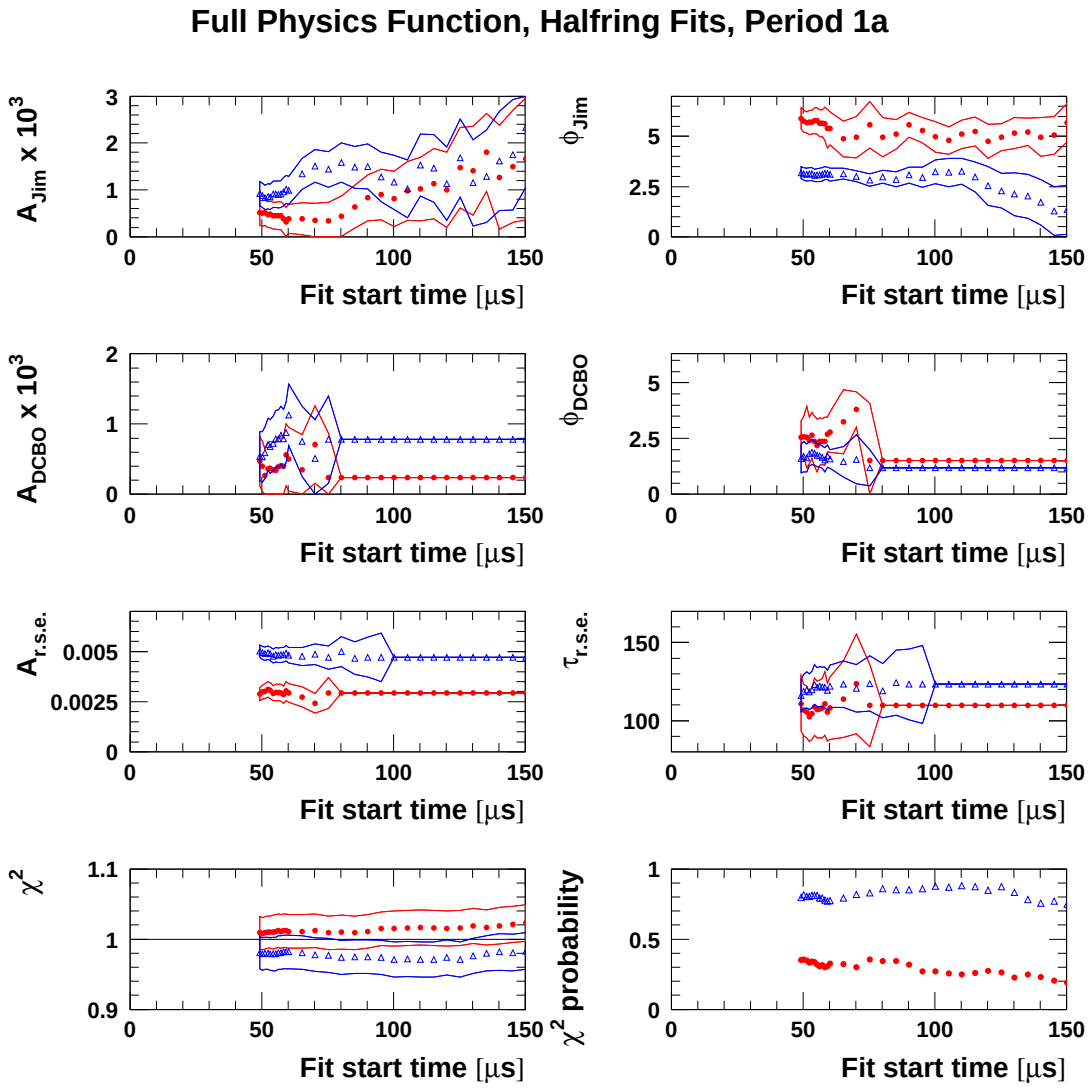
Full Physics Function, Halfring Fits, Period 1a
A_{Jim} x 10^3
ϕ_{Jim}
A_{DCBO} x 10^3
ϕ_{DCBO}
$A_{r.s.e.}$
$\tau_{r.s.e.}$
χ^2
χ^2 probability
Fit start time [μs]

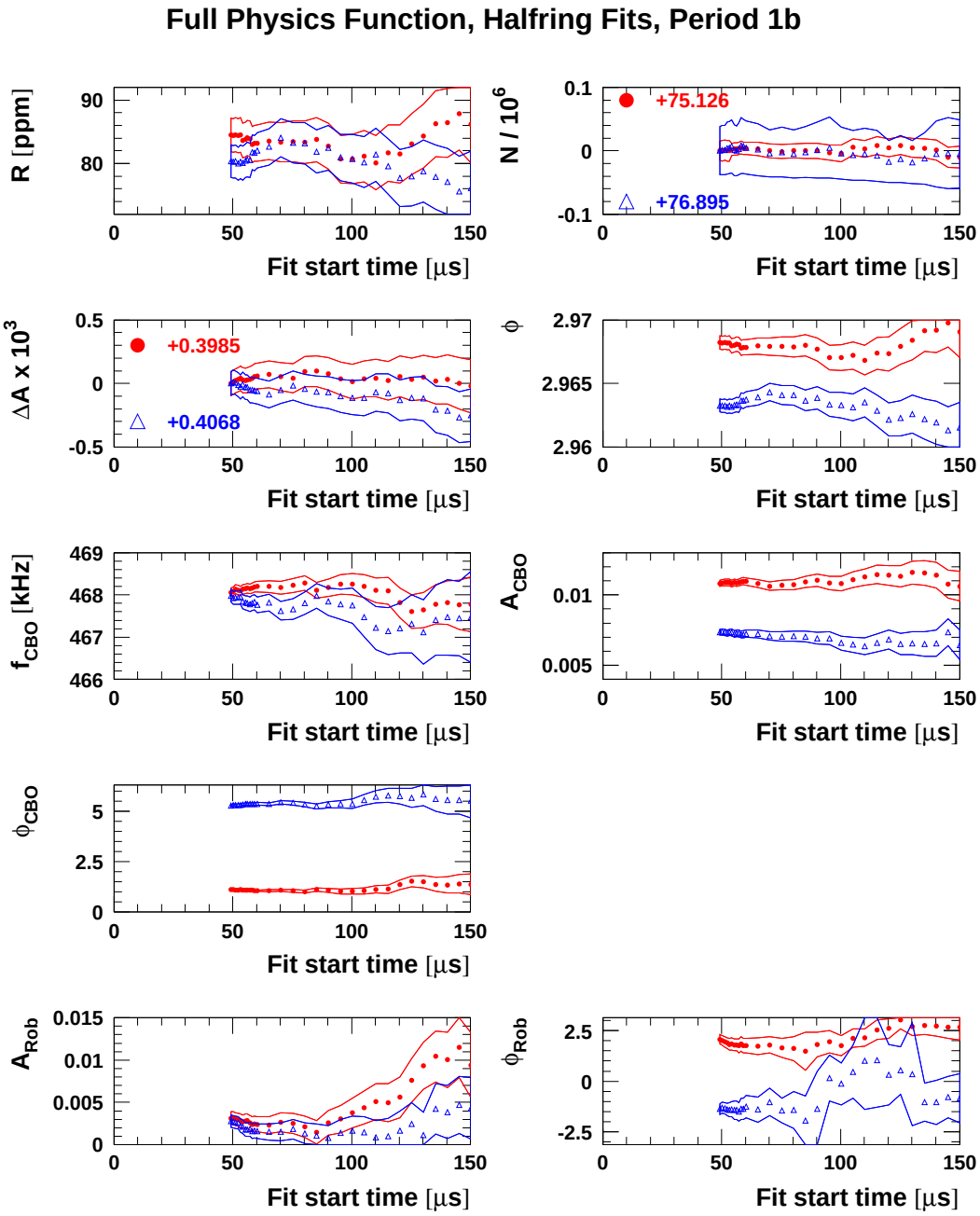

Figure 136: *Start time scan for the two half rings separately (red circles = det. 1-12, blue triangles = det. 13-24) with the physics function for run period 1b.*

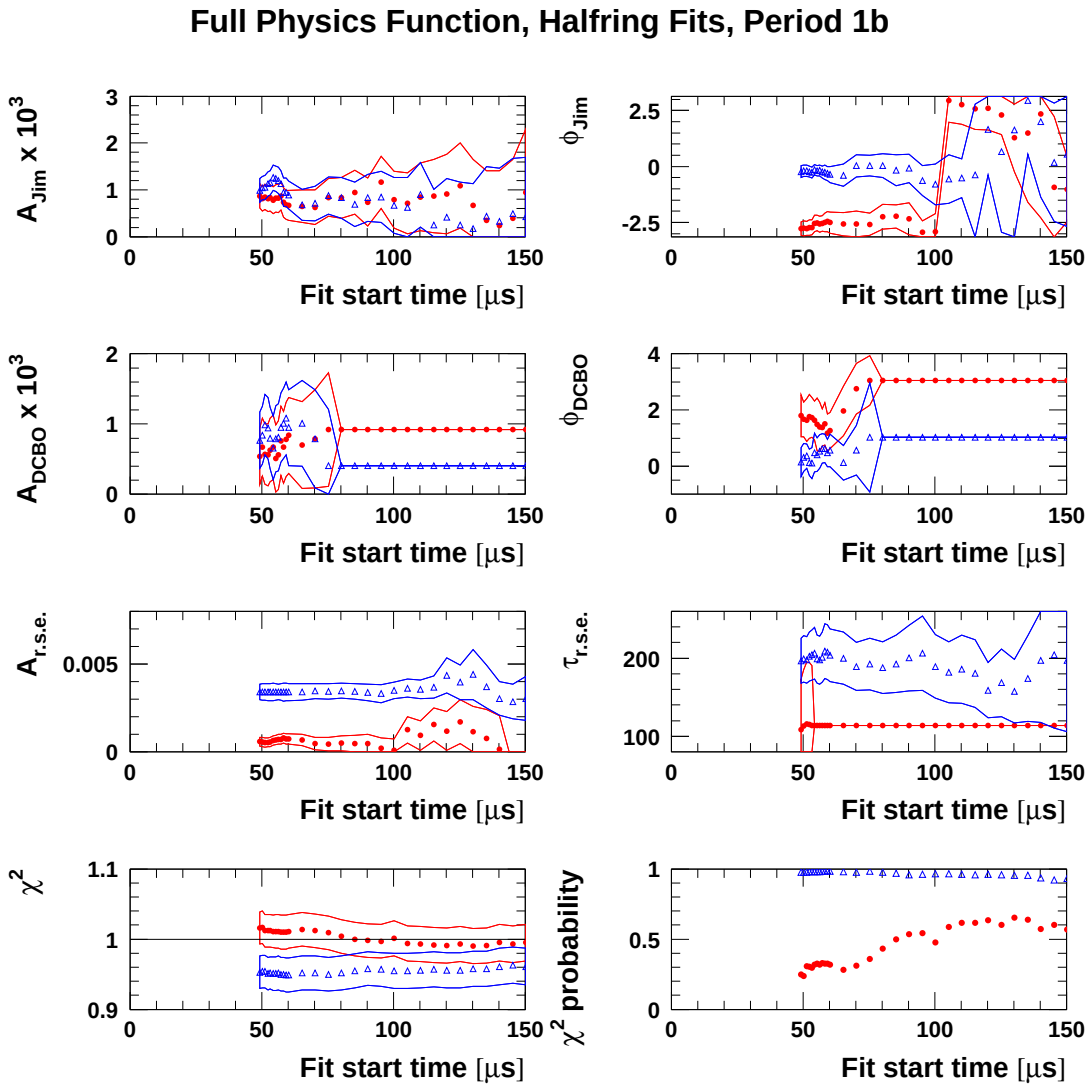
Full Physics Function, Halfring Fits, Period 1b
A_{Jim} x 10^3
ϕ_{Jim}
A_{DCBO} x 10^3
ϕ_{DCBO}
$A_{r.s.e.}$
$\tau_{r.s.e.}$
χ^2
χ^2 probability
Fit start time [μs]

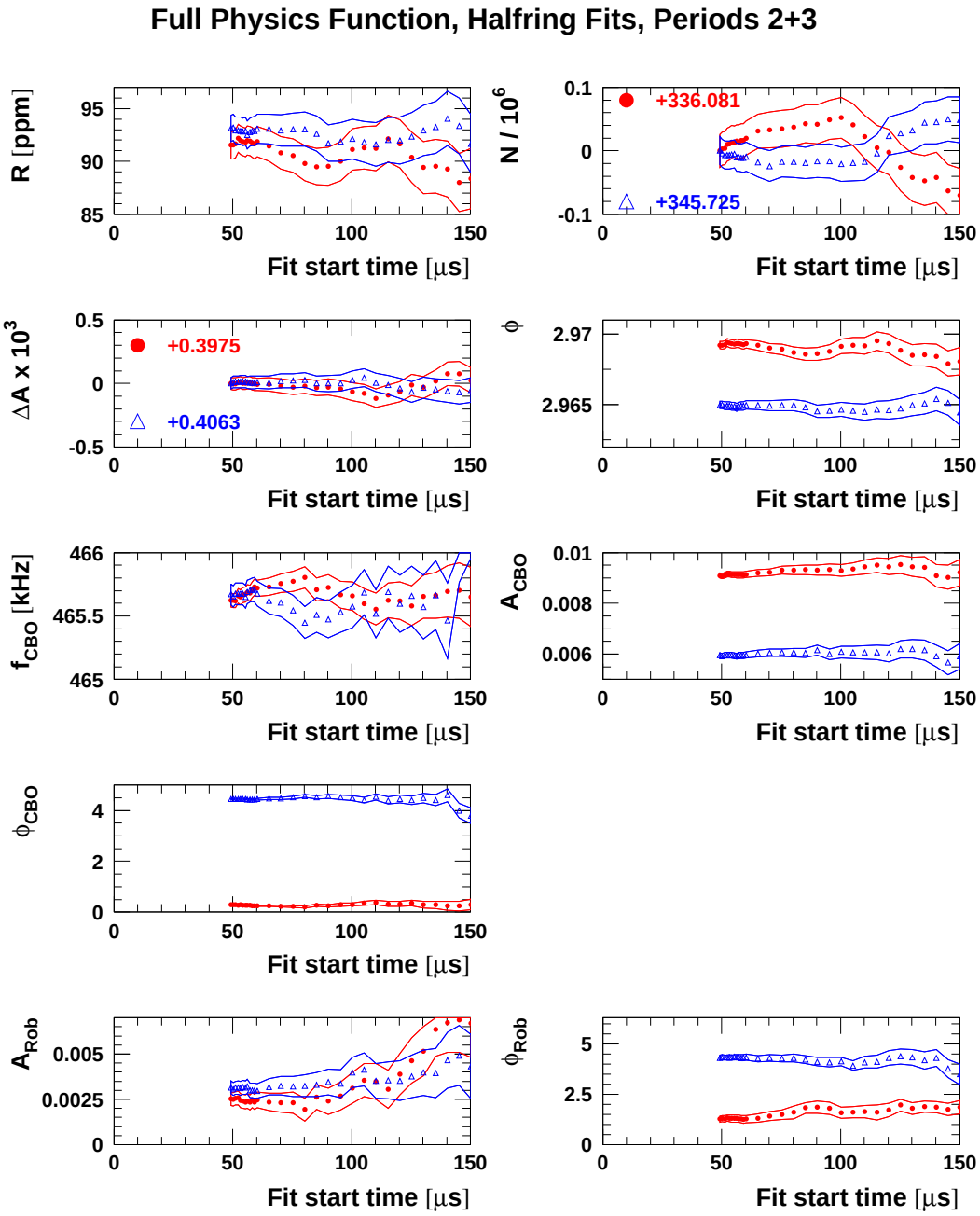

Figure 137: *Start time scan for the two half rings separately (red circles = det. 1-12, blue triangles = det. 13-24) with the physics function for run periods 2+3.*

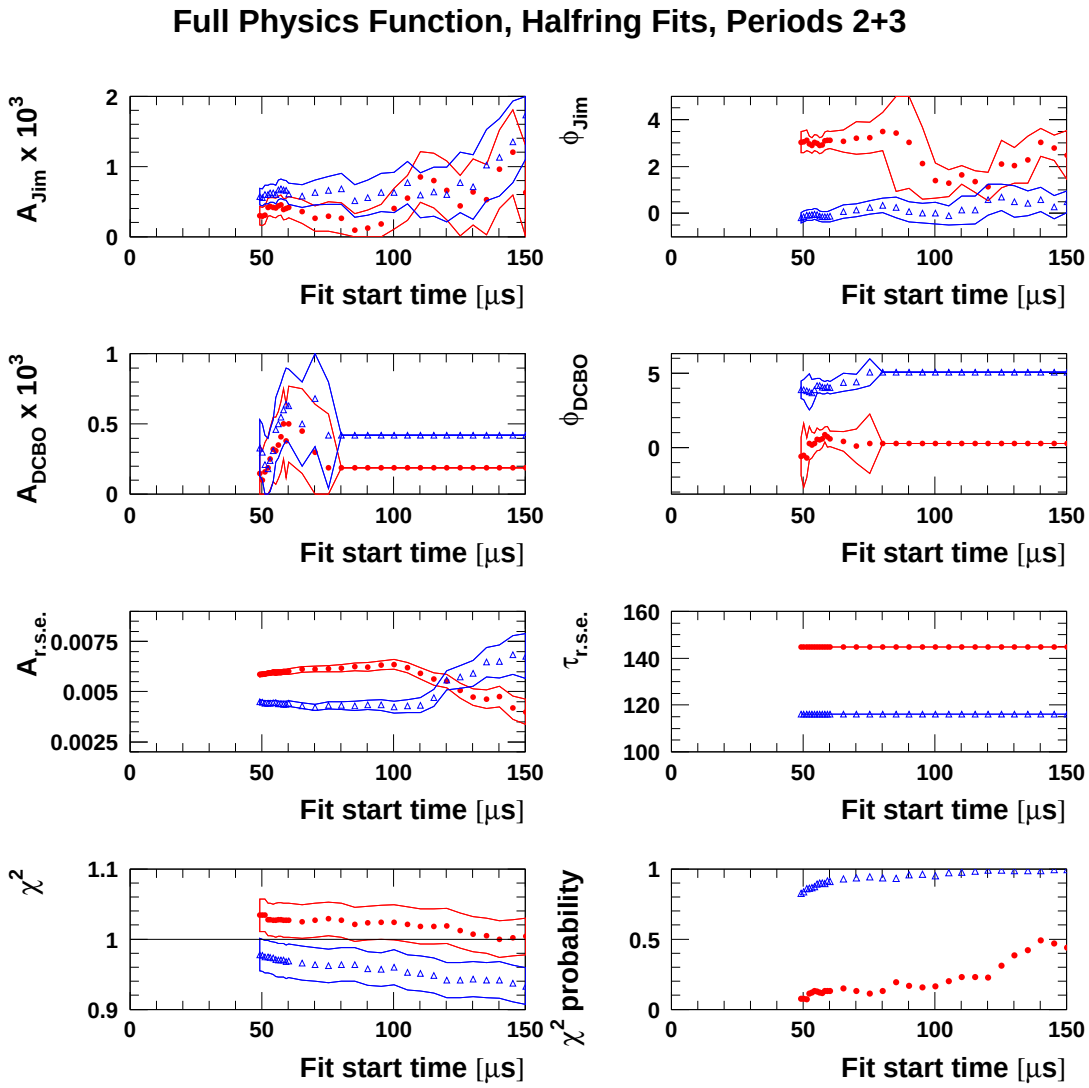
Full Physics Function, Halfring Fits, Periods 2+3
A_{Jim} x 10^3
ϕ_{Jim}
A_{DCBO} x 10^3
ϕ_{DCBO}
$A_{r.s.e.}$
$\tau_{r.s.e.}$
χ^2
χ^2 probability
Fit start time [μs]

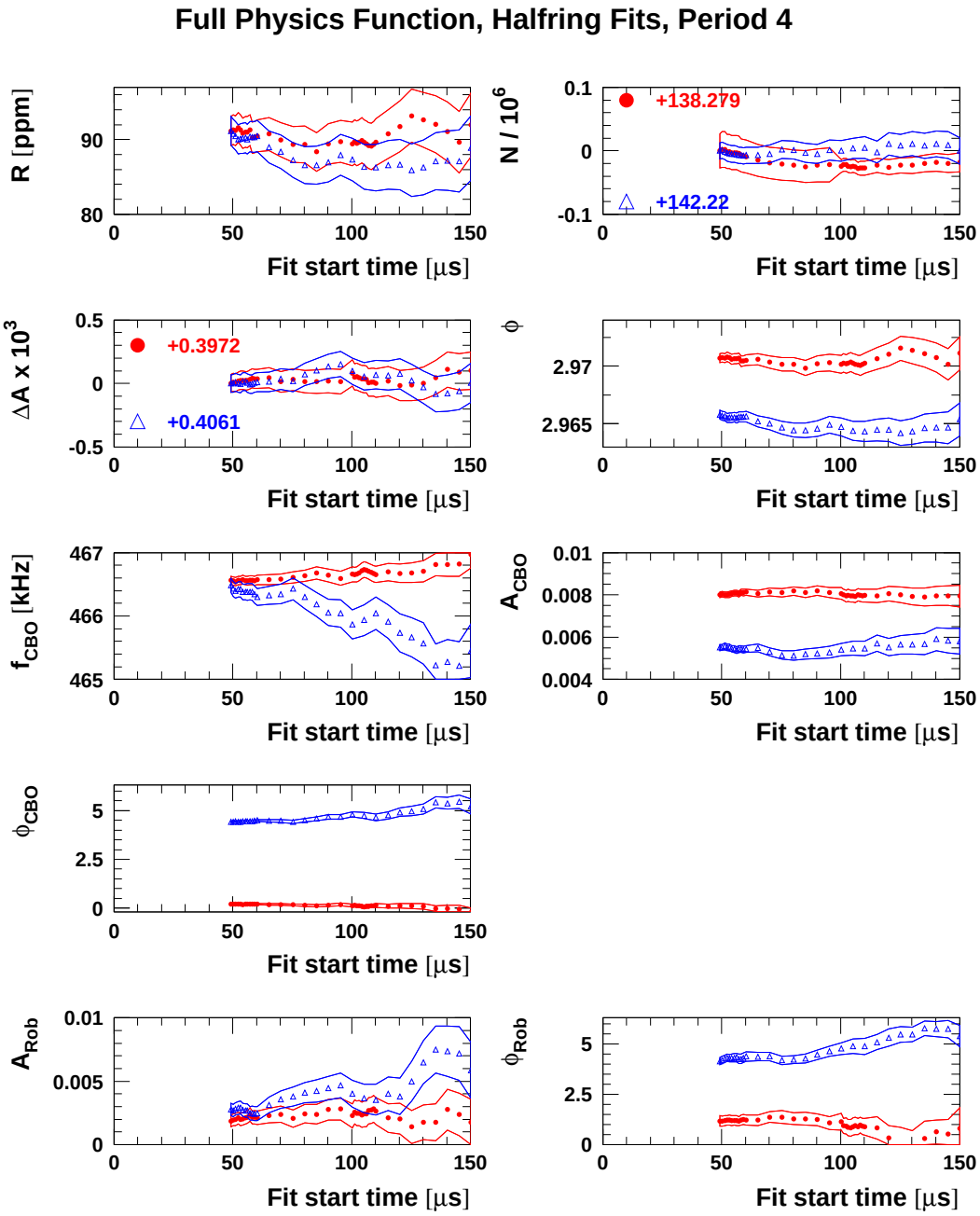

Figure 138: *Start time scan for the two half rings separately (red circles = det. 1-12, blue triangles = det. 13-24) with the physics function for run period 4.*

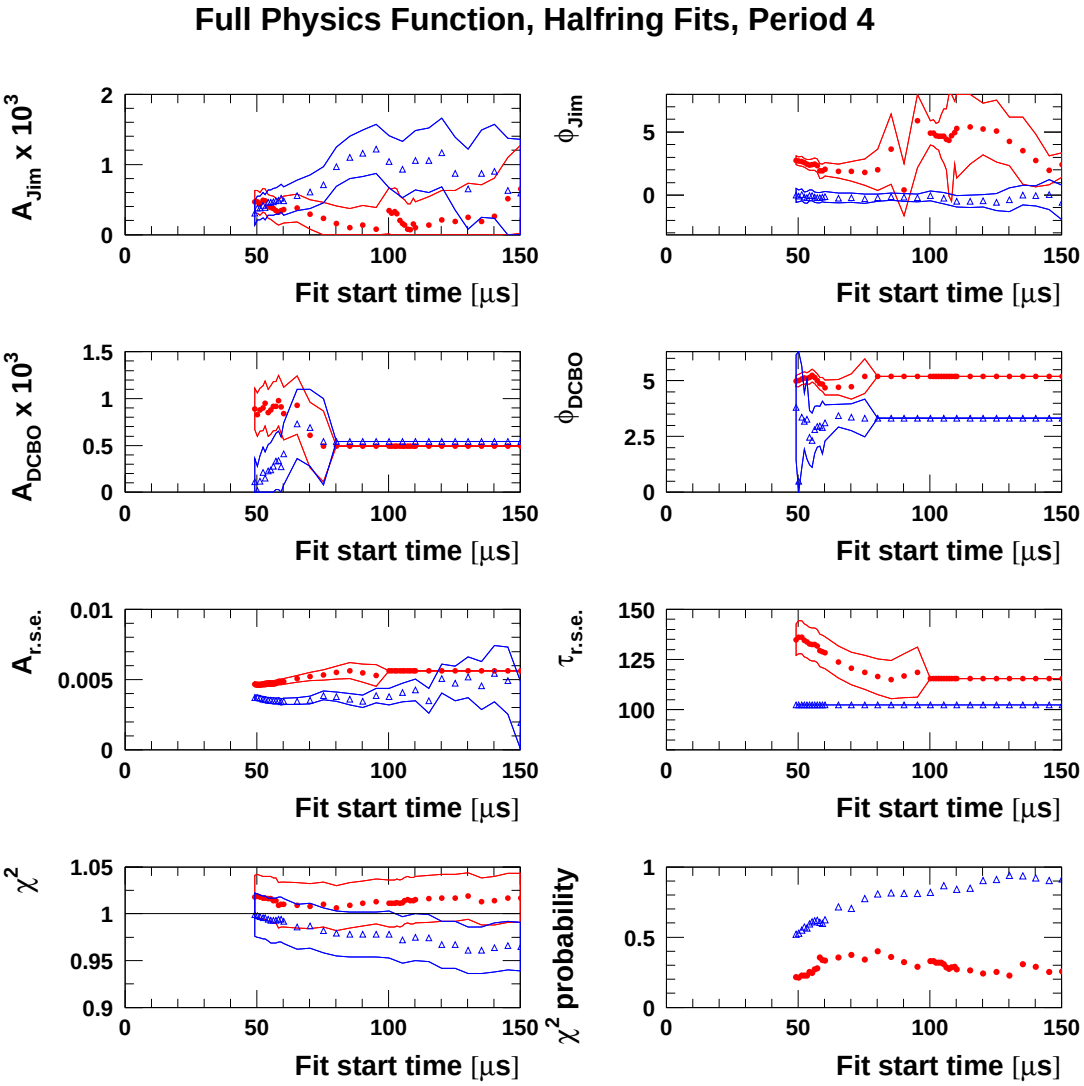
Full Physics Function, Halfring Fits, Period 4
A_{Jim} x 10^3
ϕ_{Jim}
A_{DCBO} x 10^3
ϕ_{DCBO}
$A_{r.s.e.}$
$\tau_{r.s.e.}$
χ^2
χ^2 probability
Fit start time [μs]

C.3 Individual Detector Fits Starting at 49.2 μs

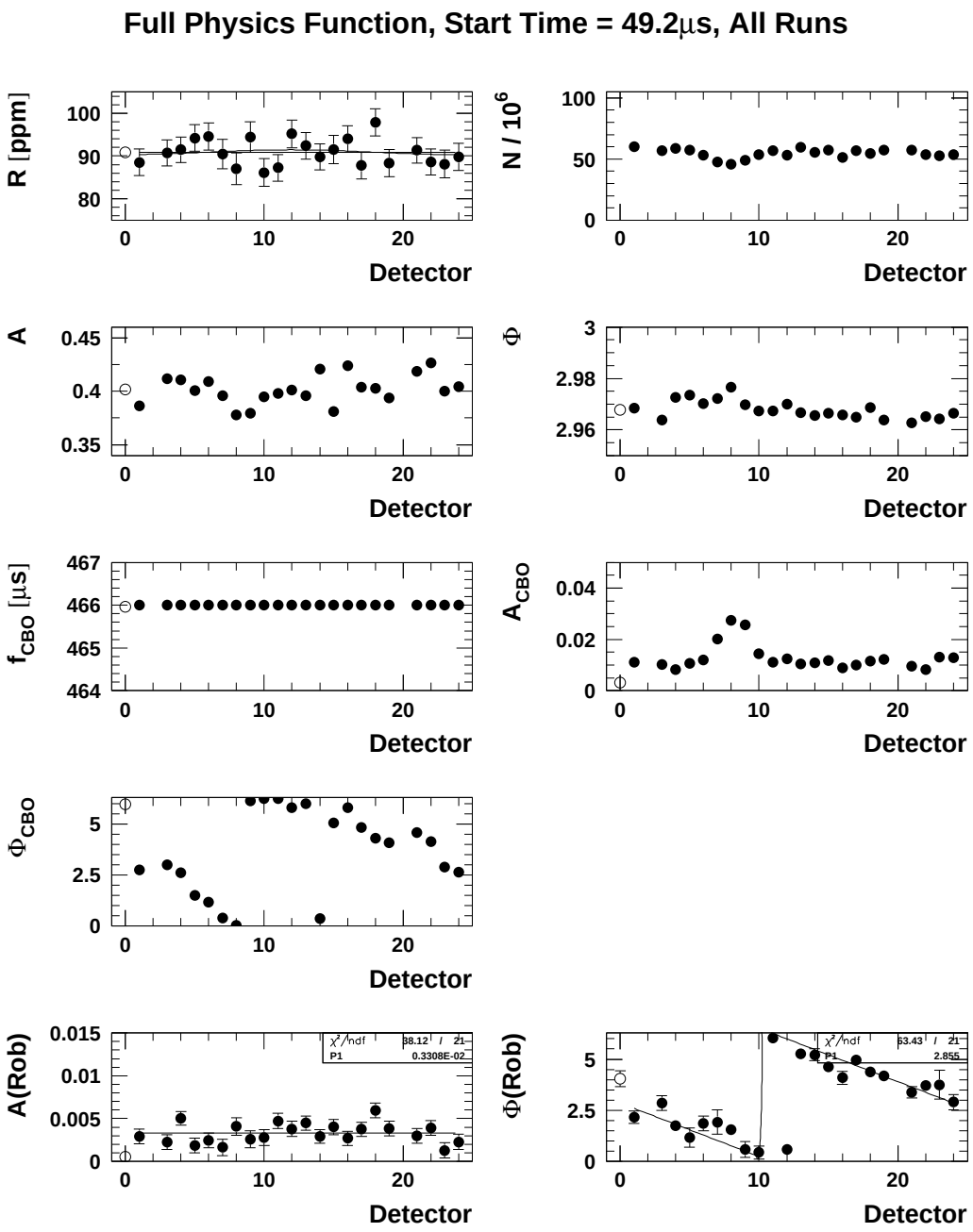

Figure 139: *Fits of individual detector spectra with the physics function for all runs.*

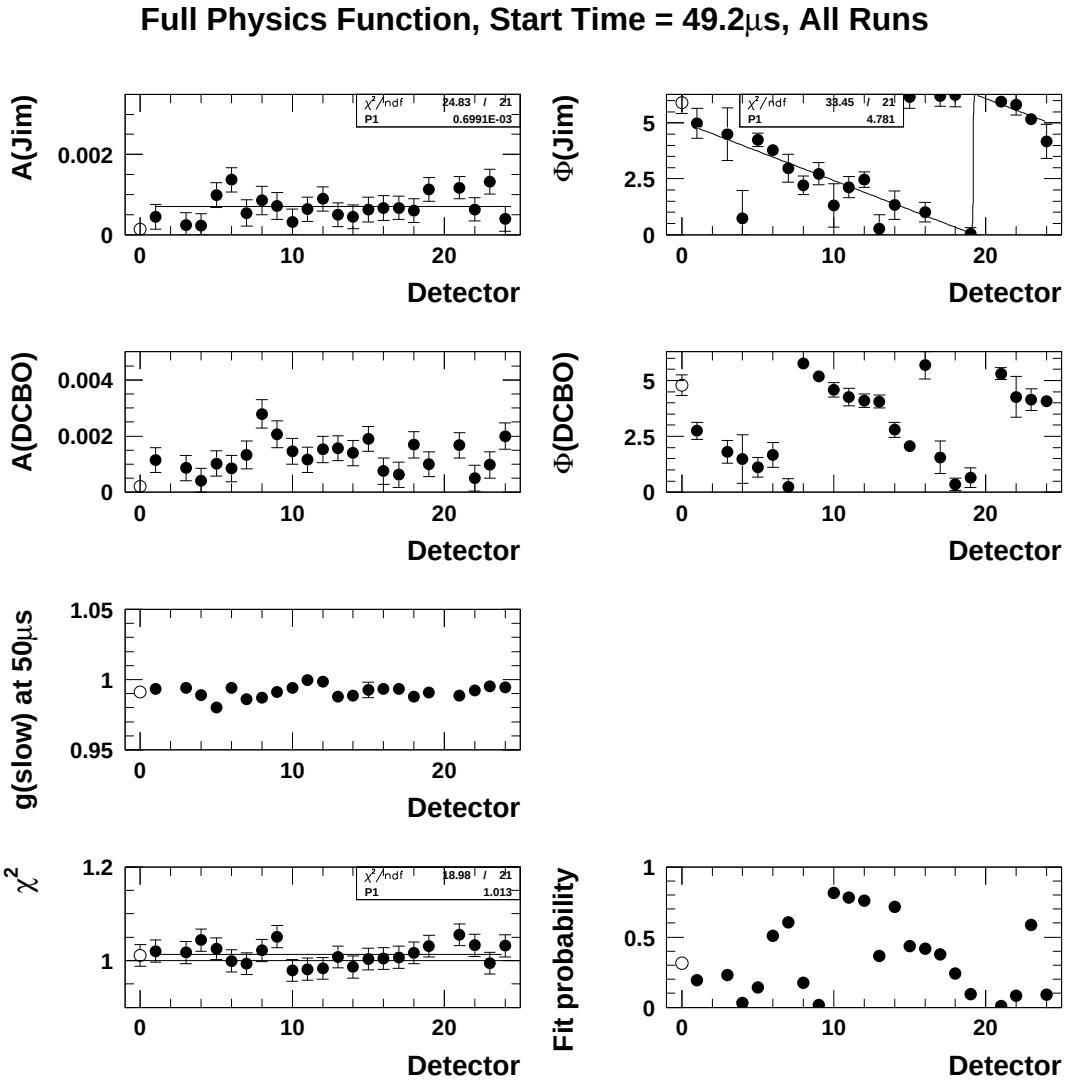
Full Physics Function, Start Time = 49.2μs, All Runs
A(Jim)
χ²/ndf 24.83 / 21
P1 0.6991E-03
Φ(Jim)
χ²/ndf 38.45 / 21
P1 4.781
A(DCBO)
Φ(DCBO)
g(slow) at 50μs
χ²
χ²/ndf 18.98 / 21
P1 1.013
Fit probability
Detector

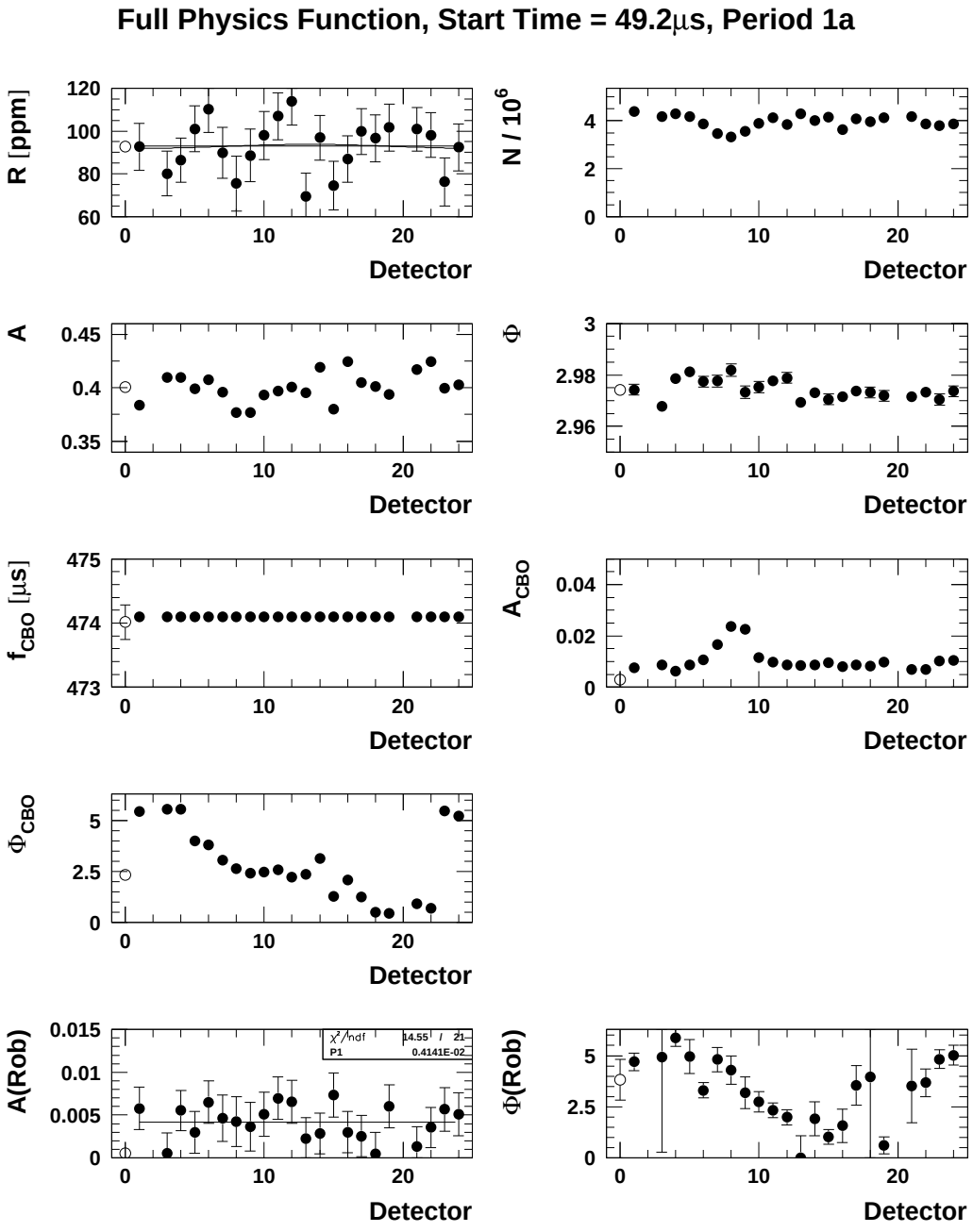

Figure 140: *Fits of individual detector spectra with the physics function for run period 1a.*

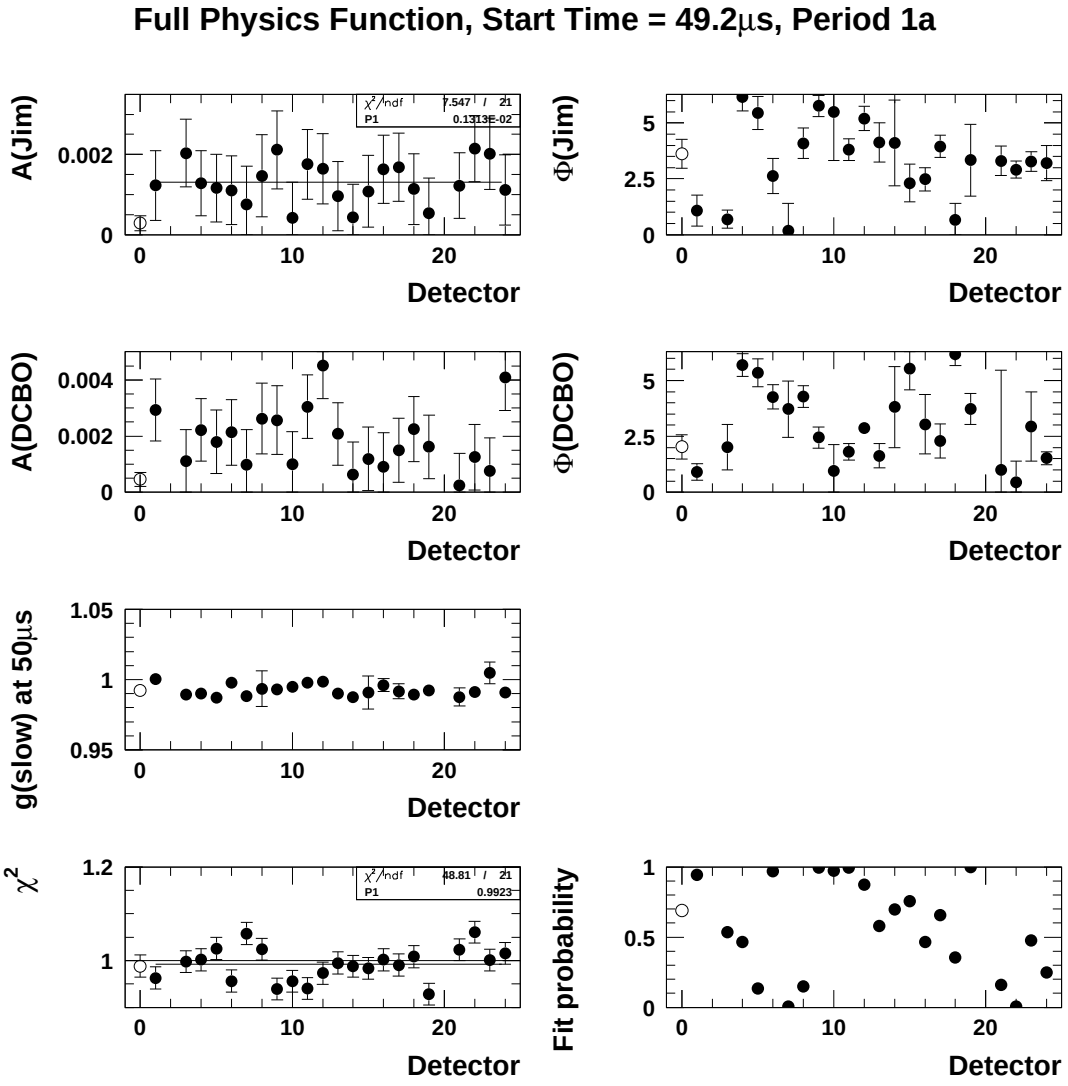
Full Physics Function, Start Time = 49.2μs, Period 1a
A(Jim)
Φ(Jim)
A(DCBO)
Φ(DCBO)
g(slow) at 50μs
χ²
Fit probability
Detector
χ²/ndf 7.547 / 21
P1 0.1313E-02
χ²/ndf 48.81 / 21
P1 0.9923

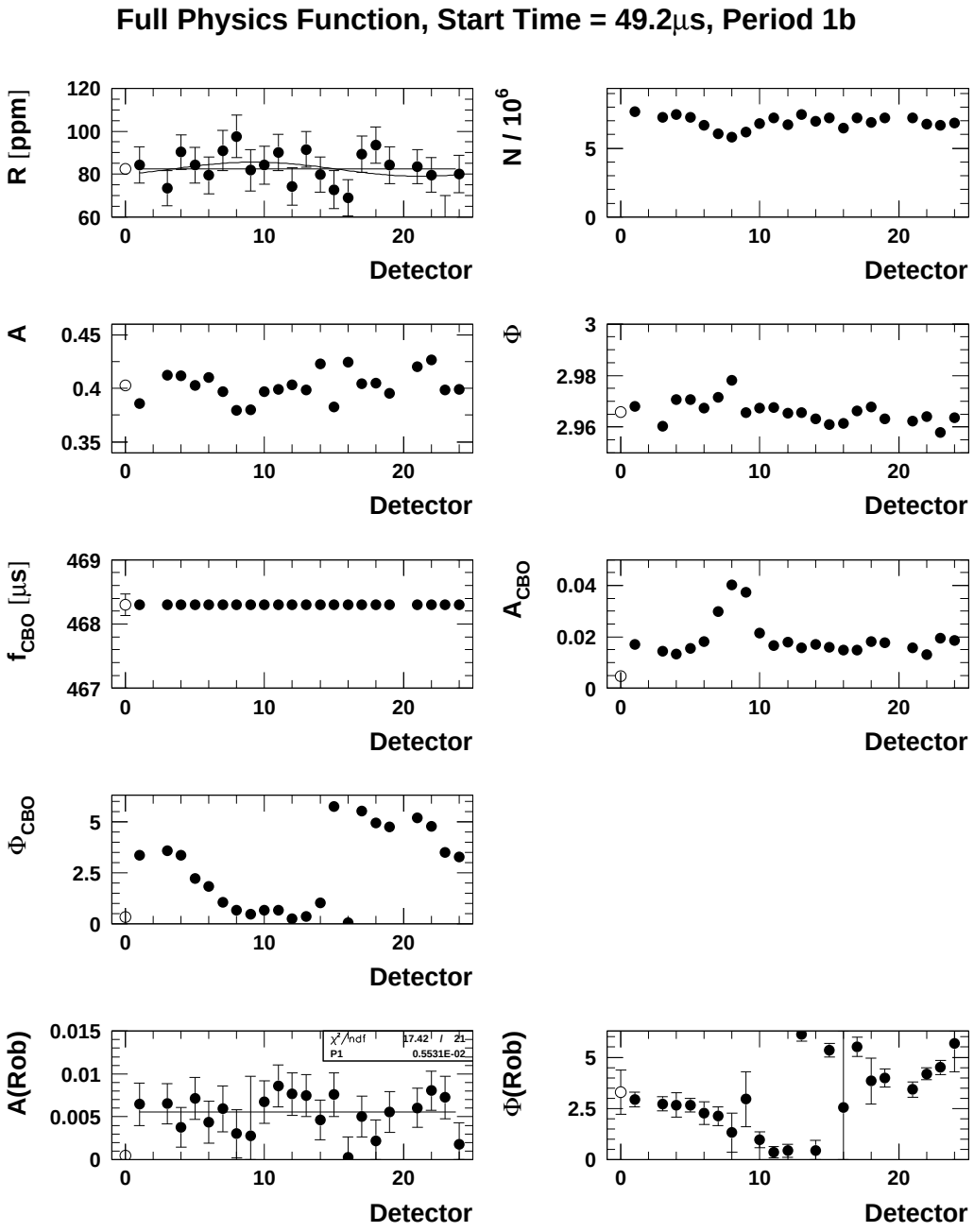

Figure 141: *Fits of individual detector spectra with the physics function for run period 1b.*

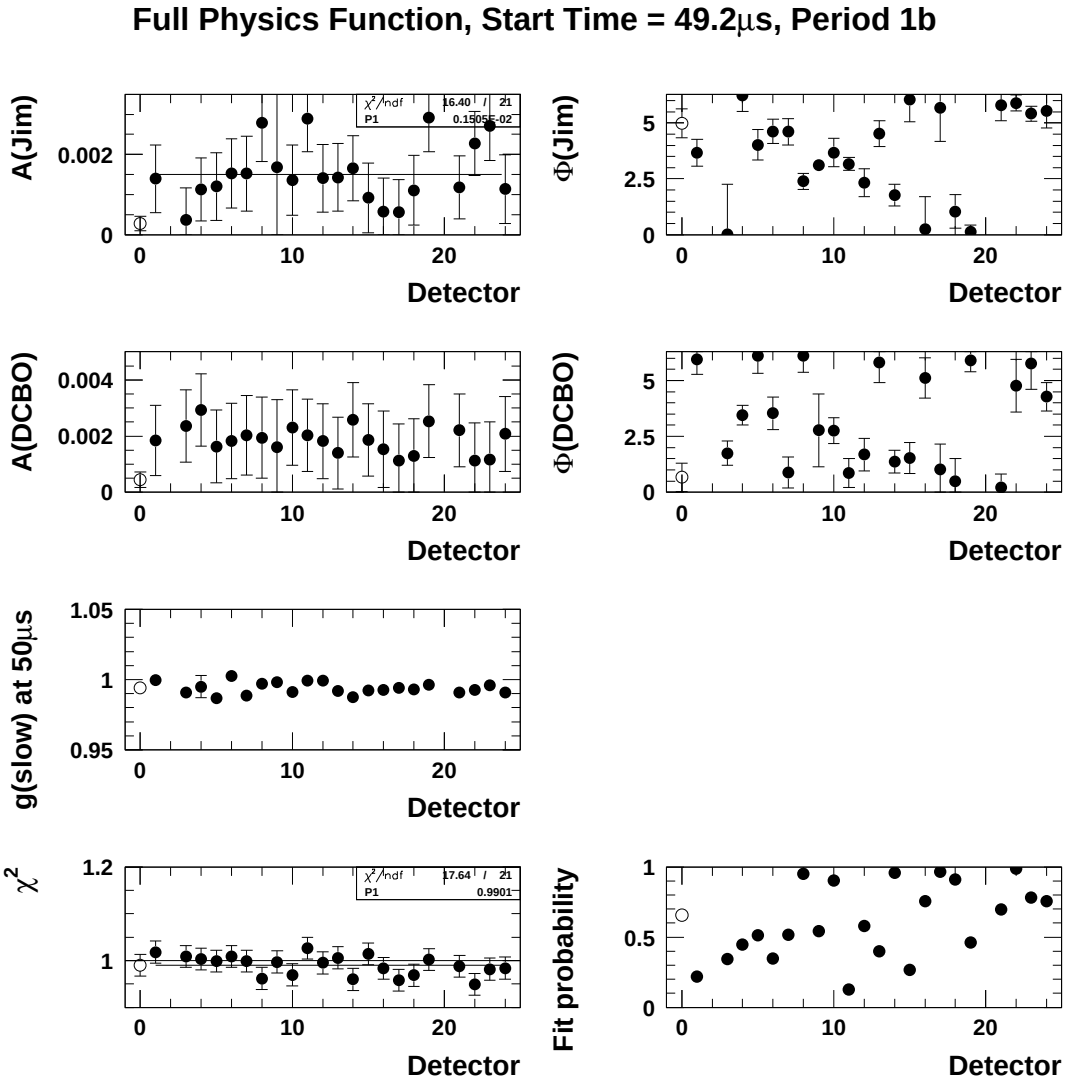
Full Physics Function, Start Time = 49.2μs, Period 1b
A(Jim)
Φ(Jim)
A(DCBO)
Φ(DCBO)
g(slow) at 50μs
χ²
Fit probability
Detector
χ²/ndf 16.40 / 21
P1 0.1505E-02
χ²/ndf 17.64 / 21
P1 0.9901

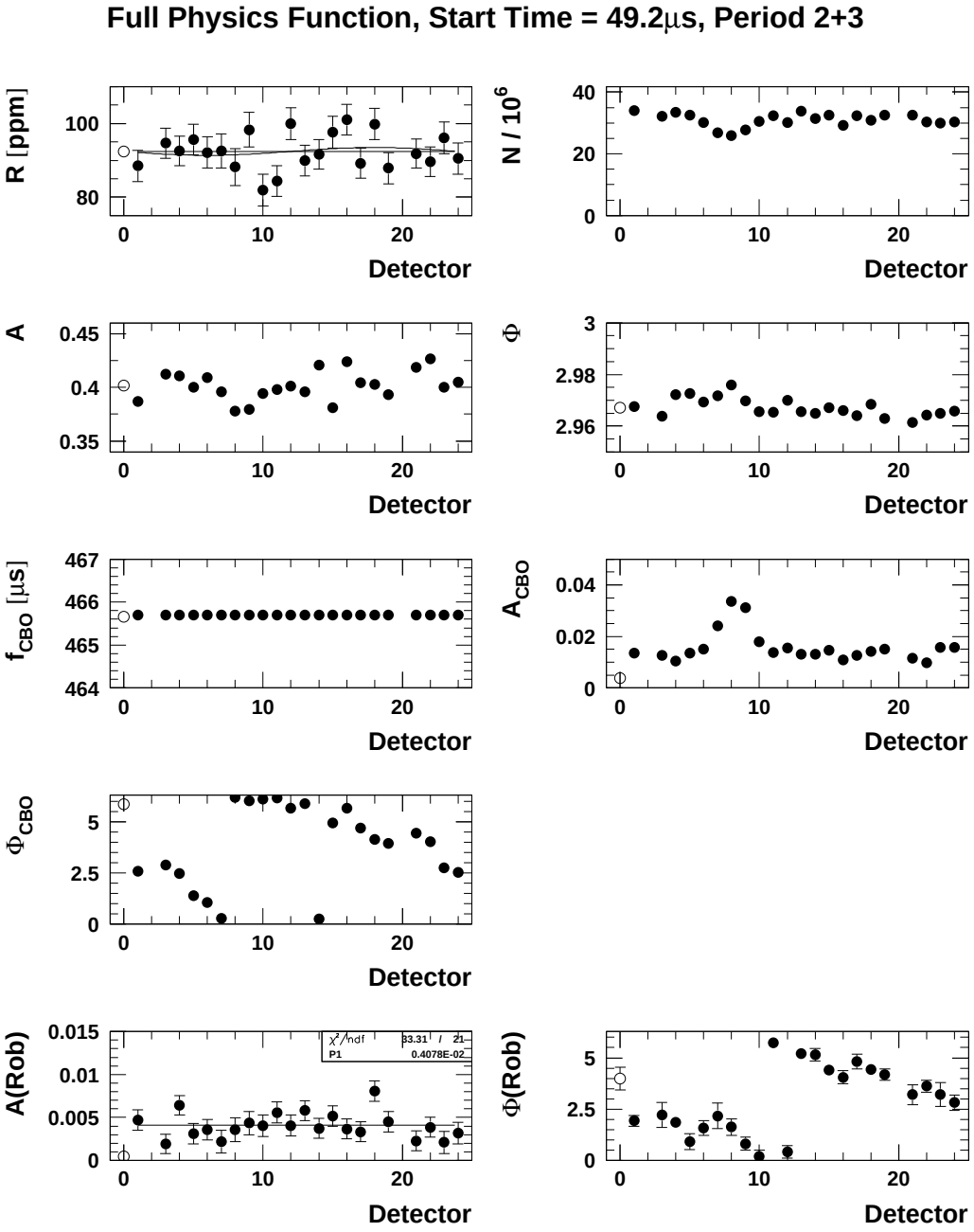

Figure 142: *Fits of individual detector spectra with the physics function for run periods 2+3.*

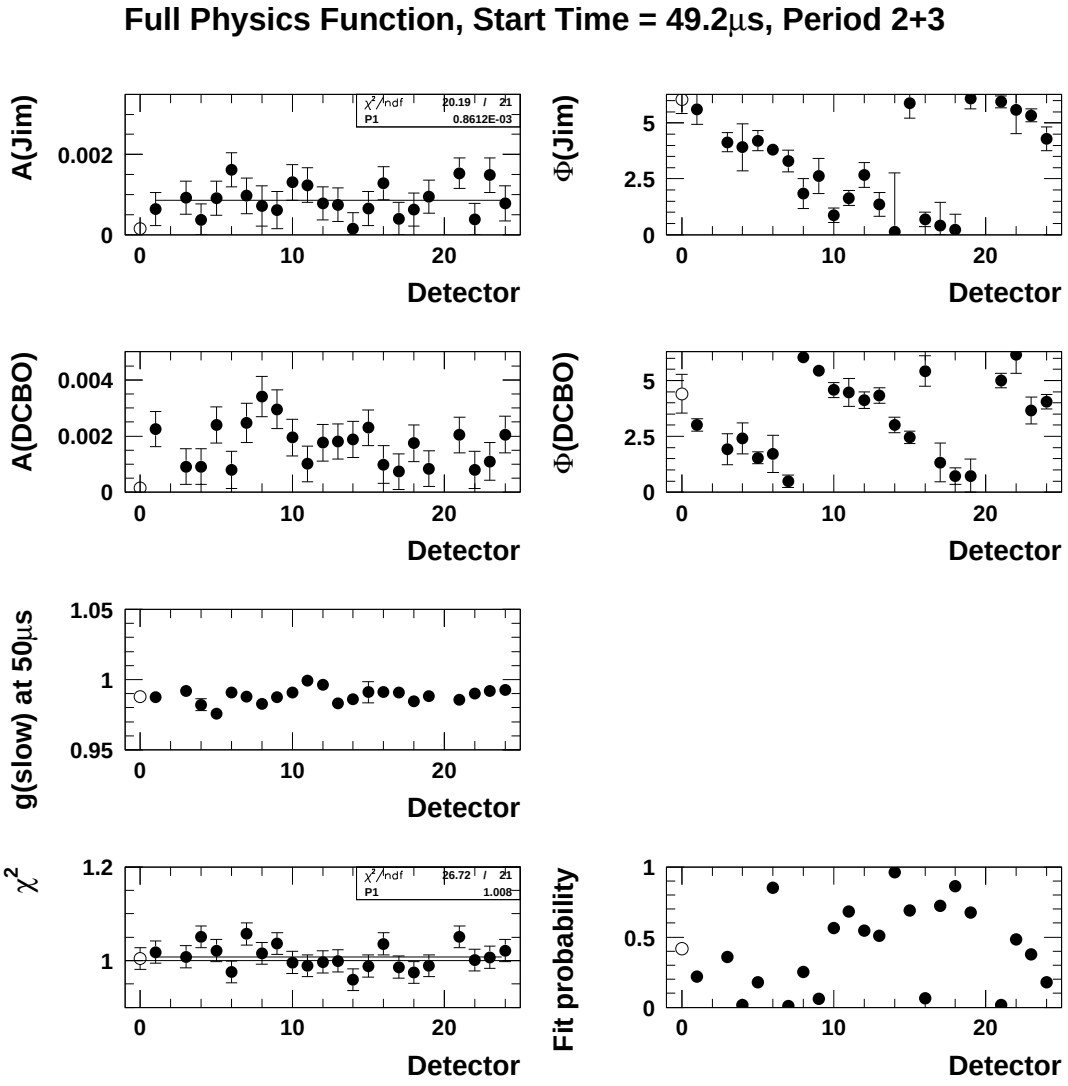
Full Physics Function, Start Time = 49.2μs, Period 2+3
A(Jim)
χ²/ndf 20.19 / 21
P1 0.8612E-03
Φ(Jim)
A(DCBO)
Φ(DCBO)
g(slow) at 50μs
χ²
χ²/ndf 26.72 / 21
P1 1.008
Fit probability
Detector

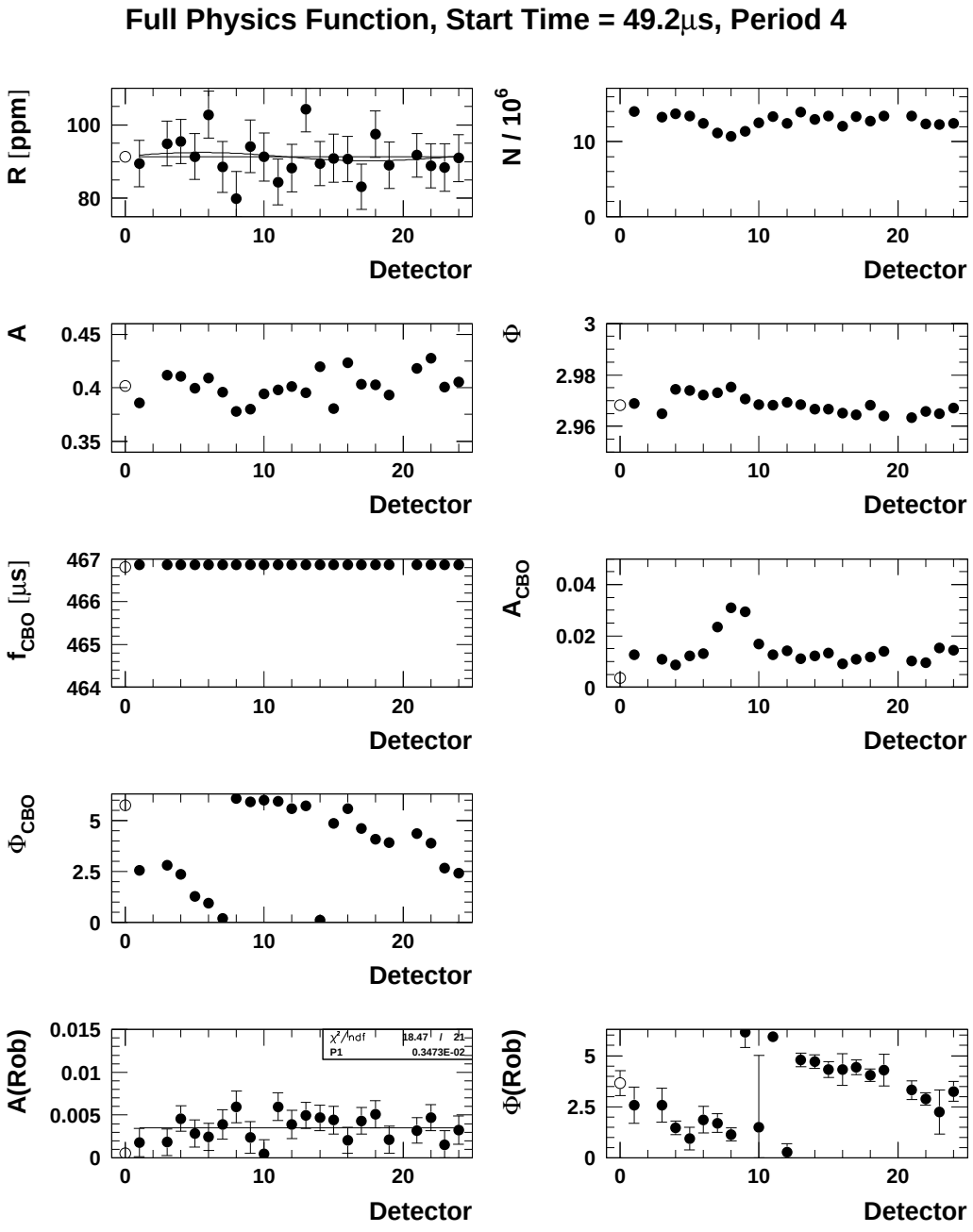

Figure 143: *Fits of individual detector spectra with the physics function for run period 4.*

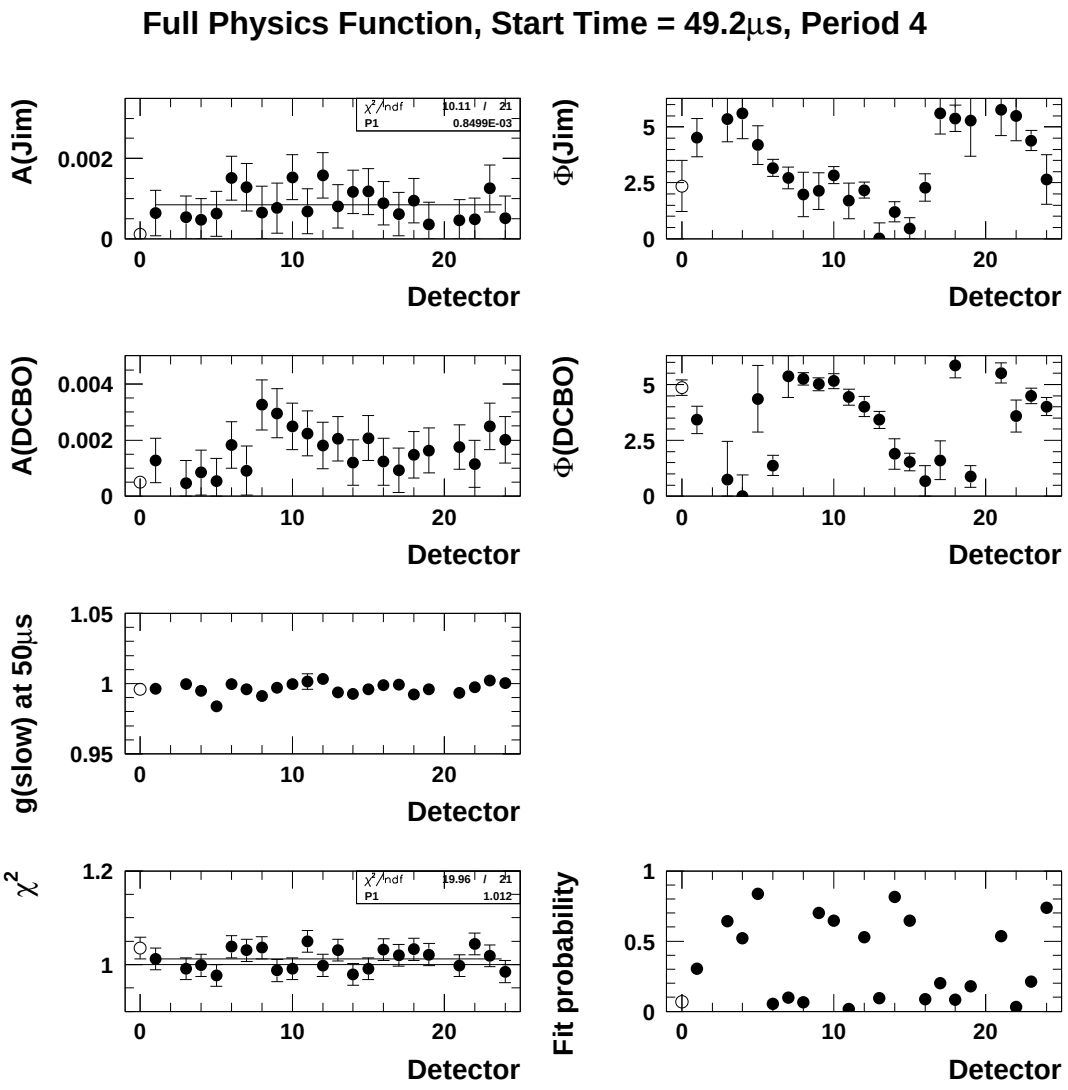
Full Physics Function, Start Time = 49.2μs, Period 4
A(Jim)
χ²/ndf 10.11 / 21
P1 0.8499E-03
0.002
0
0
10
20
Detector
Φ(Jim)
5
2.5
0
0
10
20
Detector
A(DCBO)
0.004
0.002
0
0
10
20
Detector
Φ(DCBO)
5
2.5
0
0
10
20
Detector
g(slow) at 50μs
1.05
1
0.95
0
10
20
Detector
χ²
χ²/ndf 19.96 / 21
P1 1.012
1.2
1
0
10
20
Detector
Fit probability
1
0.5
0
0
10
20
Detector

D Results from the Gain Study

D.1 Average Energy / Gain Sensitivity Factors

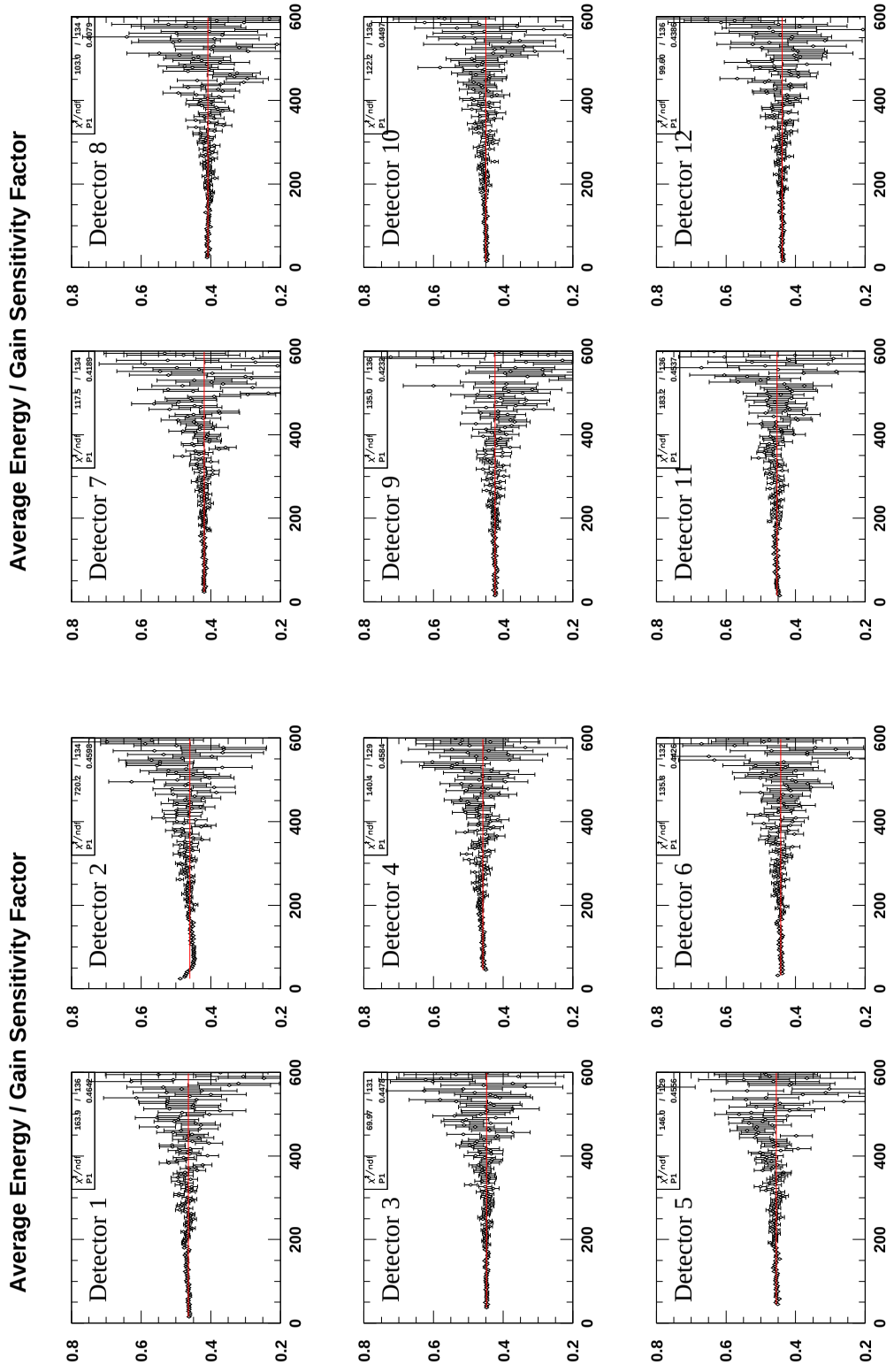

Figure 144: *Sensitivity factors for the relation between relative gain change and average energy change for a lower energy cut of 2 GeV. All run periods were combined.*

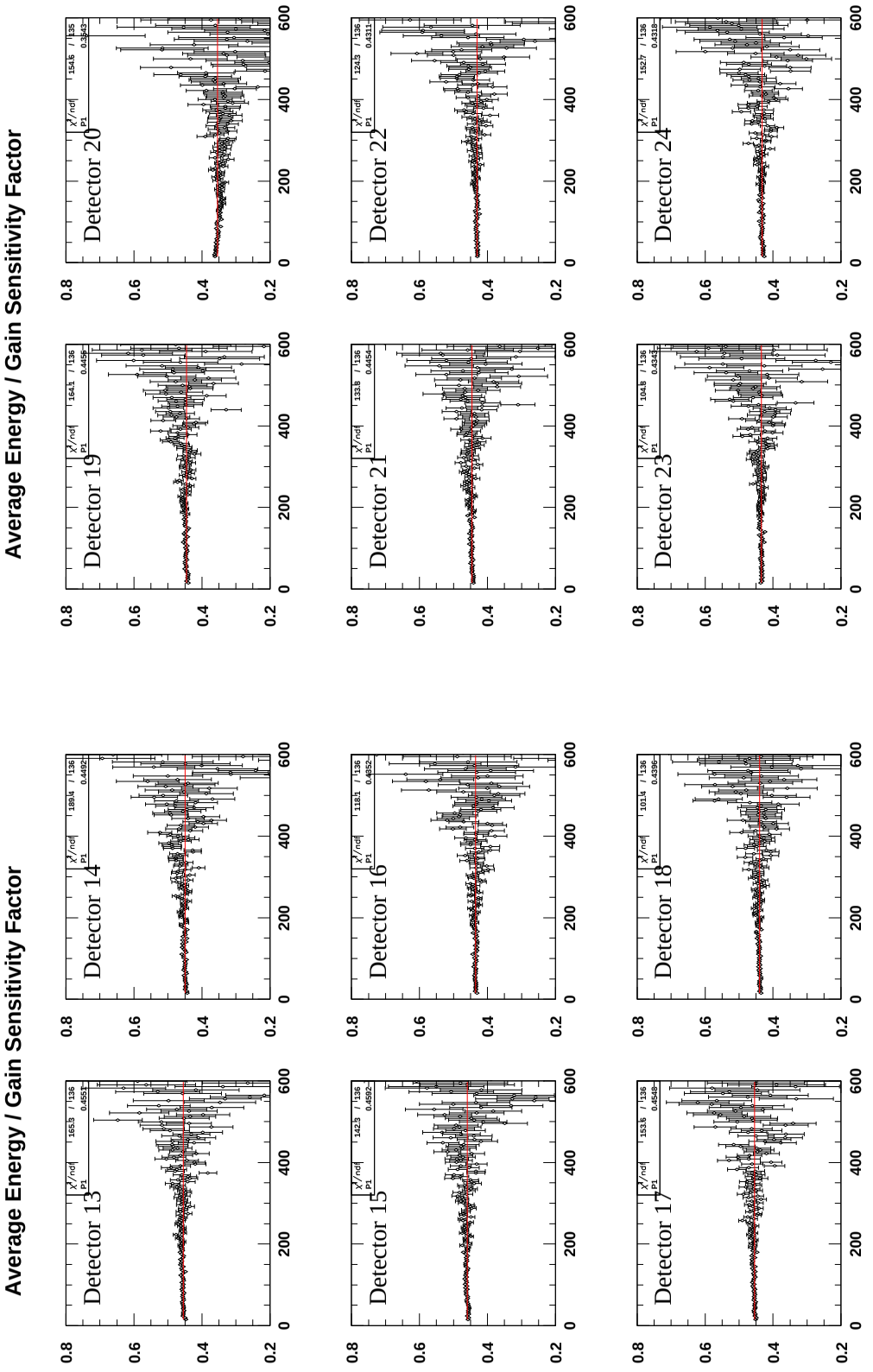

Figure 145: *Sensitivity factors for the relation between relative gain change and average energy change for a lower energy cut of 2 GeV. All run periods were combined.*

D.2 Gain versus Time for all Run Periods

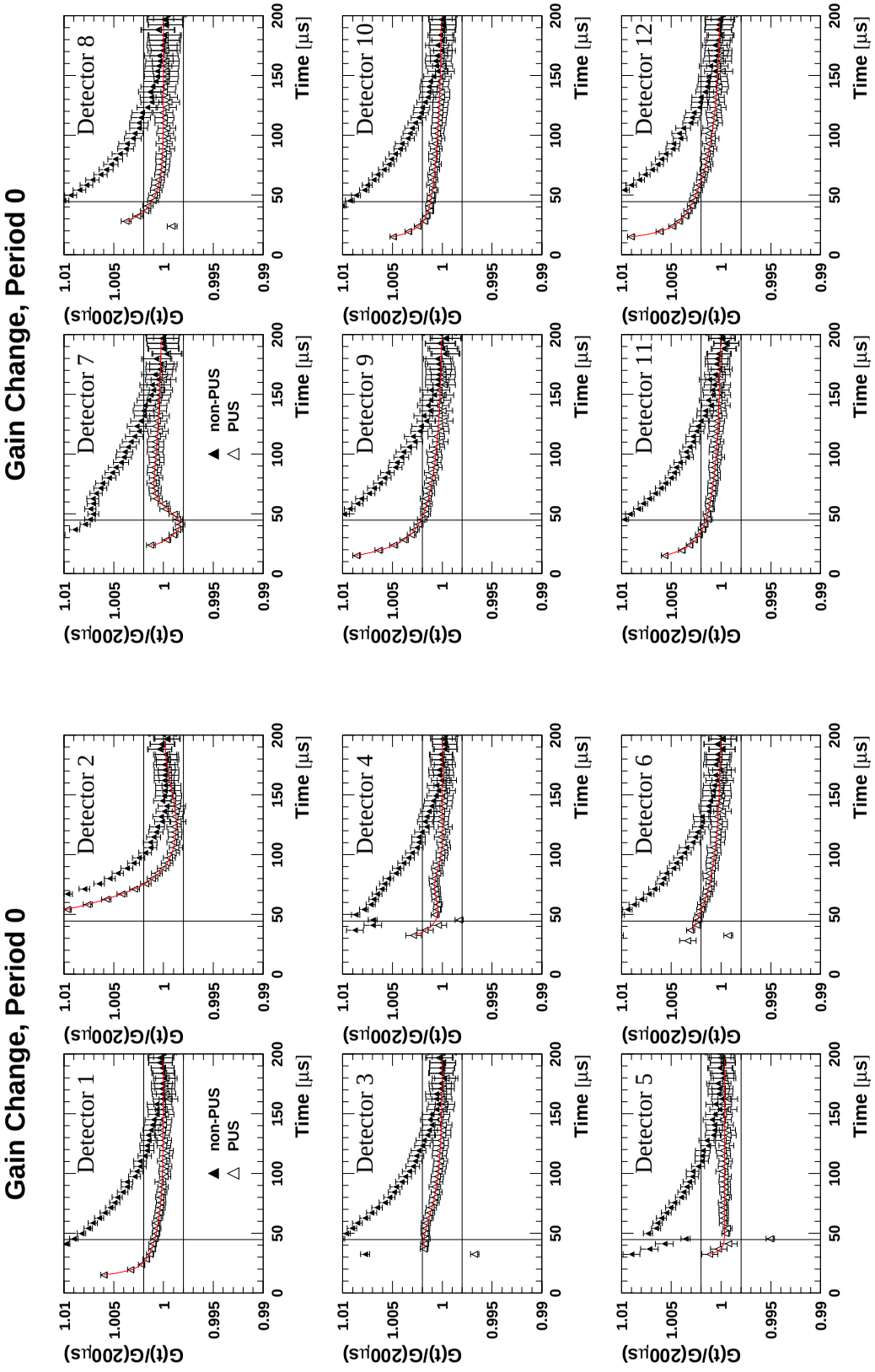

Figure 146: *Gain normalised at 200 μs for all runs (detectors 1-12).*

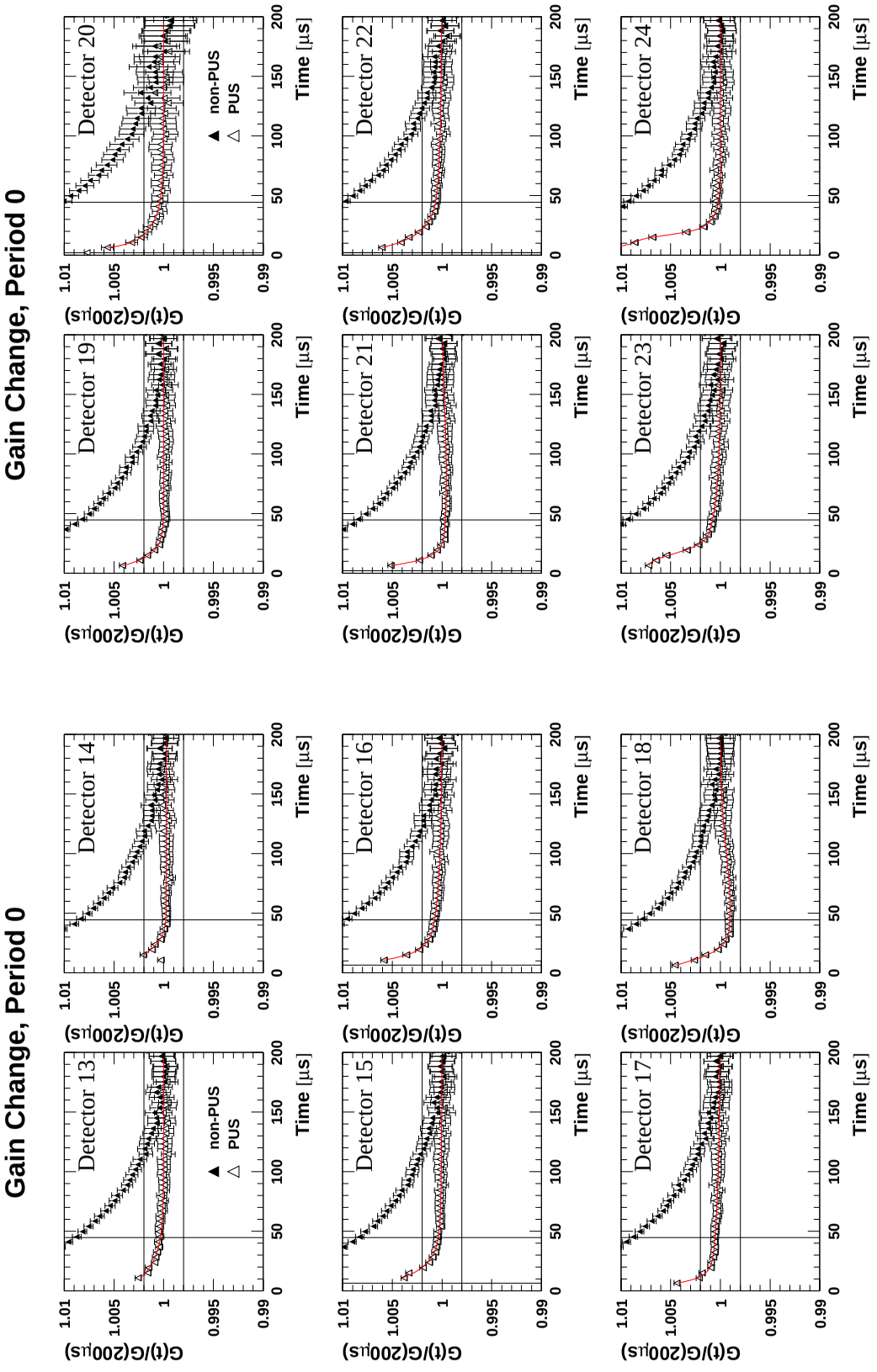

Figure 147: *Gain normalised at 200 μs for all runs (detectors 13-24).*

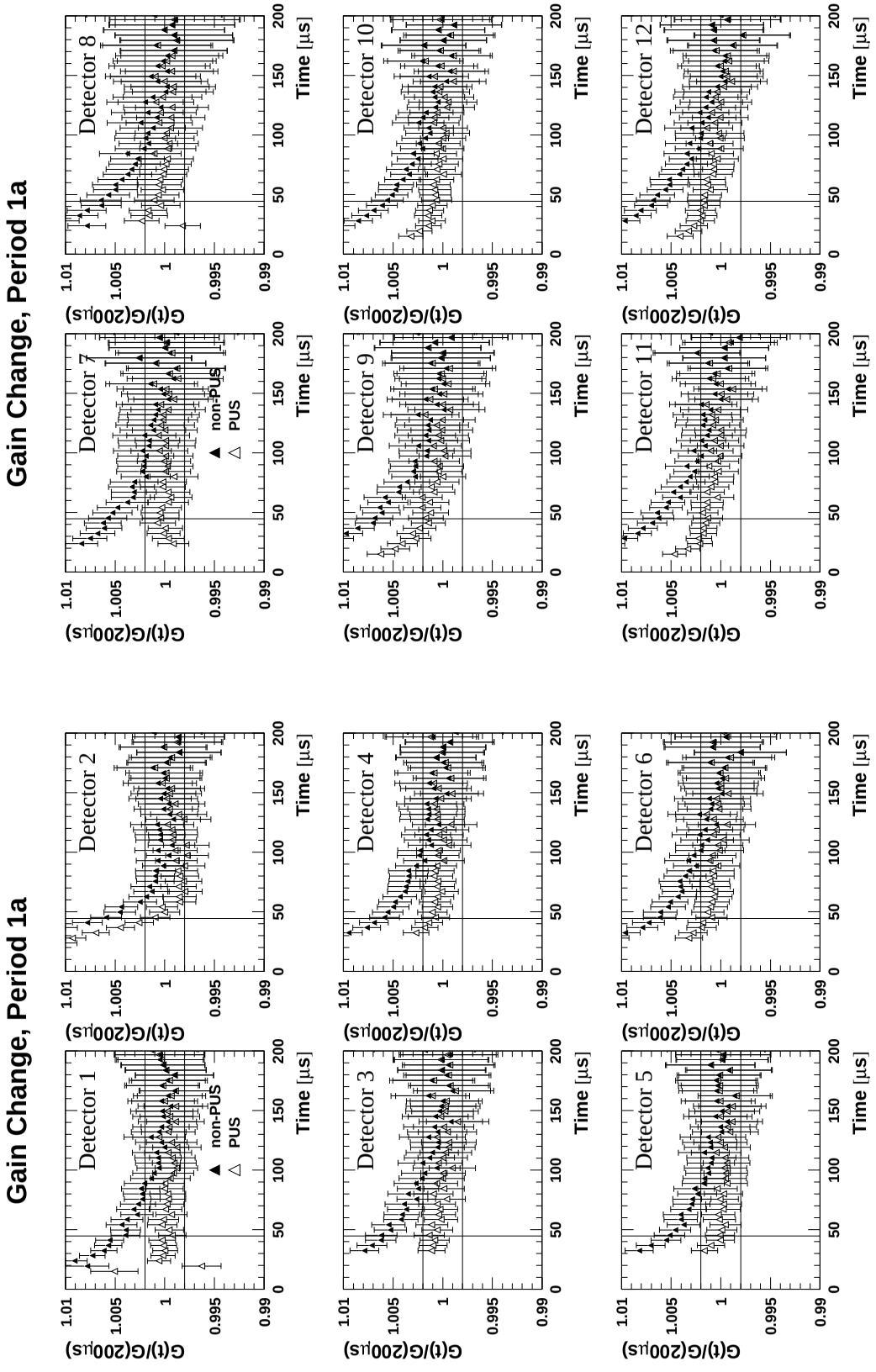

Figure 148: *Gain normalised at 200 μs for period 1a (detectors 1-12).*

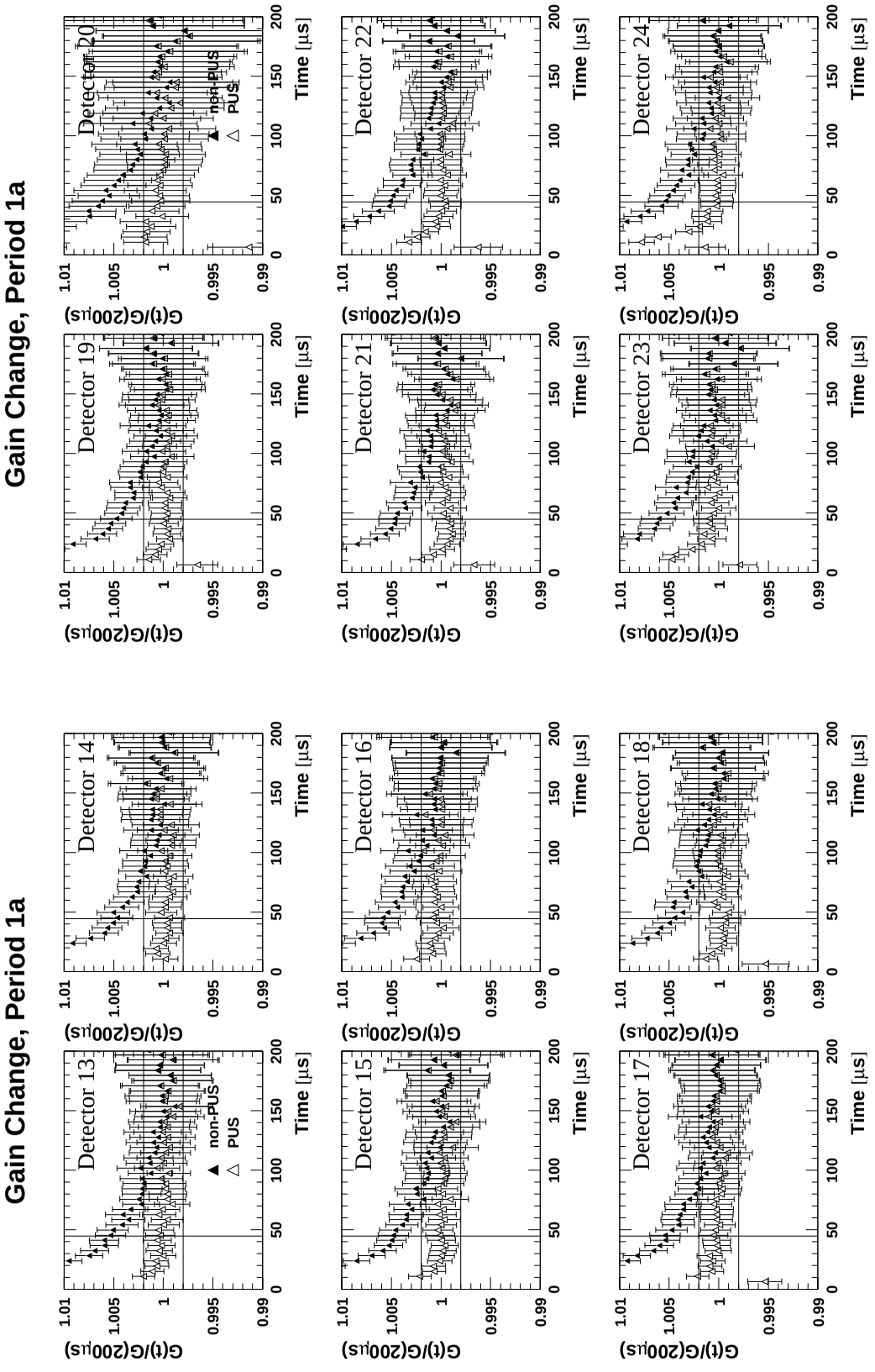

Figure 149: *Gain normalised at 200 μs for period 1a (detectors 13-24).*

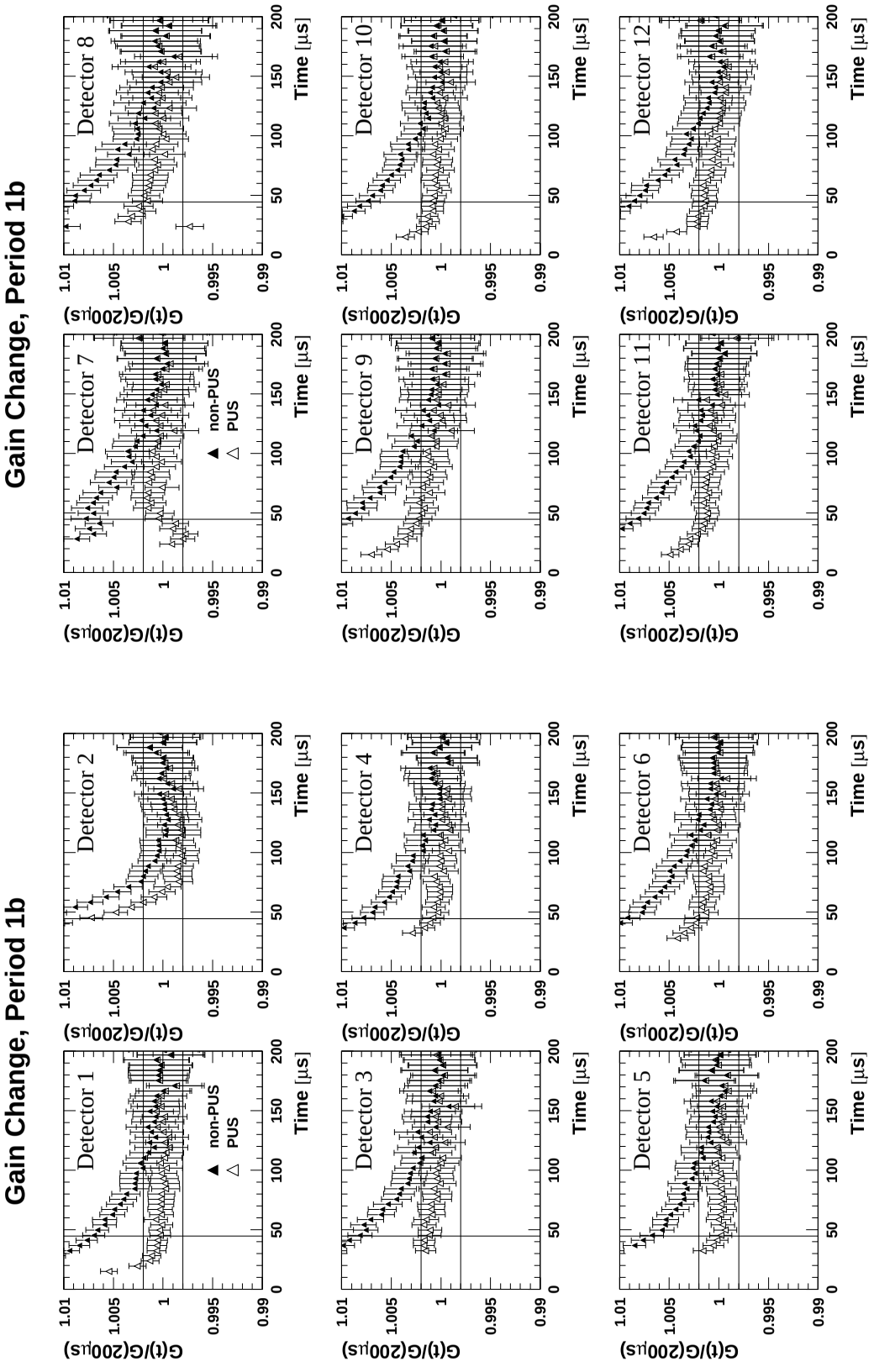

Figure 150: *Gain normalised at 200 μs for period 1b (detectors 1-12).*

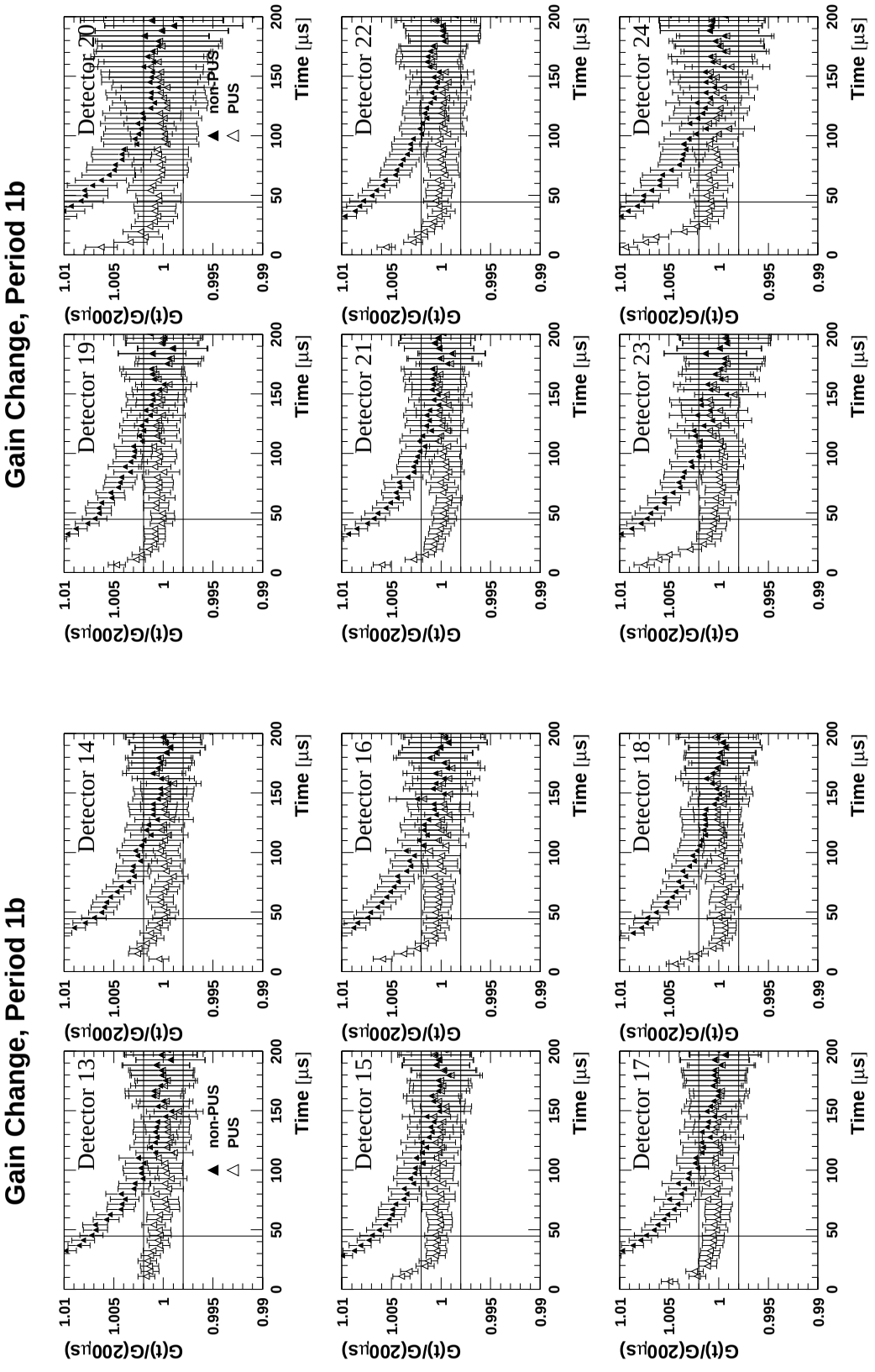

Figure 151: *Gain normalised at 200 μs for period 1b (detectors 13-24).*

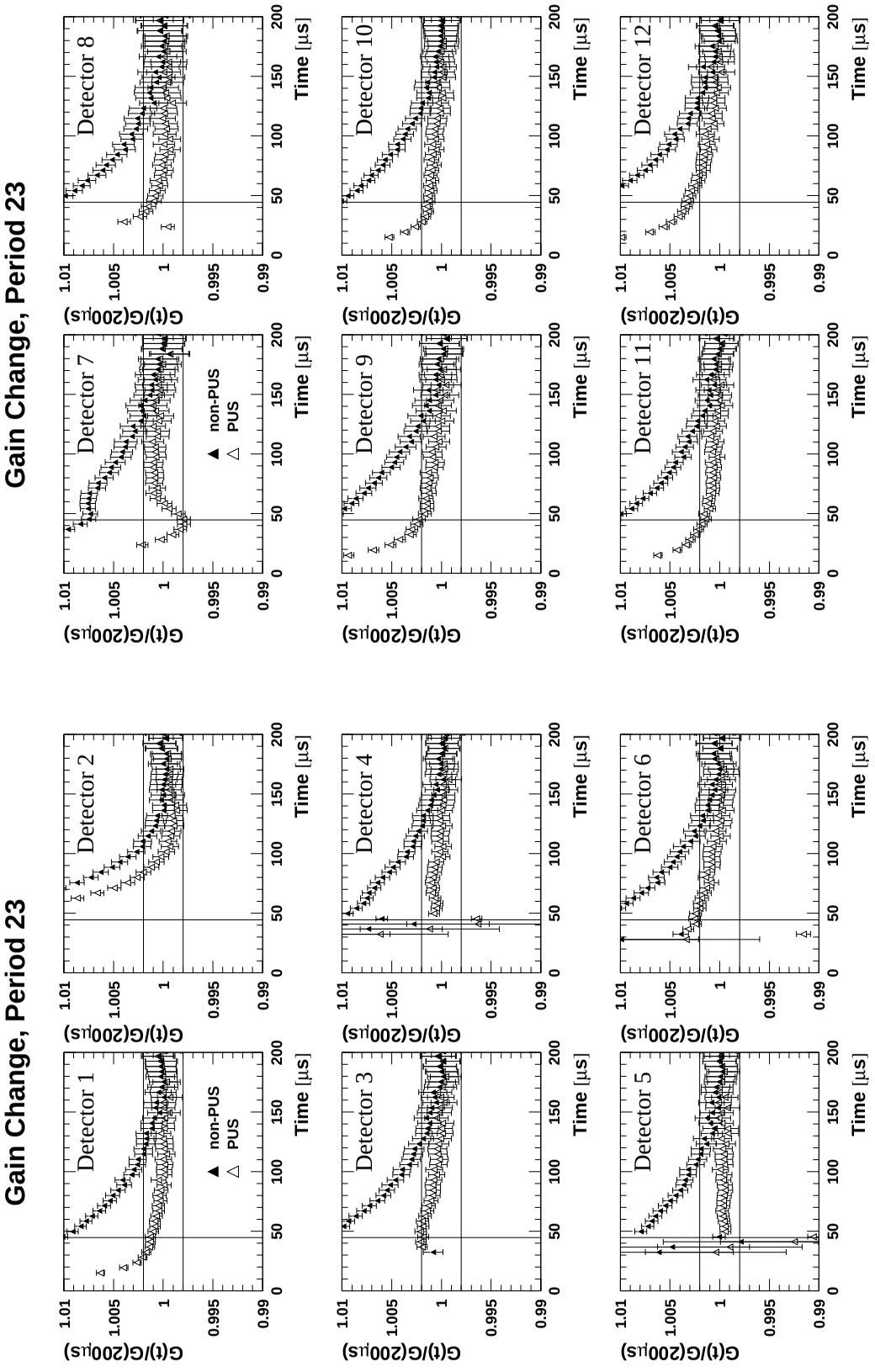

Figure 152: *Gain normalised at 200 μs for periods 2+3 (detectors 1-12).*

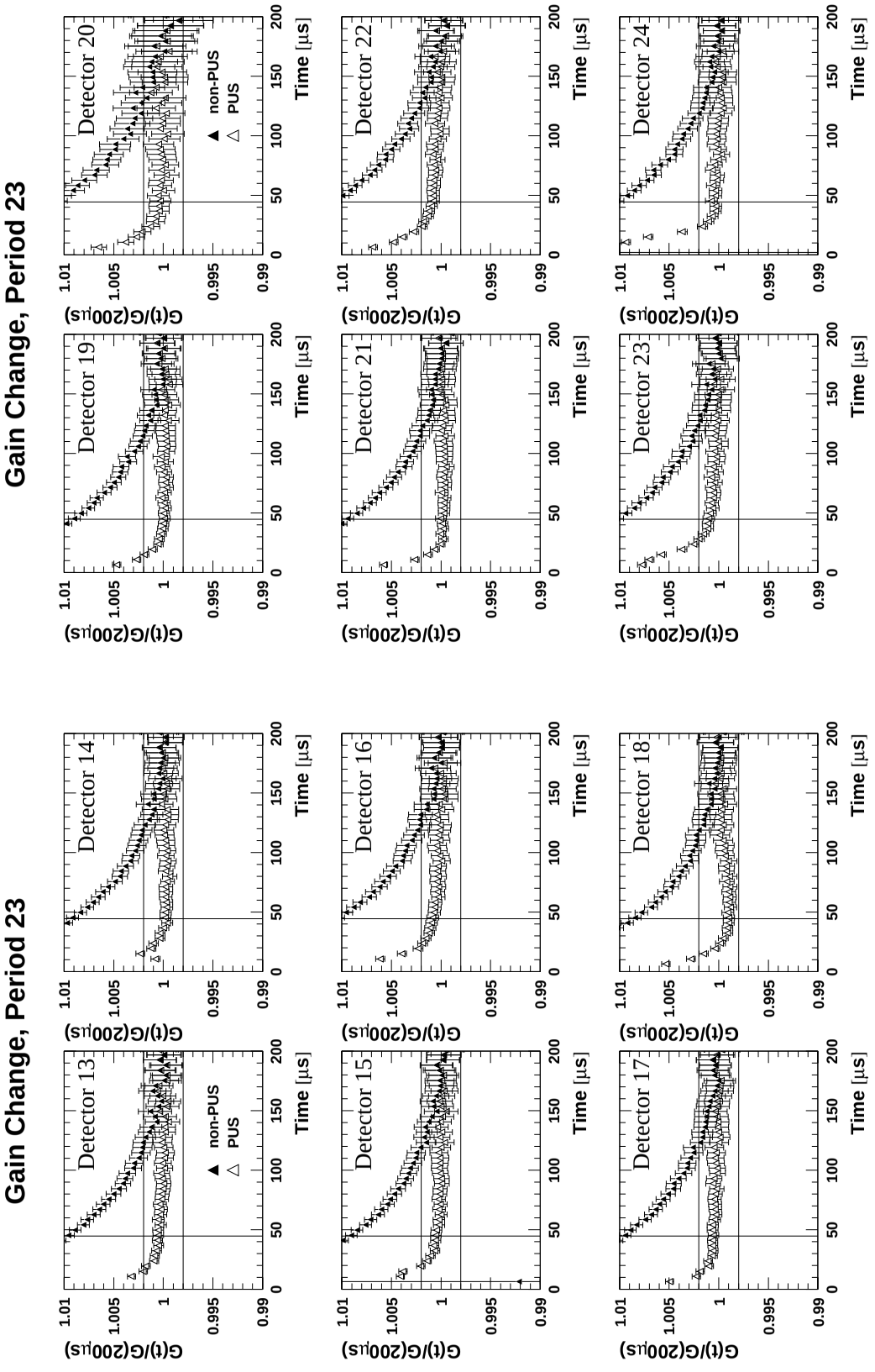

Figure 153: *Gain normalised at 200 μs for periods 2+3 (detectors 13-24).*

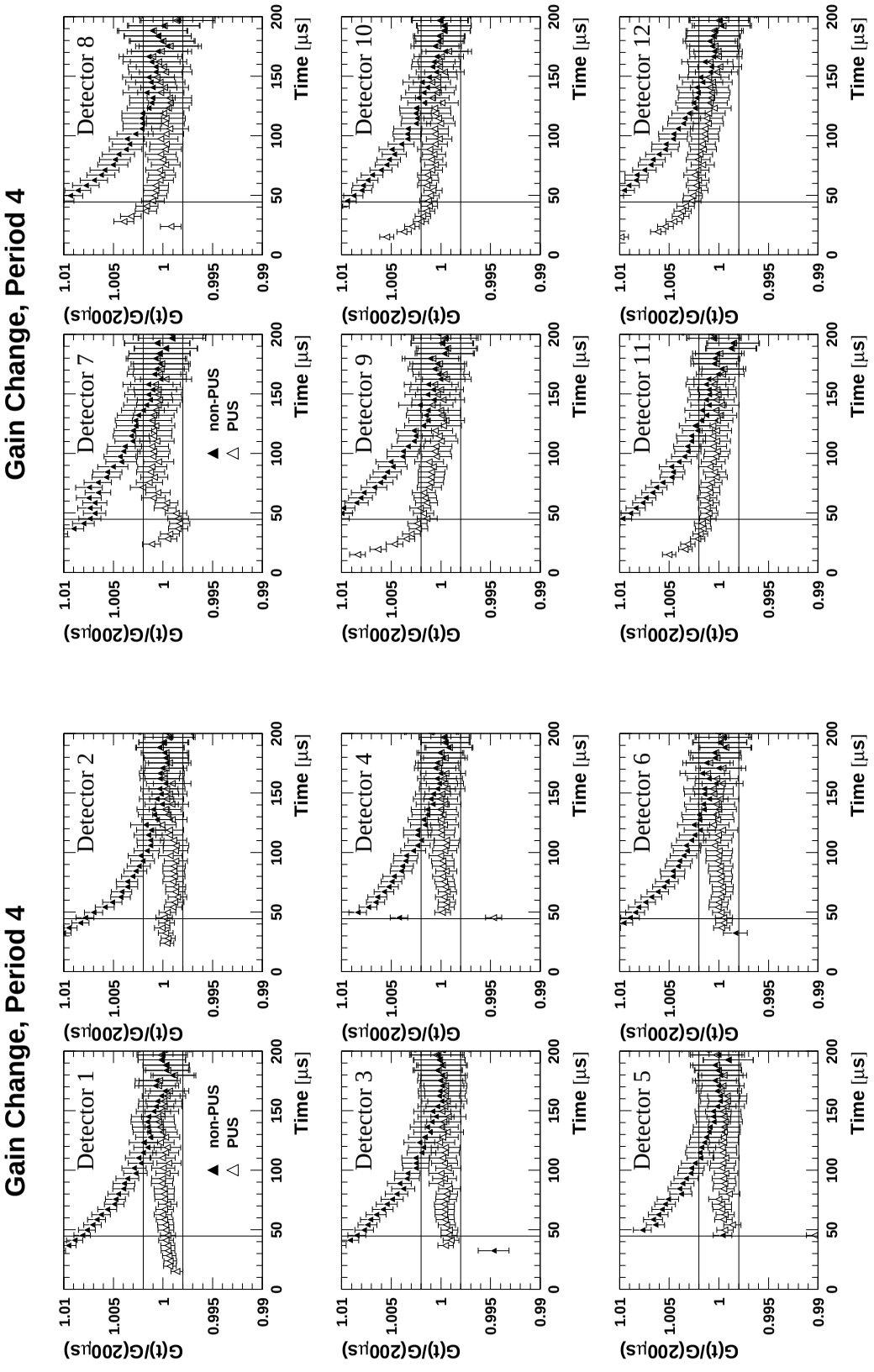

Figure 154: *Gain normalised at 200 μs for period 4 (detectors 1-12).*

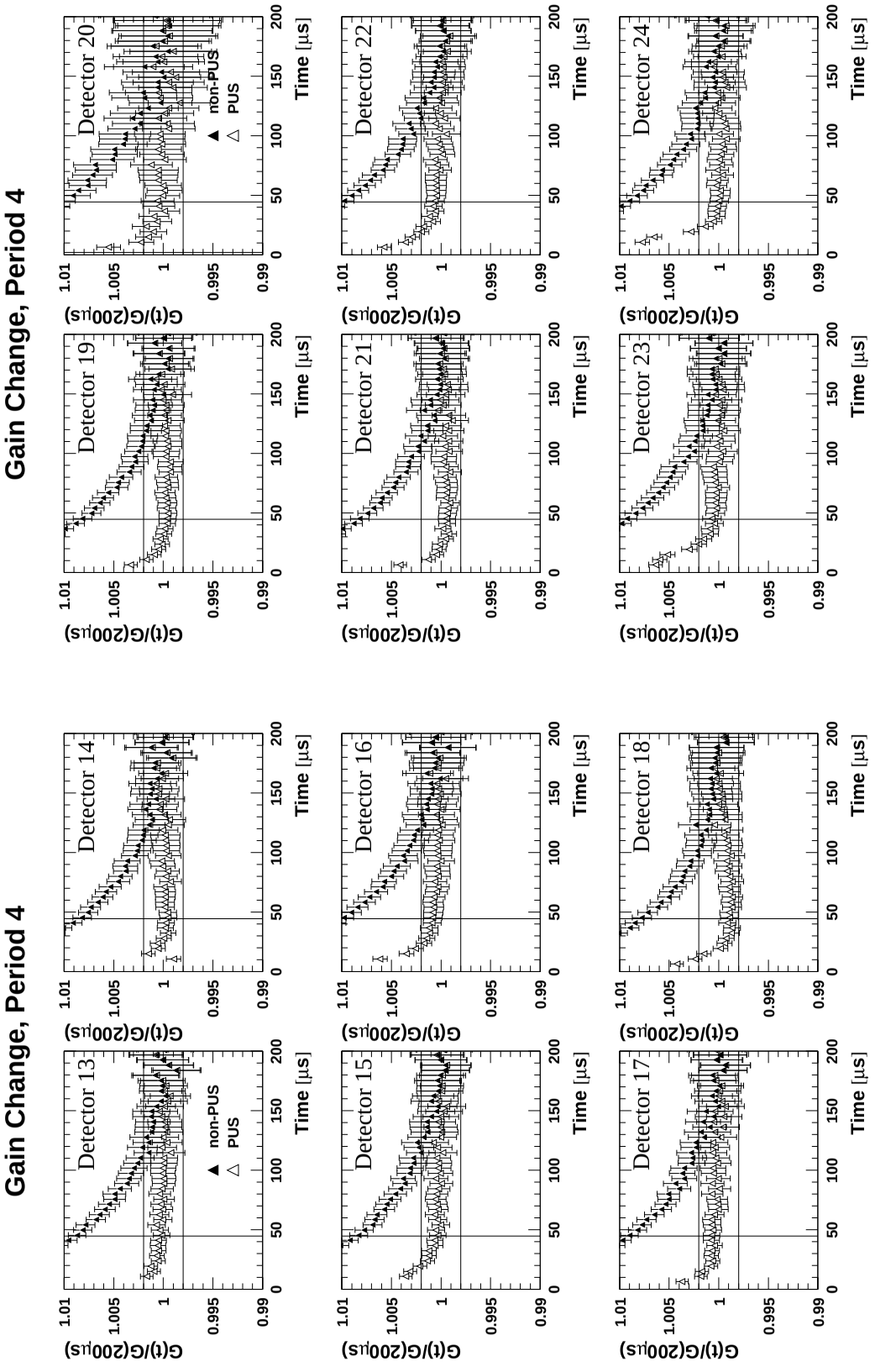

Figure 155: *Gain normalised at 200 μs for period 4 (detectors 13-24).*

D.3 Fit Results with Energy-Scale Corrected Data

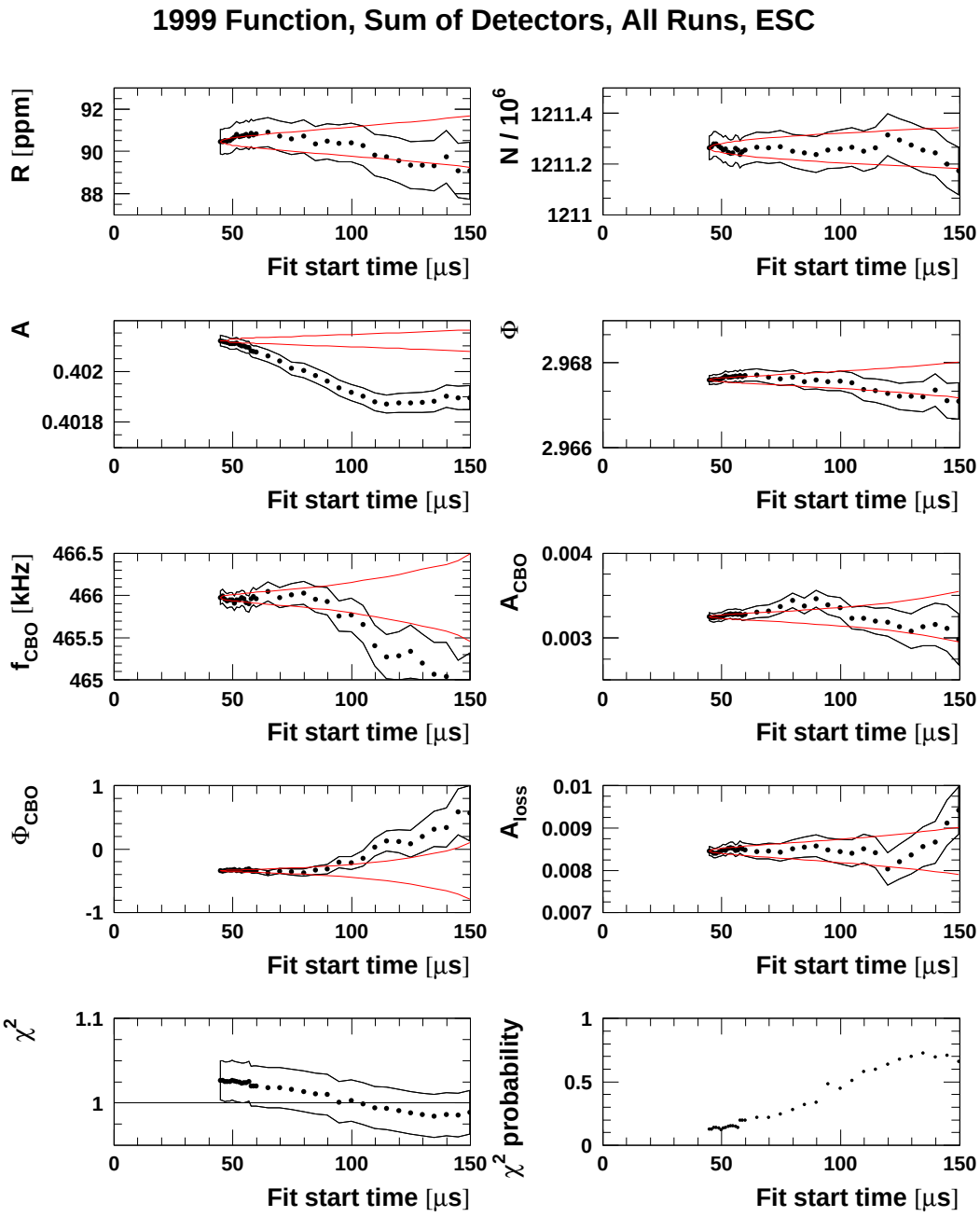

Figure 156: *Start time scan with the 1999-style function for all runs after gain correction ($\xi = 0$ in Eqn. (84)). The corresponding plot without gain correction is in Figure 97.*

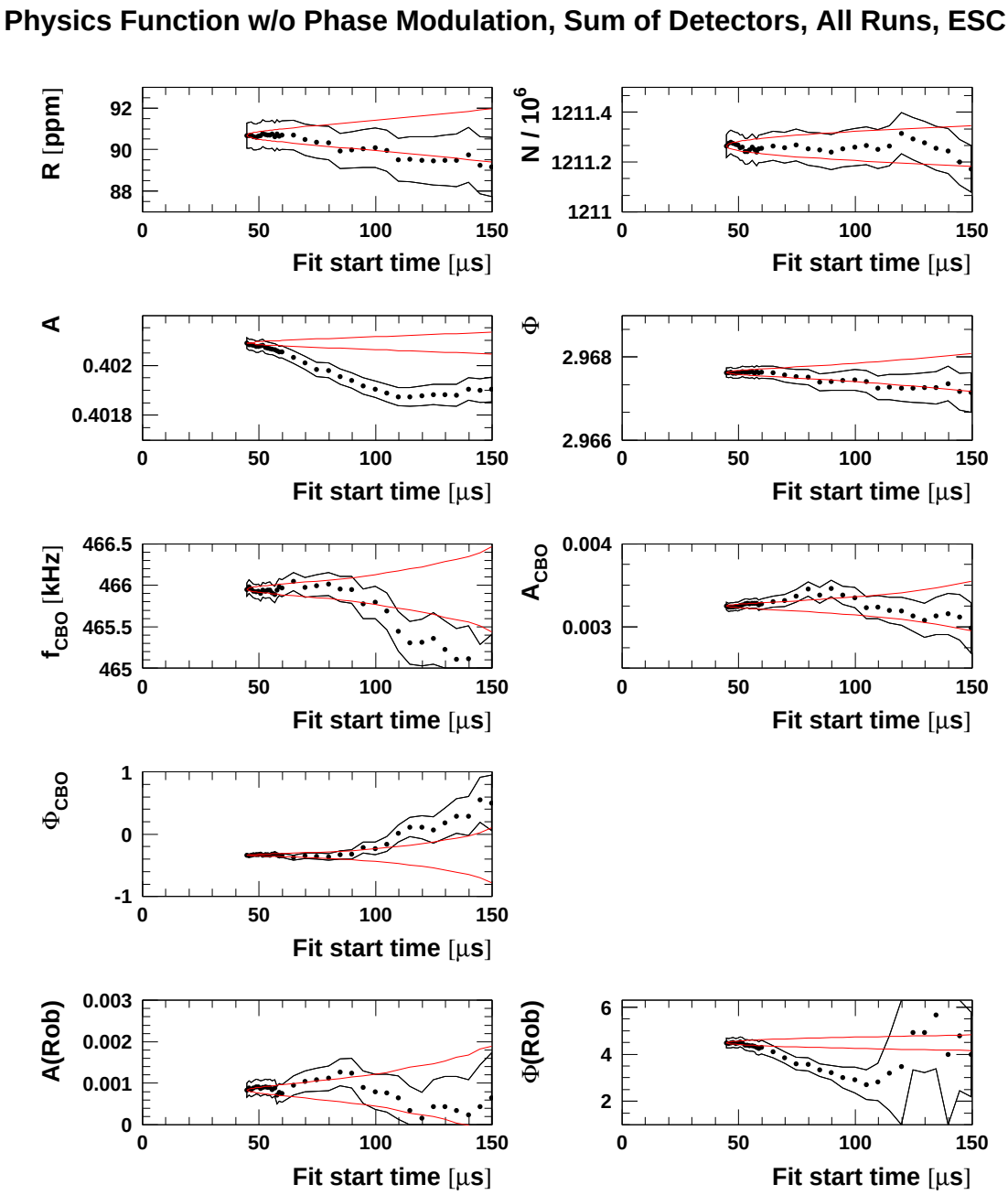

Figure 157: *Start time scan with the physics function without phase modulation for all runs after gain correction ($\xi = 0$ in Eqn. (84)). The corresponding plot without gain correction is in Figure 112.*

Physics Function w/o Phase Modulation, Sum of Detectors, All Runs, ESC

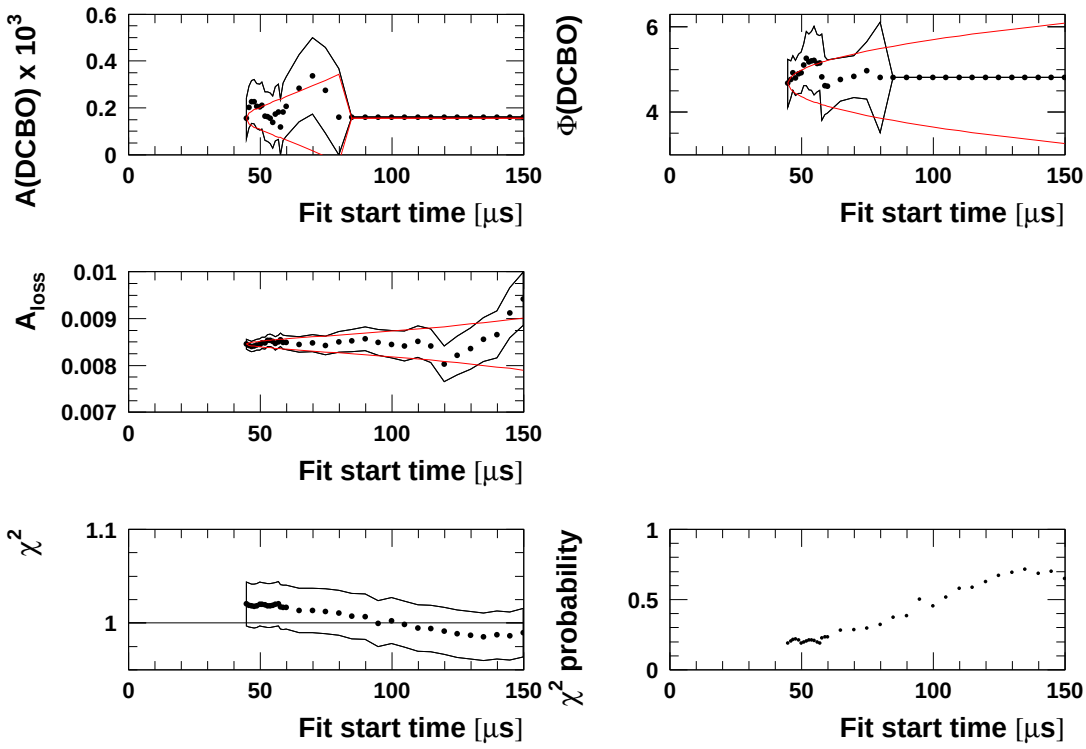

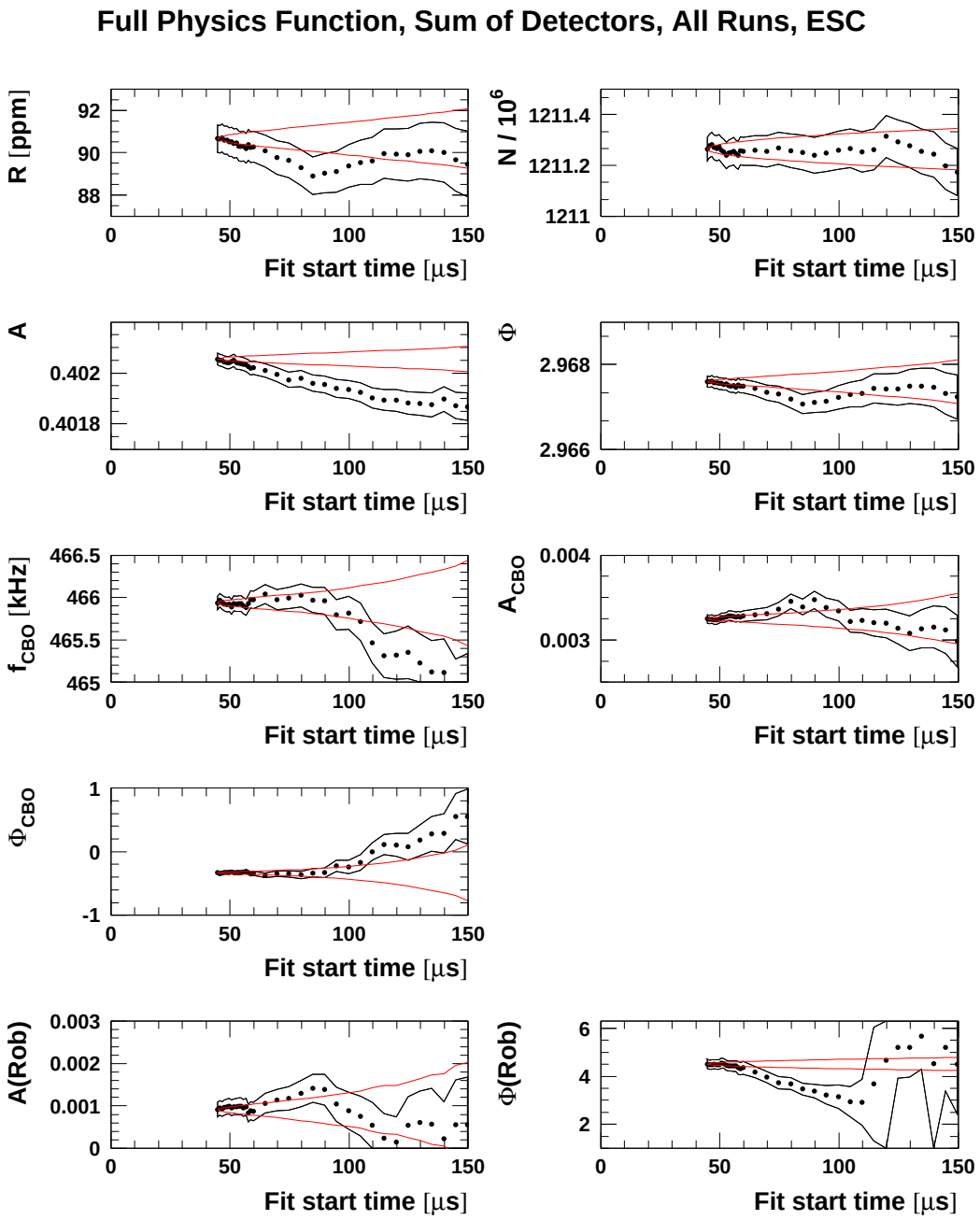

Figure 158: *Start time scan with the physics function with phase modulation (same envelope as acceptance CBO) for all runs after gain correction ($\xi = 0$ in Eqn. (84)). The corresponding plot without gain correction is in Figure 127.*

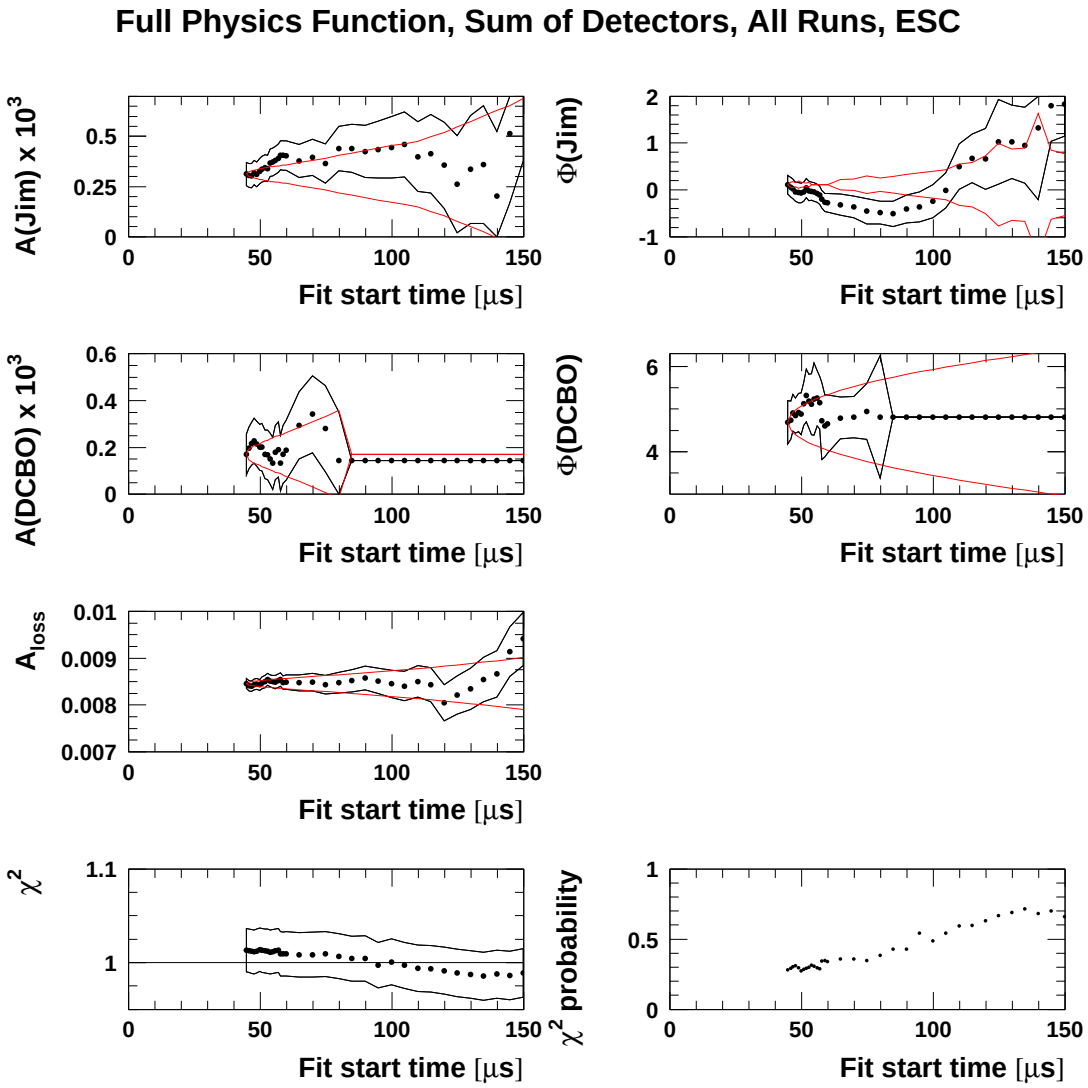
Full Physics Function, Sum of Detectors, All Runs, ESC
A(Jim) x 10^3
Φ(Jim)
A(DCBO) x 10^3
Φ(DCBO)
A_loss
χ^2
χ^2 probability
Fit start time [μs]

D.4 Study of an Energy-Scale Correction with Upper Energy Cut

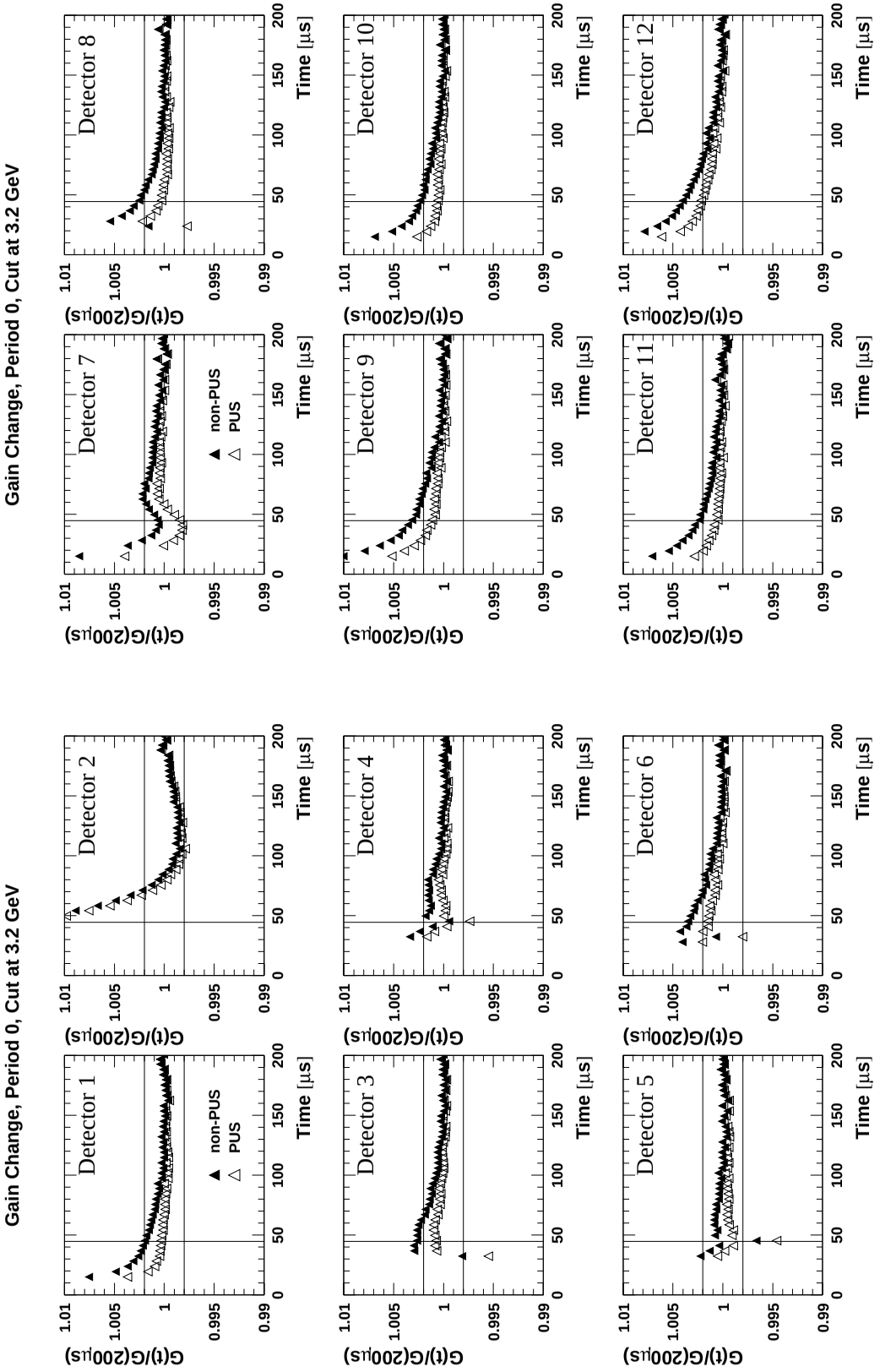

Figure 159: *Gain variations normalised at 200 μs for all runs (detectors 1-12) with an upper energy cut at 3.2 GeV.*

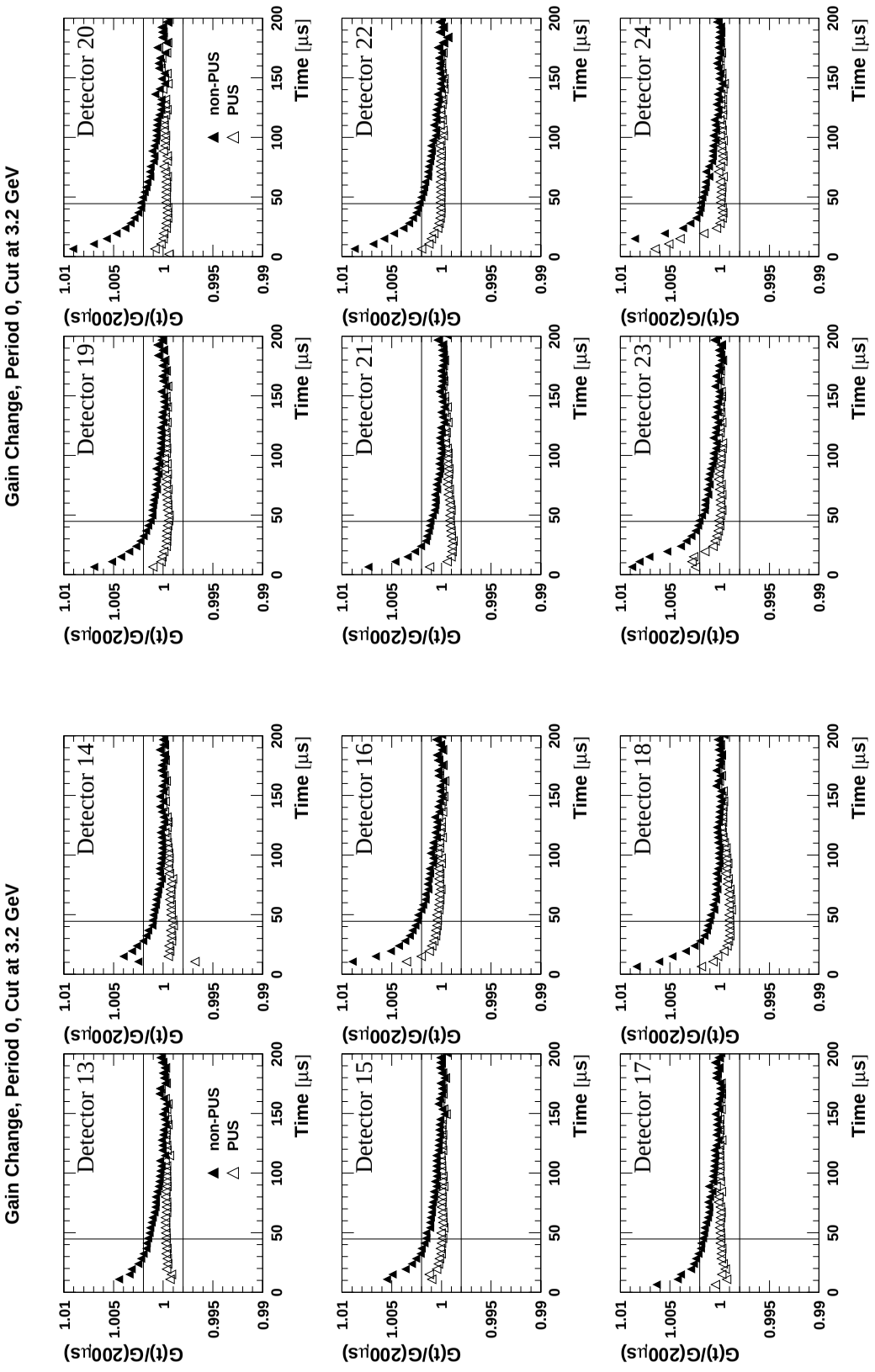

Figure 160: *Gain variations normalised at 200 μs for all runs (detectors 13-24) with an upper energy cut at 3.2 GeV.*

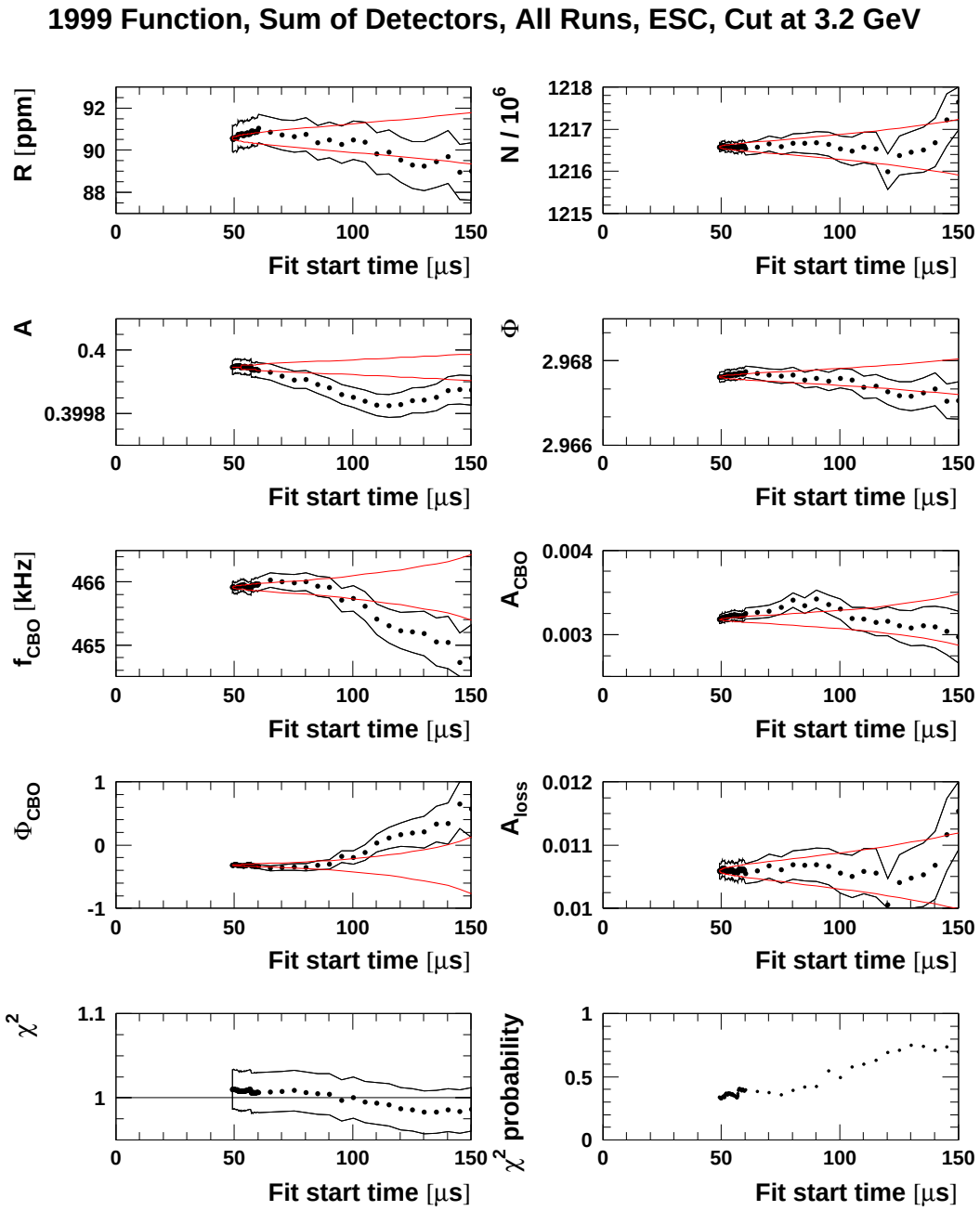

Figure 161: *Start time scan with the 1999-style function for all runs with an upper energy cut at 3.2 GeV and gain correction ($\xi = 0$ in Eqn. (84)).*

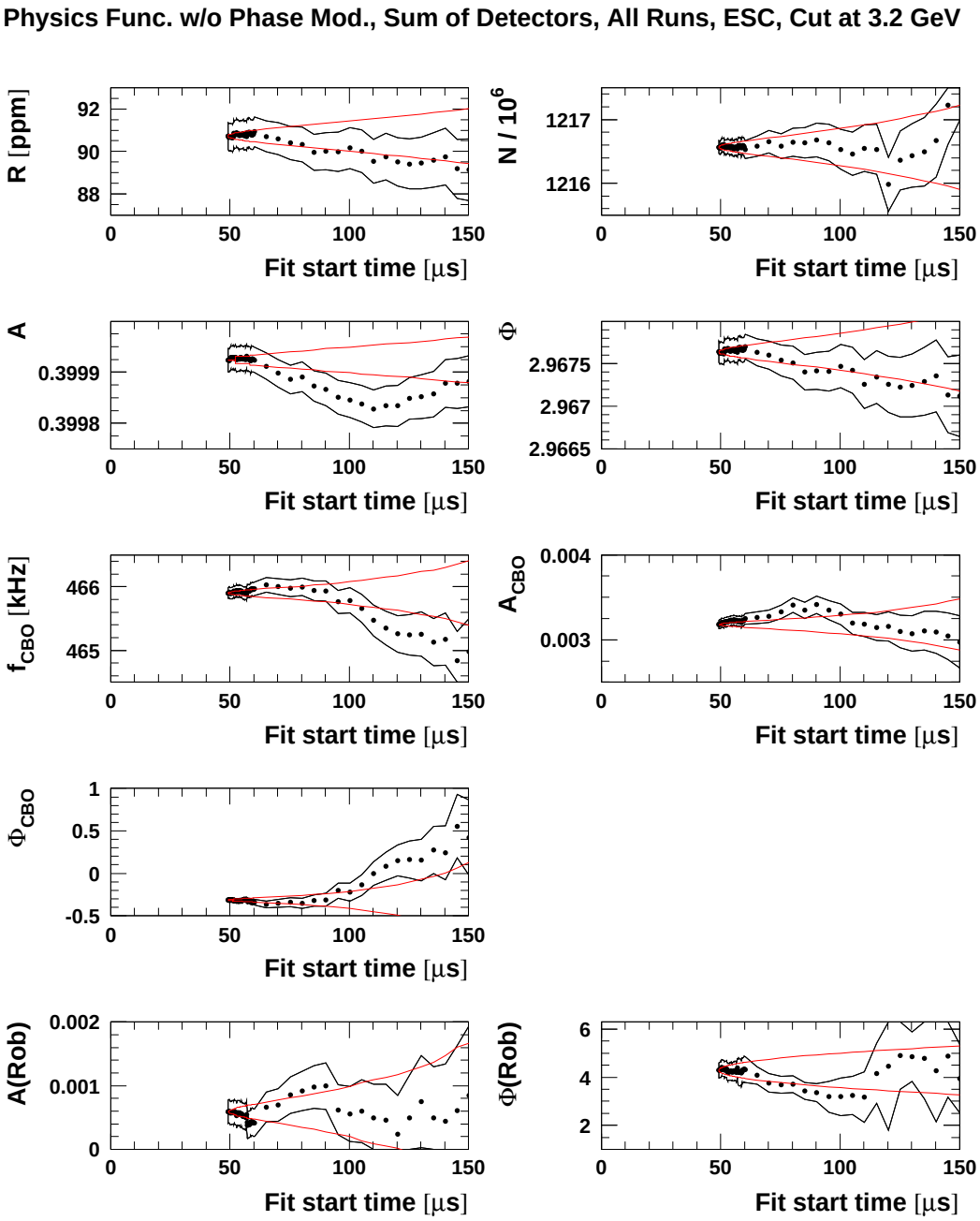

Figure 162: *Start time scan with the physics function without phase modulation for all runs with an upper energy cut at 3.2 GeV and gain correction ($\xi = 0$ in Eqn. (84)).*

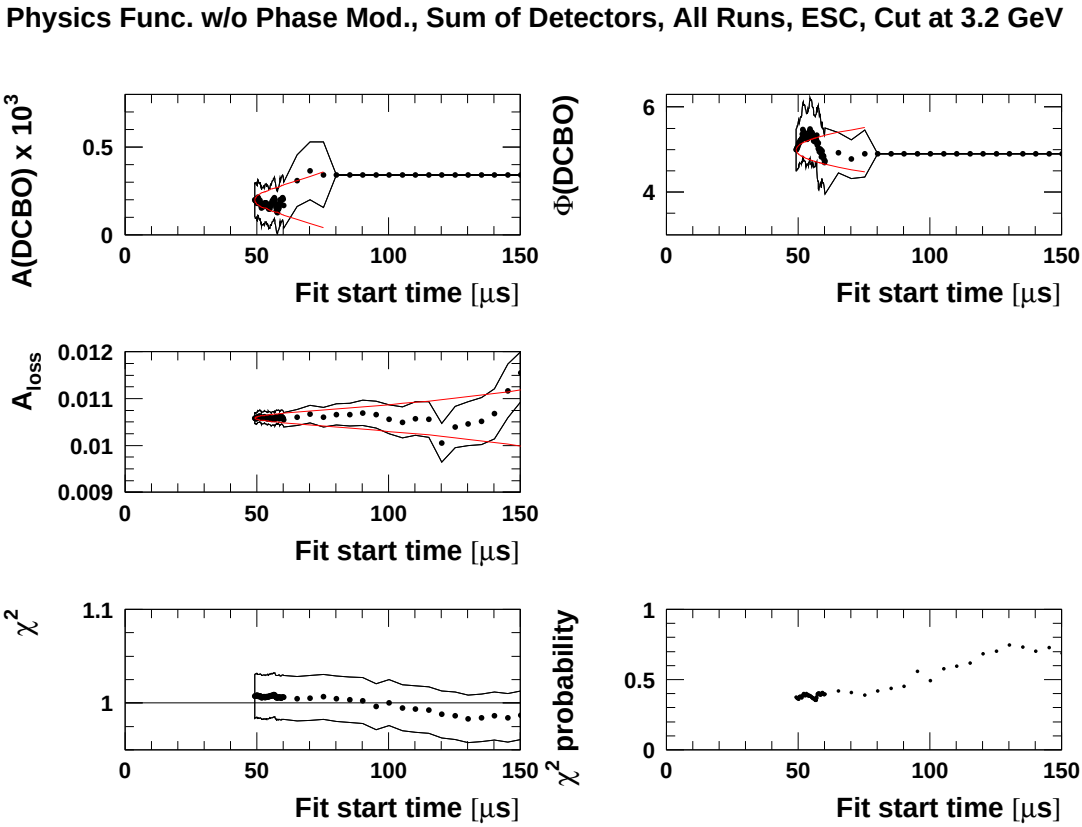
Physics Func. w/o Phase Mod., Sum of Detectors, All Runs, ESC, Cut at 3.2 GeV
A(DCBO) x 10^3
Φ(DCBO)
A_loss
χ^2
χ^2 probability
Fit start time [μs]

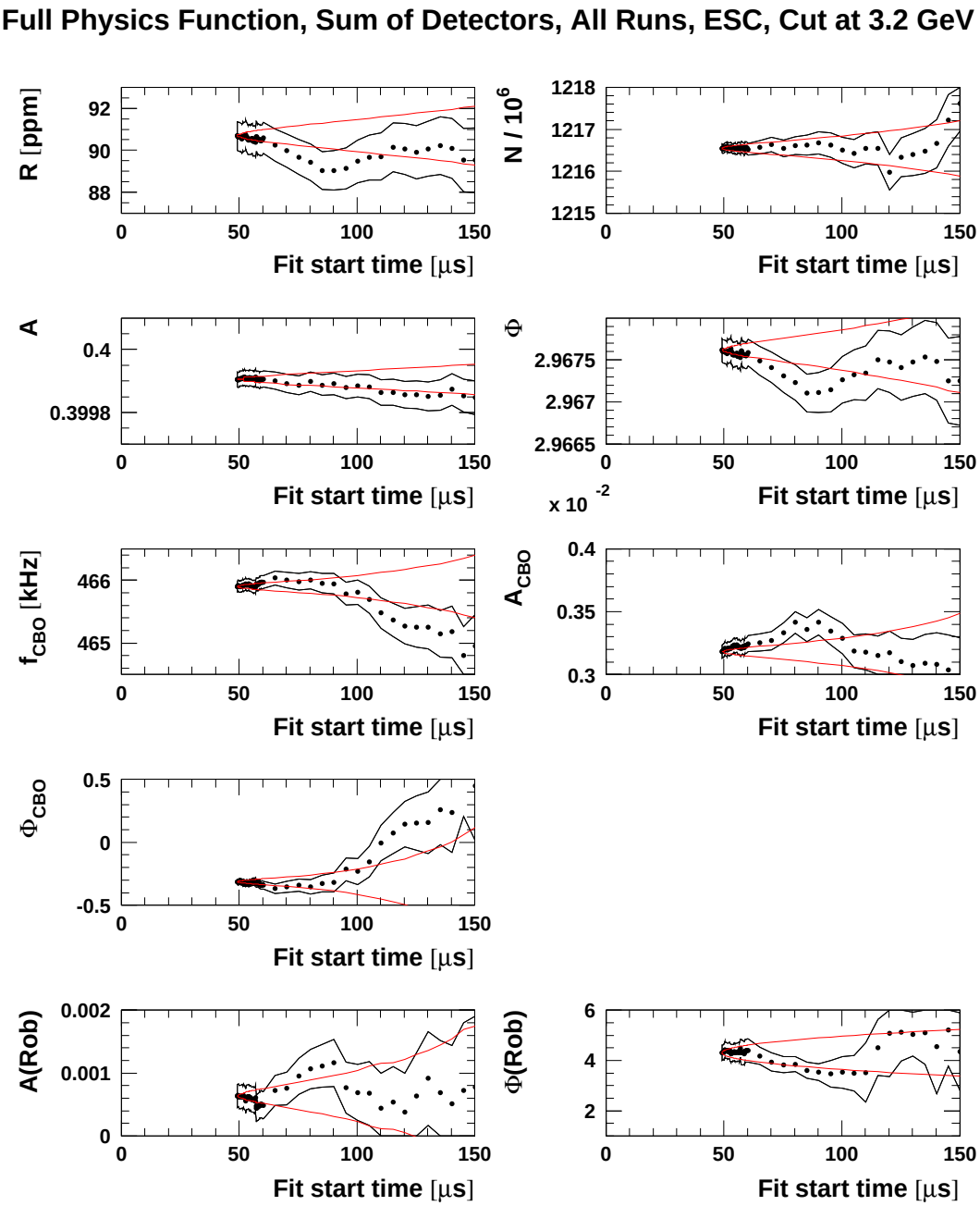

Figure 163: *Start time scan with the physics function with phase modulation (same envelope as acceptance CBO) for all runs with an upper energy cut at 3.2 GeV and gain correction ($\xi = 0$ in Eqn. (84)).*

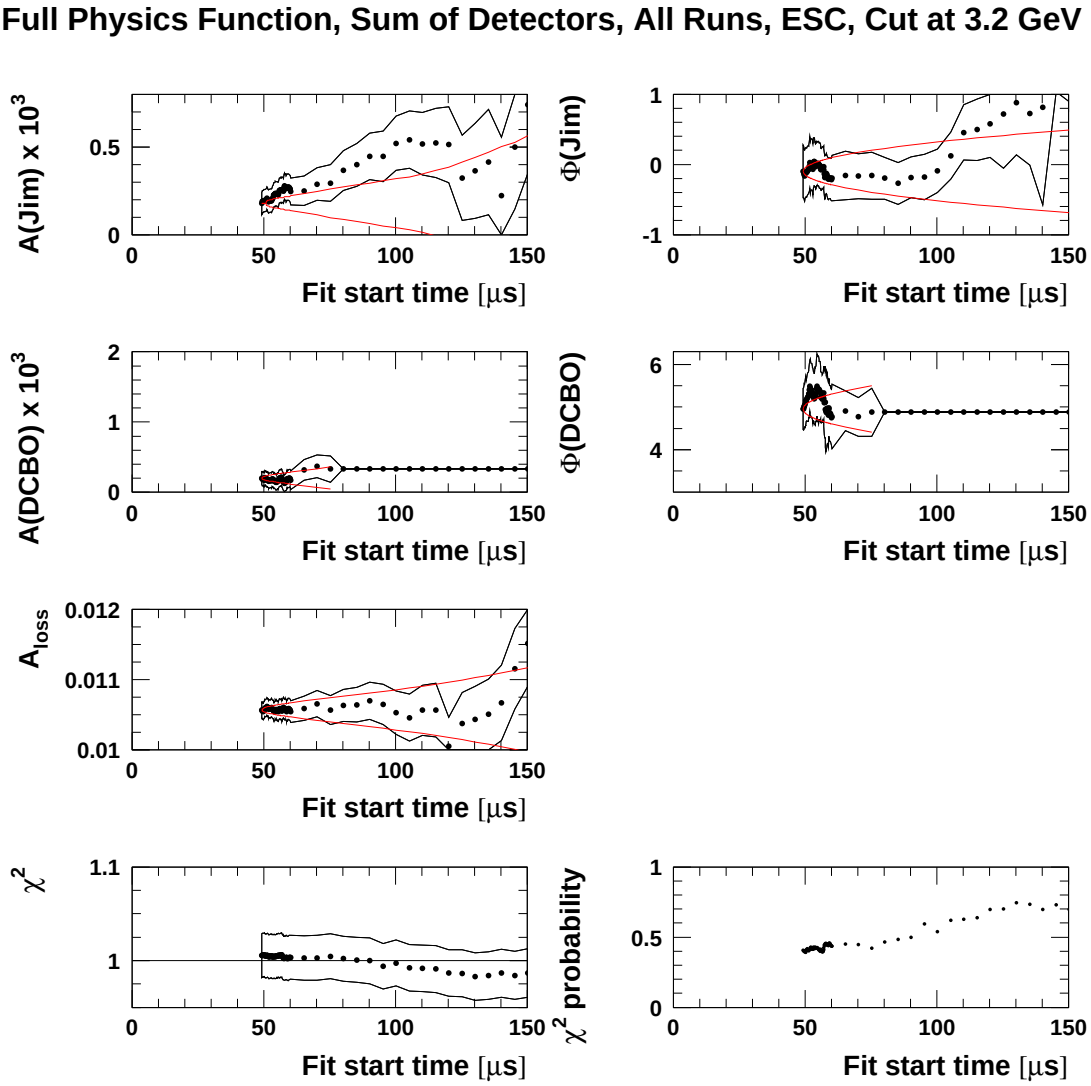
Full Physics Function, Sum of Detectors, All Runs, ESC, Cut at 3.2 GeV
A(Jim) x 10^3
Φ(Jim)
A(DCBO) x 10^3
Φ(DCBO)
A_loss
χ^2
χ^2 probability
Fit start time [μs]

E Fits to R. Carey's Monte-Carlo Data

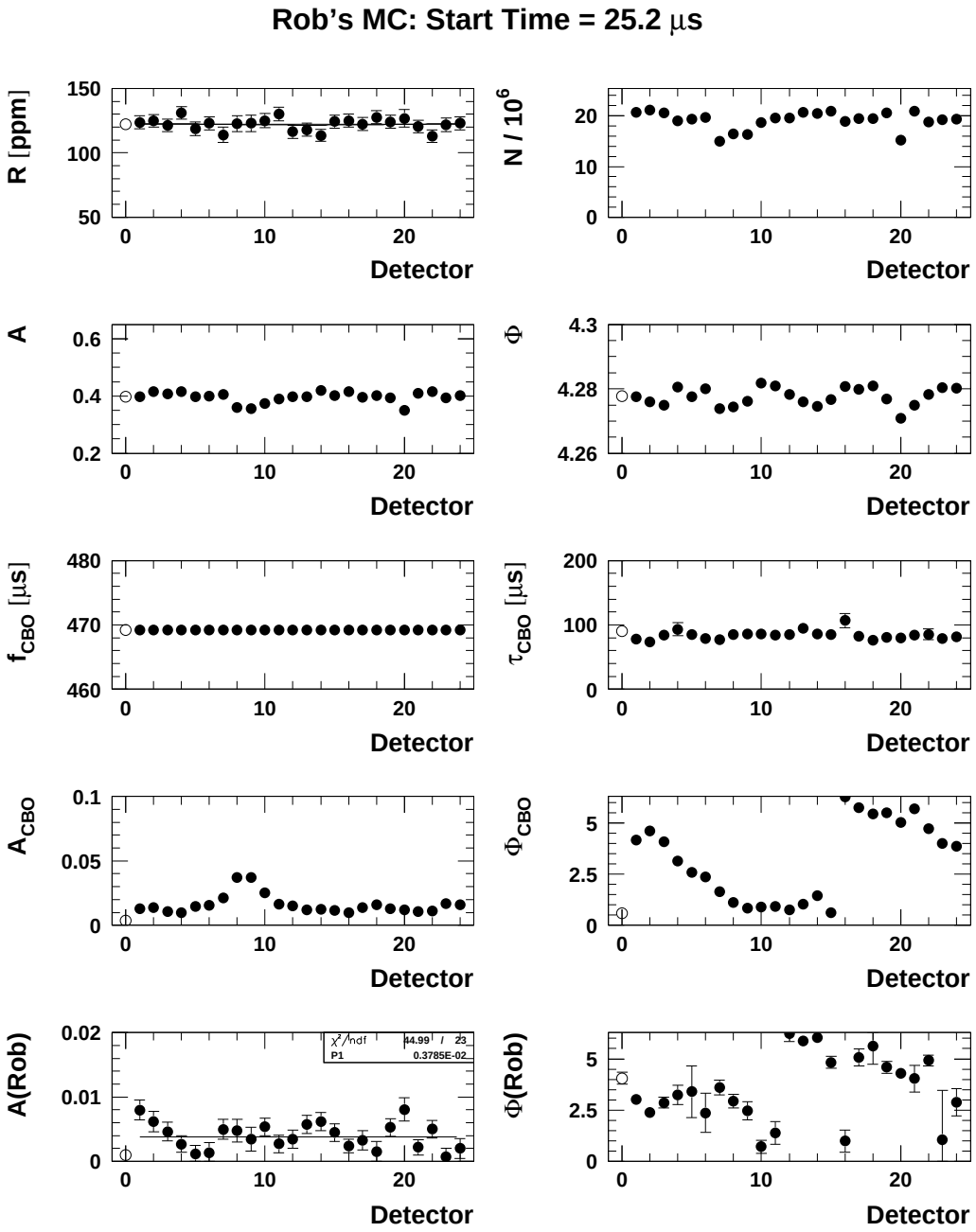

Figure 164: *Fits to individual detector spectra from simulation. The full physics function including vertical terms and without muon loss or r.s.e. terms was fitted.*

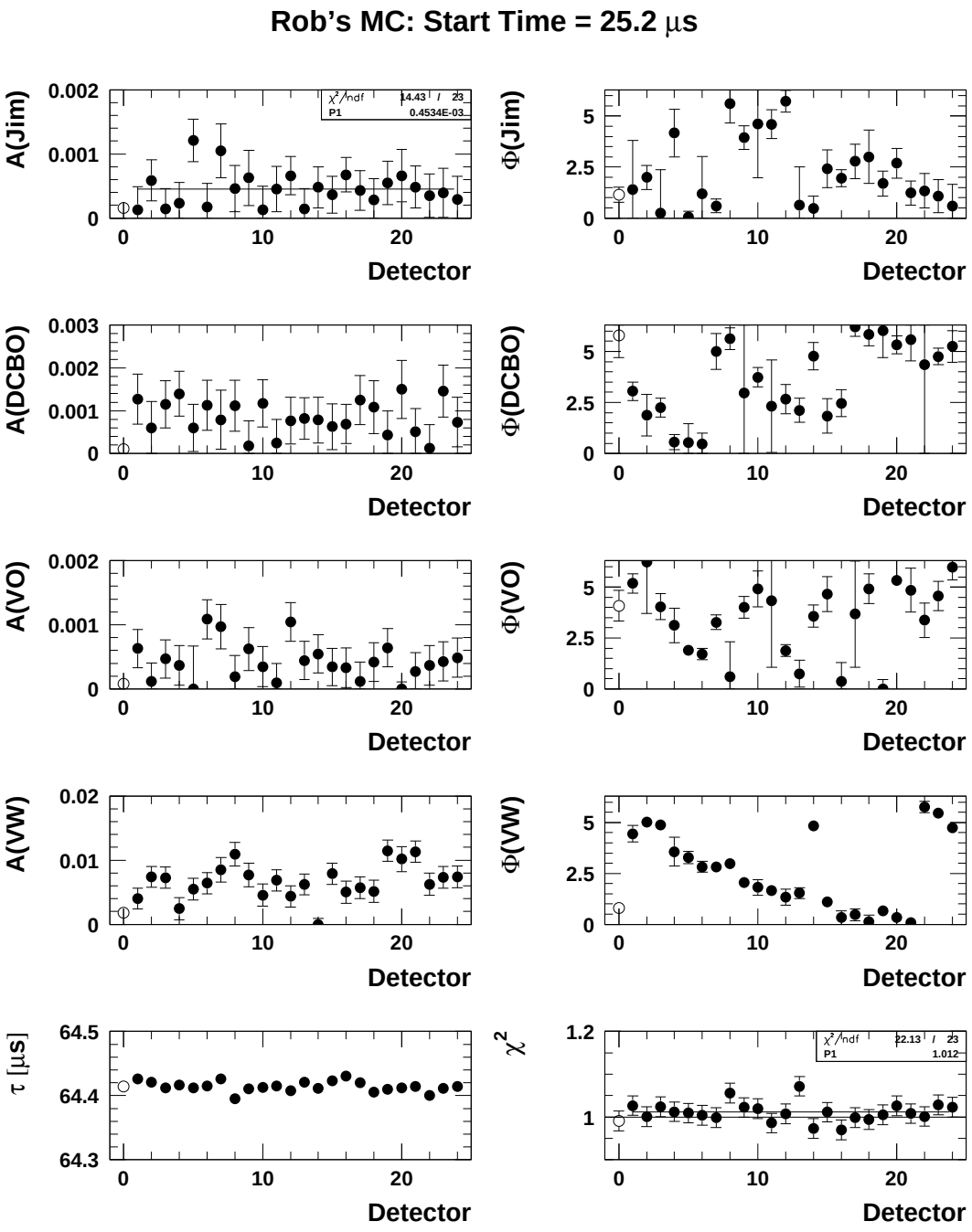
Rob's MC: Start Time = 25.2 μs
A(Jim)
Φ(Jim)
A(DCBO)
Φ(DCBO)
A(VO)
Φ(VO)
A(VW)
Φ(VW)
τ [μs]
χ²
Detector
χ²/ndf 14.43 / 23
P1 0.4534E-03
χ²/ndf 22.13 / 23
P1 1.012